The stability and assembly of sterically stabilized non-polar nanoparticles

Dissertation
zur Erlangung des Grades
des Doktors der Naturwissenschaften
der Naturwissenschaftlich- Technischen Fakultät
der Universität des Saarlandes

von

Thomas Kister

Saarbrücken
2021

Tag des Kolloquiums:	06.07.2021
Dekan:	Prof. Dr. Jörn Walter
1. Berichterstatter:	Prof. Dr. Tobias Kraus
2. Berichterstatter:	Priv.-Doz. Dr.-Ing. Guido Falk
Vorsitz:	Prof. Dr. Dominik Munz
Akad. Mitarbeiter:	Dr. Andreas Tschöpe

"It doesn't matter how beautiful your theory is, it doesn't matter how smart you are. If it doesn't agree with experiment, it's wrong. "

Richard Feynman

Acknowledgements

Ich möchte zuerst Prof. Dr. Tobias Kraus danken. Als Leiter der Gruppe Strukturbildung war er von Anfang an mein Betreuer, der mich durch die gesamte Zeit als Doktorand immer beraten und unterstützt hat. Durch seine offene und freundliche Art war die Arbeitsatmosphäre und Kommunikation innerhalb der Gruppe mehr als angenehm. Er ermöglichte mir die Teilnahme an verschiedenen internationalen Konferenzen, was nicht selbstverständlich war. Für die unzähligen Diskussionen, die Unterstützung beim Erstellen wissenschaftlicher Abhandlungen und für das Vertrauen möchte ich hier noch einmal meinen Dank aussprechen. Ich hätte die Arbeit sonst nicht abschließen können.

Ebenfalls möchte ich Prof. Dr. Eduard Arzt meinen Dank aussprechen. Als Leiter des renommierten Leibniz Institut für Neue Materialien gab er mir die Möglichkeit, meine Doktorarbeit an einem Institut zu erstellen, welches nicht nur gut ausgestattet, sondern auch weltweit bekannt ist.

Einen großen Dank auch an Prof. Dr. Gerhard Wenz, Leiter der organischen, makromolekularen Chemie. Während meiner Zeit als Doktorand war er mein wissenschaftlicher Begleiter. Durch mehrere wissenschaftliche Diskussionen hat er mir neue Wege gezeigt. Ich möchte auch hier meinem Zweitgutachter Prof. Dr. Guido Falk, Leiter der Arbeitsgruppe für Struktur- und Funktionskeramik, meinen Dank aussprechen.

Ein Dank geht auch an die restlichen Mitglieder der Gruppe Strukturbildung. Im Besonderen danke ich Anika Kleemann für die vielen Synthesen und für die Einführung ins Labor. Ich danke Johann Lacava für die Zeit, die sie mir in den ersten Monaten entgegengebracht hat und für die Unterstützung bei der Herstellung meiner ersten Suprapartikel.

Ein besonderer Dank geht auch an Dominik Gerstner, Aljosha-Rakim Jochem und Andreas Hegetschweiler. Sie waren meine ersten PhD Kollegen in einer Zeit, wo die Gruppe noch sehr klein war. Ich danke auch Johannes Maurer, Beate Reiser, Indra Backes, Anna Zimmermann, David Doblas-Jimenez, Lola Gonzalez-Garcia und Ioannis Kanelidis. Durch unzählige Diskussionen und durch Ihr Fachwissen halfen sie mir neue Ideen und Wege zu entwickeln.
Ich danke auch meinen langjährigen Bürokollegen Johanna Blass, Susanne Selzer und Arzu Colak. Durch Sie war die Arbeitsatmosphäre immer angenehm.
Ebenfalls danke ich meinen Masterstudenten Jonas Hubertus, Hei Tung Lin, Marina Cano-Bonilla und Andrea Pyttlik. Auch wenn sie es mit mir nicht immer leicht hatten, haben sie trotzdem alle hervorragende Arbeiten abgeliefert.
Am Ende möchte ich noch meiner Familie und meinen Freunden danken. Sie unterstützten mich auch in Zeiten, wo es nicht immer glatt lief, haben mich ermutigt weiter zu machen und haben mir auch gegebenenfalls die Meinung gesagt.

Publications and contribution

The thesis consists of six publications. The author contribution statement is shown hereinafter.

Publication 1

Kister, T., Monego, D., Mulvaney, P., Widmer-Cooper, A., & Kraus, T. (2018). Colloidal stability of apolar nanoparticles: The role of particle size and ligand shell structure. ACS nano, 12(6), 5969-5977.

Contribution of Thomas Kister: He performed all analytical experiments, analysed the data and drafted the experimental part of the manuscript.

Publication 2

Monego, D., Kister, T., Kirkwood, N., Mulvaney, P., Widmer-Cooper, A., & Kraus, T. (2018). Colloidal stability of apolar nanoparticles: Role of ligand length. Langmuir, 34(43), 12982-12989.

Monego, D., Kister, T., Kirkwood, N., Mulvaney, P., Widmer-Cooper, A., & Kraus, T. (2020). Correction to "On the Colloidal Stability of Apolar Nanoparticles: The Role of Ligand Length". Langmuir, 36(36), 10892-10893.

Contribution of Thomas Kister: He performed all analytical experiments, analysed the data and drafted the experimental part of the manuscript.

Publication 3

Monego, D., Kister, T., Kirkwood, N., Doblas, D., Mulvaney, P., Kraus, T., & Widmer-Cooper, A. (2020). When Like Destabilizes Like: Inverted Solvent Effects in Apolar Nanoparticle Dispersions. ACS nano, 14(5), 5278-5287.

Contribution of Thomas Kister: He performed a part of the analytical experiments, and analysed the data.

Publication 4

Doblas, D., Kister, T., Cano-Bonilla, M., González-García, L., & Kraus, T. (2019). Colloidal solubility and agglomeration of apolar nanoparticles in different solvents. Nano Letters, 19(8), 5246-5252.

Contribution of Thomas Kister: He developed the measurement techniques, performed a part of the analytical experiments, and analysed the data.

Publication 5

Kister, T., Maurer, J. H., González-García, L., & Kraus, T. (2018). Ligand-Dependent Nanoparticle Assembly and Its Impact on the Printing of Transparent Electrodes. ACS applied materials & interfaces, 10(7), 6079-6083.
Contribution of Thomas Kister: He synthesized and modified all nanoparticles, analysed them and drafted the manuscript.

Publication 6

Kister, T., Mravlak, M., Schilling, T., & Kraus, T. (2016). Pressure-controlled formation of crystalline, Janus, and core–shell supraparticles. Nanoscale, 8(27), 13377-13384.

Contribution of Thomas Kister: He performed all analytical experiments, analysed the data, and drafted the manuscript.

Abstract

Sterically stabilized, non-polar nanoparticles find already first applications beyond research. Predictions how such particles behave in different medias are difficult. To get a better understanding of the physical and chemical connections between core, ligand, and solvent, two fields were investigated in this dissertation: The stability of non-polar nanoparticles at different temperatures and the controlled assembly during confinement.

It was shown, that the stability of sterically stabilized nanoparticles depends on core-diameter, ligand, and solvent. The temperature induced assembly of the nanoparticles showed two different areas: Ligand-dominated and core-dominated. The non-linear transition is thereby a function of the core-diameter and the ligand length.

With the help of emulsion, it was possible to produced binary supraparticles from binary nanoparticle dispersions. By varying the pressure during the production process binary supraparticles with three different structures were produced: Crystalline, Janus, and core-shell. The pressure was either applied by the surfactant (Laplace-pressure) or externally. In-situ measurements with small angle X-ray scattering shown, that the pressure influences the dispersity of the nanoparticles.

Zusammenfassung

Sterisch stabilisierte, unpolare Nanopartikel finden bereits erste Anwendungen außerhalb der Forschung. Vorhersagen, wie sich solche Partikel in verschiedenen Medien verhalten, fällt dabei schwer. Um die physikalischen und chemischen Zusammenhänge zwischen den Kernen, Liganden und Lösemittel besser zu verstehen, wurden in dieser Dissertation zwei Gebiete untersucht: Die Stabilität von unpolaren Nanopartikeln bei verschiedenen Temperaturen und die kontrollierte Anordnung bei räumlicher Restriktion.

Es konnte gezeigt werden, dass die Stabilität von sterisch stabilisierten Nanopartikeln abhängig vom Kerndurchmesser, Ligand und Lösemittel ist. Die temperaturinduzierte Anordnung von den Nanopartikeln hat zwei Bereiche aufgezeigt: Liganden-dominiert und Kern-dominiert. Der nichtlineare Übergang hängt dabei vom Durchmesser des Kerns und von der Länge des Liganden ab.

Mit der Hilfe von Emulsionen konnten binäre Suprapartikel aus binären Nanopartikel Dispersionen herstellt werden. Durch die Variation vom Druck während des Herstellungsprozesses konnten binäre Suprapartikel mit drei verschiedenen Strukturen hergestellt werden: Kristallin, Janus und Kern-Hülle. Der Druck konnte dabei entweder durch das Tensid (Laplace-Druck) oder extern angewendet werden. In-situ Messungen mittels Kleinwinkel-Röntgenstreuung haben gezeigt, dass der Druck die Dispersität der Nanopartikel beeinflusst.

Contents

1. Introduction

Nanoparticles have been in use for many centuries, but their users did not know this. A famous object with embedded nanoparticles is the Lycurgus Cup (see Fig. 1.1). It was already produced by the Romans in the 4^{th} century. Gold and silver nanoparticles in the glass make the cup appear red when illuminated from behind and green when illuminated from the front [1]. The effect is related to the surface plasmon resonance of the embedded metal nanoparticles.

FIGURE 1.1: Lycurgus Cup with two different illuminations. From the back (left) and from the front (right). Adapted from the webpage of the British museum.

It took more than 1000 years until a first dispersion of metallic colloids was purposefully prepared. Michael Faraday published on the preparation of a gold colloid in 1857 [2]. A synthesis route that is still popular was published 100 years later by John Turkevich, who also discussed the particle nucleation and growth mechanism [3]. Similarly popular is the route described by Frens 20 years later that provides citrate stabilized gold nanoparticles with more narrow size distribution by the reduction of hydrogen tetrachloroaurate with sodium citrate in water. Simply varying the sodium citrate concentration during synthesis leads to gold nanoparticles with diameters between 16 nm to 150 nm[4].

The history of nanoparticles that can be dispersed in non-polar solvents is more recent. A popular protocol for non-polar nanoparticles was introduced 1994 by Mathias Brust [5]. The particles were smaller than those of Turkevich and Frens, had spherical shapes and were passivated with an organic ligand. The last two to three decades brought a plethora of synthesis protocols that yield nanoparticles with controllable size, shape, and dispersity which can be dispersed in non-polar solvents [6, 7, 8, 9]. It is now possible to synthesize non-polar plasmonic, magnetic, and semiconductor nanoparticles [10, 11, 12]. Due to the small size and high surface to volume ratio, the nanoparticles exhibit unique properties which are different from bulk properties [13]. They change their optical properties like absorption or fluorescence [14], their chemical properties like catalysis [13] or their physical properties like magnetism [15]. In nanotechnology, these properties are interesting for fields like printing technologies [16], or catalytic technologies [17]. By mixing different elements during synthesis, it is possible to produce alloys, core-shell or crystalline structures [18, 19, 20]. Nanoparticles can be coated, for instance to create superparamagnetic iron oxide cores with gold shells. This combines physical properties, here the superparamagnetism of iron oxide and the plasmonic behaviour of gold [21].

Another way to combine the properties of nanoparticles is the controlled assembly in clusters [22]. Assemblies of nanoparticles that can be dispersed in solvents are often called "supraparticles" [23]. Techniques that have been introduced for these assemblies include capillarity-assisted particle assembly [16], spray-drying techniques [24], temperature induced agglomeration [25], and emulsion-assisted particle assembly [26].

The assembly of nanoparticles in larger objects with defined structures requires an understanding of the interaction potentials between nanoparticles. It is known that core, ligand, and solvent can have an effect on the interaction potentials and thus the stability and dispersity of particles [27]. While core interactions are usually attractive and van der Waals-type, the interaction between ligand and solvent can be attractive or repulsive [28]. This thesis will focus on interaction of the ligand with the solvent and their role in the stability of non-polar nanoparticles. I will compare different interactions (particle-ligand, ligand-solvent and ligand-ligand) and compare their contribution to that of ligand-solvent interactions.

The first part of the thesis introduces the colloidal interactions between alkanethiol coated gold nanoparticles and discusses experiments to asses them depending on size, ligand, and solvent. The measurements were performed using small angle X-ray scattering at different temperatures. The experimental results were supported by molecular dynamics simulations and compared with calculated interaction potentials.

The second part of the thesis discusses the assembly of nanoparticles into thin clustered films and supraparticles. The goal was to create nanostructured materials by arranging particles into films such as to create transparent and conductive coatings [29]. Such coatings were prepared from both nanoparticles and nanowires by controlling their interactions.

The last part of the thesis discusses the arrangement of nanoparticles into binary supraparticles [30]. By controlling the ambient conditions, binary dispersions of nanoparticles were arranged into binary supraparticles with crystalline, Janus, or core-shell geometries.

The thesis is structured according to work that was published in peer-reviewed scientific journals in the last four years. The manuscripts are included in their final form (as printed by the journal). I am the first author of the publications 1 and 6, shared the first authorship of the publications 2 and 5, and I am co-author of the publications 3 and 4.

Publications 1, 2 and 3 discuss the colloidal interactions and the stability of alkanethiol coated gold and cadmium selenide nanoparticles and their dependence on size (publication 1), ligand length (publication 2), and solvent (publication 3). The experimental results were compared with simulations and the current theoretical models. The results indicate, that under certain conditions existing theoretical models can be used to predict nanoparticle stability. Furthermore, the results also showed, at which conditions the stability regarding size, ligand, and solvent can be increased.

Publication 4 discusses the colloidal stability of alkanethiol coated gold nanoparticles in different solvents during solvent evaporation. It provides concentration ranges (depending on size and solvent) for stable dispersions and concentrations for the onset of agglomeration or assembly.

Publication 5 discusses how sterically coated gold nanoparticles can be used as building blocks to produce transparent and conductive films. The effect of the ligand length and bonding group on the conductivity is described in detail.

Publication 6 discusses the assembly mechanism of binary nanoparticle mixtures into binary supraparticles inside emulsion droplets. The impact of pressure during evaporation on the final structure is discussed.

2. State of the Art

This chapter briefly summarizes the current knowledge on the synthesis, stabilization, properties, interactions, agglomeration, and assembly of sterically coated non-polar nanoparticles (NPs). Sterically coated NPs are surrounded by an organic shell which acts as a barrier between the cores [31]. First, the effect of the steric layer on the stability of non-polar NPs is discussed. Afterwards, the synthesis of non-polar NPs and their properties are discussed. Such NPs were used in all of the work discussed in this thesis. Relevant interactions between such NPs are then described. The relation of these interactions is responsible for the colloidal stability of the particles, and thus also for the agglomeration and assembly. Finally, temperature induced agglomeration, solvent induced agglomeration and evaporation assisted particle assembly are described.

2.1 Stabilization of non-polar, metallic nanoparticles

Stable dispersions of metal NPs in non-polar solvents require a suitable stabilization layer, such as a ligand. Charged ligand such as citrate ions stabilize NPs in water [32]. Polar organic ligands such as 11-mercaptoundecanoic acid can be used to disperse NPs in alcohols [33] or water [34] and non-polar ligands such

as oleylamine or alkanethiols stabilize NPs in non-polar solvents such as alkanes [10]. The stability of such NPs depends on the solubility of the ligand in the solvent (see section 2.4) [28].

The core material of the NPs implies suitable bonding group to stabilize the particles in non-polar solvents. For instance, iron oxide NPs can be stabilized with oxides or amines. Silver NPs can be stabilized with oxides, amines or thiols and gold NPs (AuNPs) with amines or thiols [35, 36, 10]. Ligands with a phosphate bonding group can be used on silver NPs or AuNPs [37]. The bonding energy between the ligand and the core can be either strong or week. Strong bonds have for instance gold and sulphur or iron and oxide. Week bonds have for instance gold and nitrogen or cadmium selenide and sulphur. The binding energies on gold vary by an order of magnitude between an amine like oleylamine (approximately 0.2 eV) and thiols like hexadecanethiol (approximately 1.7 eV) [38, 39]. Such a differences explains why it is so easy to perform a ligand exchange from oleylamine to alkanethiol for AuNPs [40] as it was done for almost all results shown in publications 1 to 6.

The amount of free ligand molecules in the solution can affect also the stability if the bonding energy is relatively weak. Sufficient ligand coverage and thus, colloidal stability of the NPs can require free ligand molecules to achieve a balance between detaching and attaching. If there are not enough free ligand molecules in the solvent, more ligand molecules detach than attach from the surface of the NPs until the ligand density decreases under a critical value which is needed for a stable dispersion [41]. Such an effect cannot directly be seemed for strongly bonded ligands. But since more time is needed for such ligand to be released from the NP surface, it is important to have here also enough free ligand in the solvent. It is known that also such NPs tend to age after a certain time [42].

2.2 Synthesis of non-polar, metallic nanoparticles

Nanoparticle syntheses are often categorized into top-down and bottom-up processes [43, 44, 45, 46]. Ablation from a bulk material with mechanical means (milling, cutting or abrasion) or using strong fields (laser) yields particles, but their sizes and shapes are usually not well defined [47]. This thesis relies on bottom-up syntheses based on molecular precursors in solution. The decomposition of such a precursor, releases single atoms or molecules that assemble into the desired nanostructures [3, 48]. Particles with narrow size distributions ("monodisperse") can be obtained by separation of nucleation and growth during the decomposition, as described by the LaMer model [49]. This can be achieved by a homogeneous reduction of the molecular precursor using a chemical reduction agent or by thermal decomposition. After nucleation occurs, the particles further growth by absorbing free atoms and by Ostwald ripening, where bigger NPs further growth by the degradation of smaller ones [50].

The synthesis of non-polar sterically coated NPs that were used for all work in this thesis starts with a mixture of the precursor chloroauric acid, the ligand oleylamine and a non-polar solvent [51]. Size, shape, and dispersity of NPs depend on temperature, solvent, and reaction time. Smaller NPs form at higher temperatures or with shorter alkanes as solvents during synthesis [51, 52]. Replacing alkanes by aromatic hydrocarbons such as benzene or toluene results in bigger NPs [52]. Immediate reduction of the precursor with the solvent/oleylamine mixture leads to larger NPs, waiting in between yields smaller particles. Fig. 2.1 shows transmission electron microscopy micrographs of the resulting oleylamine coated AuNPs at different magnifications.

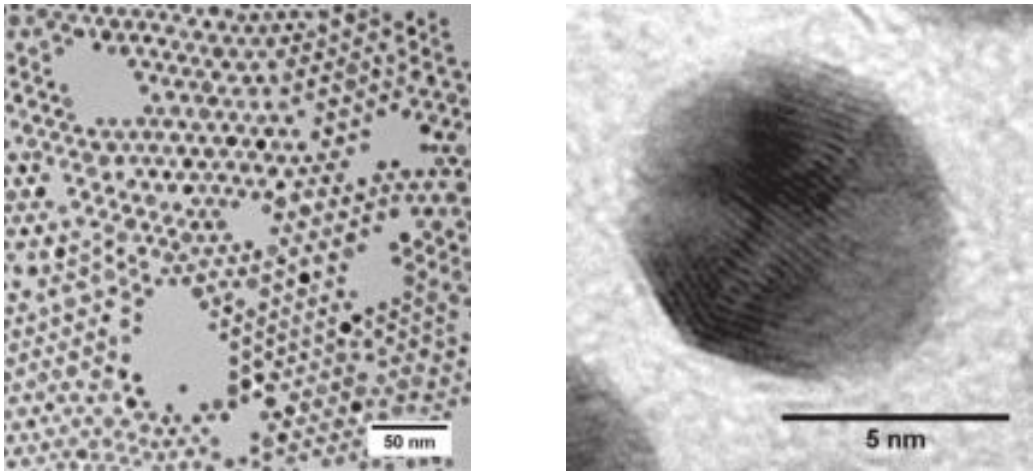

FIGURE 2.1: TEM micrographs of oleylamine coated AuNPs at different magnifications.

2.3 Properties of non-polar, metallic nanoparticles

In this section, the surface plasmon oscillation resonance of metallic NPs and the fluorescence of semiconductor NPs is described.

2.3.1 Surface plasmon oscillation resonance

Nanoparticles with cores of gold, silver, or copper have a strong surface plasmon resonance absorption due to collective oscillations of free electrons [53, 54]. This absorption is responsible for the colour of the particles. It can be used for instance to heat particles [55]. *Free* electrons do not feel a local bonding, can move inside the metal [56], and induce oscillations of the electron density, which are known as plasmon oscillation. The frequency ω of this oscillation depends on the size and the material of the particle. An incident electromagnetic field with the same frequency as the oscillating electron can further increase the amplitude. Thus, energy can be transferred from the light to the particles.

When an external electromagnetic field E_0 is applied on the particles, a collective oscillation of the electron starts and polarization occurs. The oscillation frequency ω of such particles at resonance conditions can be calculated by

$$\omega = \sqrt{\frac{ne^2}{m_e \epsilon_0 (1 + 2\epsilon_m)}} \tag{2.1}$$

where n is oscillation electron density, e the elementary charge, m_e the electron mass, ϵ the dielectric constant of vacuum and ϵ_m the dielectric constant of the medium.

The optical absorption caused by surface plasmon resonance (SPR) is easy to observe in a standard UV-vis spectrometer, or even by eye. It provides a convenient probe to observe the assembly of plasmonic NPs. The SPR peak position of such NPs depends on the size, the ligand, and the surrounding medium [57, 58]. Agglomeration can cause electron coupling and a shift of the peak [54]. During the agglomeration, pairs of NPs are formed. Due to electronically coupling of the NPs, the SPR oscillation changes since the coupling effects the plasma modes of the NPs [59]. Such agglomerated NPs often exhibit a red-shift in absorption and a broadening of the SPR [59, 60]. Heteroagglomerates, for example of plasmonic Au and non-plasmonic Fe_3O_4 particles, exhibit a red-shift after agglomeration, too. This can be attributed to changes of the medium and thus changes of the dielectric constant of the medium during agglomeration [61, 62, 63].

2.3.2 Fluorescence of semiconductor nanoparticles

Semiconductor NPs exhibit a size-dependent fluorescence peak that is due to the confinement of electrons and leads to the name “quantum dots” (QDs) [64]. The size effect is so strong, that cadmium selenide (CdSe) QDs can fluoresce in almost all colours of the visible range, for example [65]. The band gap of bulk CdSe E_g

(between valence and conductive band) is approximately 1.7 eV for CdSe, corresponding to a wavelength of 760 nm. If an electron is excited from the valence band to the conductive band, a "hole" is formed in the valance band. The hole and the excited electron are the so-called exciton pair [66]. The distance between them is known as the Bohr exciton radius a_B [67]. The radius can be calculated by

$$a_B = \frac{\hbar^2 \epsilon}{m^* e^2} \tag{2.2}$$

where $\hbar$ is the reduced Planck´s constant, m^* the effective mass of the exciton and e the elementary charge. As long a as the Bohr radius is smaller than the diameter of the NP, the only contribution to the total energy of the particle is E_g. If the diameter of the NP is of the order of the Bohr exciton radius (approximately 4.9 nm for CdSe), quantum confinement effects occur [68] and the potential well energy E_w, which surrounds the local minimum has to be considered. The potential well energy can be calculated by

$$E_w = \frac{h^2 \epsilon}{2m^* d^2} \tag{2.3}$$

where d is the diameter of the particle. This energy strongly depends on the diameter of the NP (d^2). Due to the linear combination of the band gab energy E_g and the potential well energy E_w, the total energy of the exciton increases by decreasing the size of the QDs (lower wavelength for smaller QDs) [69].

The agglomeration of QDs has usually also an effect on the fluorescence. As soon as QDs are close enough, the fluorescence is quenched. The quenching is very likely caused by electronic coupling between the QDs [70, 71].

2.4 Interactions between sterically stabilized nanoparticles

The standard description of interactions between colloidal particles is the so-called DLVO (Derjaguin, Landau, Verwey, Overbeek) theory [72]. The theory combines attractive van der Waals (vdW) and repulsive electrostatic interactions of charged stabilized NPs in an aqueous dispersion and can be used to describe the kinetics during the agglomeration of such NPs [73, 74].

Sterically stabilized, non-polar NPs in organic solvents have interfaces that fundamentally differ from that on charged stabilized NPs in water. The interaction between such NPs do not only depend on the core material of the NPs, but also on ligand density, ligand length, temperature, and solvent [28]. Not only vdW can contribute to attractive part, but depending on temperature or solvent also the ligand-solvent interaction [25, 75]. There is no generally accepted theory that would predict the stability of such NPs in the way DLVO theory does it for electrostatic stabilized NPs in aqueous solutions. Existing models such as the one published by Khan et al. [28] can be apply in certain regimes and proved to be useful for some applications, for example the calculation of interaction potentials of sterically coated AuNPs in a mixture of non-polar and polar solvent [76]. This model describes the vdW interaction in an acceptable way, but has limitations in the ligand-solvent interactions since especially the ligands cannot be count as "free" [77, 78].

According to these models [28, 77, 78], the total interaction G is a linear combination of vdW interaction G_{vdW}, the ligand compression G_{com} and the free energy of mixture G_{mix}.

$$G = G_{vdW} + G_{com} + G_{mix} \tag{2.4}$$

vdW interaction for NPs are proportional to the reduced Hamaker coefficient A and to a geometrical factor which depends on the core-to-core distance r between the particles, and the particle diameter d.

$$G_{vdW} = -\frac{A}{12}\left[\frac{1}{r^2/d^2 - 1} + \frac{d^2}{r^2} + 2ln\left(1 - \frac{d^2}{r^2}\right)\right] \tag{2.5}$$

The reduced Hamaker coefficient can be calculated by

$$A = \left(A_{11}^{1/2} - A_{22}^{1/2}\right)^2 \tag{2.6}$$

where A_{11} and A_{22} are the Hamaker constants of the particles and of the medium, respectively [79].

Ligand compression becomes important when the distance between two particles surfaces is below twice the ligand length. A repulsive "spring" force then appears due to ligand compression. This repulsive interaction U_{com} is proportional to the temperature T and can be calculated by

$$\frac{G_{com}}{k_b T} = \pi v d\left[(r-d)\left(ln\frac{r-d}{L} - 1\right)\right] \tag{2.7}$$

where v is the ligand density, L the ligand length and k_b the Boltzmann constant [28].

The free energy of mixing G_{mix} describes the interaction between the ligand and the solvent and can be calculated by:

$$\frac{G_{mix}}{k_b T} = \frac{\pi d}{\nu_S} L^2 \left(N_L \frac{\nu_L}{V_{Sh}}\right)^2 \left(\frac{1}{2} - \chi\right)\left(3ln\frac{L}{r-d} + 2\frac{r-d}{L} - \frac{3}{2}\right) \tag{2.8}$$

where ν_S is the volume of a solvent molecule, ν_L the volume of a ligand molecule, N_L the number of ligands per NP, V_{Sh} the volume of the ligand

shell and χ the Flory parameter. The Flory parameter describes how "well" a ligand dissolves in a solvent. It depends on the Hildebrand solubility parameters (or Hansen solubility parameter if the solvent or ligand is slightly polar) of the solvent δ_S and the ligand δ_L and can be calculated by

$$\chi = \frac{V_m}{RT}(\delta_L - \delta_S)^2 + 0.34 \tag{2.9}$$

where V_m is the molar volume of the solvent and R the universal gas constant [80, 81]. This is a linear combination of an enthalpic and entropic component. For the entropic part of non-polar ligands and solvents a value between 0.3 and 0.4 is often used. The common value of 0.34 was calculated from the solubility of polymers in non-polar solvents [82].

The Flory parameter sets whether the free energy of mixing contribute to attraction or repulsion. If it is above 0.5, G_{mix} is contribute to attraction; below 0.5, G_{mix} contribute is repulsion. The solvent thus has a major role in the stability of sterically coated NPs [28].

The theory explains why alkanethiol coated NPs can be dispersed in non-polar solvents like alkanes, why such NPs agglomerate in mixtures of non-polar and polar solvents [76, 75], but show limitations regarding temperature changes. Previous worked showed, that alkanethiol coated NPs tend to agglomerate as soon as the temperature is reduced to a value around the melting point of the free ligand [83]. Since the theory do not consider the molecular structure of the ligand shell and its crystallization at low temperatures more investigations (experimental and theoretical) are needed for an extension [84, 85, 86].

2.5 Agglomeration and assembly of nanoparticles

Agglomeration is a process whereby particles form clusters. Such clusters are usually irregular. The assembly or self-assembly of particles is a spontaneous organization of particles by noncovalent interactions. Typical noncovalent interactions are vdW, π-π, electrostatic interactions, and hydrogen bonds [87].

The agglomeration or assembly of NPs can be governed by different changes or mechanisms. The most common ones are temperature, solvent, or evaporation. These were studied in previous works and are important for the understanding of the results part of this work. Therefore, the key issues regarding these mechanisms are going to be discussed in this section.

2.5.1 Temperature induced agglomeration

Temperature can induce agglomeration and switch the state of sterically coated NPs between agglomerated and deagglomerated [88]. The agglomeration temperature depends on factors such as solvent type, particle concentration, and ligand [83, 25, 89]. An example is shown in Fig. 2.2: hexadecanethiol coated AuNPs were deagglomerated at 60°C and agglomerated at room temperature. Transmission electron micrographs of the two states were prepared by drying the dispersion at the indicated temperatures. The insets show optical images of the liquid dispersion at the same temperatures.

Boal et. al reported in 2000 that thymine-functionalized alkanethiol coated AuNPs agglomerate upon cooling. In their work, the size of the aggregates was controllable by the temperature – the smaller the temperature, the bigger the agglomerated clusters [88].

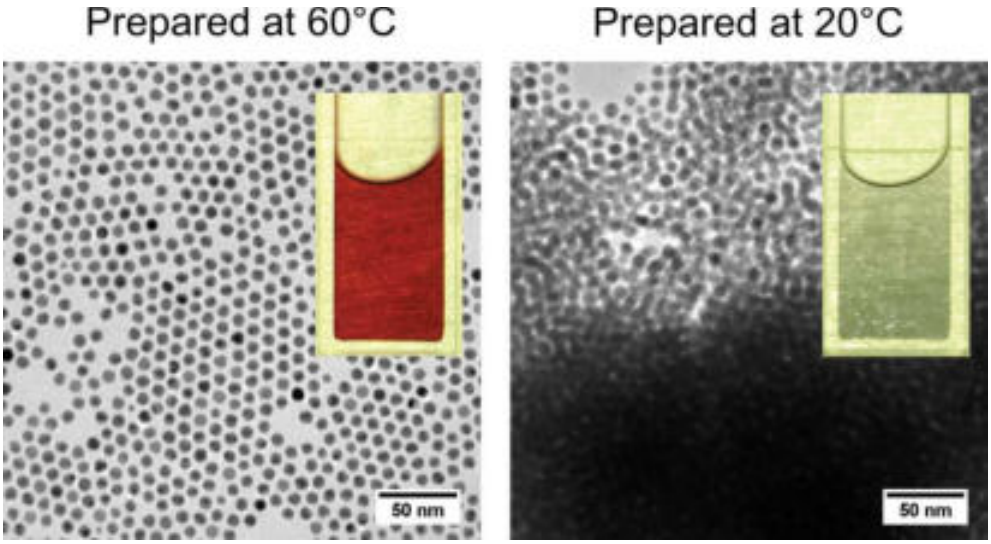

FIGURE 2.2: Transmission electron micrographs of 1-hexadecanethiol coated AuNPs. The NPs were deagglomerated at 60°C (left) and agglomerated at room temperature (right). TEM samples were prepared by putting a drop of the dispersion at 60°C (left) and room temperature, respectively. The figure was adapted from publication 1.

Similar results were observed for AuNPs which were coated with different alkanethiols. Such particles underwent also a temperature dependent transition from a fully dispersed state to large percolated and unordered agglomerates by decreasing the temperature [25]. It was shown, that for AuNPs with core diameters around 6 nm, the agglomeration temperature depends on the ligand length [25]. For particles coated with dodecane-, hexadecane- or octadecanethiol, the agglomeration temperature increased for longer ligands and was comparable with the melting temperatures of the pure ligands [83]. Furthermore, the temperature affects the size and the growth rate of the clusters. Lower temperatures increased size and the growth rate [88, 25].

Core interactions of particles are dominated by vdW that weakly changes with temperature. Ligand compression G_{com} increases with the temperature, but its maximal effective range is twice the ligand length [28]. The free energy of

mixing G_{mix} depends strongly on the Flory parameter, which is a function of the balance between entropy and enthalpy. Temperature can have a strong effect on this balance [88]. At temperatures around the melting point, alkanethiol shells get an ordered structure [75]. This was also confirmed by simulations. It was shown that a self-assembled monolayer of alkanethiols on a planar Au surface undergoes a transition from a molten state to a crystalline state when decreasing the temperature and that the transition temperature is a function of the ligand length [84, 90]. Similar effects can happen on the curved surface of NPs. Fig. 2.3 shows snapshots of 1-hexadecanethiol coated NPs above (left) and below (right) the transition temperature and illustrates the order-disorder transition of their ligand shell.

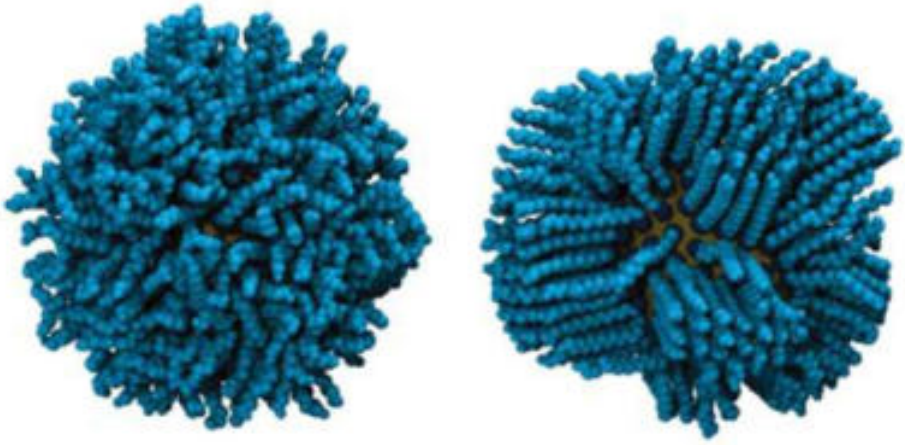

FIGURE 2.3: 1-Hexadecanethiol coated AuNPs with a core diameter of 4 nm at temperatures above the melting point (left) and temperature below the melting point of the ligand (right). Figure was adapted from publication 1.

Due to these changes in the structure of the ligand, the solubility of the ligand in the solvent and thus the balance between entropy and enthalpy is affected [88, 75] and the free energy of mixing do not contribute to repulsion [28].

Furthermore, the agglomeration temperature of alkanethiol coated AuNPs is also affected by the concentration of the NPs. Born et al. showed that

1-dodecanethiol coated AuNPs agglomerate at higher temperatures for increased concentrations [25] using concentration- and temperature-dependent dynamic light scattering measurements. The transition temperature changed from 3°C to 11°C when the concentration was increased from approximately 2.7 mg/mL to 4.6 mg/mL.

2.5.2 Solvent induced agglomeration

Stable dispersions of NPs can agglomerate when a second miscible solvent is added [91]. Born et al. and Gerstner et al. showed that well-dispersed alkanethiol coated AuNPs in heptane agglomerate when 1-proponal is added. Agglomeration is due to solvent polarity [75, 76]: the solvent has an effect on the Hildebrand or Hansen solubility parameter of the solvent. Due to this, the Flory parameter and thus the free energy of mixing is affected [28]. The addition of 1-propanol changed the solubility parameter of the solvent. As soon as a critical value between 1-propanol and heptane was reached, the repulsion from the free energy of mixing G_{mix} disappear and the NPs agglomerated [76].

During the agglomeration, the internal structure of the agglomerates depends on the ligand and the temperature. At low temperatures, amorphous clusters form; higher temperatures lead to crystalline superlattices [75]. As described above in the section 2.5.1, the ligand shell is mobile at high temperatures and ordered at low temperatures. Mobile ligands let the particles move against each other so that they can reach a minimum energy structure and arrange in crystalline lattices. Ordered ligand shells have a static structure; when particles with ordered shells touch, they cannot slide and remain in an amorphous state [75, 76].

2.5.3 Evaporation assisted particle assembly

Evaporation induces liquid motion and can lead to capillary bridges that have been used for the assembly of particles into define structures [92]. Two- or three-dimensional films [93], meshes [29], and three-dimensional structures [26] have been created by drying different particles on surfaces or in templates. This chapter introduces two methods, one that is based on soft stamps and one that uses emulsion droplets as templates.

Imprint assisted particle assembly

NPs can be assembled into homogeneous films by drying [94]. During the evaporation of the films, the assembly mechanisms that are active depend on concentration, ligand, solvent, and size, among others [95, 96, 97]. Films of nanoscale metal lines are useful as flexible and optical transparent electrodes. Such grids can be produced by imprinting NPs with a soft stamp and can have optical transparencies above 90% and sheet resistances around 30 Ω/sq [29].

The NP dispersion is confined into thin lines by the stamp. During the evaporation of the solvent, the concentration of the NPs in the liquid increases, and the particles assemble into predefined structures as they interact [98]. Such a grid is shown in Fig. 2.4. Due to the percolation of the NPs inside the thin lines, the sheet is conductive.

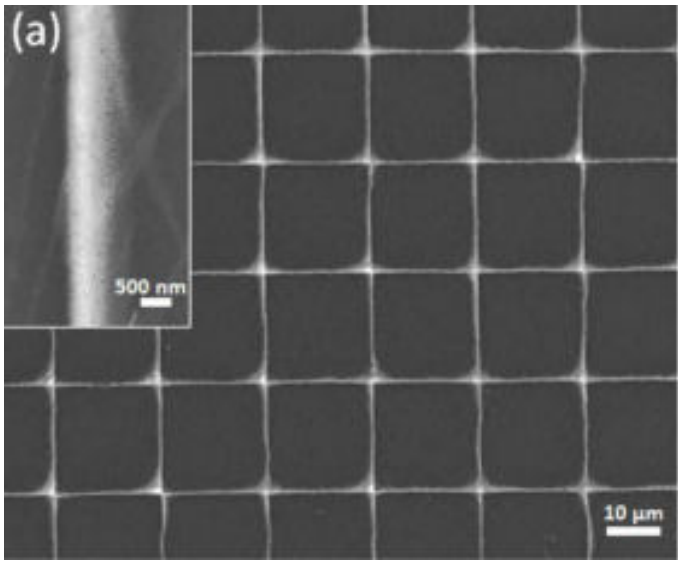

FIGURE 2.4: Scanning electron microscopy image of an imprinted grid. Figure was adapted from publication 5.

Emulsion assisted particle assembly

The assembly of NPs inside liquid droplets can lead to three dimensional structures known as supraparticles (SPs) [99, 100, 101, 23]. Particles are dispersed inside the droplets that form the dispersed phase of the emulsion. To stabilize the emulsion from breakdown and to block the interface for particles, a surfactant is needed [102]. Evaporating the dispersed phase of the emulsion increases the concentration of the confined particles until SPs are formed [26]. This technique was used to arranged SPs in geometries that resemble Lennard-Jones clusters [26]. The technique enables control over size, dispersity, and the internal structure of the SPs [103].

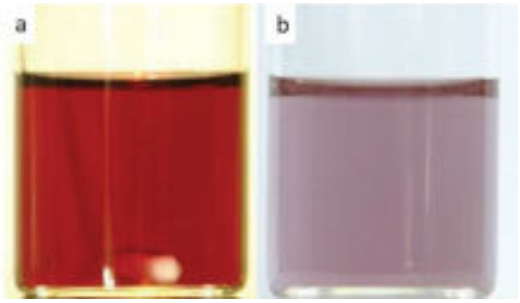

FIGURE 2.5: Optical comparison between ligand coated AuNPs and surfactant coated AuSPs. Due to electronic coupling between the NPs the colour shifted from red to purple.

The SPs remain dispersed in the continuous phase of the former emulsion. They are coated by the surfactant that originally stabilized the emulsion. An optical comparison between dispersed NPs and dispersed SPs is shown in Fig. 2.5a and b, respectively. The colour shifted from red to purple due to electronic coupling between the assembled NPs [26]. A TEM micrograph of such SPs is shown in Fig. 2.6.

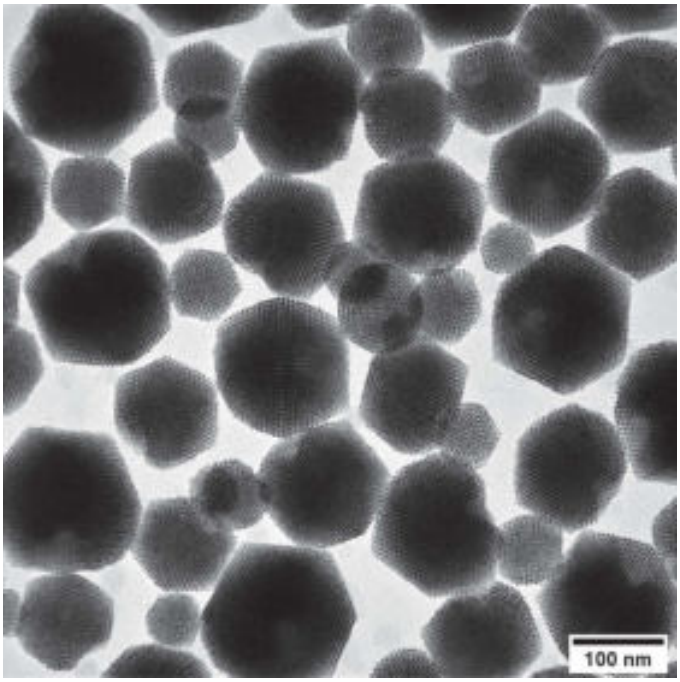

FIGURE 2.6: Transmission electron micrograph of SPs.

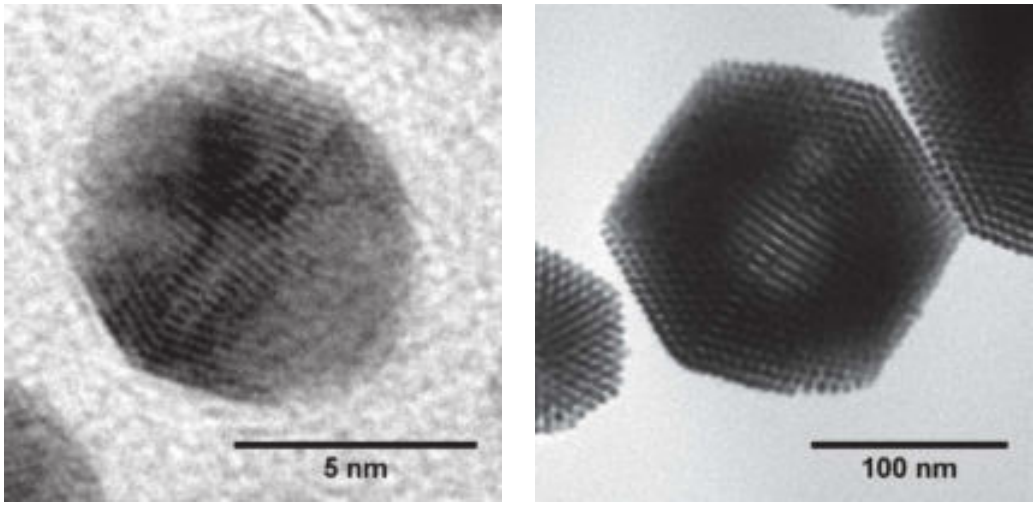

FIGURE 2.7: TEM micrographs of a AuNP (left) and of a SP (right) made from AuNPs. The structure of both (NP and SP) is comparable.

The remarkable internal structure of such SPs can follow an energy minimum arrangement. SPs produced from alkanethiol coated AuNPs tend to assembly in such arrangements [26]. Similar internal structures were observed for alkanethiol coated AuNPs [104]. Figure 2.7 shows the internal structure of a 1-hexadecanethiol coated AuNP with a diameter of approximately 6 nm on the left side. SPs can have the same internal structure, shape, and form as it is shown in the figure on the right side. Furthermore, one can recognize that the number and the orientation of the facets is the same for the NP and the SP.

The structure of SPs also depends on the number of NPs which are confined in the droplets. It was shown, that the internal structure of SPs can change from Mackay icosahedron to anti-Mackay rhombicosidodecahedron and finally to a face-centred cubic cluster just by increasing the total number of NPs which assembly to a SP [103].

Temperature affects the assembly of supraparticles along the lines discussed in section 2.5.1. Assembly below a certain temperature led to the formation of amorphous supraparticles [25]. Figure 2.8 shows SPs which were produced with 1-hexadecanethiol coated AuNPs similar to those in Fig. 2.7.

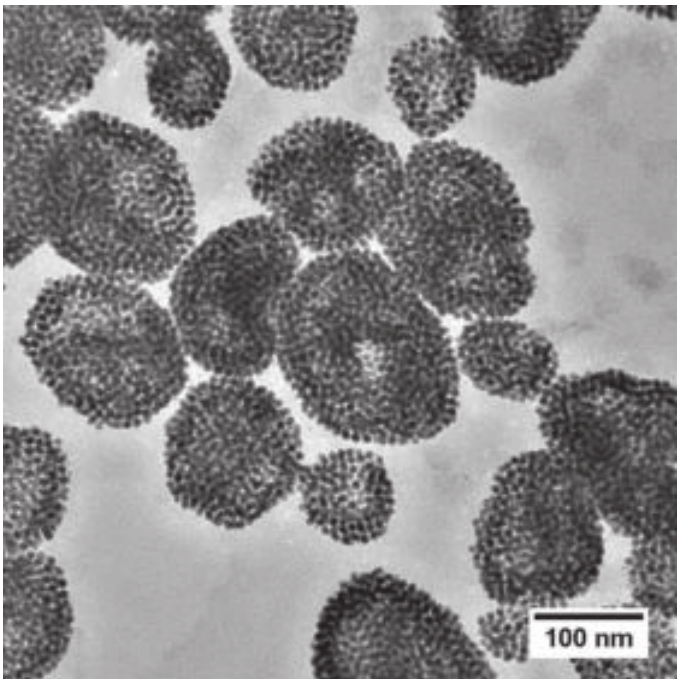

FIGURE 2.8: SPs produced with 1-hexandecanethiol coated AuNPs. The emulsion was evaporated at room temperature.

3. Results

3.1 Publication 1

Kister, T., Monego, D., Mulvaney, P., Widmer-Cooper, A., & Kraus, T. (2018). Colloidal stability of apolar nanoparticles: The role of particle size and ligand shell structure. ACS nano, 12(6), 5969-5977.

DOI: 10.1021/acsnano.8b02202

ACS NANO
Cite This: ACS Nano 2018, 12, 5969−5977
www.acsnano.org

ARTICLE

Colloidal Stability of Apolar Nanoparticles: The Role of Particle Size and Ligand Shell Structure

Thomas Kister,[†] Debora Monego,[‡] Paul Mulvaney,[§] Asaph Widmer-Cooper,[‡] and Tobias Kraus*[,†,∥]

[†]INM−Leibniz Institute for New Materials, Campus D2 2, 66123 Saarbrücken, Germany
[‡]ARC Centre of Excellence in Exciton Science, School of Chemistry, University of Sydney, Sydney, New South Wales 2006, Australia
[§]ARC Centre of Excellence in Exciton Science, School of Chemistry, University of Melbourne, Parkville, Victoria 3010, Australia
[∥]Colloid and Interface Chemistry, Saarland University, Campus D2 2, 66123 Saarbrücken, Germany

Supporting Information

ABSTRACT: **Being able to predict and tune the colloidal stability of nanoparticles is essential for a wide range of applications, yet our ability to do so is currently poor due to a lack of understanding of how they interact with one another. Here, we show that the agglomeration of apolar particles is dominated by either the core or the ligand shell depending on the particle size and materials. We do this by using small-angle X-ray scattering and molecular dynamics simulations to characterize the interaction between hexadecanethiol passivated gold nanoparticles in decane solvent. For smaller particles, the agglomeration temperature and interparticle spacing are determined by ordering of the ligand shell into bundles of aligned ligands that attract one another and interlock. In contrast, the agglomeration of larger particles is driven by van der Waals attraction between the gold cores, which eventually becomes strong enough to compress the ligand shell. Our results provide a microscopic description of the forces that determine the colloidal stability of apolar nanoparticles and explain why classical colloid theory fails.**

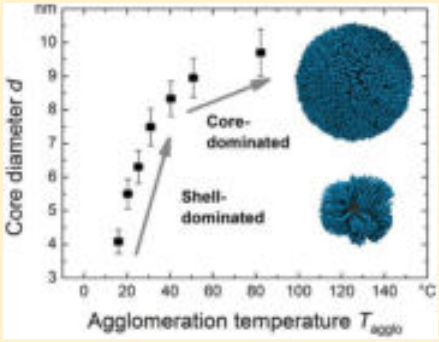

KEYWORDS: *nanoparticles, dispersion, apolar, colloidal stability, ligand shell, DLVO, agglomeration*

Following the advent of the hot-injection method for nanocrystal synthesis,[1] there has been a plethora of studies on the preparation of an enormous range of materials in nanocrystal form including noble metals, magnetic materials such as Fe_3O_4 and FePt, quantum dots such as CdS and CdSe, upconverters including $YLaF_4$, core−shell nanocrystals such as Au@Ag, ternary materials like $CuInS_2$, perovskites, and alloys. In all these diverse systems, inorganic core particles are stabilized in an apolar solvent by a self-assembled layer of surfactant. Prototypical examples are metal and semiconductor nanocrystals or quantum dots[2] with ligand shells of alkanethiols that are stable in organic solvents. Their applications include inkjet printed structures for detectors,[3,4] conductive inks, and color-improving additives for OLEDs.[5,6] Despite their widespread study, there is no generally accepted theory that explains when and why such systems will be colloidally stable, i.e., no extant model correctly predicts the colloidal stability of hydrocarbon capped inorganic nanoparticles dispersed in organic solvents.

Existing approaches based on classical colloid theory describe the interaction between apolar nanoparticles by assuming a linear combination of contributions from dispersive van der Waals (vdW) attraction between the inorganic cores, the free energy of ligand/solvent demixing, and elastic energy due to deformation of the ligand shell.[7−9] While the vdW attraction between the cores should be well described by Hamaker−Lifshitz theory, the model of the shell appears to be lacking. The free energy of ligand/solvent demixing is currently modeled using Flory−Huggins theory using Hildebrand solubility parameters[10] that were developed for molecular solutions and assumes that the ligand/solvent interface can be adequately described by a density distribution that is radially symmetric and constant with temperature. The theory used to describe the elastic energy makes a similar assumption about how the ligands are distributed in space.

In contrast, there is substantial evidence from both simulation and experiment that the structure of the ligand shell depends on core size, temperature, and solvent quality. Linear ligands change their arrangement in space in response to a decrease in temperature or solvent quality, aligning with one another and packing together.[11−16] This affects both the ligand

Received: March 23, 2018
Accepted: May 29, 2018
Published: May 29, 2018

DOI: 10.1021/acsnano.8b02202
ACS Nano 2018, 12, 5969−5977

and solvent density distributions, which can become highly asymmetric about small particles[11−13,17] and can be expected to result in deviations from the theory described above. Indeed, simulations have already shown that the interaction between particles can change rapidly from repulsive to attractive as the ligands order.[17,18] The importance of such breakdowns from the assumptions of classical colloid theory, and some of the effects that they can have on the interaction between nanoparticles regardless of ligand and solvent polarity, has recently been highlighted.[19]

Here, we combine experiments and simulations to characterize the stability of hexadecanethiol-coated gold nanoparticles with core diameters of 4−10 nm in decane. Their agglomeration and interparticle spacing was characterized as a function of particle diameter and temperature using X-ray scattering and compared with molecular dynamics studies of the ligand order and the interaction potential between pairs of particles. We find two different regimes depending on particle size: for small particles, the agglomeration is driven by the ordering of the ligand shells, while for larger particles, the vdW attraction between the cores becomes strong enough to drive agglomeration before the ligands order. This transition from ligand- to core-dominated agglomeration results in a nonlinear change in the interparticle spacing as the size increases. In the ligand-dominated regime, the interparticle spacing increases with particle size as the ligand shell becomes denser and the gaps between the ordered bundles decrease in size until the spacing is roughly equal to twice the thickness of the ligand shell. Beyond this point, the core−core vdW attraction drives the transition, eventually leading to compression of the ligand shell and a decrease again in the particle spacing.

The temperature-dependent stability that we measured and simulated for our nanoparticle dispersions was irreconcilable with interaction potentials calculated using Khan's expressions,[7] even when modifying the Flory−Huggins parameters. Classical colloid theory predicts colloidal stability near room temperature for the small particles used here, while our experiments show rapid agglomeration, in some cases well above room temperature. We conclude that improved models will need to account for temperature-dependent transitions in the ligand shell, including their potential to change the symmetry of the ligand distribution about the particles.

RESULTS AND DISCUSSION

Gold particles (AuNP) with seven different mean core diameters between 4 and 9.7 nm and size distributions with widths below 10% (mean diameter over standard deviation) were coated with 1-hexadecanethiol and dispersed in decane. Small-angle X-ray scattering (SAXS) and transmission electron microscopy (TEM) data of the NPs are shown in Supporting Information (SI), Figures S1 and S2. The dispersions had concentrations of 2.5 mg mL^{-1} (0.013 vol %) and ligand shell densities of 5.5 nm^{-2} (see SI, Figure S3). Table 1 provides a summary of all particles used.

The temperature-dependent colloidal stability was quantified using in situ small-angle X-ray scattering. Figure S4 (see SI) shows how the data was analyzed. At high temperatures, all particles were dispersed and the scattering corresponded to the form factor $P(q)$ of dispersed spheres:[20] a Bessel function, as expected for spherical particles. Upon cooling, the particles agglomerated (see SI, Figure S4a) and a peak appeared (for example, at q = 0.594 nm^{-1} for AuNP with a diameter of 9.7 nm, SI, Figure S4b)[21,22] due to the agglomerates' structure factor $S(q)$. The peak height and area are directly proportional to the fraction of nanoparticles that have agglomerated.[23] We fitted the form factor with a Lorentz function to find the agglomeration temperature of the particles and the spacing between the particles (SI, Figure S4c).

Table 1. AuNPs Used for This Study, With Diameters Obtained from Transmission Electron Microscopy and Small Angle X-ray Scattering

no.	d (TEM)	d (SAXS)
Au01	4.1 nm ± 10%	4.1 nm ± 9.3%
Au02	5.6 nm ± 8.4%	5.5 nm ± 8.3%
Au03	6.4 nm ± 6.3%	6.2 nm ± 8.3%
Au04	7.4 nm ± 7.4%	7.5 nm ± 6.7%
Au05	8.5 nm ± 7.1%	8.3 nm ± 6.7%
Au06	8.9 nm ± 8.5%	8.9 nm ± 6.8%
Au07	9.8 nm ± 5.8%	9.7 nm ± 7.3%

Figure 1a shows TEM micrographs of AuNP with a diameter of 7.5 nm prepared at 60 °C and 20 °C. The insets show the AuNP dispersion at the corresponding temperatures. A clear temperature dependent change is observable. Figure 1b shows how the fraction of agglomerated particles increased upon cooling for different core diameters. Smaller particles were more stable and agglomerated at lower temperatures than larger particles. The agglomeration temperature T_{agglo}, defined as the temperature at which 20% of particles had agglomerated, showed a strong nonlinear dependence on particle size, increasing rapidly beyond a diameter of roughly 8 nm (Figure 1c). At the same time, the particle separation at T_{agglo} reached a maximum around a diameter of 8 nm before decreasing again (Figure 1d).

We believe that the nonlinear, size-dependent stability of the nanoparticle colloids is due to a transition from ligand- to core-dominated agglomeration as the particle size increases. Large-scale molecular dynamics simulations of the nanoparticles in explicit *n*-decane solvent support this hypothesis. Snapshots show the structure of the ligand shell well above (Figure 2a) and below (Figure 2b) the agglomeration temperature. At high temperature, the ligands are mobile and the shell disordered. In contrast, at low temperature, the ligands are well-ordered and much less mobile, with the ligands adopting mostly all-trans conformations and aligning with one another. This causes the ligands to cluster into bundles and results in ligand shells that are increasingly anisotropic as the particle size decreases. Similar changes have been observed in simulations of other small spherical and rod-shaped nanoparticles as the temperature or solvent quality was reduced.[11,13,17]

The degree of order of the ligand shell can be quantified using the dihedral angle of the ligand molecules in the shell. Figure 2c shows the average dihedral angle as a function of temperature for different core diameters. We define an "ordering temperature" T_{order} at which the average dihedral angle equals 140°. For particles from 4 to 7.6 nm in diameter, the ligand ordering (small symbols) preceded particle agglomeration (large crosses) and exhibited the same dependence on particle size, indicating that the agglomeration is driven by ordering of the ligand shell. This is supported by analytical calculations of the vdW interaction between small Au cores that turn out to be too weak to cause agglomeration at the experimentally observed particle separations (see Figure 4b below).

DOI: 10.1021/acsnano.8b02202
ACS Nano 2018, 12, 5969−5977

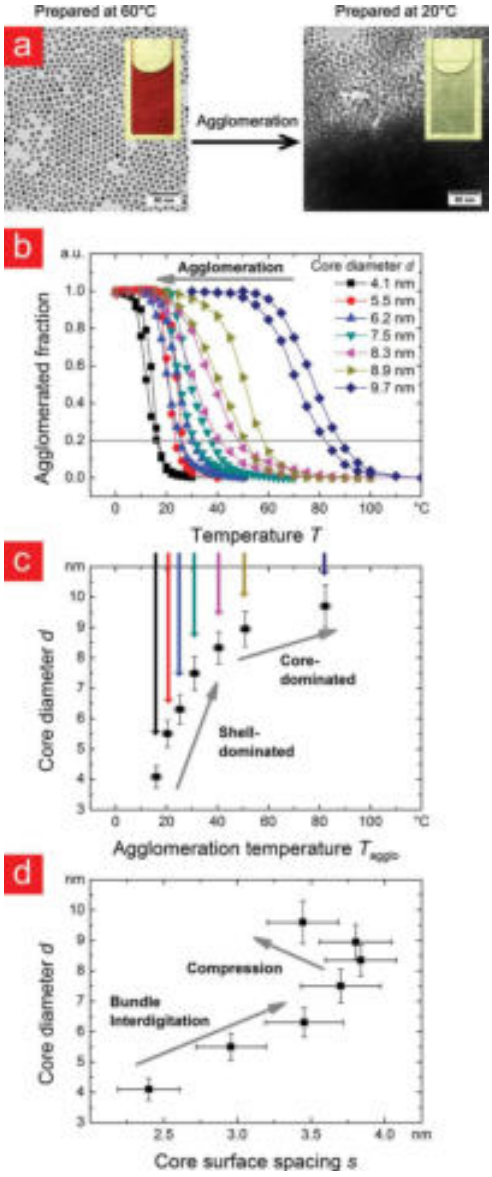

Figure 1. Temperature-dependent agglomeration of AuNP with 1-hexadecanethiol shells and different core diameters in decane. (a) Transmission electron micrographs of AuNP with a diameter of 7.5 nm. The samples were prepared at 60 °C and 20 °C, respectively. Insets show optical photographs of macroscopic dispersions at the respective temperature. (b) Fraction of agglomerated particles as determined by in situ small-angle X-ray scattering. All particles were dispersed at high temperatures, and agglomeration occurred upon cooling as indicated by the increase in structure factor. (c) Agglomeration temperature (where 20% of particles were agglomerated) as a function of core size. Note the change near a core diameter of 8.3 nm. (d) Core surface spacing between AuNP at the agglomeration temperature. The spacing was largest for the 8.3 nm particles.

In contrast, larger particles agglomerated before the ligands had ordered, indicating that their agglomeration is driven primarily by attraction between the nanocrystal cores. Analytical calculations of the Au−Au vdW interaction are consistent with a shift to core-dominated agglomeration, with

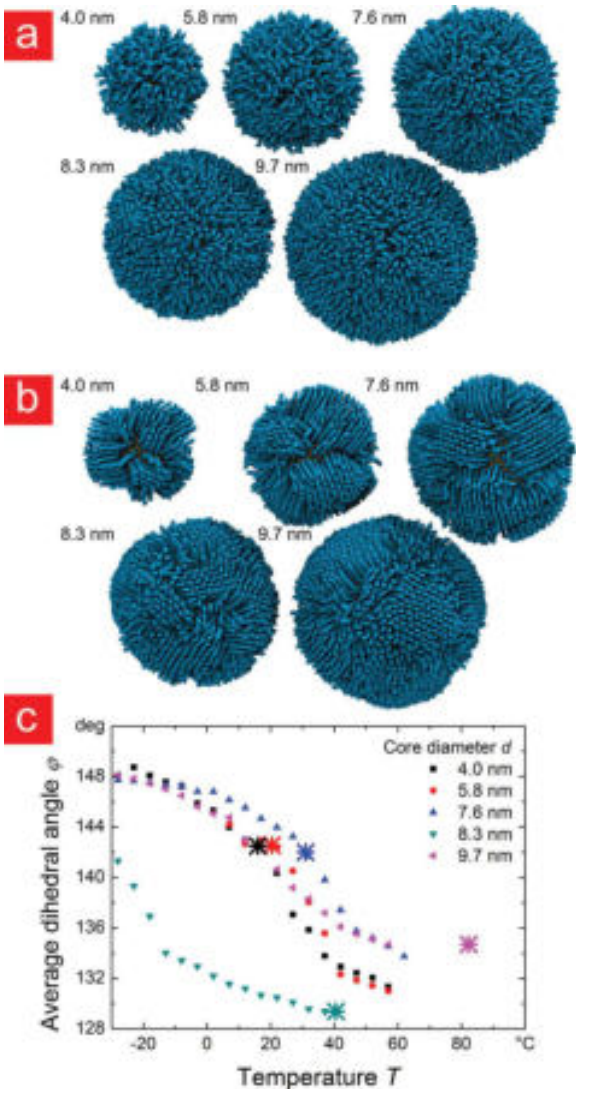

Figure 2. Simulation snapshots at (a) high and (b) low temperature show that the structure of the ligand shell depends on both temperature and particle size (decane solvent not shown). These changes are quantified by (c) the average dihedral angle of the ligands, which increases rapidly as the ligands order. For comparison, the experimental agglomeration temperatures have been indicated by large crossed symbols.

the Au−Au interaction predicted to exceed 0.5 k_BT at the experimental interparticle spacing at T_{agglo} around a diameter of 8 nm. In agglomerates, each particle will have an average of roughly 12 neighbors, which at 0.5k_BT per interaction would result in a total stabilization energy per particle of 6 × 0.5 = 3 k_BT. In comparison, Lennard-Jones particles, which have a slightly longer relative interaction range, are known to aggregate around an interaction energy of 0.75 k_BT per particle pair.[24] The sudden drop in T_{order} above a diameter of 8 nm is not essential for this conclusion, but the much smaller drop in vacuum (see SI, Figure S5) indicates that it is due to a significant change in how the solvent interacts with the ligands as the diameter increases. The radial probability distributions for the ligand and solvent (see SI, Figure S7) show that the

DOI: 10.1021/acsnano.8b02202
ACS Nano 2018, 12, 5969−5977

solvent becomes increasingly excluded from the ligand shell, especially in the disordered state.

Our simulations explain a second unexpected experimental result: the nonlinear relation between core size and core surface spacing (the distance between the gold surfaces of two adjacent particles) shown in Figure 1d. We used Ehrenfest's equation to calculate the spacing of particles in amorphous agglomerates and Bragg's equation for the spacing in crystalline agglomerates.[25] The resulting surface spacings (Figure 1d) were remarkably well-defined and reproducible. The spacings increased with particle core size up to a diameter of 8.3 nm and decreased for larger cores, an effect that is readily explained by the molecular shell structure seen in simulation: small particles have large surface curvatures, and the average ligand density (see SI, Figure S7) rapidly decreases when moving away from their center (the "hairy ball effect"). This facilitates interlocking of ligand bundles (see snapshot in Figure 3a), which reduces spacing as the core diameter decreases. In particular, we find that particles preferentially orient themselves so that an ordered bundle on one particle points into the groove between ordered bundles on the other particle, similar to how cogwheels fit together. This bundle interdigitation is distinct from the interdigitation of individual ligands that is often drawn in illustrations and appears to be favored because it allows for a denser and more energetically stable packing of the ligands. In this case, it is the anisotropy of the ligand shell at low temperature, rather than only the particle curvature, that allows for particle separations that are less than twice the average shell thickness. As the core diameter increases, the ability of the bundles to interpenetrate decreases, resulting in particle separations that *increase* with core size in the ligand-dominated regime. On the other hand, as we enter the core-dominated regime, the strong vdW attraction between the metal cores exerts an increasing pressure on the disordered shell, which causes compression and leads to the *decreased* spacing for the largest particles.

In summary, we propose that two transitions dominate the colloidal agglomeration of apolar nanoparticles with short ligands: a phase transition between ligand order and disorder (that can be driven by temperature or change in solvent quality), and a transition between core- and shell-dominated interaction (that depends on the core size and material). In the following, we quantitatively discuss the temperature- and size-dependent interaction potential between apolar nanoparticles using simulation results and a common analytical model.

Using constrained molecular dynamics simulations, we calculated the interaction potential between a pair of 4 nm Au particles in decane at T_{agglo} + 20 °C, T_{agglo} + 5 °C, and T_{agglo} − 10 °C (Figure 3b–d). The total potential curves (green inverted triangles) show that the interaction between the particles changes from repulsive to attractive as the ligands align with one another and form ordered bundles on the surface of the particles. This dramatic change in how the particles interact with one another is due to a subtle change in the balance between the ligand–ligand and ligand–solvent interactions as the ligands order, with the former gradually becoming more attractive, especially at shorter range. In contrast, the vdW interaction between the Au cores (black squares) remains negligibly small until separations well below those observed experimentally. While accurate calculation of the interaction potential is difficult due to statistical sampling issues, we note that the minimum in the potential at T_{agglo} + 5 °C = T_{order} occurs very close to the experimentally observed core surface spacing of 2.4 nm. These results constitute a direct demonstration that ordering of ligands on small nanoparticles induces attraction between the particles even in a good solvent. Previous simulation studies of the interaction between small

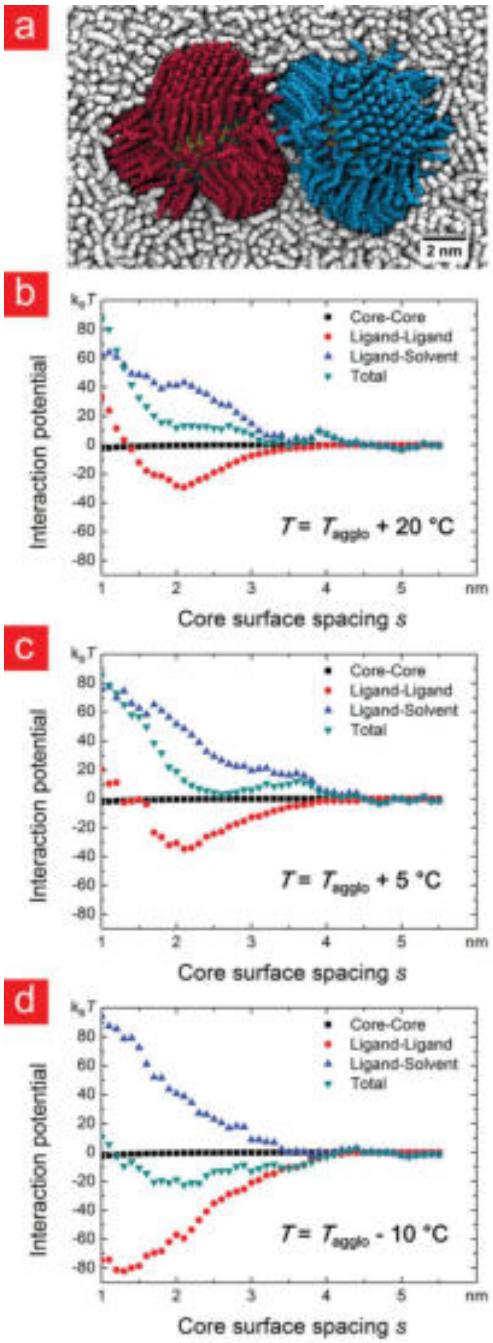

Figure 3. (a) Simulation snapshot at T_{agglo} + 5 °C showing two 4 nm particles at 2.4 nm separation. Different colors have been used for the ligands on the two particles and the solvent partially hidden. Interaction potentials for pairs of 4 nm Au particles in decane at (b) T_{agglo} + 20 °C, (c) T_{agglo} + 5 °C, and (d) T_{agglo} − 10 °C, obtained from constrained molecular dynamics simulations. The total potential is green, the ligand–ligand contribution is red, the ligand–solvent contribution is blue, and the core–core contribution is black.

DOI: 10.1021/acsnano.8b02202
ACS Nano 2018, 12, 5969–5977

gold nanoparticles in solvents were limited to the high-temperature regime where the particles repel one another.[26−28]

We stress that the present discussion is relevant to the interaction between nanoparticles in good solvents such as decane. In vacuum, by contrast, the interaction between the particles is attractive irrespective of ligand conformation (see SI, Figure S6). The strong attraction in vacuum is due to the much stronger vdW attraction between the ligands in the absence of solvent, as has been noted previously for other nanoparticles.[17,26,29,30]

The existing analytical models for the interaction between apolar NPs assume a radially uniform ligand density around the particles and do not consider the ability of the ligand shell to change its order and symmetry. In the following, we summarize the state of the art in analytical modeling and briefly introduce a model based on the work of Khan et al.[7] that was modified for the particles used here. Most theoretical approaches assume a linear superposition of core−core van der Waals attraction, entropic repulsion due to ligand compression, and the free energy of mixing of ligands and solvents.[7,8] The van der Waals (vdW) interaction G_{vdW} is usually described using the reduced Hamaker coefficient A for the inorganic core interacting through an organic ligand/solvent medium[31−33] and a geometrical factor that depends on the rescaled spacing $\tilde{s}$ (center-to-center distance divided by the core diameter of the particles):

$$G_{vdW} = -\frac{A}{12}\left(\frac{1}{\tilde{s}^2 - 1} + \frac{1}{\tilde{s}^2} + 2\ln\left(1 - \frac{1}{\tilde{s}^2}\right)\right) \quad (1)$$

When the ligand shells overlap at a surface separation below one ligand length L, ligand compression, and associated loss of conformational entropy, causes a repulsive force. This interaction G_{com} is usually taken to be proportional to the ligand surface coverage υ,

$$\frac{G_{com}}{k_B T} = \pi \upsilon d^2\left((\tilde{s} - 1)\left(\ln\frac{\tilde{s} - 1}{\tilde{L}} - 1\right) + \tilde{L}\right) \quad (2)$$

where d is the core diameter, $\tilde{L}$ is the rescaled ligand length (ligand length divided by core diameter), k_B is the Boltzmann's constant, and T is the absolute temperature.

Interactions between the solvent and the ligand shell add a free energy of mixing G_{mix} that is often estimated using Flory−Huggins theory and can be either attractive or repulsive. When the particles are close enough to interpenetrate but do not deform ($1 + \tilde{L} < \tilde{s} < 1 + 2\tilde{L}$), this interaction can be estimated as

$$\frac{G_{mix1}}{k_B T} = \frac{\pi d^3}{2\nu_S}\phi^2\left(\frac{1}{2} - \chi\right)(\tilde{s} - 1 - 2\tilde{L})^2 \quad (3)$$

When the particles are so close that the ligand shells are compressed ($\tilde{s} < 1 + \tilde{L}$), the contribution becomes

$$\frac{G_{mix2}}{k_B T} = \frac{\pi d^3}{\nu_S}\phi^2\tilde{L}^2\left(\frac{1}{2} - \chi\right)\left(3\ln\frac{\tilde{L}}{\tilde{s} - 1} + 2\frac{\tilde{s} - 1}{\tilde{L}} - \frac{3}{2}\right) \quad (4)$$

where $\phi = \left(N_L \frac{\nu_L}{V_{Sh}}\right)^2$ is the volume fraction occupied by the ligand shell, ν_S is the volume of a solvent molecule, ν_L the volume of a ligand molecule, N_L the number of ligands per NP, V_{Sh} the volume of the ligand shell, and χ the Flory parameter that describes how well a single ligand molecule is solvated. This empirical parameter can be calculated from the Hildebrand solubility parameters of the solvent δ_S and the ligand δ_L:

$$\chi = \frac{V_S}{RT}(\delta_L - \delta_S)^2 + 0.34 \quad (5)$$

where V_S is the molar volume of the solvent and R the universal gas constant. A Flory parameter below 0.5 indicates that $G_{mix} < 0$. Note that Flory−Huggins theory has been developed for flexible polymers, not short ligands, and its use for ligand shells (as introduced by Khan in ref 7) should be seen merely as a phenomenological approach.

We used this model to calculate interaction potentials (parameters are shown in Table 2) for our particles at their agglomeration temperatures (Figure 4a). The predicted particle separations are larger than experimentally observed for all of the particles, and the predicted minima are too shallow to explain the observed agglomeration for all but the largest particles. While the attractive interactions between the gold cores (Figure 4b) are probably correctly represented in the model, it does not correctly describe the interaction of the ligand shells with the solvent and with other particles during agglomeration.

Table 2. Parameters Used for Analytical Calculations of the Interaction Potential Using eqs 1−5[7,47]

parameter	value
Hamker constant A of gold	3.12×10^{-19} J
ligand length L for hexadecanethiol	2.2 nm
ligand surface coverage υ	5.5 nm^{-2}
volume solvent molecule ν_S	0.324 nm^3
volume ligand molecule ν_L	0.505 nm^3
molar volume solvent V_S	0.000195 m^3/mol
solubility parameter δ_s decane	$1.58 \times 10^4 \sqrt{Pa}$
solubility parameter δ_s hexadecane	$1.63 \times 10^4 \sqrt{Pa}$
solubility parameter δ_L hexadecanethiol	$1.69 \times 10^4 \sqrt{Pa}$

The simulations above indicate that much of this failure of the analytical model stems from its inability to account for ordering of the ligand shell. The ligand ordering has two important consequences: first, it provides an additional source of attraction between the particles that drives agglomeration in the absence of strong vdW attraction between the cores, and second, it reduces the compressive repulsion between the particles when they are oriented such that their ligand bundles can interdigitate, which allows for smaller particle separations than would otherwise be possible. The analytical model also appears to overestimate the energy required to compress the disordered ligand shell, predicting separation distances that are too large even in the core-dominated regime.

We conclude that the existing analytical models are not suitable to predict the stability of apolar nanoparticles and that they predict incorrect particle spacings, regardless of the shell structure. An extension of the models would have to consider the temperature-dependent, possibly anisotropic structure of the shell. It is insufficient to merely change the solubility parameters.

The size and temperature dependence of particle stability has several interesting consequences. First, our results indicate that it might be possible to size-separate sufficiently large particles by temperature-induced agglomeration because of the strong

DOI: 10.1021/acsnano.8b02202
ACS Nano 2018, 12, 5969−5977

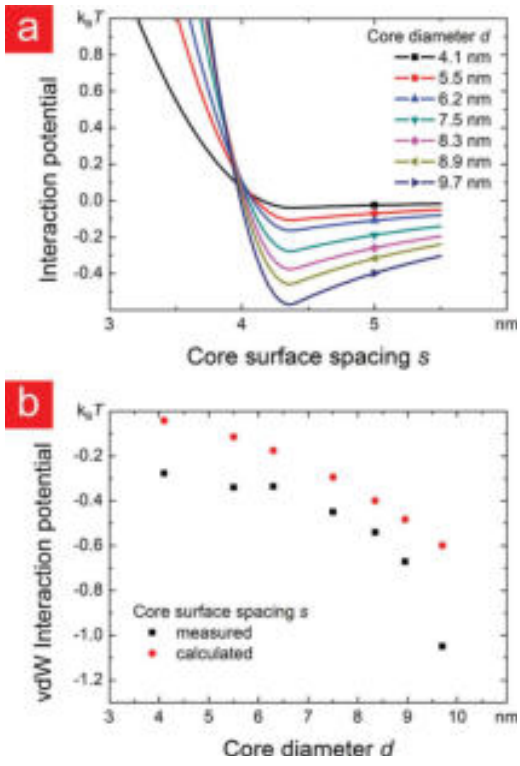

Figure 4. (a) Interaction potentials calculated using eqs 1−5 using solubility parameters of the free ligands. The predicted potentials are incompatible with experiments and simulations. (b) van der Waals interaction potentials between the Au cores at the experimental and the calculated particle separations in units of thermal energy at T_{agglo} and s_{agglo} as estimated using Hamaker−Lishitz theory.

variation in agglomeration temperature with particle size. For example, the slope of the agglomeration curves was smallest for our largest particles (Figure 1b) despite all of our samples having similar size dispersity (Table 1). Second, the crystallinity of the agglomerates increased with increasing temperature for particles with diameters above 7.5 nm, i.e., in or near the core-dominated regime. The transition is illustrated in SI, Figure S8. This size-dependence may reflect the change in shape of the ligand shell from anisotropic to isotropic at T_{agglo}, although further work is needed to confirm this. We note that a similar increase in crystallinity with temperature has been reported for 6.4 nm diameter Au particles where the agglomeration was driven by the addition of a poor solvent.[34]

CONCLUSIONS

We systematically evaluated the size-dependent stability of gold NPs with hexadecanethiol shells in decane experimentally and found a nonlinear size dependency. Molecular dynamics simulations and analytical calculations of the core−core vdW interaction indicate that a transition between core- and shell-dominated agglomeration occurs around a core diameter of 8 nm. This transition affects stability and particle spacing in the agglomerates and can potentially occur for all hybrid particles consisting of a core that has a different Hamaker constant from the shell and a shell that is composed of discrete molecules that are anchored at one end. The transition diameter depends on the particular combination of core and ligand.

As a rough estimate for whether a specific particle will be in the core- or the shell-dominated regime, one may calculate eq 1 at $\tilde{s} = 1 + 2\tilde{L}$, i.e., the vdW attraction between the cores at the point where the ligands shells first come into contact. For our particles, this quantity corresponds to the red symbols in Figure 4b, which show that if $G_{vdW} > 0.35\ k_BT$ at this point, then the particles are in the core-dominated regime and otherwise they are in the shell-dominated regime.

The dispersion used here arguably contains the simplest apolar nanoparticle available: a core with uniform density and a narrow size distribution is coated with a relatively uniform density of linear ligand molecules in a simple solvent that is structurally similar to the ligand. The fact that the existing theories are insufficient to predict its stability suggest that extended models are needed. Colloidal stability in the ligand-dominated regime depends so strongly on the difference in free energy between the ordered and disordered states that even small changes in ligand surface coverage should considerably affect it,[18] which may explain the commonly observed batch-to-batch variations in the stability of freshly prepared apolar nanoparticles and their aging.[35,36] Other factors that are likely to affect the free energy balance of the ligand shell and associated stability of the particles in solvents include more complex ligand structures (for example, a kink in the case of oleylamine), mixtures of ligands, and lateral diffusion of ligands on the nanocrystal surface.[37,38]

The results presented here suggest that even small changes in ligand and solvent molecule length may have a strong effect on colloidal stability. Initial experiments do indeed indicate ligand and solvent dependencies that run counter to the predictions of conventional colloid theory. These results will be presented in forthcoming publications.

METHODS

All chemicals were obtained from Sigma-Aldrich (unless noted otherwise) and used without further purification.

Nanoparticle Synthesis. Gold nanoparticles (Au NPs) with diameters between 4 and 9.7 nm were synthesized using a modified protocol based on Wu and Zheng.[39] Au NPs with a diameter of 8 nm were produced as follows. A mixture of 8 mL of benzene (puriss ≥ 99.7%), 8 mL of oleylamine (technical grade, 70%), and 100 mg of $HAuCl_4 \cdot H_2O$ was stirred at 20 °C and 500 rad min^{-1} for 1 min under argon atmosphere. Afterward, 40 mg of *tert*-butylamine borane (ABCR, 97%) which was dissolved in 2 mL of benzene and 2 mL of oleylamine (OAm) was added to the solution. The color of the solution immediately became dark purple. After stirring for 60 min at 20 °C, the nanoparticles were purified once by precipitating with 30 mL of ethanol and centrifugation at 4000 rad min^{-1} for 5 min. The precipitated nanoparticles were redispersed in 20 mL of heptane (puriss ≥ 99%). AuNP with a diameter of 4 nm were obtained using pentane (reagent grade, 98%) instead of benzene and stirring for 30 min before adding the *tert*-butylamine borane complex.

Nanoparticle Characterization. The core size of the NPs was measured by small-angle X-ray scattering (SAXS, device explained in more details below) and by analyzing transmission electron microscopy (TEM) micrographs. The angle-dependent scattering intensity was then fitted using SASfit (version 0.94.6) provided by the Paul Scherrer Institute. TEM micrographs were taken with a JEOL JEM 2010 at 200 kV. Around 2000 particles were counted with the ImageJ 1.45s software for each size, and the arithmetic mean and the standard deviation were calculated.

Ligand Exchange. Ligand exchange was performed using previously published methods.[40] Oleylamine-stabilized AuNP were heated to 80 °C under argon. 1-Hexadecanethiol (≥95.0% GC, 10 times the molar amount of gold) was added to the solution, and the mixture was stirred at 80 °C for 10 min. The resulting particles were

DOI: 10.1021/acsnano.8b02202
ACS Nano 2018, 12, 5969−5977

purified once by precipitation with ethanol, centrifugation, and resuspension in decane (≥95%).

Thermogravimetric Analyses. Thermogravimetric analyses were performed on a Netzsch STA 449 F3 Jupiter instrument. The measurements started at room temperature and ran up to 800 °C. The heating rate was kept at 10 K min^{-1}. All measurements were done under an inert atmosphere.

Small-Angle X-ray Scattering. All scattering experiments were performed at a Xeuss 2.0 from Xenocs SA (Grenoble, France). The setup was equipped with a copper K_α X-ray source with a wavelength λ = 0.154 nm and a PILATUS 1 M hybrid photon counting detector from DECTRIS (Baden, Switzerland). The sample to detector distance was kept at 1200 mm.

A quantity of 20−40 μL of the respective dispersion was filled into single-used capillaries with a diameter of 2 mm that was sealed with epoxy and introduced to the vacuum of the sample chamber. Pure solvent was measured in a reference capillary with the same diameter.

Temperature was controlled using a Peltier-based temperature stage (Omega CN8200) in a range between −20 and 120 °C. All measurements started at high temperatures to ensure that the NPs were deagglomerated. The temperature was then decreased or increased in steps of 2 or 5 °C. At each step, 20 min equilibration time was allowed before acquisition of scattering data during 10 min.

To achieve the pure particle signal $I(q)_{NPs}$, the total scattering intensity $I(q)$ was corrected by the transmission factor of the NPs T_{NPs}, followed by a subtraction with the scattered intensity $I(q)_S$ of the pure solvent, which was also corrected by the transmission factor T_S of the solvent.[20] This is shown by the equation below. The correction factors T_{NPs} and T_S were extracted from the pin diode signal which was mounted in the direct beam.

$$I(q)_{NPs} = \frac{I(q)}{T_{NPs}} - \frac{I(q)_S}{T_S} \tag{6}$$

To extract the degree of agglomeration versus the temperature, the "structure-factor" $S(q)$ was calculated by dividing all corrected spectra with the form-factor $P(q)_{NPs}$. The scattered intensity is a product of $S(q)$ and $P(q)$. When NPs are fully dispersed (high temperatures), $S(q)$ is equal to 1. Because of this, the signal at high temperature is $P(q)$.

$$S(q)_{NpS} = \frac{I(q)_{NPs}}{P(q)_{NPs}} \tag{7}$$

Molecular Dynamics Simulations. The NPs were modeled as spherical Au cores covered in alkyl thiolate ligands in the presence of *n*-decane, as illustrated in SI, Figure S9. The ligands were assumed to be irreversibly bound to the gold surface at the surface coverage determined by TGA measurements (5.5 nm^{-2}). The positions of the sulfur atoms were constrained by the RATTLE algorithm[41] and determined by placing them on a spherical shell around the implicit metallic core (0.15 nm further out) and allowing them to find their optimal positions on this shell subject to a repulsive interaction between them (standard Coulombic potential with a dielectric constant ϵ = 10 kcal mol^{-1}, truncated at 24 Å). This ensured that the binding sites were approximately equidistant from one another. The sulfur atoms were subsequently treated as part of the rigid core of the particle. The rest of the ligand and solvent molecules were modeled using a united-atom representation, with each CH_x group being represented by a single particle. These particles interacted with one another according to the 12−6 Lennard-Jones (LJ) potential, with parameters as used and described previously.[17] Bond stretching, bond bending, and dihedral torsion terms were also considered within each molecule.[42] The interaction between the CH_x groups and the Au core was modeled using a 9−3 LJ potential (with ϵ/k_B = 88K and σ = 3.54 Å,[43] truncated at 30 Å). This provides a good approximation to CH_x−core interactions for NPs ≥ 4 nm in diameter.

Molecular dynamics (MD) simulations on systems of up to 565000 particles were performed using LAMMPS[44] with periodic boundary conditions, at temperatures ranging from 245 to 330 K (depending on the core diameter). Individual NPs were initially equilibrated in explicit decane at a temperature sufficiently high to ensure that the ligands were in the disordered state (*e.g.*, 400 K). During this run, the periodic simulation cell was slowly compressed until the solvent density far from the NP was equal to the experimental density of pure decane at the relevant temperature. Subsequent runs were carried out at fixed pressure (80 atm) and temperature, maintained with a Nosé−Hoover thermostat and barostat. This yielded bulk solvent densities within 1% of experimental values. Systems were equilibrated for at least 12 ns before 1−2 ns production runs were performed.

Interaction Potentials. The interaction potential between a pair of 4 nm particles was calculated as a potential of mean force (PMF) at selected temperatures using constrained MD. As the particles were brought together (at a rate of 1 Å ns^{-1}), they were allowed to freely rotate about their centers of mass. To allow the ligands to reorganize and find more stable configurations at and below T_{order}, we performed an additional thermal annealing step at separations where the ligand shells overlapped. This was done by increasing the temperature of these systems by 50K over 1 ns and subsequently cooling it back to the initial temperature over the course of 3 ns. We found that long subsequent simulation times (>10 ns at each separation) were required to adequately sample the PMF, especially at lower temperatures where the ligands are less mobile.

The spherical gold cores were assumed to interact with each other via the Hamaker potential,[45] with a Hamaker constant of 2 eV.[46,47] This approach treats the solvent and ligands as a single continuum, with the interaction constant scaled to include the effect of the hydrocarbon medium.

The PMF between two nanoparticles is given by

$$\phi_{MF}(r) = \int_r^\infty F_{mean}(s)\, ds \tag{8}$$

where F_{mean} is the average force in the direction of the line connecting the two particles and is given by

$$F_{mean}(r) = \frac{1}{2}\langle(\vec{F}_2 - \vec{F}_1)\cdot\vec{r}\rangle_{NVT} \tag{9}$$

In the above, $\vec{F}_1$ and $\vec{F}_2$ are the total forces acting on the first and second NP, respectively, $\vec{r}$ is the unit vector pointing from one particle's center to the other's, and the angular brackets denote an average in the canonical ensemble.

ASSOCIATED CONTENT

Supporting Information

The Supporting Information is available free of charge on the ACS Publications website at DOI: 10.1021/acsnano.8b02202.

SAXS and TEM data of the oleylamine capped AuNPs, TGA data of 1-hexadecanethiol capped AuNPs, analyzed SAXS data of AuNPs, average dihedral angles in vacuum, and radial density distributions of ligand and solvent (from simulation), structure factors of AuNPs and a snapshot of the simulation setup (PDF)

AUTHOR INFORMATION

Corresponding Author

*E-mail: tobias.kraus@leibniz-inm.de.

ORCID

Thomas Kister: 0000-0002-9827-1380
Paul Mulvaney: 0000-0002-8007-3247
Asaph Widmer-Cooper: 0000-0001-5459-6960
Tobias Kraus: 0000-0003-2951-1704

Notes

The authors declare no competing financial interest.

DOI: 10.1021/acsnano.8b02202
ACS Nano 2018, 12, 5969−5977

ACKNOWLEDGMENTS

A.W. thanks the Australian Research Council for a Future Fellowship (FT140101061). P.M., D.M. and A.W. were supported by the ARC Centre of Excellence in Exciton Science (CE170100026). Computational resources were generously provided by the University of Sydney HPC service, the National Computational Infrastructure National Facility (NCI-NF) Flagship program, and the Pawsey Supercomputer Centre Energy and Resources Merit Allocation Scheme. T.K. and T.K. thank the DFG Deutsche Forschungsgemeinschaft for funding and E. Arzt for his continuing support of this project. P.M. and T.K. also thank the DAAD for travel support.

REFERENCES

(1) Murray, C.; Norris, D. J.; Bawendi, M. G. Synthesis and Characterization of Nearly Monodisperse CdE (E= Sulfur, Selenium, Tellurium) Semiconductor Nanocrystallites. *J. Am. Chem. Soc.* **1993**, *115*, 8706−8715.

(2) Badia, A.; Singh, S.; Demers, L.; Cuccia, L.; Brown, G. R.; Lennox, R. B. Self-Assembled Monolayers on Gold Nanoparticles. *Chem. - Eur. J.* **1996**, *2*, 359−363.

(3) Singh, M.; Haverinen, H. M.; Dhagat, P.; Jabbour, G. E. Inkjet Printing-Process and Its Applications. *Adv. Mater.* **2010**, *22*, 673−685.

(4) Jensen, G. C.; Krause, C. E.; Sotzing, G. A.; Rusling, J. F. Inkjet-Printed Gold Nanoparticle Electrochemical Arrays on Plastic. Application to Immunodetection of a Cancer Biomarker Protein. *Phys. Chem. Chem. Phys.* **2011**, *13*, 4888−4894.

(5) Li, Y.; Rizzo, A.; Mazzeo, M.; Carbone, L.; Manna, L.; Cingolani, R.; Gigli, G. White Organic Light-Emitting Devices with CdSe/ZnS Quantum Dots as a Red Emitter. *J. Appl. Phys.* **2005**, *97*, 113501.

(6) Talapin, D. V.; Lee, J.-S.; Kovalenko, M. V.; Shevchenko, E. V. Prospects of Colloidal Nanocrystals for Electronic and Optoelectronic Applications. *Chem. Rev.* **2010**, *110*, 389−458.

(7) Khan, S. J.; Pierce, F.; Sorensen, C.; Chakrabarti, A. Self-Assembly of Ligated Gold Nanoparticles: Phenomenological Modeling and Computer Simulations. *Langmuir* **2009**, *25*, 13861−13868.

(8) Goubet, N.; Richardi, J.; Albouy, P.-A.; Pileni, M.-P. Which Forces Control Supracrystal Nucleation in Organic Media? *Adv. Funct. Mater.* **2011**, *21*, 2693−2704.

(9) Sigman, M. B.; Saunders, A. E.; Korgel, B. A. Metal Nanocrystal Superlattice Nucleation and Growth. *Langmuir* **2004**, *20*, 978−983.

(10) Flory, P. J. Thermodynamics of High Polymer Solutions. *J. Chem. Phys.* **1942**, *10*, 51−61.

(11) Luedtke, W. D.; Landman, U. Structure and Thermodynamics of Self-Assembled Monolayers on Gold Nanocrystallites. *J. Phys. Chem. B* **1998**, *102*, 6566−6572.

(12) Ghorai, P. K.; Glotzer, S. C. Molecular Dynamics Simulation Study of Self-Assembled Monolayers of Alkanethiol Surfactants on Spherical Gold Nanoparticles. *J. Phys. Chem. C* **2007**, *111*, 15857−15862.

(13) Lane, J. M. D.; Grest, G. S. Spontaneous Asymmetry of Coated Spherical Nanoparticles in Solution and at Liquid-Vapor Interfaces. *Phys. Rev. Lett.* **2010**, *104*, 235501.

(14) Ramin, L.; Jabbarzadeh, A. Odd−Even Effects on the Structure, Stability, and Phase Transition of Alkanethiol Self-Assembled Monolayers. *Langmuir* **2011**, *27*, 9748−9759.

(15) Bolintineanu, D. S.; Lane, J. M. D.; Grest, G. S. Effects of Functional Groups and Ionization on the Structure of Alkanethiol-Coated Gold Nanoparticles. *Langmuir* **2014**, *30*, 11075−11085.

(16) Shah, P. S.; Holmes, J. D.; Johnston, K. P.; Korgel, B. A. Size-Selective Dispersion of Dodecanethiol-Coated Nanocrystals in Liquid and Supercritical Ethane by Density Tuning. *J. Phys. Chem. B* **2002**, *106*, 2545−2551.

(17) Widmer-Cooper, A.; Geissler, P. Orientational Ordering of Passivating Ligands on CdS Nanorods in Solution Generates Strong Rod-Rod Interactions. *Nano Lett.* **2014**, *14*, 57−65.

(18) Widmer-Cooper, A.; Geissler, P. L. Ligand-Mediated Interactions between Nanoscale Surfaces Depend Sensitively and Nonlinearly on Temperature, Facet Dimensions, and Ligand Coverage. *ACS Nano* **2016**, *10*, 1877−1887.

(19) Silvera Batista, C. A.; Larson, R. G.; Kotov, N. A. Nonadditivity of Nanoparticle Interactions. *Science* **2015**, *350*, 1242477.

(20) Schnablegger, H.; Singh, Y. *The SAXS Guide: Getting Acquainted with the Principles*; Anton Paar GmbH: Graz, Austria, 2013; Vol. 2.

(21) Pontoni, D.; Narayanan, T.; Petit, J.-M.; Grübel, G.; Beysens, D. Microstructure and Dynamics Near an Attractive Colloidal Glass Transition. *Phys. Rev. Lett.* **2003**, *90*, 188301.

(22) Sztucki, M.; Narayanan, T.; Belina, G.; Moussaid, A.; Pignon, F.; Hoekstra, H. Kinetic Arrest and Glass-Glass Transition in Short-Ranged Attractive Colloids. *Phys. Rev. E* **2006**, *74*, 051504.

(23) Johnson, J. E. X-Ray Diffraction Studies of the Crystallinity in Polyethylene Terephthalate. *J. Appl. Polym. Sci.* **1959**, *2*, 205−209.

(24) Johnson, J. K.; Zollweg, J. A.; Gubbins, K. E. The Lennard-Jones Equation of State Revisited. *Mol. Phys.* **1993**, *78*, 591−618.

(25) Guinier, A. *X-ray Diffraction on Crystals, Imperfect Bodies, and Amorphous Bodies*; translated by Lorrain, P., Sainte-Marie Lorrain, D., translators; W. H. Freeman: San Francisco, 1963.

(26) Schapotschnikow, P.; Pool, R.; Vlugt, T. Molecular Simulations of Interacting Nanocrystals. *Nano Lett.* **2008**, *8*, 2930−2934.

(27) Jabes, B. S.; Yadav, H. O. S.; Kumar, S. K.; Chakravarty, C. Fluctuation-Driven Anisotropy in Effective Pair Interactions Between Nanoparticles: Thiolated Gold Nanoparticles in Ethane. *J. Chem. Phys.* **2014**, *141*, 154904.

(28) Yadav, H. O. S.; Shrivastav, G.; Agarwal, M.; Chakravarty, C. Effective Interactions Between Nanoparticles: Creating Temperature-Independent Solvation Environments for Self-Assembly. *J. Chem. Phys.* **2016**, *144*, 244901.

(29) Landman, U.; Luedtke, W. D. Small Is Different: Energetic, Structural, Thermal, and Mechanical Properties of Passivated Nanocluster Assemblies. *Faraday Discuss.* **2004**, *125*, 1−22.

(30) Waltmann, C.; Horst, N.; Travesset, A. Capping Ligand Vortices as Atomic Orbitals in Nanocrystal Self-Assembly. *ACS Nano* **2017**, *11*, 11273−11282.

(31) Bargeman, D.; van Voorst Vader, F. Van Der Waals Forces Between Immersed Particles. *J. Electroanal. Chem. Interfacial Electrochem.* **1972**, *37*, 45−52.

(32) Ohara, P. C.; Leff, D. V.; Heath, J. R.; Gelbart, W. M. Crystallization of Opals from Polydisperse Nanoparticles. *Phys. Rev. Lett.* **1995**, *75*, 3466.

(33) Morrison, I. D.; Ross, S. *Colloidal Dispersions: Suspensions, Emulsions, and Foams*; Wiley-Interscience, 2002.

(34) Geyer, T.; Born, P.; Kraus, T. Switching Between Crystallization and Amorphous Agglomeration of Alkyl Thiol-Coated Gold Nanoparticles. *Phys. Rev. Lett.* **2012**, *109*, 128302.

(35) Lacava, J.; Weber, A.; Kraus, T. Ageing of Alkylthiol-Stabilized Gold Nanoparticles. *Part. Part. Syst. Charact.* **2015**, *32*, 458−466.

(36) Horn, A. B.; Russell, D. A.; Shorthouse, L. J.; Simpson, T. R. E. Ageing of Alkanethiol Self-Assembled Monolayers. *J. Chem. Soc., Faraday Trans.* **1996**, *92*, 4759−4762.

(37) Boles, M. A.; Engel, M.; Talapin, D. V. Self-Assembly of Colloidal Nanocrystals: From Intricate Structures to Functional Materials. *Chem. Rev.* **2016**, *116*, 11220−11289.

(38) Yang, Y.; Qin, H.; Jiang, M.; Lin, L.; Fu, T.; Dai, X.; Zhang, Z.; Niu, Y.; Cao, H.; Jin, Y.; Zhao, F.; Peng, X. Entropic Ligands for Nanocrystals: From Unexpected Solution Properties to Outstanding Processability. *Nano Lett.* **2016**, *16*, 2133−2138.

(39) Wu, B.-H.; Yang, H.-Y.; Huang, H.-Q.; Chen, G.-X.; Zheng, N.-F. Solvent Effect on the Synthesis of Monodisperse Amine-Capped Au Nanoparticles. *Chin. Chem. Lett.* **2013**, *24*, 457−462.

(40) Kister, T.; Mravlak, M.; Schilling, T.; Kraus, T. Pressure-Controlled Formation of Crystalline, Janus, and Core−Shell Supraparticles. *Nanoscale* **2016**, *8*, 13377−13384.

(41) Andersen, H. C. Rattle: A "Velocity" Version of the Shake Algorithm for Molecular Dynamics Calculations. *J. Comput. Phys.* **1983**, *52*, 24−34.

DOI: 10.1021/acsnano.8b02202
ACS Nano 2018, 12, 5969−5977

(42) Martin, M. G.; Siepmann, J. I. Transferable Potentials for Phase Equilibria. 1. United-Atom Description of n-Alkanes. *J. Phys. Chem. B* **1998**, *102*, 2569−2577.
(43) Pool, R.; Schapotschnikow, P.; Vlugt, T. J. H. Solvent Effects in the Adsorption of Alkyl Thiols on Gold Structures: A Molecular Simulation Study. *J. Phys. Chem. C* **2007**, *111*, 10201−10212.
(44) Plimpton, S. Fast Parallel Algorithms for Short-Range Molecular Dynamics. *J. Comput. Phys.* **1995**, *117*, 1−19.
(45) Hamaker, H. C. The London - Van Der Waals Attraction Between Spherical Particles. *Physica* **1937**, *4*, 1058−1072.
(46) Ederth, T. Computation of Lifshitz - van der Waals Forces between Alkylthiol Monolayers on Gold Films. *Langmuir* **2001**, *17*, 3329−3340.
(47) Kokkoli, E.; Zukoski, C. F. Effect of Solvents on Interactions Between Hydrophobic Self-Assembled Monolayers. *J. Colloid Interface Sci.* **1999**, *209*, 60−65.

DOI: 10.1021/acsnano.8b02202
ACS Nano 2018, 12, 5969−5977

On the Colloidal Stability of Apolar Nanoparticles: The Role of Particle Size and Ligand Shell Structure

Thomas Kister,[†] Debora Monego,[‡] Paul Mulvaney,[¶] Asaph Widmer-Cooper,[‡] and Tobias Kraus[*,§]

†*INM — Leibniz Institute for New Materials, Campus D2 2, 66123 Saarbrücken, Germany*

‡*ARC Centre of Excellence in Exciton Science, School of Chemistry, University of Sydney, Sydney, New South Wales 2006, Australia*

¶*ARC Centre of Excellence in Exciton Science, School of Chemistry and Bio21 Institute, University of Melbourne, Parkville, Victoria 3010, Australia*

§*INM — Leibniz Institute for New Materials, Campus D2 2, 66123 Saarbrücken, Germany*

Colloid and interface chemistry, Saarland University, Campus D2 2, 66123 Saarbrücken, Germany

E-mail: tobias.kraus@leibniz-inm.de

Figures 1 and 2 show SAXS and TEM data of the as-synthesized, oleylamine-capped AuNPs. We used the program SASfit 0.94.6 from the Paul Scherrer Institute to fit the SAXS data with a sphere scattering model and ImageJ 1.45s to evaluate the particle size from TEM micrographs.

Figure 3 shows the evaluated TGA data for 4 different core diameters. After ligand

exchange with 1-hexadecanethiol, the AuNPs were washed 3 to 5 times by precipitation with methanol/ethanol and centrifugation and finally redispersed in hexane. The dispersion was dried and 20 mg to 40 mg of AuNPs were placed in TGA crucibles for each measurement.

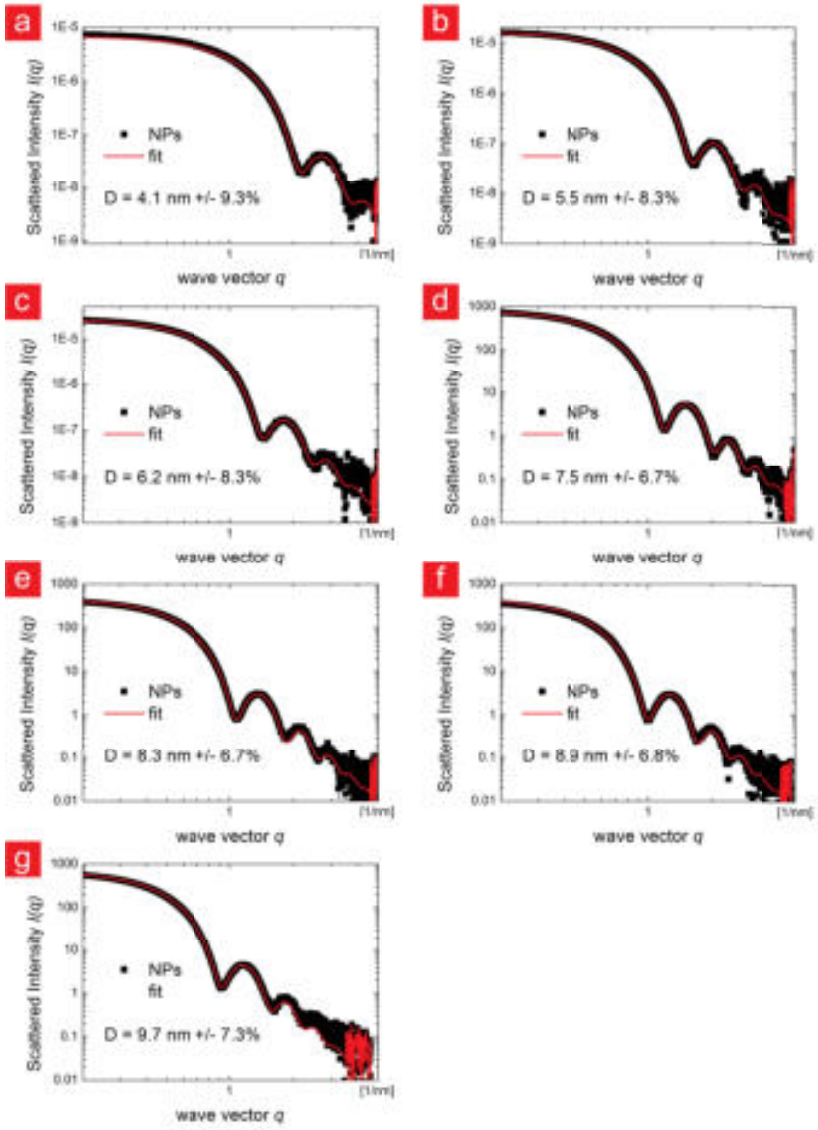

Figure 1: Small angle X-ray scattering data of the used AuNPs. The data was fitted to a sphere scattering model to obtain diameter and width of size distribution.

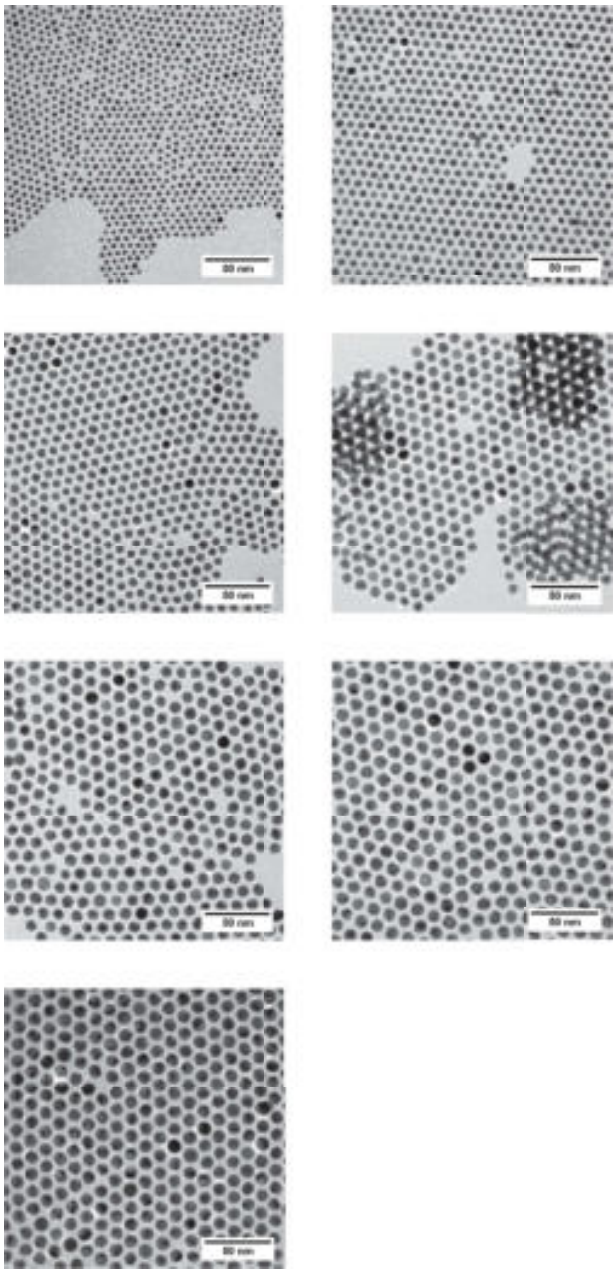

Figure 2: Transmission electron microscopy micrographs of the used AuNPs. Image analysis was performed to obtain diameter and width of size distribution.

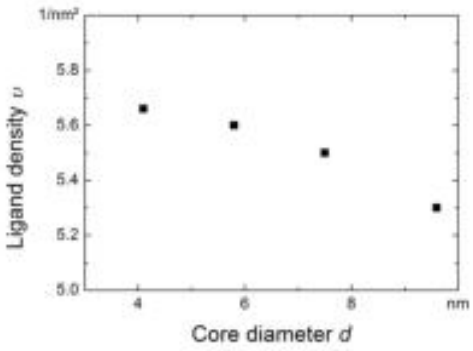

Figure 3: Thermogravimetric analysis data of AuNPs with 4 different sizes. The ligand density was between 5.65 nm^{-2} and 5.3 nm^{-2} for all particles.

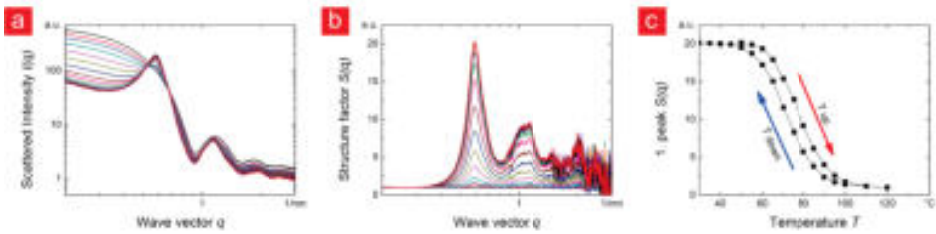

Figure 4: Temperature-dependent scattering of AuNPs with a diameter of 9.7 nm. a) Raw data. b) The calculated structure factors. The peaks increase upon cooling. c) Evolution of the height of the first peak during a temperature cycle from 120 °C to 30 °C and back to 120 °C over 16 h.

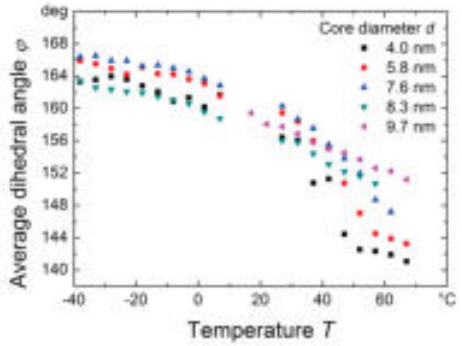

Figure 5: Average dihedral angle of the ligands as a function of temperature for different particle core diameters in vacuum. As in decane, there is a crossover in behavior near a diameter of 8 nm, but this is no longer associated with a large drop in the ordering temperature.

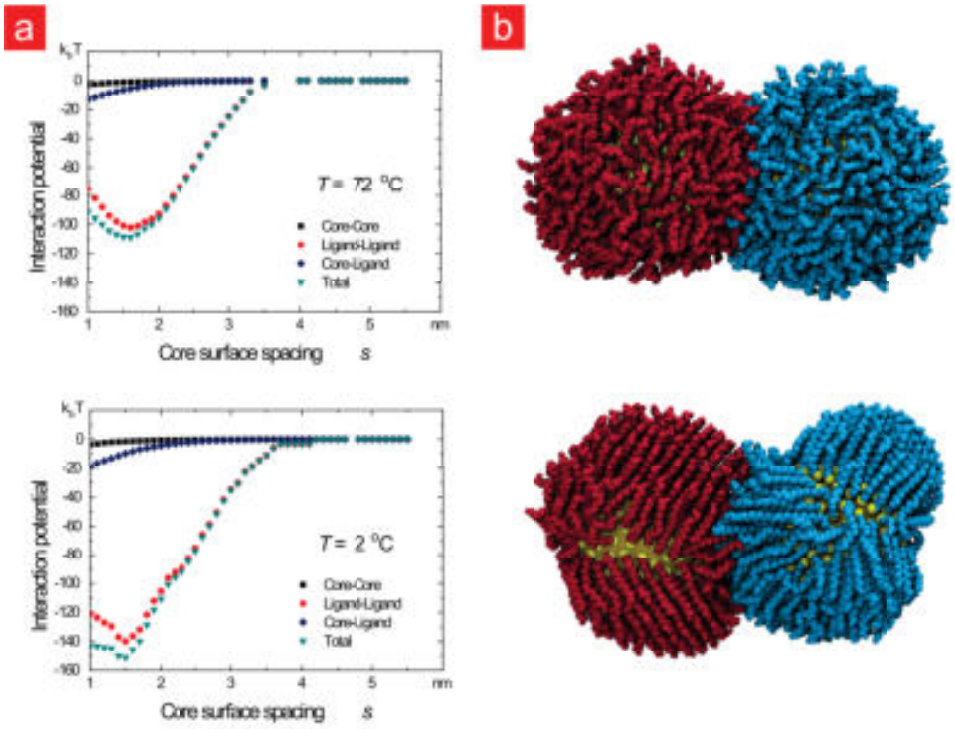

Figure 6: (a) Interaction potentials for pairs of 4 nm Au particles in vacuum obtained by calculating the potential of mean force between the particles using constrained molecular dynamics simulations. The total potential is green, the ligand-ligand contribution is red, the ligand-core contribution is blue, and the core-core contribution is black. The interaction potential in vacuum is attractive irrespective of the conformation of the ligands. (b) Simulation snapshots for the two particles at 1.5 nm separation at the respective temperatures.

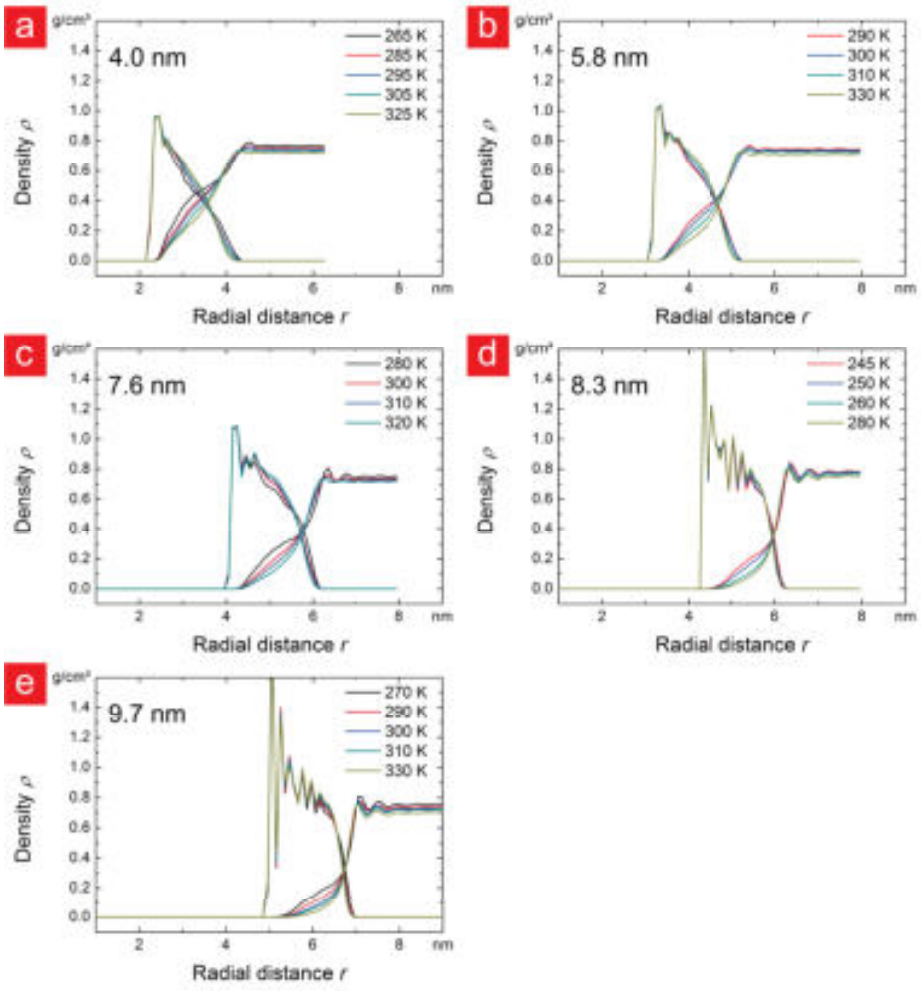

Figure 7: Radial density distributions for the ligand and solvent for different particle core diameters, plotted as a function of the distance r from the center of the nanoparticle core. The dark blue lines indicate the density profile at the ligand ordering temperature T_{order} for each particle. For all core sizes, as the temperature decreases and the ligands order, the space between bundles on the surface of the particle becomes larger, allowing for more solvent to occupy that region. As the particles get larger, this space becomes smaller and the interface between the ligands and the solvent becomes more sharply defined, limiting the amount of solvent that is able to enter the ligand shell.

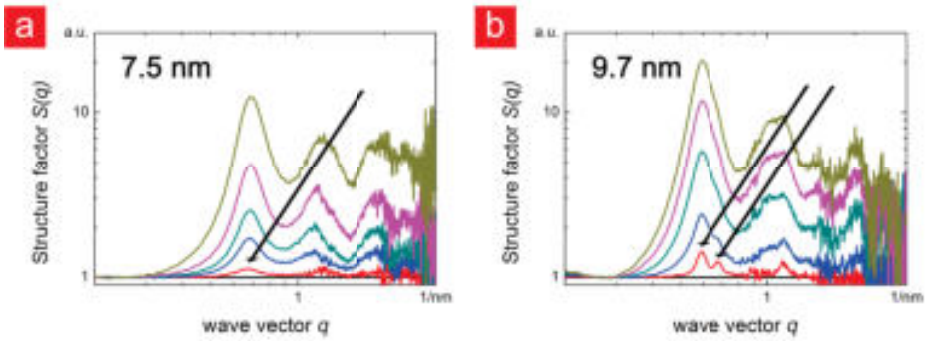

Figure 8: Temperature dependent structure factor for AuNPs with diameters of 7.5 nm and 9.7 nm. Smaller NPs formed amorphous agglomerates (no visible crystalline structure at the beginning of the agglomeration). For bigger NPs crystalline structure (fcc) appeared at the beginning of the agglomeration. This is indicated by the formation of two peaks (marked by arrows).

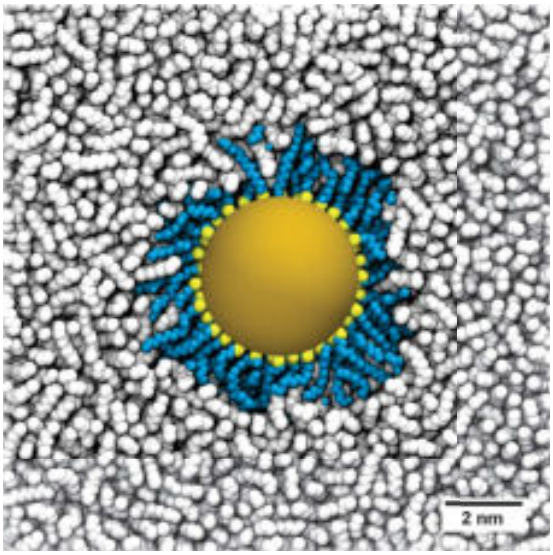

Figure 9: Snapshot of a simulation cell that has been cut in half showing the set up of our model for a gold nanocrystal (golden sphere at the center) covered in hexadecyl thiolate ligands (yellow and blue particles) and solvated by n-decane (white particles).

3.2 Publication 2

Monego, D., Kister, T., Kirkwood, N., Mulvaney, P., Widmer-Cooper, A., & Kraus, T. (2018). Colloidal stability of apolar nanoparticles: Role of ligand length. Langmuir, 34(43), 12982-12989.

DOI: 10.1021/acs.langmuir.8b02883

Monego, D., Kister, T., Kirkwood, N., Mulvaney, P., Widmer-Cooper, A., & Kraus, T. (2020). Correction to “On the Colloidal Stability of Apolar Nanoparticles: The Role of Ligand Length”. Langmuir, 36(36), 10892-10893.

DOI: 10.1021/acs.langmuir.0c02478

LANGMUIR Article
Cite This: Langmuir 2018, 34, 12982−12989 pubs.acs.org/Langmuir

Colloidal Stability of Apolar Nanoparticles: Role of Ligand Length

Debora Monego,[†,⊥] Thomas Kister,[‡,⊥] Nicholas Kirkwood,[§] Paul Mulvaney,[§] Asaph Widmer-Cooper,[†] and Tobias Kraus*[,‡,∥]

[†]ARC Centre of Excellence in Exciton Science, School of Chemistry and The University of Sydney Nano Institute, University of Sydney, Sydney, New South Wales 2006, Australia

[‡]INM—Leibniz Institute for New Materials, Campus D2 2, 66123 Saarbrücken, Germany

[§]ARC Centre of Excellence in Exciton Science, School of Chemistry, University of Melbourne, Parkville, Victoria 3010, Australia

[∥]Colloid and Interface Chemistry, Saarland University, Campus D2 2, 66123 Saarbrücken, Germany

Supporting Information

ABSTRACT: Inorganic nanoparticle cores are often coated with organic ligands to render them dispersible in apolar solvents. However, the effect of the ligand shell on the colloidal stability of the overall hybrid particle is not fully understood. In particular, it is not known how the length of an apolar alkyl ligand chain affects the stability of a nanoparticle dispersion against agglomeration. Here, small-angle X-ray scattering and molecular dynamics simulations have been used to study the interactions between gold nanoparticles and between cadmium selenide nanoparticles passivated by alkanethiol ligands with 12−18 carbons in the solvent decane. We find that increasing the ligand length increases colloidal stability in the core-dominated regime but decreases it in the ligand-dominated regime. This unexpected inversion is connected to the transition from ligand-dominated to core-dominated agglomeration when the core diameter increases at constant ligand length. Our results provide a microscopic picture of the forces that determine the colloidal stability of apolar nanoparticles and explain why classical colloid theory fails.

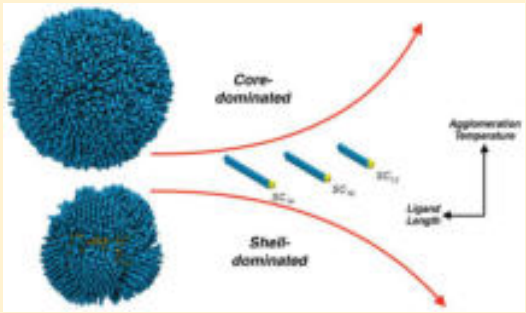

INTRODUCTION

The most common way to stabilize inorganic nanoparticles in apolar solvents is to coat them with sufficiently dense layers of molecules with apolar chains.[1−3] Nanoparticles made from noble metals (for instance Au, Ag, or Pt),[4] semiconductors (for instance CdSe, CdTe, or PbSe),[5] metal oxides (for instance Fe_3O_4, TiO_2, or Al_2O_3),[6] and alloys (AuAg, AuCu, or FePt),[7,8] have thus been coated with organic compounds[9] that lower their interfacial energy and add steric stabilization.[10] Suitable organic compounds include alkanethiols,[4] fatty acids,[6] other surfactants,[11] and polymers.[12] They require binding groups with sufficient affinity for the nanoparticle surface[13] that usually contain nitrogen,[14] oxygen,[15] phosphorus,[5] or sulfur (as in alkanethiols).[4] Coinage metal nanocrystals are often stabilized with alkanethiols or alkylamines,[4,16] less frequently with carboxylic acids, phosphines, or phosphonates.[17,18] Conversely, metal oxide nanoparticles are often coated with alkylamines or carboxylic acids,[6,16] while all of the above classes of surfactant have been used to passivate semiconductor nanocrystals.

The resulting "ligand shells" have similarities to self-assembled monolayers, but the curvature and the typical facets of inorganic nanoparticles complicate the structure and dynamics of the ligand shell. Ligand molecules may bind to different nanocrystal facets at different densities, an effect that is important for the growth of anisotropic nanostructures in solution,[19,20] while the high curvature of small particles leads to the "hairy ball effect", where the tails of the ligands have access to considerably more free volume than the head groups. Ligand shells are also more dynamic than sometimes envisioned; even simple alkanethiol coatings exhibit phase transitions where the shell changes from a more mobile disordered state to a less mobile ordered state where the ligands are aggregated into crystalline bundles.[21−25]

Recent work indicates that this ability of the ligand shell to change its structure can result in interactions between nanoparticles that deviate substantially from those predicted by theoretical approaches which assume a uniform ligand density around the particles.[26−28] Simulations have shown that the interaction between particles in dispersion can change rapidly from repulsive to attractive as the ligands order,[24,29] while experiments indicate that the structure of nanoparticle agglomerates is affected by short-range interactions between the ligand shells.[30] Recently, using a combination of experiment and computer simulations, we demonstrated that the agglomeration of smaller hexadecanethiol-coated gold nano-

Received: August 24, 2018
Revised: October 8, 2018
Published: October 9, 2018

DOI: 10.1021/acs.langmuir.8b02883
Langmuir 2018, 34, 12982−12989

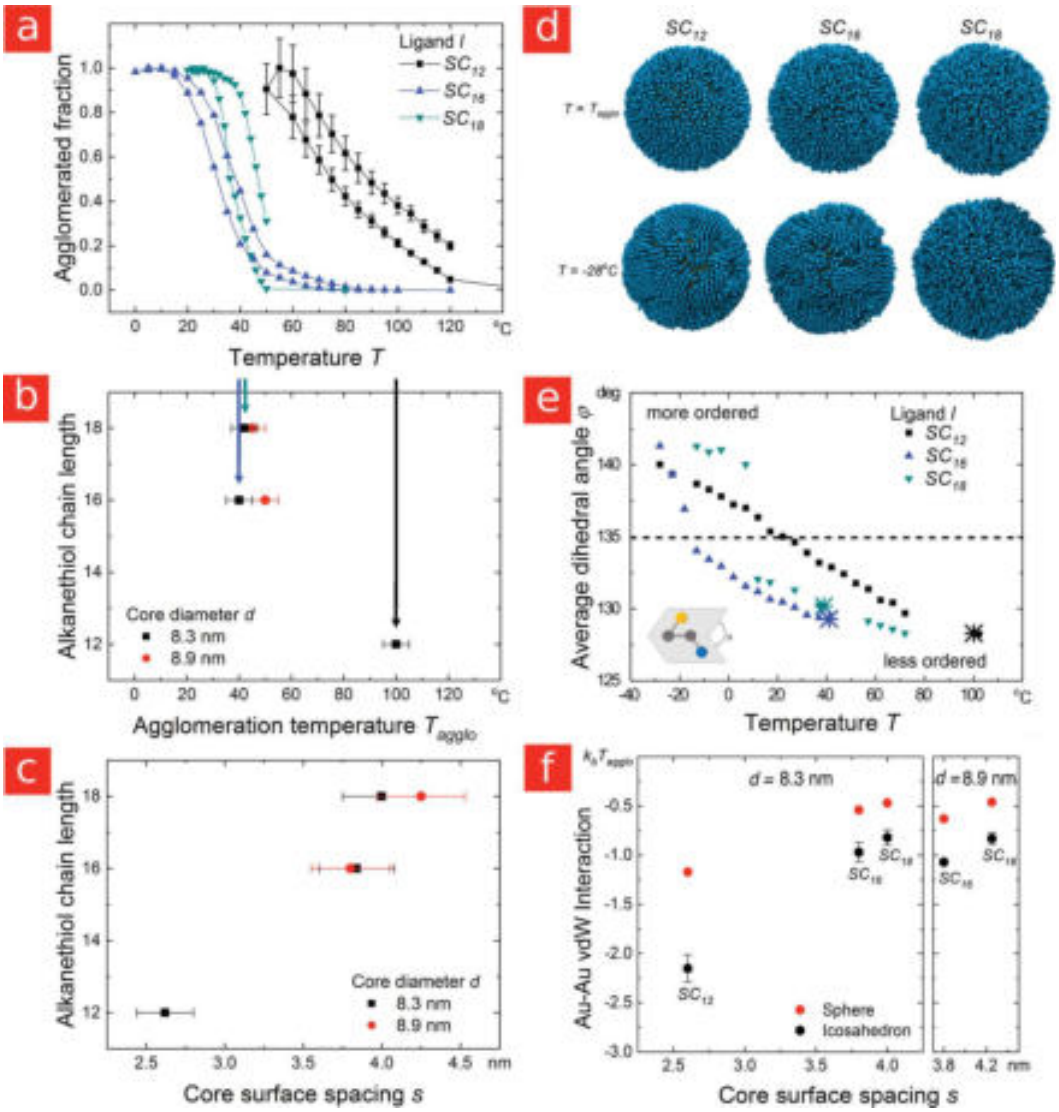

Figure 1. Temperature-dependent agglomeration of AuNP with 8.3 and 8.9 nm diameter cores studied by SAXS (left row) and theoretical models (right row). (a) Fraction of agglomerated 8.3 nm particles covered with alkanethiol ligands of different lengths in decane as determined by in situ SAXS. All particles were dispersed at high temperatures and agglomeration occurred upon cooling, as indicated by the increase in structure factor. (b) Agglomeration temperature (where 20% of the particles were agglomerated) as a function of ligand chain length. (c) Core surface spacing between AuNPs at the agglomeration temperature. The much smaller separation between SC_{12} coated particles indicates substantial compression of the ligand shell. The error bars in (b) and (c) represent one standard error. (d) Molecular dynamics simulation snapshots at T_{agglo} (top row) and −28 °C (bottom row), and (e) the average dihedral angle of the ligands, demonstrate that, regardless of the ligand length, 8.3 nm AuNPs agglomerate before the ligands order (the experimental agglomeration temperatures are indicated by large crossed symbols). The scheme at the bottom left of (e) shows the definition of the dihedral angle φ, and the dashed line is a guide to the eye. In the snapshots, decane solvent is hidden for clarity. (f) Analytically estimated core−core vdW interaction at the experimental particle spacings for 8.3 and 8.9 nm AuNPs. The values are substantially higher for icosahedral cores oriented face-to-face than for spherical cores. Error bars for the icosahedral case represent confidence intervals (see Methods for details).

particles is driven by the ordering of the ligand shell, while for larger particles the van der Waals (vdW) attraction between the cores becomes strong enough to drive agglomeration before the ligands order.[31] This transition from shell- to core-dominated agglomeration was shown to result in a nonlinear change in the interparticle spacing, and should have other important consequences.

Here, we systematically investigate the effect of the ligand length on colloidal stability for a range of particle sizes. Naively, one may expect the stability of inorganic nanoparticles with apolar ligands to increase as the ligand shell becomes thicker and keeps the cores further apart. We show that this is only true for large particles, and that there exists an inversion in the dependence of the agglomeration temperature on the ligand length. In particular, we consider here both Au and CdSe nanocrystals suspended in decane and coated with linear alkanethiols ranging in length from 12 to 18 carbons. These two systems were chosen because they can be synthesized as size tunable spherical colloids with relatively narrow size distributions. In addition, the Hamaker constants differ

DOI: 10.1021/acs.langmuir.8b02883
Langmuir 2018, 34, 12982−12989

considerably, allowing us to explore the role of van der Waals forces on the agglomeration temperature. We find that, for larger Au particles, the agglomeration temperature *decreases* with ligand length, as one would expect if agglomeration were driven by vdW attraction between the cores; for smaller Au and CdSe particles, however, the agglomeration temperature *increases* with ligand length, because the agglomeration is now driven by attraction between the ligand shells as they order, and longer alkane chains order at higher temperatures. Further, we show that ligand length has a strong effect on particle spacing in the core-dominated regime but only a small effect in the shell-dominated regime.

RESULTS AND DISCUSSION

First, consider "large" gold nanoparticles (AuNPs) with core diameters above 8 nm coated with alkanethiol ligands. Dispersions with 8.3 and 8.9 ± 0.8 nm cores and dodecanethiol (SC_{12}), hexadecanethiol (SC_{16}), and octadecanethiol (SC_{18}) shells with a coverage of 5.5 ligands nm^{-2} were analyzed at a concentration of 2.5 mg mL^{-1} by in situ small-angle X-ray scattering (SAXS). When fully extended, these ligands are approximately 1.78, 2.28, and 2.54 nm in length, respectively. The experiments were designed to be fully comparable to the experiments on particles with SC_{16} shells on different cores reported previously;[31] additional details can be found there and in the Methods section. Briefly, thoroughly purified AuNPs in decane were introduced into an X-ray beam and the scattering was recorded using a large two-dimensional detector while changing the temperature in small steps. Below a certain temperature, the particles began to agglomerate, clearly indicated by the appearance of a peak in the structure factor $S(q)$.[32] We define the agglomeration temperature, T_{agglo}, as the temperature at which 20% of the particles are agglomerated.

Cores larger than 8 nm coated in SC_{16} ligands have been shown to attract each other sufficiently strongly that the particles agglomerate while the ligands are still disordered (the "core-dominated regime").[31] Because the vdW attraction between the cores increases as the particles approach, one would therefore expect a decreased thermal stability for shorter ligands. This is precisely what we observe in the current study: Figure 1a,b shows that 8.3 nm cores with SC_{12} ligands agglomerated roughly 60 °C above those with SC_{16} and SC_{18} ligands. Increasing the particle size to 8.9 nm further increased the vdW attraction between the cores and resulted in additional destabilization of particles coated in shorter ligands (see Figure 1b and Figure 1 in the Supporting Information). At this size, SC_{12}-stabilized particles were too attractive to be dispersed, and the SC_{16}-stabilized particles agglomerated at higher temperatures than the SC_{18}-stabilized particles. This is consistent with previous observations that exchanging for longer organic ligands facilitates the transfer of gold nanoparticles from water into organic solvents.[33,34]

Molecular dynamics simulations of 8.3 nm core particles in explicit *n*-decane confirmed that the ligand shells are mobile and disordered at the experimental agglomeration temperatures. Snapshots of the particles at T_{agglo} are shown in Figure 1d, top row, where the solvent molecules have been hidden to reveal the structure of the ligand shell more clearly. A quantitative measure of ligand order is provided by the average dihedral angle of the alkane tails, which indicates the degree to which the ligands are extended in all-trans conformations (180°). Figure 1e and Figure 1d (bottom row) show that the ligands did not extend and start clustering together until well below T_{agglo}, where the experimental agglomeration temperatures have been indicated by large crossed symbols. Overall, simulations and experiments consistently indicate that when the agglomeration is core-dominated, shorter ligands result in particles which are less stable to agglomeration.

The experimental core surface spacings reported in Figure 1c indicate minimal overlap between the SC_{18} and SC_{16} ligand shells, with the spacings close to twice the thickness of the shell around an isolated particle (see Figure 2 in the Supporting Information). This is consistent with the uniform and mobile ligand shells observed in our simulations, which should result in entropic steric repulsion between the particles as their shells start to overlap and the conformational freedom of the ligands becomes restricted.[24,31]

We have calculated the core−core vdW interaction at these separations using both spherical and icosahedral models for the gold core (see Figure 1f). Transmission electron microscopic (TEM) images indicate that the cores have substantial faceting, with some triangular facets (typical of icosahedra) visible (see Figure 3 in the Supporting Information). Our calculations show that the core−core interaction is substantially stronger when such faceted particles are oriented face-to-face than would be estimated from a spherical model. For the SC_{18} and SC_{16} coated cores, the interaction is roughly $-1k_BT_{agglo}$ for regular icosahedra, not far from the $-1.5k_BT$ necessary to drive agglomeration in the limit of low particle concentration. In contrast, the experimental spacings indicate substantial compression of the SC_{12} ligands, with the spacing now substantially less than twice the thickness of the shell around an isolated particle (roughly 2.6 nm versus 3.2 nm). This compression appears to be the result of stronger core−core attraction once the shells are thinner, with analytical calculations indicating a core−core vdW interaction around $-2.2k_BT_{agglo}$ at the experimental spacing. Decreasing the ligand length in the core-dominated regime thus appears to have the same effect as increasing the particle size;[31] i.e., the vdW attraction between the metal cores becomes stronger, which eventually results in substantial compression of the disordered ligand shell.

Next, consider "smaller" gold particles with core diameters of around 6 nm. When coated with SC_{16} ligands, their agglomeration in decane is dominated by the attraction that arises between the shells as the ligands cluster together to form ordered bundles like those shown in Figure 2a (the "shell-dominated regime").[31] Our molecular dynamics simulations show that the temperature at which the ligands order depends strongly on ligand length: longer ligands order at higher temperatures for the same 5.8 nm core diameter, as shown in Figure 2b. This is consistent with previous studies of ligand behavior in the absence of solvent,[21−23,25] and reflects a change in the balance between chain energy and entropy that is also seen in the tendency of longer alkanes to freeze at higher temperatures. Consequently, our simulations predict that smaller particles coated in longer ligands will agglomerate at higher temperatures, the exact opposite of the trend found for larger particles.

Experiments with 6 nm AuNP in heptane are consistent with these predictions.[35] In particular, the experimental agglomeration temperatures, indicated by the crossed symbols in Figure 2b, increased with ligand length in a way that correlates with the increase in the ligand ordering temperature. Moreover, our simulations indicated that the ligands are ordered at the

DOI: 10.1021/acs.langmuir.8b02883
Langmuir 2018, 34, 12982−12989

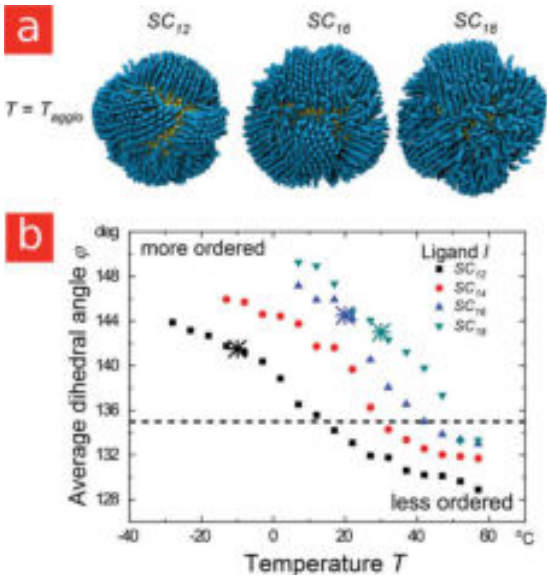

Figure 2. (a) Simulation snapshots of 5.8 nm AuNPs in decane showing that the ligands are ordered at the experimental agglomeration temperature. (b) Degree of ordering at different temperatures as quantified by the average dihedral angle of the ligands. T_{agglo}, indicated by the large crossed symbols, corresponds to the experimental agglomeration temperature for 6 nm AuNPs dispersed in heptane.[35]

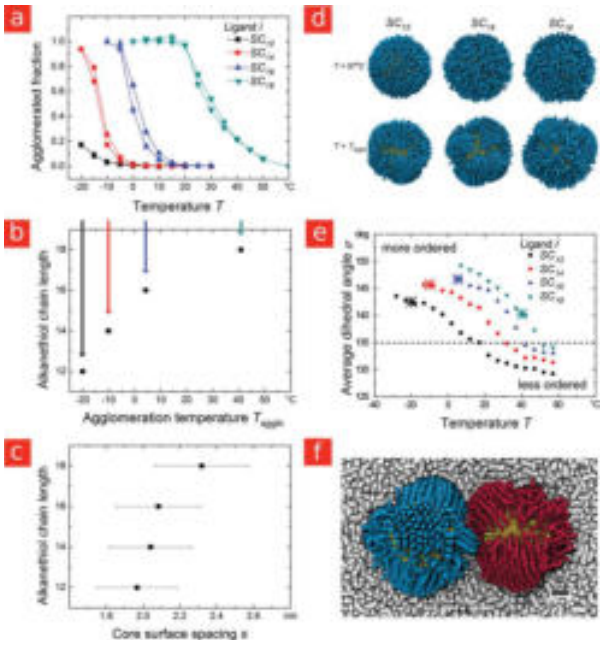

Figure 3. (a) Fraction of 5.8 nm CdSeNPs agglomerated in decane as a function of temperature and ligand length, as determined by in situ small-angle X-ray scattering. (b) Agglomeration temperature as a function of ligand chain length. As for the small AuNP, there is an increase in T_{agglo} with ligand length. (c) Core surface spacing between particles at the agglomeration temperature. The error bars in (b) and (c) represent one standard error. (d) Simulation snapshots at 57 °C (top row) and at T_{agglo} (bottom row). (e) Average dihedral angle of the ligands. Comparison with the experimental agglomeration temperatures, indicated by large crossed symbols, shows that the particles agglomerate after the ligands order. (f) Simulation snapshot at T_{agglo} + 10 °C showing two SC_{16} covered CdSeNPs interacting at 2.1 nm separation. Different colors have been used for the ligands on the two particles, and the solvent was partially hidden.

experimental agglomeration temperatures in all cases (see Figure 2a). Note that the experimental results in this case are for particles in heptane rather than decane, which probably offsets the small difference in core diameter.

Based on our results, we propose the following rule for the ligand-dependent colloidal stability of apolar nanoparticles covered in linear alkyl ligands: Long ligands stabilize larger core-dominated particles and destabilize smaller shell-dominated particles. This rule is not restricted to AuNPs. As we show in Figure 3, the agglomeration of cadmium selenide particles (CdSeNPs) with 5.8 nm diameter cores in decane is shell-dominated, with a temperature-dependent stability that follows the same trends as shell-dominated AuNPs. Experimentally, the agglomeration temperatures increased with ligand length (see Figure 3a,b), consistent with the trend in ligand ordering temperatures predicted by simulation (see Figure 3d,e). Moreover, the simulations indicate that the ligands order prior to particle agglomeration.

The experimental CdSeNP spacing is consistent with the ligands ordering prior to agglomeration, with a mean value close to, and in most cases smaller than, the length of one extended ligand (Figure 3c). At the coverage that we measured experimentally, this close spacing suggests interdigitation of ligand bundles as shown in Figure 3f. Previously, we have shown that such configurations correspond to the minimum in the potential of mean force acting between AuNPs with similar size and ligand coverage.[31] Interdigitation of alkanethiol chains was inferred from high-resolution TEM images of dried agglomerates in 1993;[36] the results here indicate that in the liquid it occurs at the bundle level and that the extent depends on particle size.

Recently, an alternative explanation has been offered for particle spacings close to one ligand length in assemblies of 2–5 nm CdSe particles coated with alkylamine ligands.[37] Simulations in the absence of solvent indicated ligand shell collapse, with the majority of ligands wrapping around the core rather than extending out from it. While this type of ligand collapse may be possible on small particles at low surface coverage in poor solvents, our simulations in decane do not show such behavior. Even at only 70% of our measured coverage, the ligands form distinct ordered bundles that tilt with respect to the particle surface, but do not wrap around it (see Figure 7 in the Supporting Information and Figure 3d,f), resulting in an average ligand shell thickness considerably above half a ligand length (Figure 8 in the Supporting Information).

Thus, while we do not expect drastic changes in the ligand shell geometry for the range of ligand shell densities encountered here, we note that even small differences in the ligand coverage affect agglomeration temperatures. Our experimental results show that the agglomeration of CdSeNPs is sensitive to the ligand concentration in solution (see Figure 6 in the Supporting Information), and our simulations show that the ligands order at lower temperature when the surface coverage is reduced from 5.5 to 3.6 ligands nm^{-2} (compare Figure 3e and Figure 7 in the Supporting Information). These simulations are consistent with earlier results for CdS nanorods,[29] and indicate a potential link between ligand

DOI: 10.1021/acs.langmuir.8b02883
Langmuir 2018, 34, 12982–12989

concentration in solution and particle stability to agglomeration.

The agglomeration of much larger silica particles also appears to be shell-dominated. The temperature-dependent stability of 72 and 246 nm diameter silica particles with similar (stearyl alcohol with 18 carbon atoms) ligands was studied previously by van Blaaderen and Bonn, who used nonlinear optical spectrometry to identify the order−disorder ligand transition.[38] They detected agglomeration ("gelation") via increased optical scattering at a temperature close to the molecular transition. Using a spherical model, we estimate that the attractive vdW interaction between silica cores in a general hydrocarbon medium will not be strong enough to induce room temperature agglomeration until a diameter of around 500 nm if the particles are coated with SC_{18} ligands. This is due to the low Hamaker constant of amorphous silica (0.41 eV), which is not much higher than that of typical organic solvents. Core materials with similarly low Hamaker constants are likely to exhibit the shell-dominated behavior we have described above for different ligand lengths, even at very large diameters. On the other hand, CdSe particles are likely to exhibit a crossover to core-dominated agglomeration at a similar diameter to Au particles (i.e., around 8 nm) due to their significant dipole moments.

Conventional colloid theory, as represented by Khan et al.,[26] predicts the right trends for the agglomeration temperature and interparticle spacing in the core-dominated regime, but fails completely in the shell-dominated regime (see Figure 4).

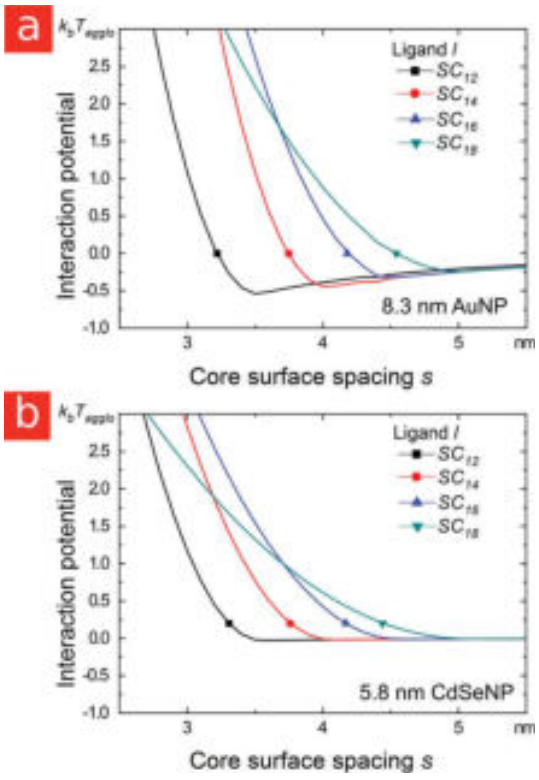

Figure 4. Interaction potentials for (a) 8.3 nm AuNPs and (b) 5.8 nm CdSeNPs calculated using conventional colloid theory, as represented by Khan et al.[26] The predicted potentials are incompatible with our experiments and simulations.

Even for the core-dominated case, the predicted particle separations are larger than those observed experimentally. We conclude that improved models will need to account for temperature-dependent transitions in the ligand shell and provide a more accurate description of the core shape and the compressibility of the ligand shell in different states.

Our results also differ in important ways from simulation studies of particles interacting without a solvent. In the absence of solvent, the interaction between the particles is strongly attractive irrespective of whether the ligands are ordered or disordered,[24,31] and chain length seems to have a negligible effect on the particle spacing for gold cores ranging from 2 to 9 nm in diameter and ligand lengths ranging from 4 to 12 or from 9 to 19 carbons.[39−42] In contrast, we find that in good solvents both the particle interaction and spacing depend strongly on the ligand length, with very different effects depending on particle size.

CONCLUSIONS

The effect of ligand length on the colloidal stability of apolar metallic and semiconducting nanoparticles depends strongly on core size. Our experiments and simulations consistently showed that the relationship inverts when the agglomeration changes from core-dominated to shell-dominated. In the core-dominated regime, i.e., for gold cores with diameters larger than approximately 8 nm, increasing the ligand length increased the stability of the suspension by extending the range of repulsion between the disordered ligand shells, thereby reducing the vdW attraction between the cores. In contrast, the colloidal stability of particles with smaller cores in the shell-dominated regime increased for shorter ligands that order at lower temperatures. Classical theories do not account for the possibility of the ligand shell structure becoming anisotropic, or its sensitivity to changes in temperature and solvent nature, and therefore fail to predict colloidal stability.

Our results also indicate that it is insufficient to simply consider the core/shell ratio when seeking to understand the effect of the ligand length on particle stability to agglomeration. Increasing the core size always decreases colloidal stability, whereas increasing the ligand length can either increase or decrease colloidal stability depending on whether the particle is in the core- or shell-dominated regime.

More generally, our results show that even small changes in the ligand length can significantly affect the free energy balance between the disordered and ordered ligand states. This is especially relevant for particles that fall in the shell-dominated regime. We expect that other changes to the ligand structure, such as the presence of double bonds or branches, will also strongly affect particle stability to agglomeration by modifying the relative free energies of the ordered and disordered ligand states. This may help explain other intriguing results in the recent literature,[43,44] and further studies are currently underway.

METHODS

All chemicals were obtained from Sigma-Aldrich (unless noted otherwise) and used without further purification. Note that all methods were chosen to provide samples that are as comparable as possible to the data published previously.[31]

Nanoparticle Synthesis. Gold nanoparticles (AuNPs) with core diameters of 8.3 and 8.9 nm were synthesized as before using a modified protocol based on the method of Wu and Zheng.[45] To prepare gold cores with a diameter of 8.3 nm, a mixture of 8 mL of

DOI: 10.1021/acs.langmuir.8b02883
Langmuir 2018, 34, 12982−12989

benzene (puriss. ≥99.7%), 8 mL of oleylamine (technical grade, 70%), and 100 mg of $HAuCl_4$ (with crystal water) was stirred at 20 °C and 500 rad min^{-1} for 1 min under argon atmosphere. A solution of 40 mg of *tert*-butylamine borane (ABCR, 97%) in 2 mL of benzene and 2 mL of oleylamine (OAm) was then added. The color of the solution immediately became dark purple. After stirring for 60 min at 20 °C, the nanoparticles were purified once by precipitating with 30 mL of ethanol and centrifugation at 4000 rad min^{-1} for 5 min. The precipitated nanoparticles were then redispersed in 20 mL of heptane (puriss. ≥99%). Gold cores with a diameter of 8.9 nm were produced by a second overgrowth step. A 60 mg sample of $HAuCl_4$, 5 mL of benzene, and 1 mL of oleylamine were added to 10 mL of the 8.3 nm dispersion in heptane and stirred for 5 h at 60 °C. The resulting dispersion was then purified as above.

Cadmium selenide nanoparticles (CdSeNPs) with core diameters of 6 nm were synthesized as follows. First, three stock solutions were prepared: a Se injection solution (i), a Cd growth solution (ii), and a Se growth solution (iii). (i) A 0.3265 g sample of Se was dissolved in a mixture of 2.5 g of trioctylphosphine, 2.5 g of octadecene, and 6 g of oleylamine in a nitrogen-filled glovebox to give a clear, slightly yellow solution. (ii) A solution containing 0.17 mol L^{-1} cadmium was made from 0.22 g of cadmium oxide, 0.97 g of oleic acid, and 6.23 g of 1-octadecene in a three-neck round-bottom flask on a Schlenk line. The solution was degassed under vacuum (<1 mbar) for 60 min at 80 °C, heated to 250 °C and held until clear, and then cooled to room temperature. While cooling 1.13 mL of oleylamine was added. The final solution was clear and slightly yellow. (iii) A solution containing 1.7 mol L^{-1} selenium was prepared by dissolving 0.25 g of selenium in 1.55 g of trioctylphosphine in a nitrogen-filled glovebox to give a clear colorless solution.

The synthesis started with 0.22 g of cadmium oxide, 3 g of oleic acid, and 30 g of octadecene in a three-neck round-bottom flask that was degassed under vacuum (<1 mbar) for 60 min at 80 °C. The mixture was then heated to 260 °C until a clear solution (iv) had formed. The selenium injection solution (i) was loaded into a 24 mL disposable syringe equipped with a 16 G needle and rapidly injected into the cadmium solution (iv) at 260 °C. The temperature of the reaction solution was allowed to recover to 250 °C where it was held for NP growth. After 20 min, 2 mL of 0.17 mol L^{-1} cadmium growth stock (ii) and 0.2 mL of 1.7 mol L^{-1} selenium growth stock (iii) were added dropwise to the reaction. The addition of cadmium and selenium growth solutions (ii, iii) was continued every 10 min. After three additions, the reaction was left for a further 10 min at 250 °C, and then cooled to room temperature. The NPs were washed three times via precipitation with acetone and resuspended in toluene.

Nanoparticle Characterization. Small-angle X-ray scattering (Xenocs Xeuss 2.0) and transmission electron microscopy (JEOL JEM 2010) were used to measure the core size of the NPs (Table 1) as previously described.[31] Scattering data from SAXS was analyzed using SASfit (version 0.94.6, Paul Scherrer Institute) and TEM micrographs were analyzed using ImageJ distributed by NIH (version 1.45s).

Table 1. AuNPs Used for This Study, with Diameters Obtained from Transmission Electron Microscopy and Small-Angle X-ray Scattering

number	*d* (TEM)	*d* (SAXS)
Au01	8.5 nm ± 7.1%	8.3 nm ± 6.7%
Au02	8.9 nm ± 8.5%	8.9 nm ± 6.8%
CdSe	5.8 nm ± 7.1%	6.0 nm ± 9.6%

Ligand Exchange. *AuNPs.* Ligand exchange on AuNPs was performed as described previously.[46] AuNPs coated with oleylamine were heated to 80 °C, and an excess of required alkanethiol was added. After stirring for further 10 min, the particles were purified and redispersed in decane (≥95%).

CdSeNPs. As-synthesized CdSeNPs were precipitated with acetone/ethanol and resuspended in a solution of the respective alkanethiol ligand (40 wt % in chloroform) with triethylamine (1 mol equivalent with respect to thiol). The resulting NP dispersion was heated for 3 h at 45 °C while stirring. The NPs were then washed via precipitation with antisolvent and centrifugation (3300*g* for 3 min). The antisolvent was chosen to optimally dissolve excess ligand: 1:1 (v/v) methanol/ethanol mixture for hexanethiol and octanethiol ligands, or 1:1 (v/v) acetone/ethanol mixture for dodecanethiol and longer ligands. The NPs were resuspended again in a solution of ligand (40 wt % in chloroform), stirred at 45 °C for 2 h, and then washed as before and resuspended in a 0.1 M solution of ligand in chloroform. After stirring at room temperature for 24−48 h, the NPs were washed three times and resuspended in pure chloroform. Chambrier et al. have shown this procedure leads to almost complete displacement (>92%) of amines by the alkanethiol ligands.[47]

Thermogravimetric Analysis (TGA). Thermogravimetric analyses were performed using a Netzsch STA 449 F3 Jupiter. The measurements started at room temperature and ran until 800 °C. The heating rate was kept at 10 K min^{-1}. All measurements were done under an inert atmosphere. Figure 4 in the Supporting Information shows representative TGA data of 1-hexadecanethiol coated AuNPs with a core diameter of 8.9 nm.

Small-Angle X-ray Scattering. Experiments were performed using a Xeuss 2.0 from Xenocs SA (Grenoble, France) equipped with a copper Kα X-ray source and a PILATUS 1 M detector from DECTRIS (Baden, Switzerland).

To prevent solvent evaporation during the measurements, the samples (usually a quantity of 20−40 μL) were filled into glass capillaries (diameter of 2 mm), which were then sealed with epoxy.

For each measurement, the samples were introduced into a temperature controlled sample holder (Omega CN8200), Peltier controlled with a temperature range between −20 and 120 °C. The measurements started at high temperature to ensure a fully deagglomerated state. Afterward the temperature was first decreased and later increased in 5 °C steps. At each step, the samples were first equilibrated (20 min) followed by an acquisition (10 min). Experiments with time-dependent observation of the agglomeration process as shown in Figure 5 in the Supporting Information were used to ensure that most particles that had lost colloidal stability at this temperature had agglomerated before the next temperature step was taken. Data treatment was carried out as described previously.[31,48]

Molecular Dynamics Simulations. The nanoparticles were modeled as spherical cores covered in alkanethiol ligands of various lengths ($-S(C_nH_{2n+1})$, n = 12, 14, 16, 18) and immersed in explicit *n*-decane solvent. Both 5.8 and 8.3 nm Au cores and 5.8 nm CdSe were considered, with the ligands assumed to be irreversibly bound to the Au and CdSe cores. According to TGA measurements, the surface coverages for Au and CdSe cores are very similar: 5.5 and 5.2 ligands nm^{-2}, respectively. We therefore used a coverage of 5.5 ligands nm^{-2} in all cases. To assess the effect of changing the ligand coverage on the structure and transition of the ligand shell, simulations were also performed for 5.8 nm CdSeNPs with SC_{18} ligands at a coverage of 3.6 nm^{-2}. The positions of the sulfur atoms were determined by placing them on a spherical shell around the implicit core (0.15 nm further out). They were then allowed to find their optimal positions on this shell, subject to a repulsive interaction (standard Coulombic potential with a relative dielectric constant ϵ = 10, truncated at 24 Å), which ensured that the binding sites were approximately equidistant from one another. The sulfur atoms were subsequently treated as part of the rigid core of the particle, using the RATTLE algorithm[49] to constrain their positions. This simplification ignores the possibility of ligand detachment, but should be reasonable given the high surface coverages considered in this work. The rest of the ligand and solvent molecules were modeled using a united-atom representation, with each CH_x group being represented by a single particle. These particles interacted with one another according to the 12−6 Lennard-Jones (LJ) potential, with parameters as used and described previously.[24] Bond stretching, bond bending, and dihedral torsion terms were also considered within each molecule.[50] The interaction between the CH_x groups and the cores was efficiently modeled using a 9−3 LJ potential, using the parameters in Table 2.

DOI: 10.1021/acs.langmuir.8b02883
Langmuir 2018, 34, 12982−12989

Table 2. Lennard-Jones Parameters Used To Describe Nonbonded Interactions between Au/CdSe Cores and CH_x Particles in Our Simulations, According to the Truncated Pairwise Potential[a]

core material	ϵ/k_B (K)	σ (Å)	ref
Au	88	3.54	51
CdSe	56	3.54	24

[a]The truncated pairwise potential is given by

$$V(r_{ij}) = \epsilon\left[\frac{2}{15}\left(\frac{\sigma_{ij}}{r_{ij}}\right)^9 - \left(\frac{\sigma_{ij}}{r_{ij}}\right)^3\right]$$

for $r_{ij} < r_c$. In this equation, r_{ij} is the distance between particle i and the surface of core j, and r_c = 30 Å is the cutoff distance.

Systems containing approximately 150 000 (5.8 nm cores) to 350 000 (8.3 nm cores) united atoms were investigated using molecular dynamics (MD) simulations with periodic boundary conditions. All simulations were performed using the LAMMPS simulation package.[52] Individual NPs in explicit decane were initially equilibrated at constant volume at a temperature sufficiently high to ensure that the ligands were in the disordered state (e.g., 400 K). During this run, the periodic simulation cell was slowly compressed until the solvent density far from the NP core was equal to the experimental density of pure decane at the corresponding temperature. Subsequent constant temperature runs were performed at a pressure of 80 atm, using a Nosé–Hoover thermostat and barostat, which yielded bulk solvent densities within 1% of experimental values. The particles were first equilibrated for 9–14 ns at temperatures ranging from 245 to 330 K, before 1 ns production runs were performed. Molecular graphics were produced using Visual Molecular Dynamics (VMD).[53]

Calculation of Core–Core Interaction. The vdW interaction between pairs of 8.3 and 8.9 nm gold cores in a hydrocarbon medium was estimated at the experimental particle separations using Hamaker–Lifshitz theory. Both spherical and icosahedral shapes were considered for the cores. For the spherical case, the interaction was calculated analytically using eq 1:

$$U_{vdW} = -\frac{A}{12}\left(\frac{1}{\tilde{s}^2 - 1} + \frac{1}{\tilde{s}^2} + 2\ln\left(1 - \frac{1}{\tilde{s}^2}\right)\right) \quad (1)$$

where A is the reduced Hamaker coefficient (we used a value of 2 eV) and $\tilde{s}$ is the rescaled spacing between the interacting particles (center-to-center distance divided by their core diameter). For the icosahedral case, the interaction was calculated using a coarse-grained atomistic representation, with 4087 interaction sites per particle and all interaction pairs included in the summation. Only the face-to-face relative orientation was considered, which should give the strongest interaction. Confidence intervals were estimated by placing the spherical interaction sites either completely inside or centered on the surface of the icosahedra and extrapolating to a fully atomistic representation.

■ ASSOCIATED CONTENT

Supporting Information

The Supporting Information is available free of charge on the ACS Publications website at DOI: 10.1021/acs.langmuir.8b02883.

Fraction of agglomerated 8.9 nm AuNP, radial density distributions of ligand and solvent around 8.3 nm AuNP (from simulation), TEM data of oleylamine capped AuNP and CdSeNP, TGA data of 8.9 nm AuNP, time-dependent agglomeration data of 8.3 nm AuNP, position of first peak of structure factor for CdSeNP systems as a function of ligand concentration, simulation snapshots, average dihedral angles, and radial density distributions of ligand and solvent for CdSeNPs with low ligand coverage (from simulation) (PDF)

■ AUTHOR INFORMATION

Corresponding Author

*E-mail: tobias.kraus@leibniz-inm.de.

ORCID

Debora Monego: 0000-0003-1246-3718
Thomas Kister: 0000-0002-9827-1380
Paul Mulvaney: 0000-0002-8007-3247
Asaph Widmer-Cooper: 0000-0001-5459-6960
Tobias Kraus: 0000-0003-2951-1704

Author Contributions

⊥D.M. and T.K.: These authors contributed equally.

Notes

The authors declare no competing financial interest.

■ ACKNOWLEDGMENTS

P.M., N.K., D.M., and A.W. were supported by the ARC Centre of Excellence in Exciton Science (CE170100026). A.W. thanks the Australian Research Council for a Future Fellowship (FT140101061), and D.M. thanks the University of Sydney Nano Institute for a Postgraduate Top-Up Scholarship. Computational resources were generously provided by the University of Sydney HPC service, the National Computational Infrastructure National Facility (NCI-NF) Flagship program, and the Pawsey Supercomputer Centre Energy and Resources Merit Allocation Scheme. T.K. and T.K. thank the DFG Deutsche Forschungsgemeinschaft for funding and E. Arzt for his continuing support of this project. P.M. and T.K. also thank the DAAD for travel support.

■ REFERENCES

(1) Silvera Batista, C. A.; Larson, R. G.; Kotov, N. A. Nonadditivity of Nanoparticle Interactions. *Science* **2015**, *350*, 1242477.

(2) Boles, M. A.; Engel, M.; Talapin, D. V. Self-Assembly of Colloidal Nanocrystals: From Intricate Structures to Functional Materials. *Chem. Rev.* **2016**, *116*, 11220–11289.

(3) Si, K. J.; Chen, Y.; Shi, Q.; Cheng, W. Nanoparticle Superlattices: The Roles of Soft Ligands. *Advanced Science* **2018**, *5*, 1700179.

(4) Zheng, N.; Fan, J.; Stucky, G. D. One-Step One-Phase Synthesis of Monodisperse Noble-Metallic Nanoparticles and Their Colloidal Crystals. *J. Am. Chem. Soc.* **2006**, *128*, 6550–6551.

(5) Murray, C.; Norris, D. J.; Bawendi, M. G. Synthesis and Characterization of Nearly Monodisperse CdE (E = Sulfur, Selenium, Tellurium) Semiconductor Nanocrystallites. *J. Am. Chem. Soc.* **1993**, *115*, 8706–8715.

(6) Park, J.; An, K.; Hwang, Y.; Park, J.-G.; Noh, H.-J.; Kim, J.-Y.; Park, J.-H.; Hwang, N.-M.; Hyeon, T. Ultra-Large-Scale Syntheses of Monodisperse Nanocrystals. *Nat. Mater.* **2004**, *3*, 891.

(7) He, R.; Wang, Y.-C.; Wang, X.; Wang, Z.; Liu, G.; Zhou, W.; Wen, L.; Li, Q.; Wang, X.; Chen, X.; et al. Facile Synthesis of Pentacle Gold–Copper Alloy Nanocrystals and Their Plasmonic and Catalytic Properties. *Nat. Commun.* **2014**, *5*, 4327.

(8) Sun, S.; Murray, C. B.; Weller, D.; Folks, L.; Moser, A. Monodisperse FePt Nanoparticles and Ferromagnetic FePt Nanocrystal Superlattices. *Science* **2000**, *287*, 1989–1992.

(9) Brust, M.; Walker, M.; Bethell, D.; Schiffrin, D. J.; Whyman, R. Synthesis of Thiol-Derivatised Gold Nanoparticles in a Two-Phase Liquid-Liquid System. *J. Chem. Soc., Chem. Commun.* **1994**, *0*, 801–802.

DOI: 10.1021/acs.langmuir.8b02883
Langmuir 2018, 34, 12982–12989

(10) Napper, D. H. Steric Stabilization. *J. Colloid Interface Sci.* **1977**, *58*, 390−407.
(11) Kvitek, L.; Panáček, A.; Soukupova, J.; Kolář, M.; Večeřová, R.; Prucek, R.; Holecova, M.; Zbořil, R. Effect of Surfactants and Polymers on Stability and Antibacterial Activity of Silver Nanoparticles (NPs). *J. Phys. Chem. C* **2008**, *112*, 5825−5834.
(12) Corbierre, M. K.; Cameron, N. S.; Sutton, M.; Mochrie, S. G.; Lurio, L. B.; Rühm, A.; Lennox, R. B. Polymer-Stabilized Gold Nanoparticles and their Incorporation Into Polymer Matrices. *J. Am. Chem. Soc.* **2001**, *123*, 10411−10412.
(13) Grubbs, R. B. Roles of Polymer Ligands in Nanoparticle Stabilization. *Polym. Rev.* **2007**, *47*, 197−215.
(14) Sánchez-Iglesias, A.; Grzelczak, M.; Pérez-Juste, J.; Liz-Marzán, L. M. Binary Self-Assembly of Gold Nanowires with Nanospheres and Nanorods. *Angew. Chem.* **2010**, *122*, 10181−10185.
(15) De Nijs, B.; Dussi, S.; Smallenburg, F.; Meeldijk, J. D.; Groenendijk, D. J.; Filion, L.; Imhof, A.; Van Blaaderen, A.; Dijkstra, M. Entropy-Driven Formation of Large Icosahedral Colloidal Clusters by Spherical Confinement. *Nat. Mater.* **2015**, *14*, 56.
(16) Mourdikoudis, S.; Liz-Marzán, L. M. Oleylamine in Nanoparticle Synthesis. *Chem. Mater.* **2013**, *25*, 1465−1476.
(17) Le, A.-T.; Tam, L. T.; Tam, P. D.; Huy, P.; Huy, T. Q.; Van Hieu, N.; Kudrinskiy, A. A.; Krutyakov, Y. A. Synthesis of Oleic Acid-Stabilized Silver Nanoparticles and Analysis of Their Antibacterial Activity. *Mater. Sci. Eng., C* **2010**, *30*, 910−916.
(18) Weare, W. W.; Reed, S. M.; Warner, M. G.; Hutchison, J. E. Improved Synthesis of Small ($d_{CORE} \approx 1.5$ nm) Phosphine-Stabilized Gold Nanoparticles. *J. Am. Chem. Soc.* **2000**, *122*, 12890−12891.
(19) Lee, S.-M.; Jun, Y.-w.; Cho, S.-N.; Cheon, J. Single-Crystalline Star-Shaped Nanocrystals and Their Evolution: Programming the Geometry of Nano-Building Blocks. *J. Am. Chem. Soc.* **2002**, *124*, 11244−11245.
(20) Lee, S.-M.; Cho, S.-N.; Cheon, J. Anisotropic Shape Control of Colloidal Inorganic Nanocrystals. *Adv. Mater.* **2003**, *15*, 441−444.
(21) Luedtke, W. D.; Landman, U. Structure and Thermodynamics of Self-Assembled Monolayers on Gold Nanocrystallites. *J. Phys. Chem. B* **1998**, *102*, 6566−6572.
(22) Ghorai, P. K.; Glotzer, S. C. Molecular Dynamics Simulation Study of Self-Assembled Monolayers of Alkanethiol Surfactants on Spherical Gold Nanoparticles. *J. Phys. Chem. C* **2007**, *111*, 15857−15862.
(23) Lane, J. M. D.; Grest, G. S. Spontaneous Asymmetry of Coated Spherical Nanoparticles in Solution and at Liquid-Vapor Interfaces. *Phys. Rev. Lett.* **2010**, *104*, 235501.
(24) Widmer-Cooper, A.; Geissler, P. Orientational Ordering of Passivating Ligands on CdS Nanorods in Solution Generates Strong Rod-Rod Interactions. *Nano Lett.* **2014**, *14*, 57−65.
(25) Bolintineanu, D. S.; Lane, J. M. D.; Grest, G. S. Effects of Functional Groups and Ionization on the Structure of Alkanethiol-Coated Gold Nanoparticles. *Langmuir* **2014**, *30*, 11075−11085.
(26) Khan, S. J.; Pierce, F.; Sorensen, C.; Chakrabarti, A. Self-Assembly of Ligated Gold Nanoparticles: Phenomenological Modeling and Computer Simulations. *Langmuir* **2009**, *25*, 13861−13868.
(27) Goubet, N.; Richardi, J.; Albouy, P.-A.; Pileni, M.-P. Which Forces Control Supracrystal Nucleation in Organic Media? *Adv. Funct. Mater.* **2011**, *21*, 2693−2704.
(28) Sigman, M. B.; Saunders, A. E.; Korgel, B. A. Metal Nanocrystal Superlattice Nucleation and Growth. *Langmuir* **2004**, *20*, 978−983.
(29) Widmer-Cooper, A.; Geissler, P. L. Ligand-Mediated Interactions between Nanoscale Surfaces Depend Sensitively and Nonlinearly on Temperature, Facet Dimensions, and Ligand Coverage. *ACS Nano* **2016**, *10*, 1877−1887.
(30) Gerstner, D.; Kraus, T. Rapid nanoparticle Self-Assembly at Elevated Temperatures. *Nanoscale* **2018**, *10*, 8009−8013.
(31) Kister, T.; Monego, D.; Mulvaney, P.; Widmer-Cooper, A.; Kraus, T. Colloidal Stability of Apolar Nanoparticles: The Role of Particle Size and Ligand Shell Structure. *ACS Nano* **2018**, *12*, 5969−5977.
(32) Johnson, J. E. X-ray Diffraction Studies of the Crystallinity in Polyethylene Terephthalate. *J. Appl. Polym. Sci.* **1959**, *2*, 205−209.
(33) Lista, M.; Liu, D. Z.; Mulvaney, P. Phase Transfer of Noble Metal Nanoparticles to Organic Solvents. *Langmuir* **2014**, *30*, 1932−1938.
(34) Karg, M.; Schelero, N.; Oppel, C.; Gradzielski, M.; Hellweg, T.; von Klitzing, R. Versatile Phase Transfer of Gold Nanoparticles from Aqueous Media to Different Organic Media. *Chem. - Eur. J.* **2011**, *17*, 4648−4654.
(35) Born, P.; Kraus, T. Ligand-Dominated Temperature Dependence of Agglomeration Kinetics and Morphology in Alkyl-Thiol-Coated Gold Nanoparticles. *Phys. Rev. E* **2013**, *87*, 062313.
(36) Giersig, M.; Mulvaney, P. Preparation of Ordered Colloid Monolayers by Electrophoretic Deposition. *Langmuir* **1993**, *9*, 3408−3413.
(37) Geva, N.; Shepherd, J. J.; Nienhaus, L.; Bawendi, M. G.; Van Voorhis, T. Morphology of passivating organic ligands around a nanocrystal. 2017, arXiv:1706.00844 [physics.chem-ph]. arXiv.org e-Print archive. https://arxiv.org/abs/1706.00844.
(38) Roke, S.; Berg, O.; Buitenhuis, J.; van Blaaderen, A.; Bonn, M. Surface molecular view of colloidal gelation. *Proc. Natl. Acad. Sci. U. S. A.* **2006**, *103*, 13310−13314.
(39) Schapotschnikow, P.; Pool, R.; Vlugt, T. Molecular Simulations of Interacting Nanocrystals. *Nano Lett.* **2008**, *8*, 2930−2934.
(40) Jabes, B. S.; Yadav, H. O. S.; Kumar, S. K.; Chakravarty, C. Fluctuation-Driven Anisotropy in Effective Pair Interactions Between Nanoparticles: Thiolated Gold Nanoparticles in Ethane. *J. Chem. Phys.* **2014**, *141*, 154904.
(41) Waltmann, C.; Horst, N.; Travesset, A. Capping Ligand Vortices as "Atomic Orbitals" in Nanocrystal Self-Assembly. *ACS Nano* **2017**, *11*, 11273−11282.
(42) Waltmann, C.; Horst, N.; Travesset, A. Potential of Mean Force for Two Nanocrystals: Core Geometry and Size, Hydrocarbon Unsaturation, and Universality With Respect to the Force Field. *J. Chem. Phys.* **2018**, *149*, 034109.
(43) Yang, Y.; Qin, H.; Jiang, M.; Lin, L.; Fu, T.; Dai, X.; Zhang, Z.; Niu, Y.; Cao, H.; Jin, Y.; et al. Entropic Ligands for Nanocrystals: From Unexpected Solution Properties to Outstanding Processability. *Nano Lett.* **2016**, *16*, 2133−8.
(44) Yang, Y.; Qin, H.; Peng, X. Intramolecular Entropy and Size-Dependent Solution Properties of Nanocrystal-Ligands Complexes. *Nano Lett.* **2016**, *16*, 2127−32.
(45) Wu, B.-H.; Yang, H.-Y.; Huang, H.-Q.; Chen, G.-X.; Zheng, N.-F. Solvent Effect on the Synthesis of Monodisperse Amine-Capped Au Nanoparticles. *Chin. Chem. Lett.* **2013**, *24*, 457−462.
(46) Kister, T.; Mravlak, M.; Schilling, T.; Kraus, T. Pressure-Controlled Formation of Crystalline, Janus, and Core−Shell Supraparticles. *Nanoscale* **2016**, *8*, 13377−13384.
(47) Chambrier, I.; Banerjee, C.; Remiro-Buenamañana, S.; Chao, Y.; Cammidge, A. N.; Bochmann, M. Synthesis of Porphyrin−CdSe Quantum Dot Assemblies: Controlling Ligand Binding by Substituent Effects. *Inorg. Chem.* **2015**, *54*, 7368−7380.
(48) Schnablegger, H.; Singh, Y. *The SAXS Guide: Getting Acquainted with the Principles*; Anton Paar GmbH: 2013; Vol. 2.
(49) Andersen, H. C. Rattle: A "Velocity" Version of the Shake Algorithm for Molecular Dynamics Calculations. *J. Comput. Phys.* **1983**, *52*, 24−34.
(50) Martin, M. G.; Siepmann, J. I. Transferable Potentials for Phase Equilibria. 1. United-Atom Description of n-Alkanes. *J. Phys. Chem. B* **1998**, *102*, 2569−2577.
(51) Pool, R.; Schapotschnikow, P.; Vlugt, T. J. H. Solvent Effects in the Adsorption of Alkyl Thiols on Gold Structures: A Molecular Simulation Study. *J. Phys. Chem. C* **2007**, *111*, 10201−10212.
(52) Plimpton, S. Fast Parallel Algorithms for Short-Range Molecular Dynamics. *J. Comput. Phys.* **1995**, *117*, 1−19.
(53) Humphrey, W.; Dalke, A.; Schulten, K. VMD: Visual Molecular Dynamics. *J. Mol. Graphics* **1996**, *14*, 33−38.

DOI: 10.1021/acs.langmuir.8b02883
Langmuir 2018, 34, 12982−12989

Supporting Information

On the colloidal stability of apolar nanoparticles: The role of ligand length

Debora Monego,[a†] Thomas Kister[a],[‡] Nicholas Kirkwood,[¶] Paul Mulvaney,[¶] Asaph Widmer-Cooper,[†] and Tobias Kraus[*,§]

†*ARC Centre of Excellence in Exciton Science, School of Chemistry and The University of Sydney Nano Institute, University of Sydney, Sydney, New South Wales 2006, Australia*

‡*INM — Leibniz Institute for New Materials, Campus D2 2, 66123 Saarbrücken, Germany*

¶*ARC Centre of Excellence in Exciton Science, School of Chemistry, University of Melbourne, Parkville, Victoria 3010, Australia*

§*INM — Leibniz Institute for New Materials, Campus D2 2, 66123 Saarbrücken, Germany*

Colloid and interface chemistry, Saarland University, Campus D2 2, 66123 Saarbrücken, Germany

E-mail: tobias.kraus@leibniz-inm.de

[a]These authors contributed equally.

Figure 1 shows how the agglomeration of 8.9 nm core diameter gold particles covered with SC_{16} and SC_{18} ligands depends on temperature. Particles stabilized with SC_{12} ligands showed strong agglomeration, with a core surface spacing of 2.72 ± 0.7 nm, but could not be dispersed even with temperatures of 120 °C.

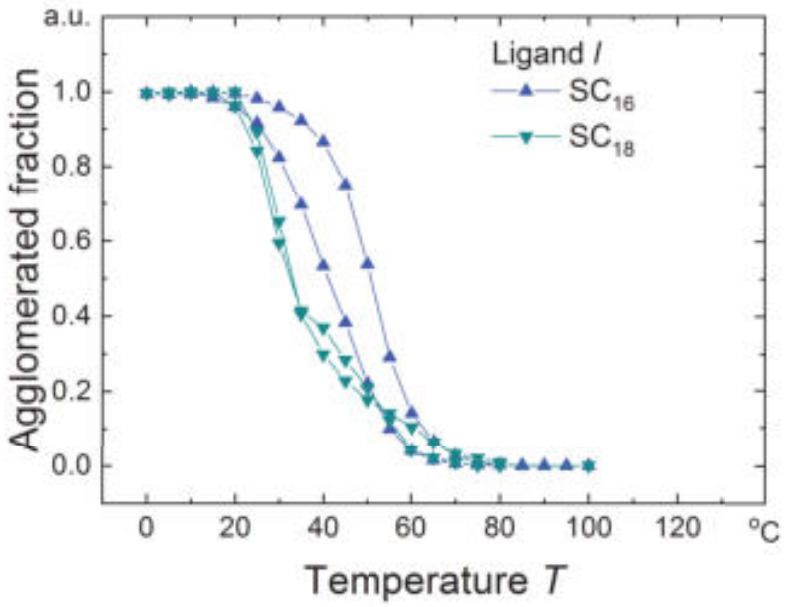

Figure 1: Fraction of agglomerated 8.9 nm particles covered with alkanethiol ligands of different lengths in decane as determined by *in situ* Small-Angle X-ray Scattering.

Figure 2 shows how the density of the solvent and different length ligands changes as we move away from the 8.3 nm gold core. The ligand-solvent interface is more sharply defined for shorter ligands, and the ordering of the ligands that occurs at low temperature allows more solvent to enter the ligand shell.

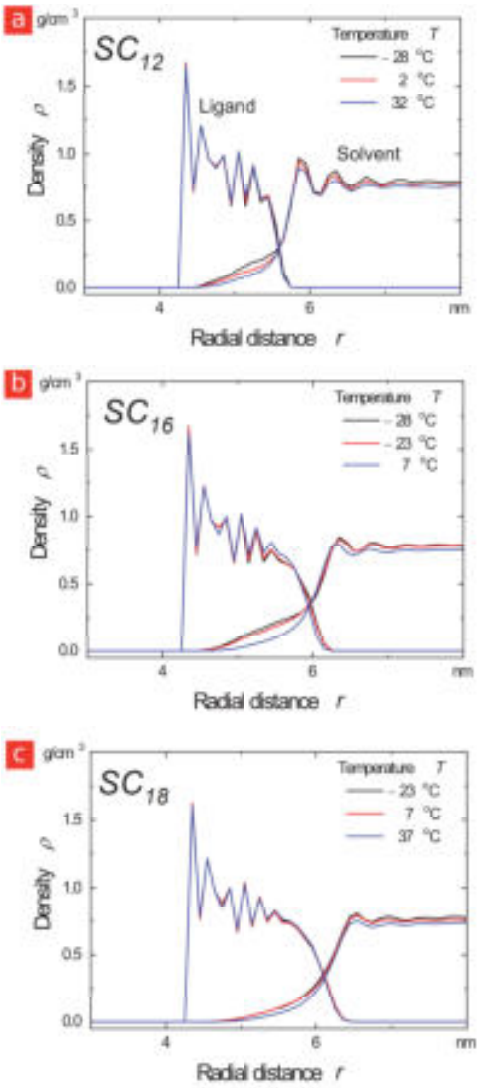

Figure 2: Radial density distributions for the decane solvent and for alkanethiol ligands of different lengths on 8.3 nm gold cores of AuNP, plotted as a function of the distance r from the center of the nanoparticle core. The red lines indicate the density profile at the ligand ordering temperature T_{order} for each particle.

Figure 3 shows TEM data of the as-synthesized, oleylamine-capped Au and CdSe nanoparticles. The particles are roughly spherical in shape, but show faceting, even at low resolutions, especially for AuNP.

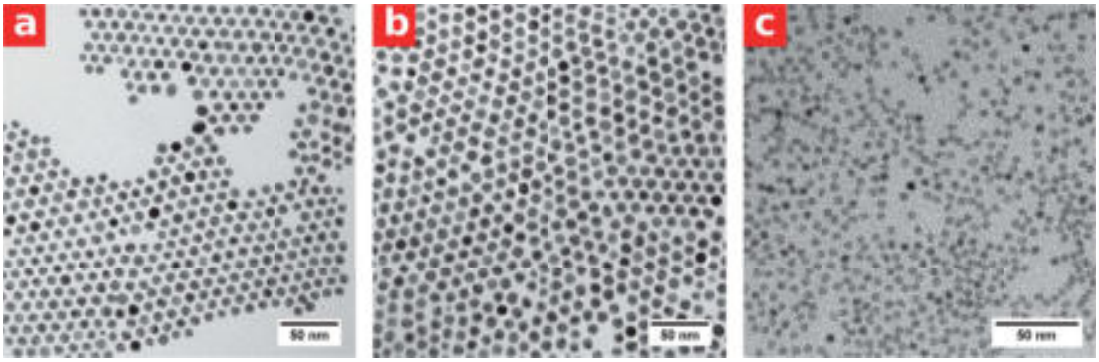

Figure 3: Transmission electron microscopy micrographs of AuNP with a diameter of (a) 8.3 nm, (b) 8.9 nm and (c) CdSeNP with a diameter of 6.0 nm.

Figure 4 shows a thermogravimetric analysis of 1-hexandecanethiol coated AuNP with a core diameter of 8.9 nm. A mass loss of around 7.3 % is due to the ligand that is fully removed at around 400 °C.

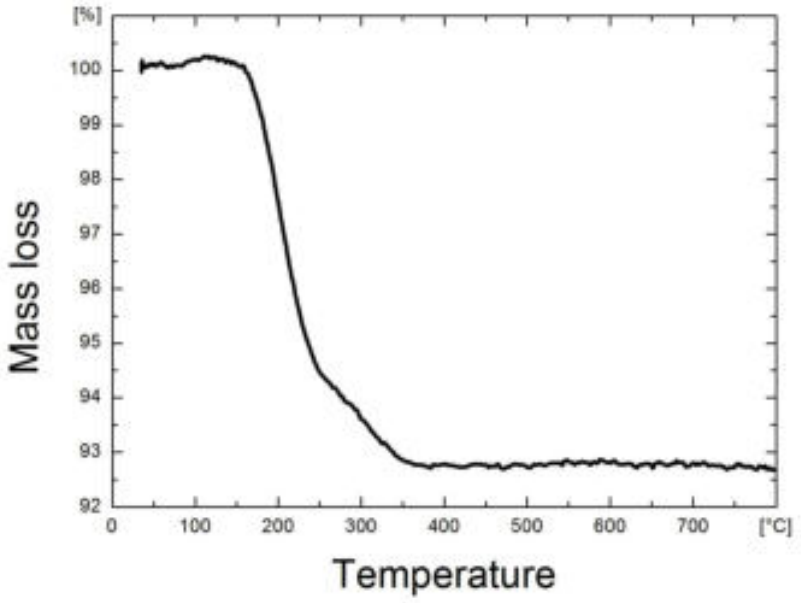

Figure 4: Thermogravimetric analysis of 1-hexandecanethiol coated AuNP with a diameter of 8.9 nm. Ligand degradation started a around 150 °C and finished at 400 °C.

Figure 5 shows the time-dependent agglomeration of 1-hexadecanethiol coated AuNP with a core diameter of 8.3 nm. Such experiments were performed to ensure that the largest

fraction of particles that lost colloidal stability at a given temperature had agglomerated. To this end, the fraction of agglomerated NPs was measured every 30 min, beginning at 80 °C with a total waiting time of 20 h for each temperature.

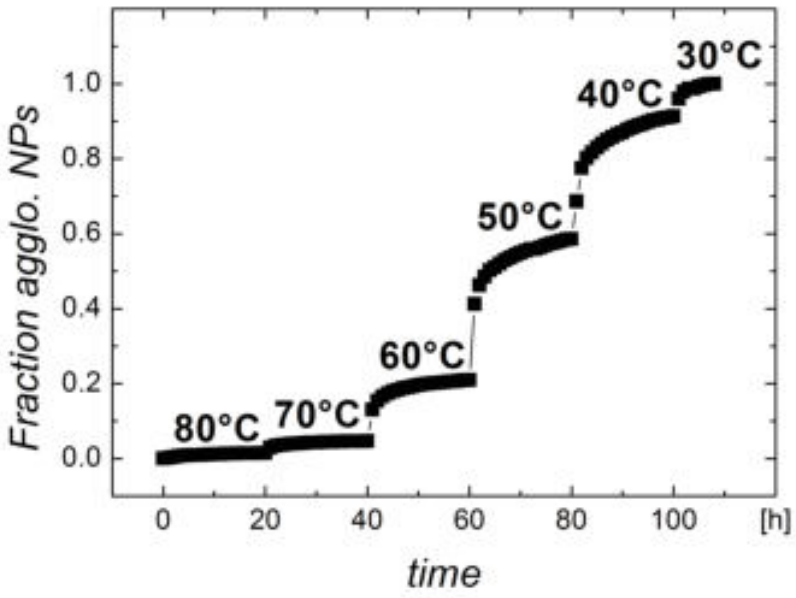

Figure 5:
Transient agglomeratino data on 1-hexadecanethiol coated AuNP with a core diameter of 8.3 nm. The fraction of agglomerated NPs was measured every 30 min. The sample was kept for 20 h at each temperature.

Figure 6 shows how CdSeNP suspensions are affected by the addition of excess ligand. In decane, a fully dispersed state was only achieved at a ligand concentration of 500 mM, indicating the adsorption/desorption equilibrium of alkanethiol ligands on these particles. This suggests that the surface coverage might vary noticeably for CdSeNP, as opposed to what was observed for AuNP.[1] As discussed in the main manuscript, we therefore performed additional simulations at a lower coverage of 3.6 nm^{-2} to obtain results reported in Figures 7 and 8.

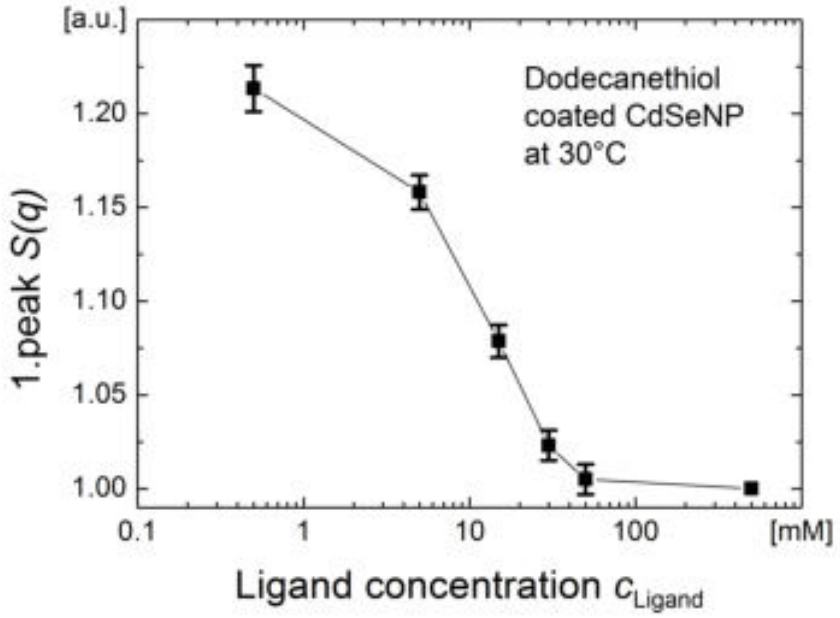

Figure 6: Change in the position of the first peak of the structure factor S(q) with dodecanethiol ligand concentration c_{Ligand} for CdSeNP suspensions in decane at 30 °C.

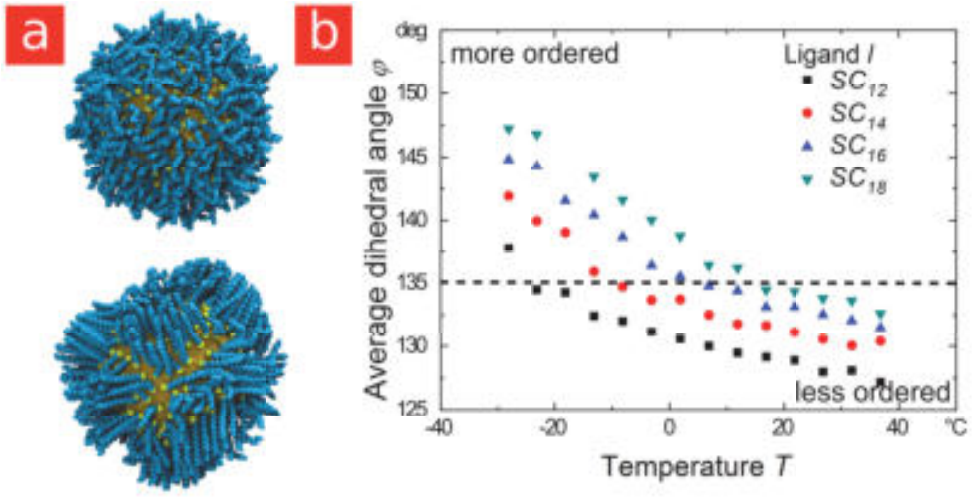

Figure 7: (a) Snapshots of the simulations of 5.8 nm CdSe particles coated with SC_{16} ligands at a surface coverage of 3.6 nm^{-2} at 57 °C (top) and −28 °C (bottom). Even at low coverage, the ligands extend in bundles on the surface of the particle towards the decane solvent. (b) Average dihedral angle for the ligands. The transition from less to more ordered is broader and shifted down by approximately 40 °C compared to when the surface coverage is 5.5 nm^{-2}.

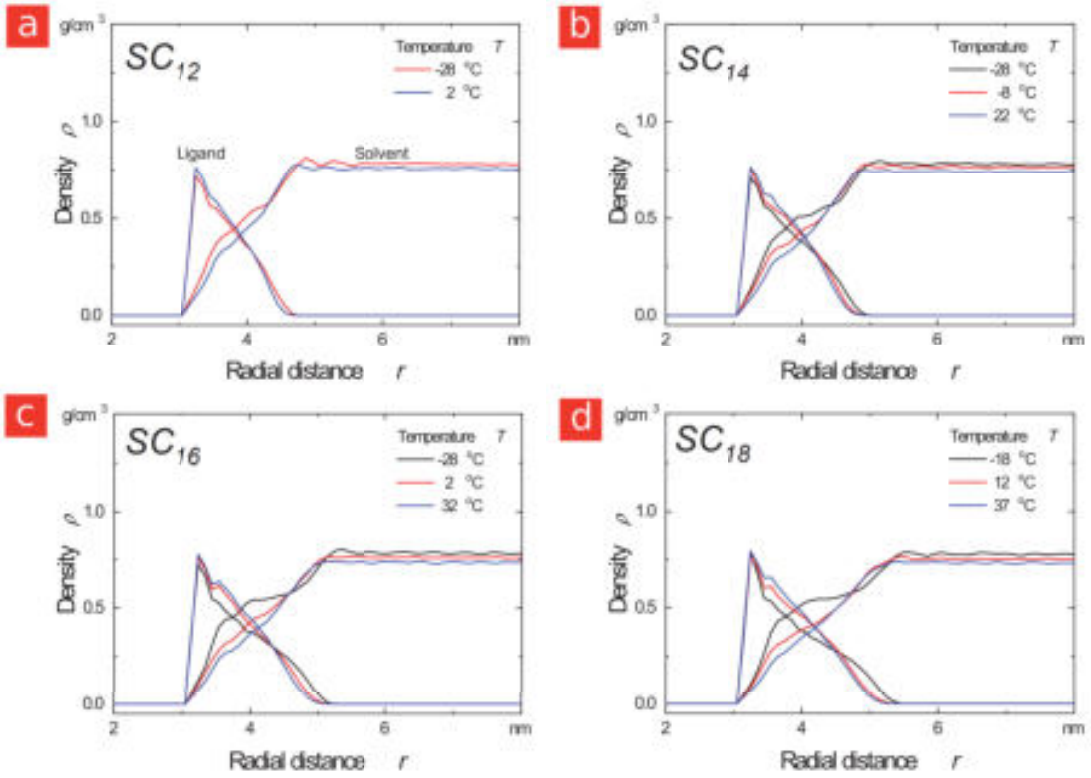

Figure 8: Radial density distributions for the decane solvent and for ligands of different lengths coating 5.8 nm CdSeNP, at a surface coverage of 3.6 nm^{-2}, plotted as a function of the distance r from the center of the nanoparticle core. The red lines indicate the density profile at the ligand ordering temperature T_{order} for each particle.

References

1. Kister, T.; Monego, D.; Mulvaney, P.; Widmer-Cooper, A.; Kraus, T. Colloidal Stability of Apolar Nanoparticles: The Role of Particle Size and Ligand Shell Structure. *ACS Nano* **2018**, *12*, 5969–5977, PMID: 29842786.

LANGMUIR

pubs.acs.org/Langmuir Addition/Correction

Correction to "On the Colloidal Stability of Apolar Nanoparticles: The Role of Ligand Length"

Debora Monego, Thomas Kister, Nicholas Kirkwood, Paul Mulvaney, Asaph Widmer-Cooper, and Tobias Kraus*

Langmuir **2018**, *34*, 43, 12982−12989, DOI: 10.1021/acs.langmuir.8b02883.

Cite This: *Langmuir* 2020, 36, 10892−10893 Read Online

ACCESS | Metrics & More | Article Recommendations

While preparing another manuscript, we found an error in the code used to calculate the average dihedral angle of the ligands given in Figures 1e, 2b, and 3e in the main manuscript and Figure 7b in the Supporting Information. Some solvent molecules were included in the analysis resulting in average dihedral angles that were too small. Additionally, the data set used to calculate the average dihedral angles of SC_{18} ligands coating 8.3 nm Au NPs was from a not fully equilibrated simulation. We have redone this analysis, and the corrected figures are shown below. The simulation snapshot of 8.3 nm Au-SC_{18} at low temperature (last NP in the bottom row of Figure 1d) now shows the typical clustering of the ligands, being consistent with what was observed for the other ligand lengths. The state of the high-temperature disordered shell did not change. There are also some small quantitative changes in the average dihedral angles, but they do not affect the conclusions reached in the article.

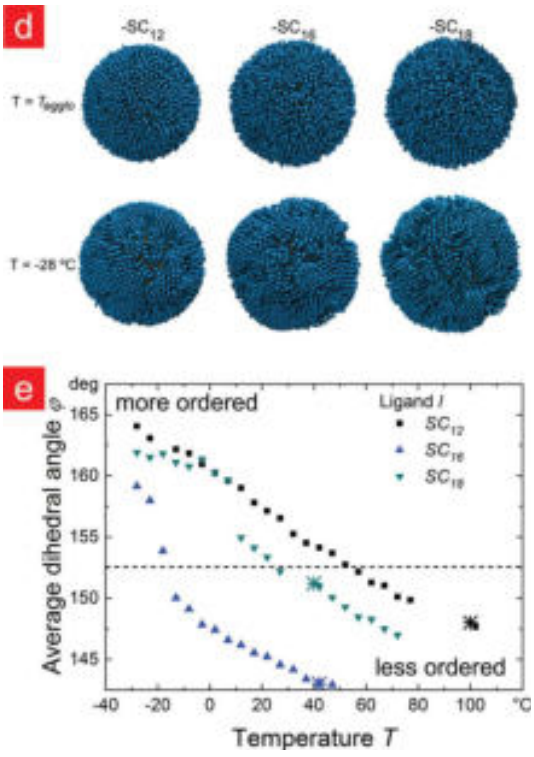

Figure 1. (d) Molecular dynamics simulation snapshots at T_{agglo} (top row) and −28 °C (bottom row) and (e) the average dihedral angle of the ligands, demonstrating that, regardless of the ligand length, 8.3 nm AuNPs agglomerate before the ligands order. (The experimental agglomeration temperatures are indicated by large crossed symbols.)

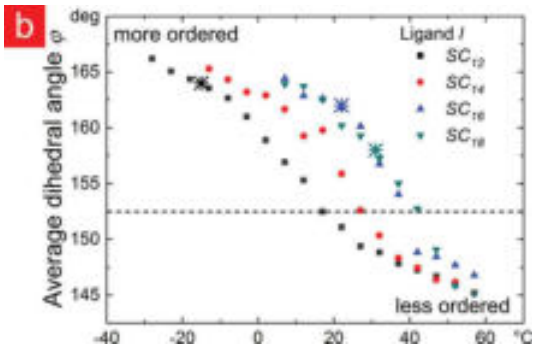

Figure 2. (b) Degree of ordering at different temperatures as quantified by the average dihedral angle of the ligands. T_{agglo}, indicated by the large crossed symbols, corresponds to the experimental agglomeration temperature for 6 nm AuNPs dispersed in heptane.[35] See the original article for references.

Published: September 3, 2020

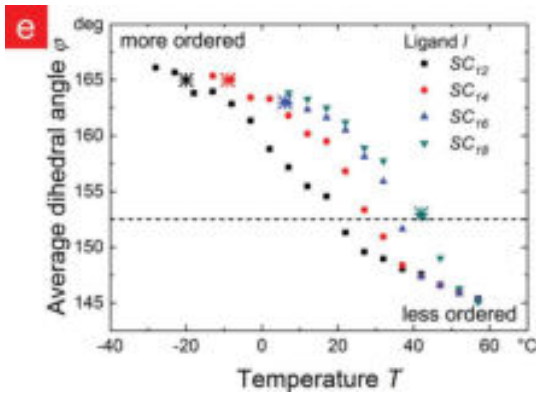

Figure 3. (e) Average dihedral angle of the ligands. Comparison with the experimental agglomeration temperatures, indicated by large crossed symbols, shows that the particles agglomerate after the ligands order.

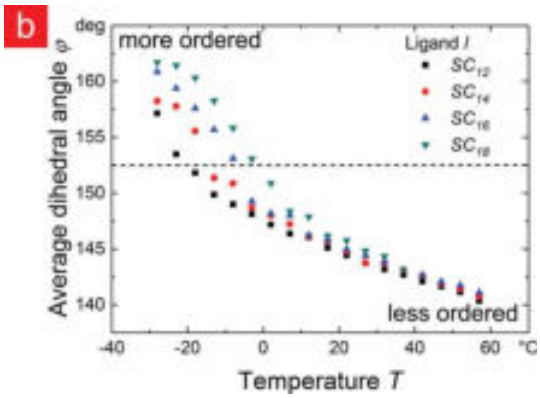

Figure 7. (b) Average dihedral angle for the ligands. The transition from less to more ordered is broader and shifted down by approximately 40 °C compared to when the surface coverage is 5.5 nm^{-2}.

https://dx.doi.org/10.1021/acs.langmuir.0c02478
Langmuir 2020, 36, 10892−10893

3.3 Publication 3

Monego, D., Kister, T., Kirkwood, N., Doblas, D., Mulvaney, P., Kraus, T., & Widmer-Cooper, A. (2020). When Like Destabilizes Like: Inverted Solvent Effects in Apolar Nanoparticle Dispersions. ACS nano, 14(5), 5278-5287.

DOI: 10.1021/acsnano.9b03552

ACSNANO

www.acsnano.org

ARTICLE

When Like Destabilizes Like: Inverted Solvent Effects in Apolar Nanoparticle Dispersions

Debora Monego, Thomas Kister, Nicholas Kirkwood, David Doblas, Paul Mulvaney, Tobias Kraus, and Asaph Widmer-Cooper*

Cite This: *ACS Nano* 2020, 14, 5278–5287

Read Online

ACCESS | Metrics & More | Article Recommendations | Supporting Information

ABSTRACT: We report on the colloidal stability of nanoparticles with alkanethiol shells in apolar solvents. Small-angle X-ray scattering and molecular dynamics simulations were used to characterize the interaction between nanoparticles in linear alkane solvents ranging from hexane to hexadecane, including 4 nm gold cores with hexadecanethiol shells and 6 nm cadmium selenide cores with octadecanethiol shells. We find that the agglomeration is enthalpically driven and that, contrary to what one would expect from classical colloid theory, the temperature at which the particles agglomerate increases with increasing solvent chain length. We demonstrate that the inverted trend correlates with the temperatures at which the ligands order in the different solvents and show that the inversion is due to a combination of enthalpic and entropic effects that enhance the stability of the ordered ligand state as the solvent length increases. We also explain why cyclohexane is a better solvent than hexadecane despite the two having very similar solvation parameters.

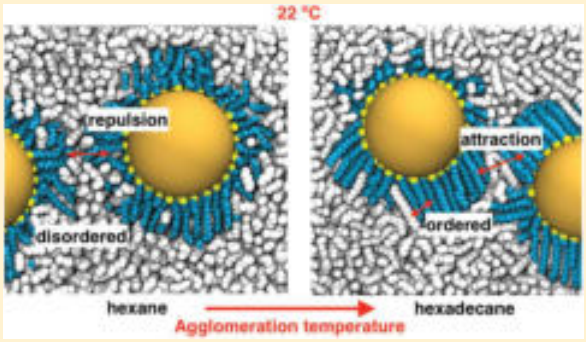

KEYWORDS: *nanoparticle, dispersion, apolar, colloidal stability, ligand, solvent, agglomeration*

Inorganic nanoparticles (NPs) made of metals,[1,2] semiconductors,[3,4] and oxides[5] are now used as functional components in catalysis,[6,7] sensing,[8,9] photovoltaics,[10,11] and color conversion in white light generation.[12−14] Many applications require the particles to be dispersed individually in organic solvents or to pass through this stage during processing.

Purely inorganic particles do not form stable dispersions in apolar solvents because van der Waals (vdW) forces cause attraction and thus agglomeration of the particles.[15] Cores are therefore coated with organic molecules during synthesis[3,6,16,17] or during subsequent ligand-exchange procedures. The adsorbed ligands provide steric stabilization and reduce the interfacial energy of the particles.[18]

The colloidal stability of ligand-coated particles in small molecule solvents is commonly explained with the classical "like dissolves like" rule, whereby the colloid interaction is assumed to be purely repulsive in solvents that are good for the tail group of the ligands.[19−21] Reducing the quality of the solvent, in turn, induces enthalpic attraction between the ligands[22−26] and is a common way of destabilizing these suspensions.[27] van der Waals attraction between the cores can also drive agglomeration, even in good solvents, if the cores are sufficiently large or the ligands are too short.[28−30]

Surprisingly, there appear to be exceptions to the rule of "like dissolves like" even for small metal and semiconductor particles whose agglomeration solely depends on the ligand shell.[30,31] Lohman *et al.* found that gold NPs with octane- or hexadecanethiol shells were more stable in alkanes shorter than the ligand chain,[32] while Hajiw *et al.* found that gold NPs with hexane- or dodecanethiol shells were more stable in cyclohexane than in heptane or dodecane, respectively.[33] In polymer solutions and melts, where the conformational entropy of free polymer molecules can drive particle agglomeration,[34,35] colloidal stability does typically decrease with polymer length.[36,37] However, a purely entropic explanation seems unlikely in relatively short solvents, like the ones described above, where the agglomeration is driven by enthalpy.

Here, we have studied the dispersibility of gold and cadmium selenide NPs in a variety of linear and cyclic alkane

Received: May 8, 2019
Accepted: April 16, 2020
Published: April 16, 2020

https://dx.doi.org/10.1021/acsnano.9b03552
ACS Nano 2020, 14, 5278–5287

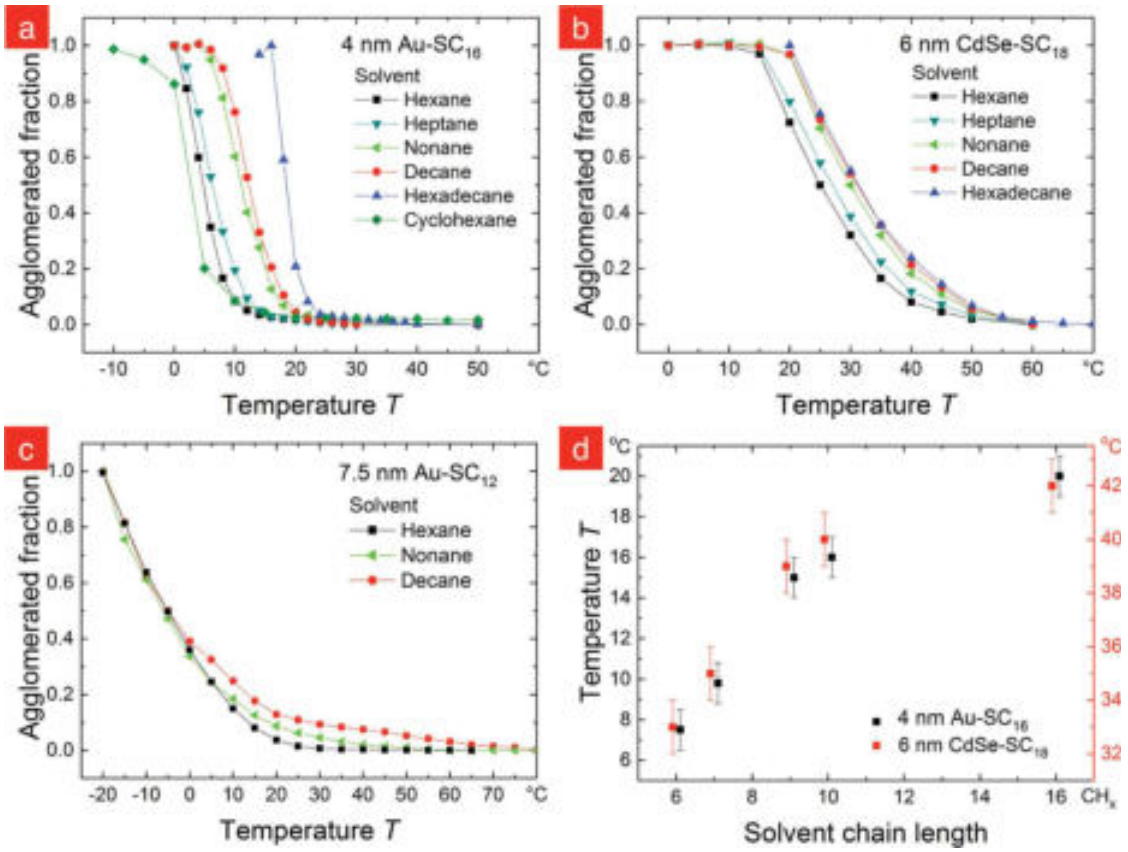

Figure 1. Fraction of agglomerated (a) 4 nm Au − SC_{16}, (b) 6 nm CdSe − SC_{18}, and (c) 7.5 nm Au − SC_{12} particles, as determined by *in situ* SAXS. All particles were dispersed at high temperatures, and agglomeration occurred upon cooling as indicated by the increase in structure factor. (d) Agglomeration temperature (where 20% of particles were agglomerated) as a function of alkane solvent chain length.

solvents using experiments that characterize their temperature-dependent colloidal stability. In all cases, colloidal stability decreased as the length of the alkane solvent approached that of the ligand tail, opposite to the rule of "like dissolves like". Further, we found that cyclohexane is a considerably better solvent for the particles than hexadecane, despite the two solvents having very similar solvation parameters. Specifically, changing the solvent from hexadecane to cyclohexane decreased the agglomeration temperature by 15 °C. It is important to understand the origin of such inversions, because the choice of solvents for stable dispersions of NPs is of considerable practical relevance; it affects the quality of nanocomposites, nanocrystal assembly,[38] and phase transfer procedures,[39] ultimately affecting device processability and performance.

In order to understand the origin of this behavior, we compared our systematic experimental data with detailed molecular dynamics (MD) simulations. Our results indicate that the inversion is a consequence of both enthalpic and entropic effects that together enhance the stability of an attractive ligand state as the solvent chain length increases. As has been shown previously, ligand shells composed of linear alkyl tails can undergo an ordering transition in solution that switches the interaction between the NPs from repulsive to attractive.[25] The temperature of this ligand phase transition is sensitive to various parameters including the particle dimensions, density of ligand coverage, and ligand length, often leading to nonlinear trends that cannot be explained using classical colloid theory.[30,31,40] We show that even small changes in the solvent structure can strongly impact the ligand ordering transition and use this insight to explain how particles can have dramatically different interactions in solvents with almost the same Hamaker, Hildebrand, and Hansen parameters.

RESULTS AND DISCUSSION

Nanoparticles (NP) with Au cores (4 and 7.5 nm in diameter) and CdSe cores (6 nm in diameter) were coated with hexadecanethiol (SC_{16}), dodecanethiol (SC_{12}), and octadecanethiol (SC_{18}) chains, respectively. These particles were dispersed in linear and cyclic alkane solvents of different chain lengths and analyzed by *in situ* small-angle X-ray scattering (SAXS) at a concentration of 2.5 mg mL^{-1} (roughly 3.8×10^{15} NP mL^{-1}). For all solvents tested, the particles agglomerated below a certain temperature (Figure 1), which was observed as a peak in the structure factor[41] $S(q)$. The agglomeration temperature, T_{aggl}, defined as the temperature at which 20% of the particles had agglomerated, increased in all cases as the solvent length approached the ligand length (Figure 1d). Similar results were obtained for 7.5 nm Au cores coated with hexadecanethiol (SC_{16}) ligands (see Figure S2 in the Supporting Information). No sign of solvent freezing was observed in any of the experiments.

https://dx.doi.org/10.1021/acsnano.9b03552
ACS Nano 2020, 14, 5278−5287

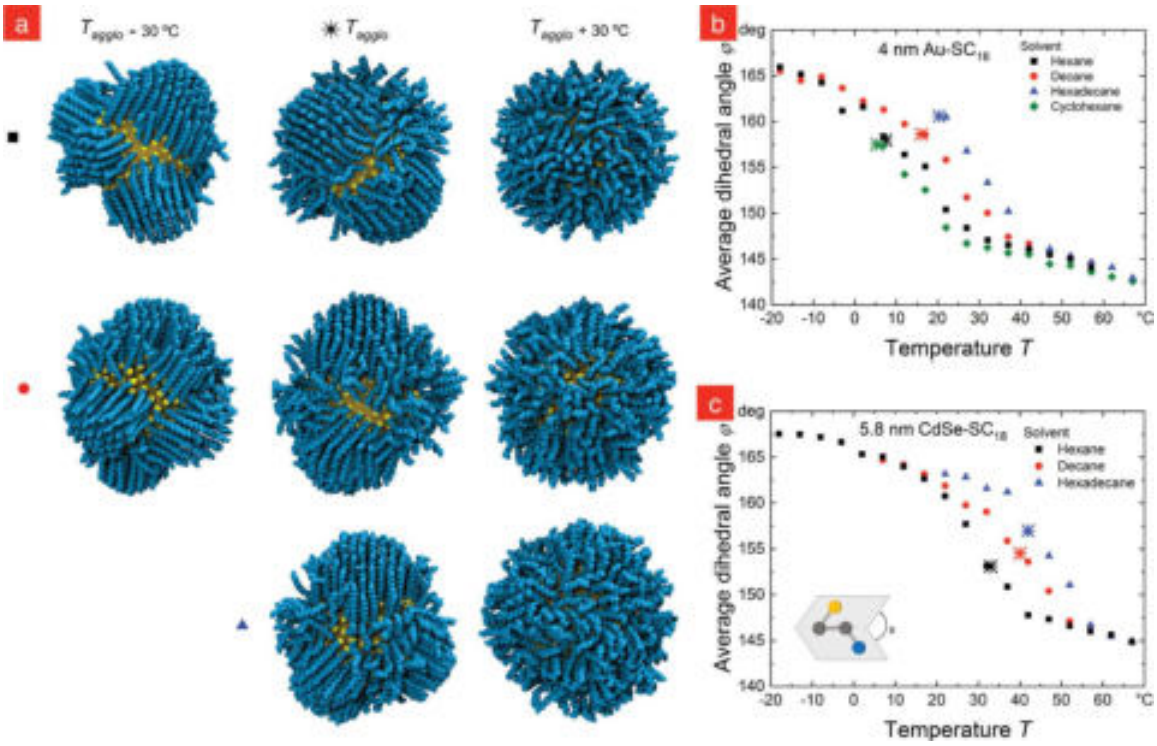

Figure 2. (a) Simulation snapshots of 4 nm Au particles at $T_{agglo} \pm 30$ °C in hexane, decane, and hexadecane. Solvent molecules have been hidden for clarity, with symbols as shown in the plot legends. The ligands order as the temperature decreases in a similar way in all solvents. This transition can be quantified by the average dihedral angle of the ligands, which increases rapidly as they order for both (b) 4 nm Au–SC_{16} and (c) 5.8 nm CdSe–SC_{18} particles. For comparison, the experimental agglomeration temperatures have been indicated by large crossed symbols. The scheme at the bottom left of (c) shows the definition of the dihedral angle ϕ.

These results show that the agglomeration is enthalpically favorable and entropically unfavorable, with cooling required to destabilize the dispersions. Extensions of classical colloid theory to describe the colloidal stability of ligand-coated NPs in solution, for example ref 23, typically include two terms that favor dispersion (the ideal entropy of mixing and the conformational entropy of the ligands) and two terms that favor agglomeration (the vdW attraction between the cores and the nonideal free energy of mixing). The vdW attraction between the cores is insignificant for our particles,[30] leaving the free energy of mixing as the deciding term in this classical approach. This can be described by the Flory–Huggins theory (eqs 1 and 2) that quantifies the affinity of the tethered ligands for the solvent in terms of the ideal entropy of mixing and the Flory χ parameter (eq 3). In these equations, d is the core diameter, $\tilde{L}$ is the rescaled ligand length (ligand length divided by core diameter), k_b the Boltzmann's constant, T the absolute temperature, $\phi = \left(N_L \frac{\nu_L}{V_{Sh}}\right)^2$ is the volume fraction occupied by the ligand shell, ν_S is the volume of a solvent molecule, ν_L the volume of a ligand molecule, N_L the number of ligands per NP, V_{Sh} the volume of the ligand shell, V_S is the molar volume of the solvent, R is the universal gas constant, and δ_L and δ_S are the Hildebrand solubility parameters for the ligands and solvent, respectively.

$$\frac{G_{mix}}{k_b T} = \frac{\pi d^3}{2\nu_S}\phi^2\left(\frac{1}{2} - \chi\right)(\tilde{s} - 1 - 2\tilde{L})^2; \quad 1 + \tilde{L} < x < 1 + 2\tilde{L} \tag{1}$$

$$\frac{G_{mix2}}{k_b T} = \frac{\pi d^3}{\nu_S}\phi^2\tilde{L}^2\left(\frac{1}{2} - \chi\right)\left(3\ln\frac{\tilde{L}}{\tilde{s} - 1} + 2\frac{\tilde{s} - 1}{\tilde{L}} - \frac{3}{2}\right); \quad x < 1 + \tilde{L} \tag{2}$$

$$\chi = \frac{V_S}{RT}(\delta_L - \delta_S)^2 + 0.34 \tag{3}$$

A Flory parameter below 0.5 indicates that the free energy of mixing of solvent and ligand is negative and that the two components should spontaneously mix. Since only the alkane tails of the ligands interact with the solvent, it seems reasonable to approximate the solubility parameters of the ligands by those of the unthiolated alkanes, that is, hexadecane (16.4 $MPa^{1/2}$) and octadecane (17.1 $MPa^{1/2}$). Thus, hexadecane is expected to be a better solvent for these coatings than decane (δ_s = 15.8 $MPa^{1/2}$) and hexane (δ_s = 14.9 $MPa^{1/2}$) (Hildebrand parameters from ref 42), even taking into account the reduction in the ideal entropy of mixing (ΔS_{mix}^{ideal}) as the solvent chain length increases (see Table S1 in the Supporting Information). A similar conclusion is reached when considering Hamaker constants or Hansen solubility parameters of the ligand and solvent molecules. Even if one were to use different solubility parameters for alkyl ligands bound to NPs, it would remain impossible within this theoretical framework to explain why cyclohexane is a much better solvent than hexadecane, since the two have almost identical solubility parameters.

An alternative explanation for deviations from the rule of "like dissolves like" in short-chain solvents was proposed by Hajiw and co-workers, who studied the temperature-dependent dispersibility of small Au particles (roughly 2.3 nm in

https://dx.doi.org/10.1021/acsnano.9b03552
ACS Nano 2020, 14, 5278–5287

diameter) in a similar range of alkane solvents.[33] They noted that the colloidal stability of polymer-grafted particles in polymer melts does typically decrease with polymer length and speculated that similar thermodynamic driving forces may explain such trends in much shorter solvents. In polymer melts, however, it is the conformational entropy of the free polymer chains that drives agglomeration. As we shall show, the solvent conformational entropy (S_{conf}^{solv}) in short-chain solvents is much smaller and unable to explain the observed dispersibility trends. In order to quantify S_{conf}^{solv}, along with enthalpic effects that are not considered in classical colloid theory, we used MD simulations (see Methods for details).

MD simulations of 4 nm core diameter Au and 5.8 nm CdSe particles in explicit solvent show that upon cooling, the ligands adopt more extended configurations and cluster together into ordered bundles in an enthalpically driven process. Snapshots of the simulations above, at, and below T_{agglo} in the linear alkane solvents are shown in Figure 2a and in Figure S3 in the Supporting Information, with solvent molecules hidden for clarity. Similar ligand shell structures were found for cyclohexane (shown in Figure S4 in the Supporting Information). The average dihedral angle of the ligand tails was used to quantify the ordering transition in the shell, with the results shown in Figure 2b,c. The simulations show that the same ligand shells "order" at higher temperature in longer alkane solvents for both Au and CdSe cores. This trend mirrors the experimental results, with the experimentally observed particle agglomeration temperatures (indicated by large crossed symbols) always occurring after the ligands have started ordering. These results indicate that particle agglomeration is driven by the ligand shell transition regardless of the core material, solvent length or structure, consistent with our previous findings for similar particles in decane[30] and with earlier experimental results for much larger silica particles in hexadecane.[43]

To explicitly test whether ordering of the ligand shell drives agglomeration regardless of solvent length, we calculated the potential of mean force between pairs of 4 nm Au particles in explicit hexane and decane (Figure 3a,b, respectively) as a function of separation and temperature. The overall interaction switched from repulsive to attractive as the ligands ordered, irrespective of solvent. This change in interaction between the ligand shells arises from changes in how the ligands interact with one another and with the solvent as their conformational state changes (see Figure S5 in the Supporting Information). The ligand–ligand component (which includes vdW interactions between the ligands) becomes more attractive as the ligands order, while the ligand–solvent component (which includes entropy changes involving the solvent) becomes less repulsive. In contrast, the overall interaction between alkyl ligand shells is always attractive in the absence of solvent, regardless of their conformational state, due to the absence of competing ligand–solvent interactions.[21,25,30,44] (The relevant results in refs 25 and 30 are located in the Supporting Information of those papers.)

So far, we have established that the NPs agglomerate because the ligands order and that the enthalpic driving force for both of these processes is the attractive vdW force that exists between the bound ligands. We now focus on the thermodynamics of the ligand ordering transition in order to explain the origin of the inverted trend in agglomeration temperatures. In particular, we will show that the trend is a consequence of both enthalpic and entropic effects that

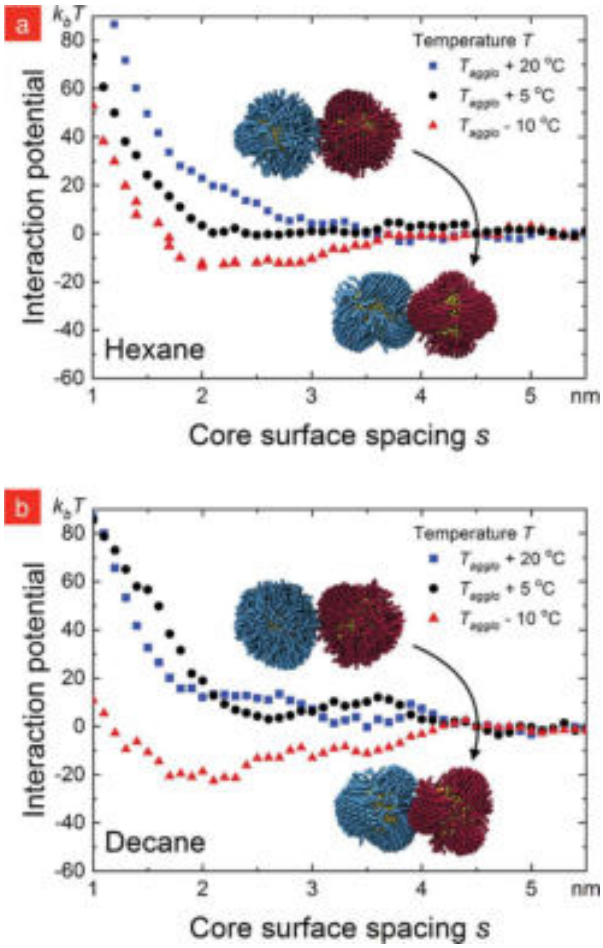

Figure 3. Potentials of mean force calculated for pairs of 4 nm Au–SC_{16} particles in (a) hexane and (b) decane, at temperatures around T_{agglo}. Simulation snapshots show the state of the ligands above and below T_{agglo}, at temperatures corresponding to the blue squares and red triangles, respectively.

together enhance the stability of the attractive ligand state as the solvent chain length increases. We start by considering a single NP and quantifying the dominant enthalpic contributions to the free energy difference between the disordered and ordered ligand states, that is, the vdW interactions between ligand molecules within the same shell (U_{LL}) and between ligand and solvent molecules (U_{LS}). These quantities are compared as a function of temperature and solvent type in Figure 4.

We find that the interaction between the ligands follows a similar trend in all solvents apart from a temperature offset: U_{LL} increases in magnitude in all cases by 3–4 k_bT/ligand during the transition (Figure 4a,c). Statistical analysis of the interatomic spacings within the ligand shell (see Figure S6 in the Supporting Information) indicates that the structure of the ligand shell is almost identical regardless of solvent when the temperature is expressed relative to T_{order}, defined as the temperature at which the average dihedral angle equals 155° (which corresponds roughly to the middle of the transition).

In contrast, we find more substantial differences in the interaction between ligand and solvent molecules. Figures 4b and 4d show that the ligand-solvent interaction energy (U_{LS})

https://dx.doi.org/10.1021/acsnano.9b03552
ACS Nano 2020, 14, 5278–5287

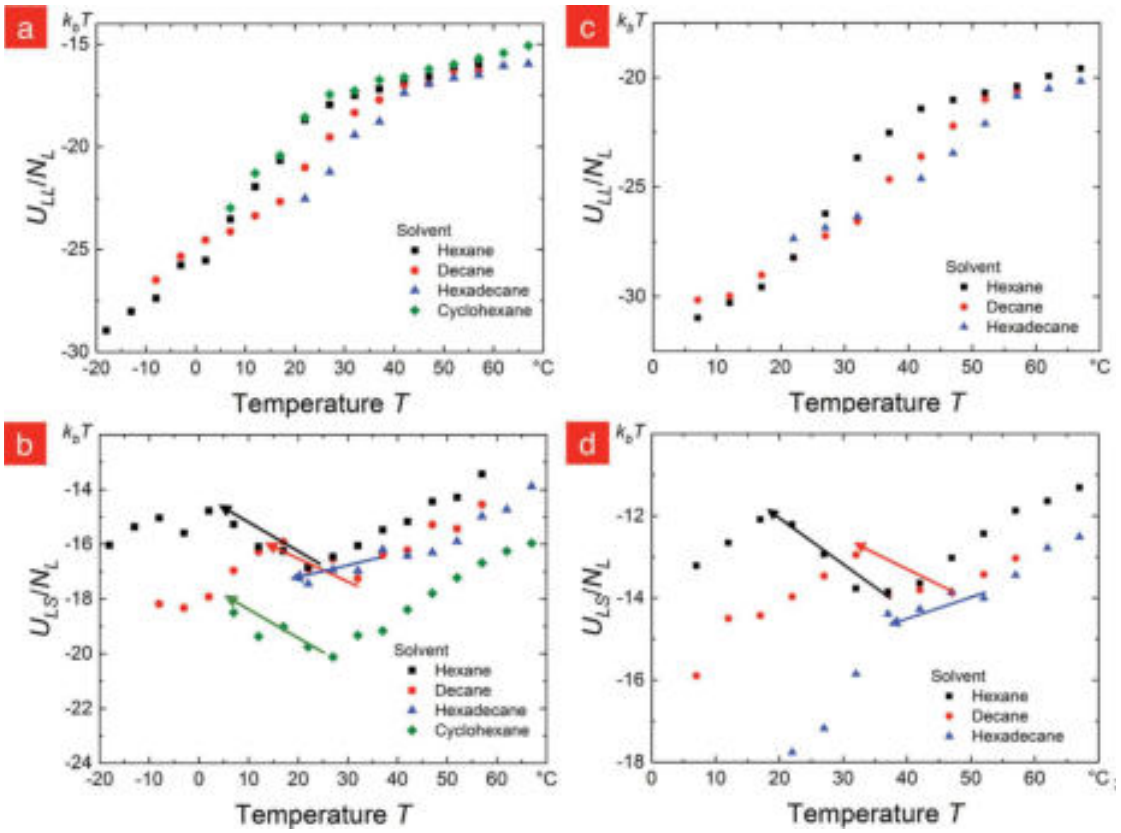

Figure 4. Energy of interaction between ligand molecules (U_{LL}) on isolated (a) 4 nm Au−SC_{16} and (c) 5.8 nm CdSe−SC_{18} particles increases upon cooling in all solvents. In contrast, the energy of interaction between ligand and solvent molecules (U_{LS}) decreases in magnitude for shorter chain alkanes and increases for hexadecane for both (b) Au and (d) CdSe NPs, as indicated by the solid arrows. All energies are normalized by the number of ligand molecules on the NP, N_L.

increases during the ordering transition in hexadecane (blue arrows) but decreases in decane, hexane and cyclohexane (red, black and green arrows), with the largest decrease in hexane (around 2 k_bT/ligand). This means that the change in internal energy driving the ligand shell to order is reduced in shorter solvents, which partly explains why the particles are more stable in hexane and cyclohexane than in hexadecane.

The differences in ΔU_{LS} during the transition are due to subtle molecular effects. As the ligands order to form dense bundles, the solvent molecules within the spherical shell occupied by the ligands become confined to the spaces between the bundles. This results in a similar increase in the radially averaged solvent density near the core surface in all solvents (Figures S7 and S4 in the Supporting Information), but with very different consequences depending on how well the solvent molecules pack with the ligand bundles. Hexane and cyclohexane do not pack as well with the ordered ligands, resulting in a loss of ligand−solvent interaction, while hexadecane packs better with the ordered ligands, resulting in a gain in ligand−solvent interaction (Figures S8 and S4 in the Supporting Information).

Entropic differences between the solvents appear to play an important role here. It is well-known that the lower freezing points of shorter chain alkanes are partly due to their higher translational entropy per atom.[45] Analysis of the average dihedral angles also reveals that longer alkanes are more extended both within and outside the ligand shell, as shown in Figure 5a for the 4 nm Au NPs. Similar results are obtained for the CdSe particles (see Figure S9 in the Supporting Information). These factors may explain why hexadecane is better able than hexane to align with the ordered ligands (Figure 5b) and thus increase the relative stability of the ordered state. We note that close alignment of hexadecane with linear alkyl ligands has also been observed in sum frequency generation spectroscopy studies of silica NPs.[43]

To more directly address how entropy affects the ligand ordering transition, we quantified the difference (between the ordered and disordered ligand states) in the ideal entropy of mixing (ΔS_{mix}^{ideal}) and in the conformational entropies of the ligands (ΔS_{conf}^{lig}) and solvent (ΔS_{conf}^{solv}). ΔS_{mix}^{ideal} is relevant because ordering of the ligands causes them to demix from the solvent. The change in entropy due to this demixing was estimated using eqs 1 and 2, setting χ = 0 and multiplying by 5 for reasons explained in the Methods. This yielded values for $-T\Delta S_{mix}^{ideal}$ ranging from roughly 0.3 k_bT/ligand for hexane to 0.1 k_bT/ligand for hexadecane, indicating a decreasing penalty for ordering as the solvent length increases.

The changes in the conformational entropies were estimated using an information theoretic approach that is described in detail in the Methods. Both ordered and disordered configurations were generated at the same temperature, T_{order}, in order to exclude contributions due to temperature differences. This was achieved by scaling the interaction energies between nonbonded ligand atoms by ±5%, which

https://dx.doi.org/10.1021/acsnano.9b03552
ACS Nano 2020, 14, 5278−5287

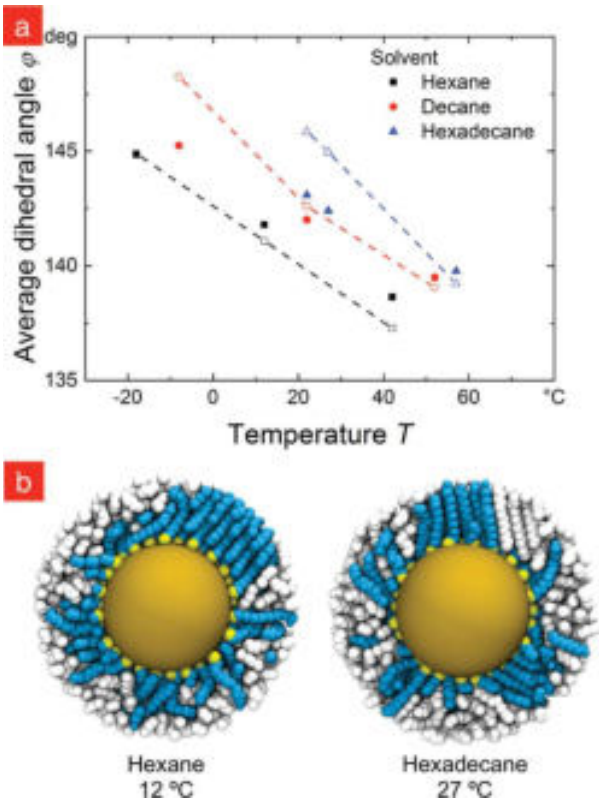

Figure 5. (a) The average dihedral angle for the solvent chains around Au NP shows that longer alkanes are more extended at a given temperature, both within the ligand shell (open symbols) and in the bulk solvent region (closed symbols). This allows hexadecane to better align with and stabilize the ligands in the ordered state, as seen in (b) snapshots of the ligand−solvent packing at T_{order} for 4 nm Au−SC_{16} particles. Ligand and solvent united-atoms are represented by blue and white spheres, respectively. The error bars in (a) are smaller than the symbols, and the lines are a guide to the eye.

resulted in ligand configurations similar to those at $T_{order} \mp 30$ K. This yielded values for $-T\Delta S^{lig}_{conf}$ ranging from 2.2−3 k_bT/ligand, with no apparent trend with solvent length. This substantial penalty is the main reason why ordering of the ligands has to be enthalpically driven. In comparison, we obtained values for $-T\Delta S^{solv}_{conf}$ ranging from 0−0.3 k_bT/ligand. Again there was no apparent trend with solvent length, indicating that the conformational entropy of the solvent makes at best a small contribution to the trend in agglomeration temperatures.

To facilitate comparison, we estimated the equivalent differences in U_{LL} and U_{LS} at T_{order} *via* linear extrapolation of the data points obtained above and below the ordering transition and collected all of the enthalpic and entropic terms in Table 1. Also included is the substantial change in the internal energy associated with the ligand dihedral angles (ΔU^{lig}_{dih}), obtained from the same biased simulations as the conformational entropies. Together, these values indicate that the main contribution to the inverted trend in the agglomeration temperatures is the reduction in ΔU_{LS} as the solvent length increases, with a minor contribution from the reduction in $-T\Delta S^{ideal}_{mix}$.

Table 1. Major Enthalpic and Entropic Contributions to the Difference in Free Energy between the Ordered and Disordered Ligand States[a]

4 nm Au-SC_{16}			
solvent	hexane	decane	hexadecane
T_{order}	290	295	300
ΔU_{LL}	−3.8	−3.7	−3.5
ΔU_{LS}	**4.0**	**2.3**	**1.0[b]**
ΔU^{lig}_{dih}	−2.6	−2.3	−1.8
$-T\Delta S_{mix}$	**0.32**	**0.22**	**0.14**
$-T\Delta S^{lig}_{conf}$	2.5	3.0	2.5
$-T\Delta S^{solv}_{conf}$	0.00	0.00	0.30
5.8 nm CdSe-SC_{18}			
solvent	hexane	decane	hexadecane
T_{order}	300	310	320
ΔU_{LL}	−4.4	−3.5	−3.1
ΔU_{LS}	**4.3**	**2.6**	**1.3**
ΔU^{lig}_{dih}	−1.9	−1.8	−1.3
$-T\Delta S_{mix}$	**0.54**	**0.37**	**0.25**
$-T\Delta S^{lig}_{conf}$	2.2	2.8	2.2
$-T\Delta S^{solv}_{conf}$	−0.17	0.12	−0.09

[a]Expressed in units of k_bT/ligand at the ligand ordering temperature T_{order}: U_{LL} is the vdW interaction between the ligands, U_{LS} is the vdW interaction between the ligands and the solvent, U^{lig}_{dih} is the internal energy due to the ligand dihedral angles, S^{ideal}_{mix} is the entropy of demixing the ligands and solvent, while S^{lig}_{conf} and S^{solv}_{conf} are the conformational entropies of the ligands and solvent, respectively. Negative quantities favor the ordered state, while positive ones favor the disordered one. The quantities highlighted in bold are the only ones that explain the trend in the agglomeration temperatures. [b]Indicates a value that was estimated by comparison with the same results obtained for CdSe. Standard errors are ±0.3 or smaller.

Our results also explain why alkanethiol-coated NPs are more stable in cyclohexane than in hexadecane, despite the two solvents having almost identical density and solubility parameters. In cyclohexane, the reduction in U_{LS} upon ordering is greater than in hexadecane (due to poorer packing with the extended ligands), while the entropic cost of demixing is also greater due to cyclohexane's smaller size and thus higher number density. The ordered ligand state is therefore less stable (relative to the disordered one) in cyclohexane than in hexadecane, which suppresses the ordering transition and results in an agglomeration temperature that is even lower than that in hexane.

Finally, to check whether S^{solv}_{conf} contributes to the trend in agglomeration temperatures regardless of the conformational state of the ligands, we calculated the difference in S^{solv}_{conf} between the solvated 4 nm Au NPs and pure solvent with the same number of solvent molecules. This yielded a similar value in all solvents for $-T\Delta S^{solv}_{conf}$ of roughly 0.2 k_bT/ligand when the ligands were in the disordered state, indicating no substantial contribution to the trend.

CONCLUSIONS

We have studied the temperature-dependent agglomeration of small apolar metallic and semiconducting NPs in a range of alkane solvents. We found that the agglomeration is enthalpically driven, with colloidal stabilities that run counter to expectations from classical colloid theory. Increasing the solvent chain length toward that of the ligands resulted in a *decrease* in colloidal stability, rather than the expected increase,

https://dx.doi.org/10.1021/acsnano.9b03552
ACS Nano 2020, 14, 5278−5287

and the colloidal stability differed strongly between cyclohexane and hexadecane despite their almost identical solvation parameters.

While this behavior is reminiscent of colloidal stability in polymer solutions and melts, the thermodynamic origins are different, with enthalpic rather than entropic effects dominating in small organic solvents. Simulations show that the NPs become attractive to one another as the ligands order and that the temperatures at which the particles agglomerate match the temperatures at which the ligands order in the various solvents. This indicates that the experimental results can be understood by considering the thermodynamics of the ordering transition and, in particular, how well the various solvents stabilize the ordered state of the ligands relative to the disordered one.

We found that the ordering transition is driven by vdW attraction between the ligand tails and internal energy associated with their dihedral angles and opposed by a combination of enthalpic and entropic terms: loss of vdW interaction between the ligands and solvent, loss of ligand conformational entropy, and a reduction in the entropy of mixing. Of these, the loss in vdW interaction with the solvent exhibits the biggest differences, with smaller losses observed as the solvent length increases due to better packing with the ordered ligands. The entropic cost of demixing the ligands from the solvent also exhibits a small decrease as the size of the solvent molecules increases. Together, these changes increase the relative stability of the ordered ligand state when the solvent is changed from hexane or cyclohexane to hexadecane, which explains the experimental results.

We hope that these results will inspire more detailed experimental studies of ligand morphology and ligand-solvent interactions, which are now possible due to recent advances in sum frequency generation spectroscopy,[43] nuclear magnetic resonance,[46,47] and small angle neutron scattering.[48] While we have not considered polar solvents in the present study, we note that linear $-(CH_2)_nX$ ligands with a variety of terminal X groups can also order in water,[49,50] raising the possibility of similar effects in polar solvents.

METHODS

All chemicals were obtained from Sigma-Aldrich (unless noted otherwise) and used without further purification. The methods were chosen to provide samples that are as comparable as possible to data published previously.[30,31]

Nanoparticle Synthesis. The synthesis of gold nanoparticles (Au NP) with core diameters of 4 and 7.5 nm was adapted from a previously described method.[30] For Au NPs with a core diameter of 4 nm, a mixture of pentane (≥98.5%, GC), 8 mL oleylamine (technical grade, 70%), and 100 mg of $HAuCl_4$ (with crystal water) was stirred at 20 °C and 500 rad min^{-1} for 10 min under argon atmosphere. Afterward a solution of 40 mg *tert*-butylamine borane (ABCR, 97%) in 2 mL pentane and 2 mL oleylamine was added. The color of the solution immediately changed. After stirring for 60 min at 20 °C, the NPs were purified once by precipitating with 30 mL ethanol and centrifugation at 4000 rad min^{-1} for 5 min. The precipitated NPs were then redispersed in 20 mL of the appropriate solvent. Gold cores with a diameter of 7.5 nm were produced in benzene instead of pentane. The mixture of benzene, oleylamine, and $HAuCl_4$ was stirred for 1 min before *tert*-butylamine borane was added. The resulting dispersion was then purified as above.

Cadmium selenide nanoparticles (CdSe NPs) with core diameters of 6 nm were synthesized as follows. First, three stock solutions were prepared, a Se injection solution (i), a Cd growth solution (ii), and a Se growth solution (iii): (i) 0.3265 g Se was dissolved in a mixture of 2.5 g of trioctylphosphine, 2.5 g of octadecene, and 6 g of oleylamine in a nitrogen-filled glovebox to give a clear, slightly yellow solution. (ii) A solution containing 0.17 mol L^{-1} of cadmium was made from 0.22 g of cadmium oxide, 0.97 g of oleic acid, and 6.23 g of 1-octadecene in a three-neck round-bottom flask on a Schlenk line. The solution was degassed under vacuum (<1 mbar) for 60 min at 80 °C, heated to 250 °C and held until clear, then cooled to room temperature. While cooling, 1.13 mL of oleylamine was added. The final solution was clear and slightly yellow. (iii) A solution containing 1.7 mol L^{-1} of selenium was prepared by dissolving 0.25 g of selenium in 1.55 g of trioctylphosphine in a nitrogen-filled glovebox to give a clear colorless solution.

The synthesis started with 0.22 g of cadmium oxide, 3 g of oleic acid, and 30 g of octadecene in a three-neck round-bottom flask that was degassed under vacuum (<1 mbar) for 60 min at 80 °C. The mixture was then heated to 260 °C until a clear solution (iv) had formed. The selenium injection solution (i) was loaded into a 24 mL disposable syringe equipped with a 16 G needle and rapidly injected into the cadmium solution (iv) at 260 °C. The temperature of the reaction solution was allowed to recover to 250 °C where it was held for NP growth. After 20 min, 2 mL of 0.17 mol L^{-1} cadmium growth stock (ii) and 0.2 mL of 1.7 mol L^{-1} selenium growth stock (iii) were added dropwise to the reaction. The addition of cadmium and selenium growth solutions (ii) and (iii) was continued every 10 min. After three additions, the reaction was left for a further 10 min at 250 °C, then cooled to room temperature. The NPs were washed three times *via* precipitation with acetone and resuspended in toluene.

Nanoparticle Characterization. Small angle X-ray scattering (Xenocs Xeuss 2.0) and transmission electron microscopy (JEOL JEM 2010) were used to measure the core size of the NPs as previously described.[30] Scattering data from SAXS were analyzed using SASfit (Version 0.94.6, Paul Scherrer Institute), and TEM micrographs were analyzed using ImageJ distributed by NIH (Version 1.45s) (see Table 2).

Table 2. NPs Used for This Study, With Diameters Obtained from Transmission Electron Microscopy and Small Angle X-ray Scattering

number	*d*(TEM)	*d*(SAXS)
Au01	4.1 nm ± 10.0%	4.1 nm ± 9.3%
Au02	7.4 nm ± 7.4%	7.5 nm ± 6.7%
CdSe	5.8 nm ± 7.1%	6.0 nm ± 9.6%

Ligand Exchange. *Au NPs.* Ligand exchange on Au NPs was performed as described previously.[51] Au NPs coated with oleylamine were heated to 80 °C, and an excess of required alkanethiol was added. After stirring for a further 10 min, the particles were purified and redispersed in the appropriate solvent.

CdSe NPs. As-synthesized CdSe NPs were precipitated with acetone/ethanol and resuspended in a solution of the respective alkanethiol ligand (40 wt % in chloroform) with triethylamine (1 mol equiv with respect to thiol). The resulting NP dispersion was heated for 3 h at 45 °C while stirring. The NPs were then washed *via* precipitation with antisolvent and centrifugation (3300*g* for 3 min). The antisolvent was chosen to optimally dissolve excess ligand: 1:1 (v/v) methanol/ethanol mixture for hexanethiol and octanethiol ligands or 1:1 (v/v) acetone/ethanol mixture for dodecanethiol and longer ligands. The NPs were resuspended again in a solution of ligand (40 wt % in chloroform), stirred at 45 °C for 2 h, then washed as before, and resuspended in a 0.1 M solution of ligand in chloroform. After stirring at room temperature for 24−48 h, the NPs were washed three times and resuspended in pure chloroform. Chambrier *et al.* have shown this procedure leads to almost complete displacement (>92%) of amines by the alkanethiol ligands.[52]

Small Angle X-ray Scattering. Experiments were performed under vacuum using a Xeuss 2.0 from Xenocs SA (Grenoble, France) equipped with a copper K_α X-ray source and a PILATUS 1 M detector from DECTRIS (Baden, Switzerland) using a sample-to-detector distance of 1235 mm.

https://dx.doi.org/10.1021/acsnano.9b03552
ACS Nano 2020, 14, 5278−5287

To prevent solvent evaporation during the measurements, the samples (usually a quantity of 20 μL to 40 μL) were filled into thin-wall glass capillaries (diameter of 2 mm) and sealed with epoxy resin.

For each measurement, the samples were introduced into a temperature-controlled sample holder (Omega CN8200), Peltier-controlled with a temperature range between −20 and 120 °C. The measurements started at high temperature to ensure a fully deagglomerated state. Afterward, the temperature was first decreased and later increased in 5 °C steps. At each step, the samples were first equilibrated (20 min) followed by an exposition of 10 min. Data treatment was carried out as described elsewhere.[30,53]

Molecular Dynamics Simulations. MD simulations with periodic boundary conditions were used to study 4 nm Au NPs and 5.8 nm CdSe NPs covered in 1-hexadecanethiol and 1-octadecanethiol ligands, respectively, in the presence of a variety of liquid alkanes (*n*-hexane, *n*-decane, *n*-hexadecane, and cyclohexane). The sulfur atoms from the ligands were randomly placed on a spherical shell around the implicit core (0.15 nm further out) and allowed to find their optimal positions on this shell while subject to a Coulombic interaction with relative permittivity ϵ = 10 and the RATTLE constraint.[54] This produced a shell with approximately equidistant binding sites, with the sulfur atoms subsequently treated as part of the rigid core of the particle. The ligands were irreversibly bound to the Au and CdSe cores at a surface coverage of 5.5 ligands nm^{-2}, consistent with thermogravimetric analyses of the experimental samples.[31] CH_x groups from ligand and solvent molecules were treated as united atoms and interacted with one another according to the 12-6 Lennard-Jones (LJ) potential and with the implicit cores through a 9-3 LJ potential, as previously employed and described for similar particles.[25,31,55] Additionally, bond stretching, bond bending, and dihedral torsion terms were considered within each molecule, with parameters taken from the TraPPE force field family.[56]

Simulations of systems with up to 165,000 particles were performed using the LAMMPS molecular dynamics simulation package,[57] at temperatures ranging from roughly the freezing point of the respective solvent to values sufficiently high to have the ligands in the disordered state (up to 340 K). Periodic simulation cells containing individual NPs and the alkane solvent were slowly compressed until the solvent density far from the NP was equal to the experimental density of the pure solvent at the chosen temperature. A preliminary run was performed at constant volume in order to accommodate the particles properly in the simulation cell. The systems were then equilibrated at constant pressure (80 atm) and temperature, maintained with a Nosé−Hoover thermostat and barostat, for at least 12 ns. Finally, the relevant data were accumulated and averaged over production runs of 1 ns. Average bulk solvent densities for these runs stayed within 1% of experimental values for linear alkanes and 5% for cyclohexane. Molecular graphics were produced using Visual Molecular Dynamics.[58]

Potentials of Mean Force. The change in free energy as a pair of 4 nm Au particles was brought together was calculated in both hexane and decane as a potential of mean force (PMF) using constrained MD. Starting from a non-interacting separation, the particles were brought together at a rate of 1 Å ns^{-1}. The particles were allowed to rotate about their centers of mass at each separation *r*, and subsequent simulations of 10 ns or more were performed in order to adequately sample the PMF. Longer runs were necessary particularly at and below T_{order}, where the ligands were less mobile. Additionally, in order to allow the ligands to reorganize and find more stable configurations at these temperatures, we included a thermal annealing step at separations where the ligand shells overlapped. This was done by increasing the temperature of these systems by 50 K over 1 ns and subsequently cooling it back to the initial temperature over the course of 3 ns.

The spherical gold cores were assumed to interact with each other *via* the Hamaker potential,[59] with a Hamaker constant of 2 eV.[60] This approach treats the solvent and ligands as a single continuum, with the interaction constant scaled to include the effect of the hydrocarbon medium.

The PMF between two NPs is given by

$$\phi_{MF}(r) = \int_r^\infty F_{mean}(s)ds \tag{4}$$

where F_{mean} is the average force in the direction of the line connecting the two particles and is given by

$$F_{mean}(r) = \frac{1}{2}\langle(\vec{F}_2 - \vec{F}_1)\cdot\vec{r}\rangle_{NVT} \tag{5}$$

where $\vec{F}_1$ and $\vec{F}_2$ are the total forces acting on the first and second NP, respectively, $\vec{r}$ is the unit vector pointing from one particle's center to the other's, and the angular brackets denote an average in the canonical ensemble.

Entropy of Mixing. The change in the ideal entropy of mixing due to spatially separating the ligand and solvent molecules was estimated using eqs 1 and 2 by setting χ = 0 and calculating the value at the average core spacing in the experimental agglomerates (2.4 nm). This value was then multiplied by 5 to roughly convert the entropy change for a pair of touching particles into the entropy change for an entire particle capable of accommodating approximately 10 nearest neighbors. The other parameters used are listed in Table S2 in the Supporting Information.

Conformational Entropies. We employed the correlation corrected multibody local approximation, as implemented in the software CENCALC,[61] to estimate changes in the conformational entropies of the ligand and solvent molecules. The molecular conformational space was represented in terms of the dihedral angles, which were discretized into subintervals delimiting the three locally stable conformational states accessible to them, that is, *trans*, *gauche*(−), and *gauche*(+). This transforms the continuous random variable θ into the discrete random variable *X*, with a probability mass function $P(X)$, where $X = \{X_1, ..., X_M\}$ and *M* is the number of dihedral angles. The entropy can then in principle be calculated as a sum over the *N* possible configurations of the system using the expression for the Shannon information entropy:

$$S_{conform} = -k_b \sum^{N} P(X)\ln P(X) \tag{6}$$

In practice, obtaining an accurate estimate for $P(X)$ is difficult, because the number of possible conformers is very large ($\sim 3^M$). Direct application of the Shannon expression would also result in large and negatively biased entropies due to correlations between the dihedral angles. However, an approximation to the total entropy can be obtained by truncating a mutual information expansion,[62] allowing the Shannon information entropy to be calculated using a reasonable number of states.

In addition, due to the large number of molecules in our system, each molecule was treated as an independent system, that is, a NP coated with *l* ligands, each with *d* dihedral angles, was analyzed as *l* independent *d*-dimensional spaces. The sum of the entropies of the individual ligands then provided an approximation for the entropy of the entire NP. This approach considered the correlations within each molecule, but ignored correlations between neighbor molecules, which are stronger for ligands in the ordered state. The conformational entropy differences that we report for the ligands therefore represent a lower bound, calculated using fully converged values from data sampled every 1 ps over 5.5 ns. While we were not able to fully converge the absolute solvent entropies using the same number of data points, the entropy differences converge more rapidly and do appear to be fully converged.

ASSOCIATED CONTENT

Supporting Information

The Supporting Information is available free of charge at https://pubs.acs.org/doi/10.1021/acsnano.9b03552.

SAXS data, fraction of agglomerated 7.5 nm Au−SC_{16} particles, simulation results for CdSe−SC_{18} particles dispersed in linear alkanes and for Au−SC_{16} particles in cyclohexane, radial density distributions of ligand and

https://dx.doi.org/10.1021/acsnano.9b03552
ACS Nano 2020, 14, 5278−5287

solvent, individual contributions to the PMF (in hexane), and number of ligand−ligand interactions and ligand−solvent interaction energy as a function of the separation between interacting pairs (PDF)

AUTHOR INFORMATION

Corresponding Author

Asaph Widmer-Cooper − *ARC Centre of Excellence in Exciton Science, School of Chemistry and The University of Sydney Nano Institute, The University of Sydney, Sydney, New South Wales 2006, Australia;* orcid.org/0000-0001-5459-6960; Email: asaph.widmer-cooper@sydney.edu.au

Authors

Debora Monego − *ARC Centre of Excellence in Exciton Science, School of Chemistry and The University of Sydney Nano Institute, The University of Sydney, Sydney, New South Wales 2006, Australia;* orcid.org/0000-0003-1246-3718

Thomas Kister − *INM - Leibniz Institute for New Materials, 66123 Saarbrücken, Germany;* orcid.org/0000-0002-9827-1380

Nicholas Kirkwood − *ARC Centre of Excellence in Exciton Science, School of Chemistry, University of Melbourne, Parkville, Victoria 3010, Australia;* orcid.org/0000-0002-7845-7081

David Doblas − *INM - Leibniz Institute for New Materials, 66123 Saarbrücken, Germany*

Paul Mulvaney − *ARC Centre of Excellence in Exciton Science, School of Chemistry, University of Melbourne, Parkville, Victoria 3010, Australia;* orcid.org/0000-0002-8007-3247

Tobias Kraus − *INM - Leibniz Institute for New Materials, 66123 Saarbrücken, Germany; Colloid and Interface Chemistry, Saarland University, 66123 Saarbrücken, Germany;* orcid.org/0000-0003-2951-1704

Complete contact information is available at: https://pubs.acs.org/10.1021/acsnano.9b03552

Notes

The authors declare no competing financial interest.

ACKNOWLEDGMENTS

P.M., N.K., D.M., and A.W. were supported by the ARC Centre of Excellence in Exciton Science (CE170100026). A.W. thanks the Australian Research Council for a Future Fellowship (FT140101061), and D.M. thanks the University of Sydney Nano Institute for a Postgraduate Top-Up Scholarship and the Australian Nanotechnology Network for an Overseas Travel Fellowship. Computational resources were generously provided by the University of Sydney HPC service, the National Computational Infrastructure National Facility (NCI-NF) Flagship program, and the Pawsey Supercomputer Centre Energy and Resources Merit Allocation Scheme. T.K., D.D., and T.K. thank the DFG Deutsche Forschungsgemeinschaft for funding. P.M. and T.K. also thank the DAAD for travel support.

REFERENCES

(1) Jana, N. R.; Peng, X. Single-Phase and Gram-Scale Routes toward Nearly Monodisperse Au and Other Noble Metal Nanocrystals. *J. Am. Chem. Soc.* **2003**, *125*, 14280−14281.

(2) Stoeva, S.; Klabunde, K. J.; Sorensen, C. M.; Dragieva, I. Gram-Scale Synthesis of Monodisperse Gold Colloids by the Solvated Metal Atom Dispersion Method and Digestive Ripening and Their Organization into Two- and Three-Dimensional Structures. *J. Am. Chem. Soc.* **2002**, *124*, 2305−2311.

(3) Peng, X.; Wickham, J.; Alivisatos, A. P. Kinetics of II-VI and III-V Colloidal Semiconductor Nanocrystal Growth: "Focusing" of Size Distributions. *J. Am. Chem. Soc.* **1998**, *120*, 5343−5344.

(4) Shim, M.; Guyot-Sionnest, P. *n*-Type Colloidal Semiconductor Nanocrystals. *Nature* **2000**, *407*, 981−983.

(5) Pileni, M.-P. The Role of Soft Colloidal Templates in Controlling the Size and Shape of Inorganic Nanocrystals. *Nat. Mater.* **2003**, *2*, 145−150.

(6) Murray, C. B.; Norris, D. J.; Bawendi, M. G. Synthesis and Characterization of Nearly Monodisperse CdE (E = S, Se, Te) Semiconductor Nanocrystallites. *J. Am. Chem. Soc.* **1993**, *115*, 8706−8715.

(7) Haruta, M. When Gold Is Not Noble: Catalysis by Nanoparticles. *Chem. Rec.* **2003**, *3*, 75−87.

(8) Shipway, A. N.; Katz, E.; Willner, I. Nanoparticle Arrays on Surfaces for Electronic, Optical, and Sensor Applications. *ChemPhysChem* **2000**, *1*, 18−52.

(9) Saha, K.; Agasti, S. S.; Kim, C.; Li, X.; Rotello, V. M. Gold Nanoparticles in Chemical and Biological Sensing. *Chem. Rev.* **2012**, *112*, 2739−2779.

(10) Talapin, D. V.; Murray, C. B. PbSe Nanocrystal Solids for *n*- and *p*-Channel Thin Film Field-Effect Transistors. *Science* **2005**, *310*, 86−89.

(11) Zhao, W.; Rovere, T.; Weerawarne, D.; Osterhoudt, G.; Kang, N.; Joseph, P.; Luo, J.; Shim, B.; Poliks, M.; Zhong, C.-J. Nanoalloy Printed and Pulse-Laser Sintered Flexible Sensor Devices with Enhanced Stability and Materials Compatibility. *ACS Nano* **2015**, *9*, 6168−6177.

(12) Chen, H.-S.; Hsu, C.-K.; Hong, H.-Y. InGaN-CdSe-ZnSe Quantum Dots White LEDs. *IEEE Photonics Technol. Lett.* **2006**, *18*, 193−195.

(13) Chen, H.-S.; Yeh, D.-M.; Lu, C.-F.; Huang, C.-F.; Shiao, W.-Y.; Huang, C. C.; Jian-Jang amd Yang; Liu, I.-S.; Su, W.-F. White Light Generation with CdSe-ZnS Nanocrystals Coated on an InGaN-GaN Quantum-Well Blue/Green Two-Wavelength Light-Emitting Diode. *IEEE Photonics Technol. Lett.* **2006**, *18*, 1430−1432.

(14) Achermann, M.; Petruska, M. A.; Koleske, D. D.; Crawford, M. H.; Klimov, V. I. Nanocrystal-Based Light-Emitting Diodes Utilizing High-Efficiency Nonradiative Energy Transfer for Color Conversion. *Nano Lett.* **2006**, *6*, 1396−1400.

(15) Korgel, B. A.; Fitzmaurice, D. Condensation of Ordered Nanocrystal Thin Films. *Phys. Rev. Lett.* **1998**, *80*, 3531−3534.

(16) Brust, M.; Walker, M.; Bethell, D.; Schiffrin, D. J.; Whyman, R. Synthesis of Thiol-Derivatised Gold Nanoparticles in a Two-Phase Liquid−Liquid System. *J. Chem. Soc., Chem. Commun.* **1994**, *0*, 801−802.

(17) Puntes, V. F.; Krishnan, K. M.; Alivisatos, A. P. Colloidal Nanocrystal Shape and Size Control: The Case of Cobalt. *Science* **2001**, *291*, 2115−2117.

(18) Napper, D. Steric Stabilization. *J. Colloid Interface Sci.* **1977**, *58*, 390−407.

(19) Sigman, M. B.; Saunders, A. E.; Korgel, B. A. Metal Nanocrystal Superlattice Nucleation and Growth. *Langmuir* **2004**, *20*, 978−983.

(20) Bodnarchuk, M. I.; Kovalenko, M. V.; Heiss, W.; Talapin, D. V. Energetic and Entropic Contributions to Self-Assembly of Binary Nanocrystal Superlattices: Temperature as the Structure-Directing Factor. *J. Am. Chem. Soc.* **2010**, *132*, 11967−11977.

(21) Schapotschnikow, P.; Pool, R.; Vlugt, T. J. H. Molecular Simulations of Interacting Nanocrystals. *Nano Lett.* **2008**, *8*, 2930−2934.

(22) Patel, N.; Egorov, S. A. Interactions between Sterically Stabilized Nanoparticles in Supercritical Fluids: A Simulation Study. *J. Chem. Phys.* **2007**, *126*, 054706.

(23) Khan, S. J.; Pierce, F.; Sorensen, C. M.; Chakrabarti, A. Self-Assembly of Ligated Gold Nanoparticles: Phenomenological Modeling and Computer Simulations. *Langmuir* **2009**, *25*, 13861−13868.

(24) Dalmaschio, C. J.; da Silveira Firmiano, E. G.; Pinheiro, A. N.; Sobrinho, D. G.; Farias de Moura, A.; Leite, E. R. Nanocrystals Self-Assembled in Superlattices Directed by the Solvent-Organic Capping Interaction. *Nanoscale* **2013**, *5*, 5602−10.
(25) Widmer-Cooper, A.; Geissler, P. Orientational Ordering of Passivating Ligands on CdS Nanorods in Solution Generates Strong Rod-Rod Interactions. *Nano Lett.* **2014**, *14*, 57−65.
(26) de Moura, F.; Bernardino, K.; Dalmaschio, C. J.; Leite, E. R.; Kotov, N. A. Thermodynamic Insights into the Self-Assembly of Capped Nanoparticles Using Molecular Dynamic. *Phys. Chem. Chem. Phys.* **2015**, *17*, 3820−3831.
(27) Talapin, D. V.; Shevchenko, E. V.; Kornowski, A.; Gaponik, N.; Haase, M.; Rogach, A. L.; Weller, H. A New Approach to Crystallization of CdSe Nanoparticles into Ordered Three-Dimensional Superlattices. *Adv. Mater.* **2001**, *13*, 1868.
(28) Abécassis, B.; Testard, F.; Spalla, O. Gold Nanoparticle Superlattice Crystallization Probed *In Situ*. *Phys. Rev. Lett.* **2008**, *100*, 115504.
(29) Khan, S. J.; Sorensen, C. M.; Chakrabarti, A. Computer Simulations of Nucleation of Nanoparticle Superclusters from Solution. *Langmuir* **2012**, *28*, 5570−5579.
(30) Kister, T.; Monego, D.; Mulvaney, P.; Widmer-Cooper, A.; Kraus, T. Colloidal Stability of Apolar Nanoparticles: The Role of Particle Size and Ligand Shell Structure. *ACS Nano* **2018**, *12*, 5969−5977.
(31) Monego, D.; Kister, T.; Kirkwood, N.; Mulvaney, P.; Widmer-Cooper, A.; Kraus, T. Colloidal Stability of Apolar Nanoparticles: Role of Ligand Length. *Langmuir* **2018**, *34*, 12982−12989.
(32) Lohman, B. C.; Powell, J. A.; Cingarapu, S.; Aakeroy, C. B.; Chakrabarti, A.; Klabunde, K. J.; Law, B. M.; Sorensen, C. M. Solubility of Gold Nanoparticles as a Function of Ligand Shell and Alkane Solvent. *Phys. Chem. Chem. Phys.* **2012**, *14*, 6509−6513.
(33) Hajiw, S.; Schmitt, J.; Imperor-Clerc, M.; Pansu, B. Solvent-Driven Interactions between Hydrophobically-Coated Nanoparticles. *Soft Matter* **2015**, *11*, 3920−3926.
(34) de Gennes, P. G. Conformations of Polymers Attached to an Interface. *Macromolecules* **1980**, *13*, 1069−1075.
(35) Koski, J. P.; Krook, N. M.; Ford, J.; Yahata, Y.; Ohno, K.; Murray, C. B.; Frischknecht, A. L.; Composto, R. J.; Riggleman, R. A. Phase Behavior of Grafted Polymer Nanocomposites from Field-Based Simulations. *Macromolecules* **2019**, *52*, 5110−5121.
(36) Sunday, D.; Ilavsky, J.; Green, D. L. A Phase Diagram for Polymer-Grafted Nanoparticles in Homopolymer Matrices. *Macromolecules* **2012**, *45*, 4007−4011.
(37) Sunday, D. F.; Green, D. L. Thermal and Rheological Behavior of Polymer Grafted Nanoparticles. *Macromolecules* **2015**, *48*, 8651−8659.
(38) Zou, Y.; Ban, M.; Cui, W.; Huang, Q.; Wu, C.; Liu, J.; Wu, H.; Song, T.; Sun, B. A General Solvent Selection Strategy for Solution Processed Quantum Dots Targeting High Performance Light-Emitting Diode. *Adv. Funct. Mater.* **2017**, *27*, 1603325.
(39) Fini, P.; Depalo, N.; Comparelli, R.; Curri, M. L.; Striccoli, M.; Castagnolo, M.; Agostiano, A. Interactions between Surfactant Capped CdS Nanocrystals and Organic Solvent. *J. Therm. Anal. Calorim.* **2008**, *92*, 271−277.
(40) Widmer-Cooper, A.; Geissler, P. L. Ligand-Mediated Interactions between Nanoscale Surfaces Depend Sensitively and Nonlinearly on Temperature, Facet Dimensions, and Ligand Coverage. *ACS Nano* **2016**, *10*, 1877−87.
(41) Johnson, J. E. X-Ray Diffraction Studies of the Crystallinity in Polyethylene Terephthalate. *J. Appl. Polym. Sci.* **1959**, *2*, 205−209.
(42) Brandrup, J.; Immergut, E. H.; Grulke, E. A. *Polymer Handbook*; Wiley-Interscience: New York, 1999; p 2250.
(43) Roke, S.; Berg, O.; Buitenhuis, J.; van Blaaderen, A.; Bonn, M. Surface Molecular View of Colloidal Gelation. *Proc. Natl. Acad. Sci. U. S. A.* **2006**, *103*, 13310−13314.
(44) Waltmann, C.; Horst, N.; Travesset, A. Potential of Mean Force for Two Nanocrystals: Core Geometry and Size, Hydrocarbon Unsaturation, and Universality with Respect to the Force Field. *J. Chem. Phys.* **2018**, *149*, 034109.
(45) Costa, J.; Mendes, A.; Santos, L. Chain Length Dependence of the Thermodynamic Properties of *n*-Alkanes and their Monosubstituted Derivatives. *J. Chem. Eng. Data* **2018**, *63*, 1.
(46) De Roo, J.; Yazdani, N.; Drijvers, E.; Lauria, A.; Maes, J.; Owen, J. S.; Van Driessche, I.; Niederberger, M.; Wood, V.; Martins, J. C.; Infante, I.; Hens, Z. Probing Solvent-Ligand Interactions in Colloidal Nanocrystals by the NMR Line Broadening. *Chem. Mater.* **2018**, *30*, 5485−5492.
(47) Ruks, T.; Beuck, C.; Schaller, T.; Niemeyer, F.; Zähres, M.; Loza, K.; Heggen, M.; Hagemann, U.; Mayer, C.; Bayer, P.; Epple, M. Solution NMR Spectroscopy with Isotope-Labeled Cysteine (13C and 15N) Reveals the Surface Structure of l-Cysteine-Coated Ultrasmall Gold Nanoparticles (1.8 nm). *Langmuir* **2019**, *35*, 767−778.
(48) Luo, Z.; Marson, D.; Ong, Q. K.; Loiudice, A.; Kohlbrecher, J.; Radulescu, A.; Krause-Heuer, A.; Darwish, T.; Balog, S.; Buonsanti, R.; Svergun, D. I.; Posocco, P.; Stellacci, F. Quantitative 3D Determination of Self-Assembled Structures on Nanoparticles Using Small Angle Neutron Scattering. *Nat. Commun.* **2018**, *9*, 1343.
(49) Lane, J. M. D.; Grest, G. S. Spontaneous Asymmetry of Coated Spherical Nanoparticles in Solution and at Liquid-Vapor Interfaces. *Phys. Rev. Lett.* **2010**, *104*, 235501.
(50) Bolintineanu, D. S.; Lane, J. M. D.; Grest, G. S. Effects of Functional Groups and Ionization on the Structure of Alkanethiol-Coated Gold Nanoparticles. *Langmuir* **2014**, *30*, 11075−11085.
(51) Kister, T.; Mravlak, M.; Schilling, T.; Kraus, T. Pressure-Controlled Formation of Crystalline, Janus, and Core-Shell Supraparticles. *Nanoscale* **2016**, *8*, 13377−13384.
(52) Chambrier, I.; Banerjee, C.; Remiro-Buenamañana, S.; Chao, Y.; Cammidge, A. N.; Bochmann, M. Synthesis of Porphyrin-CdSe Quantum Dot Assemblies: Controlling Ligand Binding by Substituent Effects. *Inorg. Chem.* **2015**, *54*, 7368−7380.
(53) Schnablegger, H.; Singh, Y. *The SAXS Guide: Getting Acquainted with the Principles*; Anton Paar GmbH: Graz, Austria, 2013; Vol. 2.
(54) Andersen, H. C. Rattle: A "Velocity" Version of the Shake Algorithm for Molecular Dynamics Calculations. *J. Comput. Phys.* **1983**, *52*, 24−34.
(55) Pool, R.; Schapotschnikow, P.; Vlugt, T. J. H. Solvent Effects in the Adsorption of Alkyl Thiols on Gold Structures: A Molecular Simulation Study. *J. Phys. Chem. C* **2007**, *111*, 10201−10212.
(56) Martin, M. G.; Siepmann, J. I. Transferable Potentials for Phase Equilibria. 1. United-Atom Description of *n*-Alkanes. *J. Phys. Chem. B* **1998**, *102*, 2569−2577.
(57) Plimpton, S. Fast Parallel Algorithms for Short-Range Molecular Dynamics. *J. Comput. Phys.* **1995**, *117*, 1−19.
(58) Humphrey, W.; Dalke, A.; Schulten, K. VMD: Visual Molecular Dynamics. *J. Mol. Graphics* **1996**, *14*, 33−38.
(59) Hamaker, H. C. The London-van der Waals Attraction between Spherical Particles. *Physica* **1937**, *4*, 1058−1072.
(60) Ederth, T. Computation of Lifshitz-van der Waals Forces between Alkylthiol Monolayers on Gold Films. *Langmuir* **2001**, *17*, 3329−3340.
(61) Suárez, E.; Díaz, N.; Méndez, J.; Suárez, D. CENCALC: A Computational Tool for Conformational Entropy Calculations from Molecular Simulations. *J. Comput. Chem.* **2013**, *34*, 2041−2054.
(62) Suárez, E.; Díaz, N.; Suárez, D. Entropy Calculations of Single Molecules by Combining the Rigid−Rotor and Harmonic-Oscillator Approximations with Conformational Entropy Estimations from Molecular Dynamics Simulations. *J. Chem. Theory Comput.* **2011**, *7*, 2638−2653.

https://dx.doi.org/10.1021/acsnano.9b03552
ACS Nano 2020, 14, 5278−5287

When Like Destabilizes Like: Inverted Solvent Effects in Apolar Nanoparticle Dispersions

Debora Monego,[†,‡] Thomas Kister,[¶] Nicholas Kirkwood,[§] David Doblas,[¶] Paul Mulvaney,[§] Tobias Kraus,[¶,‖] and Asaph Widmer-Cooper[*,†,‡]

†*ARC Centre of Excellence in Exciton Science, School of Chemistry, The University of Sydney, NSW 2006, Australia*

‡*The University of Sydney Nano Institute, The University of Sydney, NSW 2006, Australia*

¶*INM — Leibniz Institute for New Materials, Campus D2 2, 66123 Saarbrücken, Germany*

§*ARC Centre of Excellence in Exciton Science, School of Chemistry, University of Melbourne, Parkville, Victoria 3010, Australia*

‖*Colloid and Interface Chemistry, Saarland University, Campus D2 2, 66123 Saarbrücken, Germany*

E-mail: asaph.widmer-cooper@sydney.edu.au

Figure 1 shows the scattering curves of AuNPs and the structure factor contributions during a cooling cycle. The development of the first peak in the structure factor indicates the agglomeration of the nanoparticles.

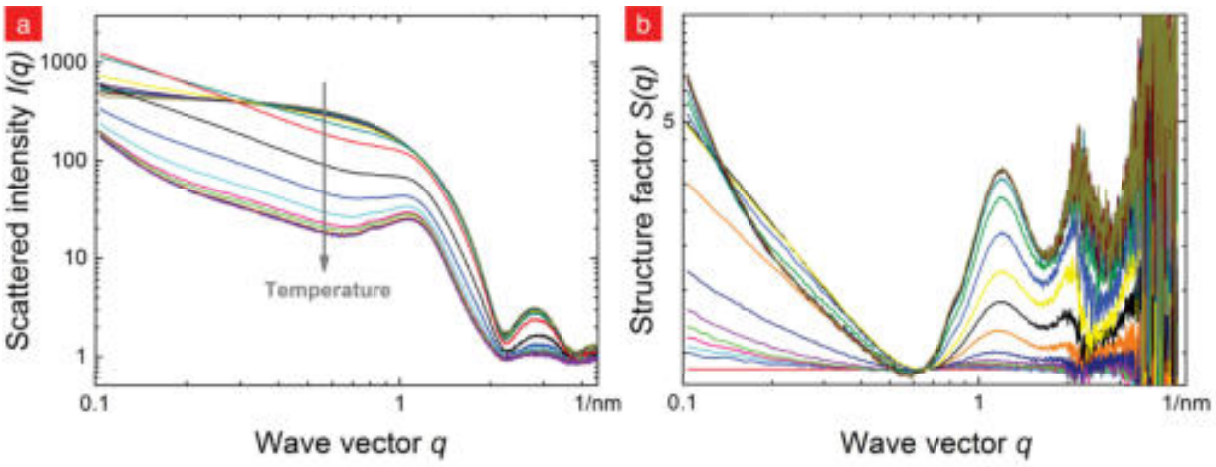

Figure 1: Temperature-dependent scattering of 4 nm Au nanoparticles. a) Raw data. b) The calculated structure factors. The peaks increase upon cooling.

The trend observed for the agglomeration temperature when changing the length of the alkane in which they are dispersed is the same for particles with a larger core diameter: Au particles of 7.5 nm in diameter coated with hexadecanethiol ligands (Figure 2).

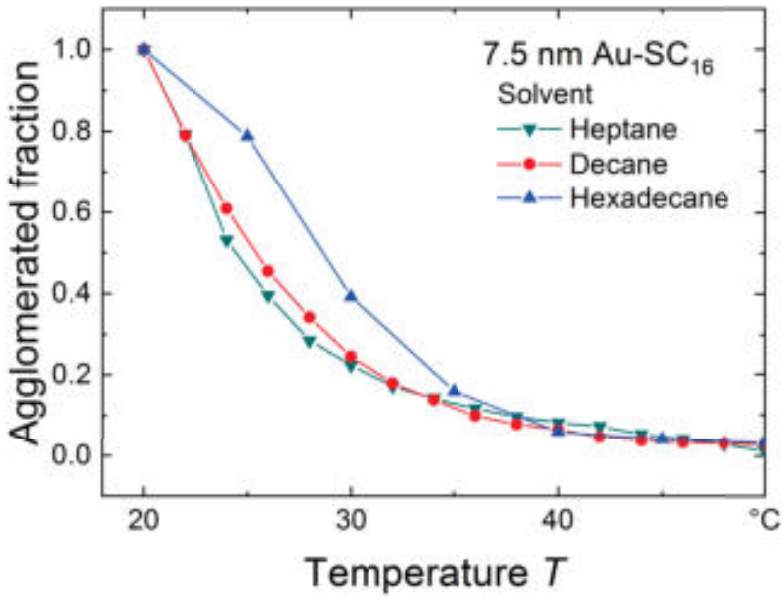

Figure 2: Fraction of agglomerated 7.5 nm Au−SC_{16} particles as determined by *in situ* small-angle X-ray scattering.

Table 1 shows the solubility parameters, from both Hildebrand and Hansen theories, for the solvents studied here.

Table 1: Hildebrand and Hansen solubility parameters for the solvents studied here and the ligand-solvent interaction Flory parameter (χ), calculated as per Equation 1. Solubility parameters for the ligands were approximated by the ones of the unthiolated alkane.

Ligand		Solvent					Flory Parameter
	Hildebrand Parameter $(Pa^{1/2})$[1]		Hildebrand Parameter $(Pa^{1/2})$[1]	Hansen Parameter[1] dispersion	dipolar	H_{bond}	
SC_{16}	16400	Hexane	14100	14100	0	0	0.62
		Decane	15800	15800	0	0	0.37
		Hexadecane	16400	16400	0	0	0.34
		Cyclohexane	16800	16800	0	200	0.35
SC_{18}	17100	Hexane	14100	14100	0	0	0.82
		Decane	15800	15800	0	0	0.47
		Hexadecane	16400	16400	0	0	0.40
		Cyclohexane	16800	16800	0	200	0.34

Figure 3 shows snapshots of our MD simulations of CdSeNPs at temperatures around the experimental agglomeration temperature T_{agglo} in alkane solvents with different chain lengths. Similarly to what is observed for AuNPs, the ligands go through a disorder-order transition when the temperature is decreased. This is responsible for changing the overall interaction between the ligand shells, switching the total interaction potential between nanoparticles from repulsive to attractive, as can be seen in Figure 5.

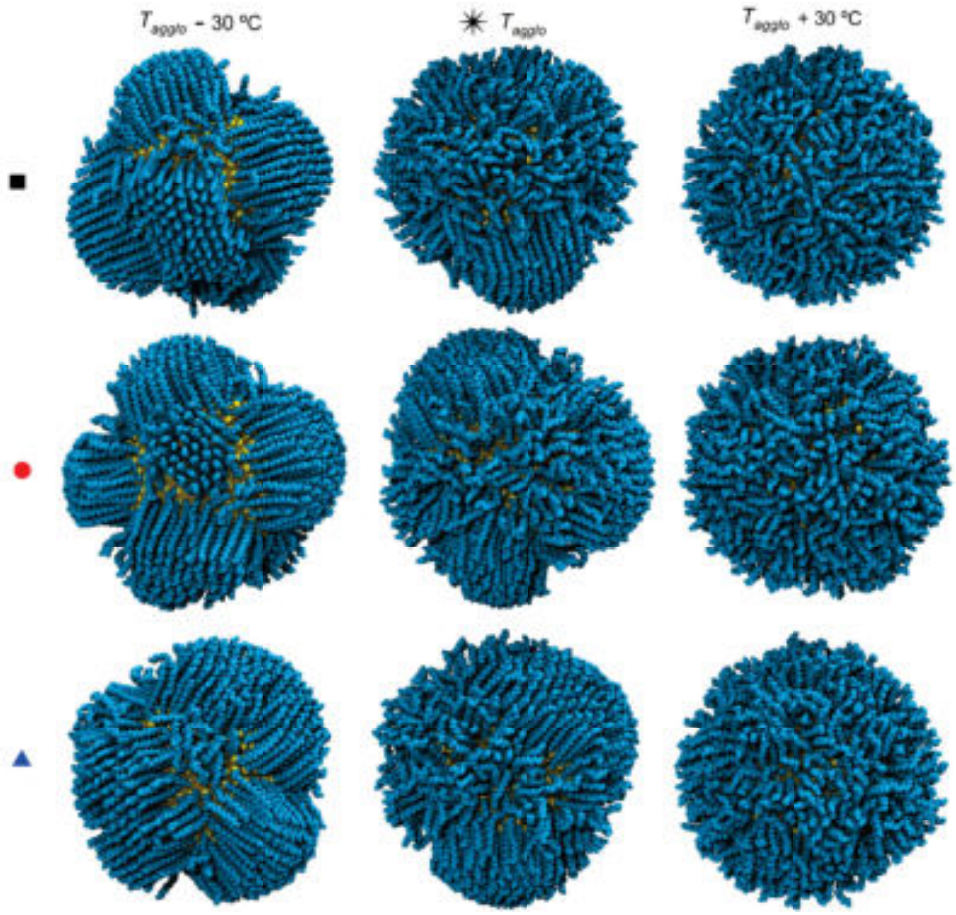

Figure 3: Simulation snapshots of 5.8 nm CdSe−SC_{18} particles at the experimental $T_{agglo} \pm 30\,°C$ in hexane (square), decane (circle), and hexadecane (triangle). Solvent molecules have been hidden for clarity.

Figure 4 shows snapshots and radial distribution functions for 4 nm Au−SC_{16} particles in cyclohexane. The ligands order when the temperature is decreased in a similar way to when the particles are dispersed in linear alkanes.

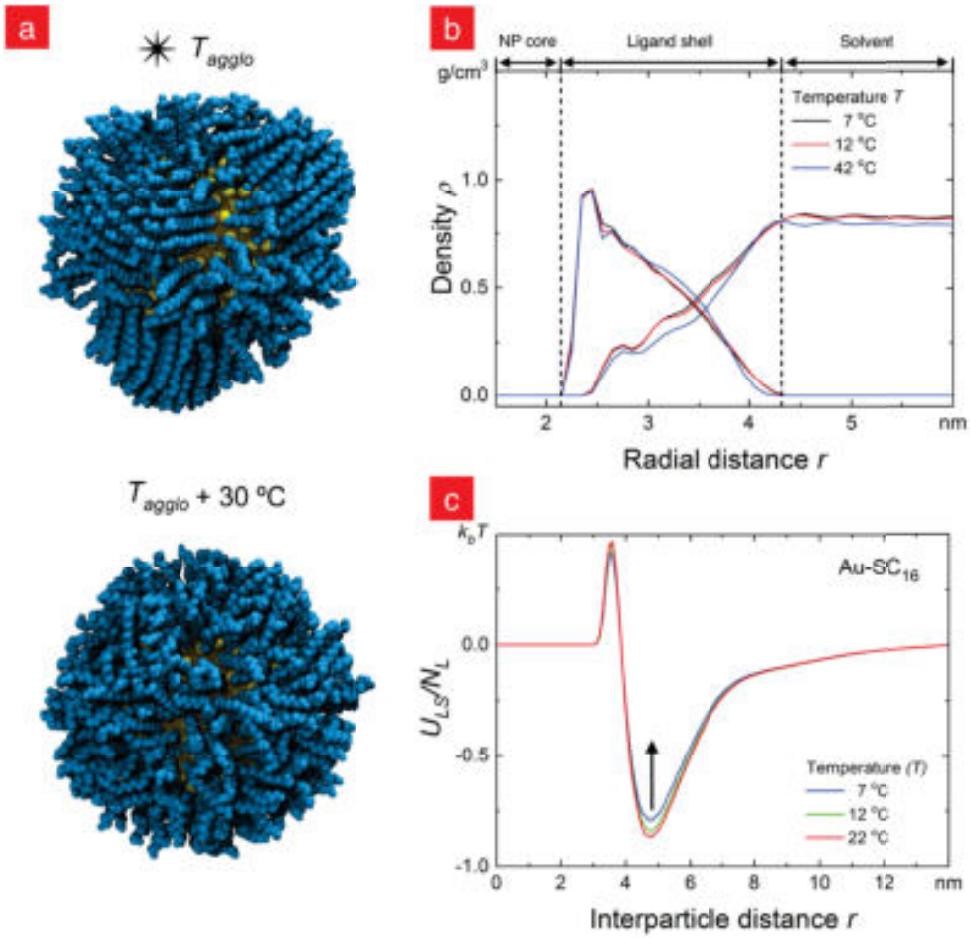

Figure 4: 4 nm Au−SC_{16} particles in cyclohexane: (a) Simulation snapshots at the experimental T_{agglo} and T_{agglo} + 30 °C. Solvent molecules have been hidden for clarity. (b) Radial density distributions for the ligand and solvent molecules as a function of the distance r from the center of the nanoparticle core at (red) and above (blue) T_{agglo}. (c) Contribution to the total ligand-solvent interaction energy as a function of distance between pairs of interacting CH_x groups. Energies are normalized by the number of ligand molecules on the nanoparticle N_L.

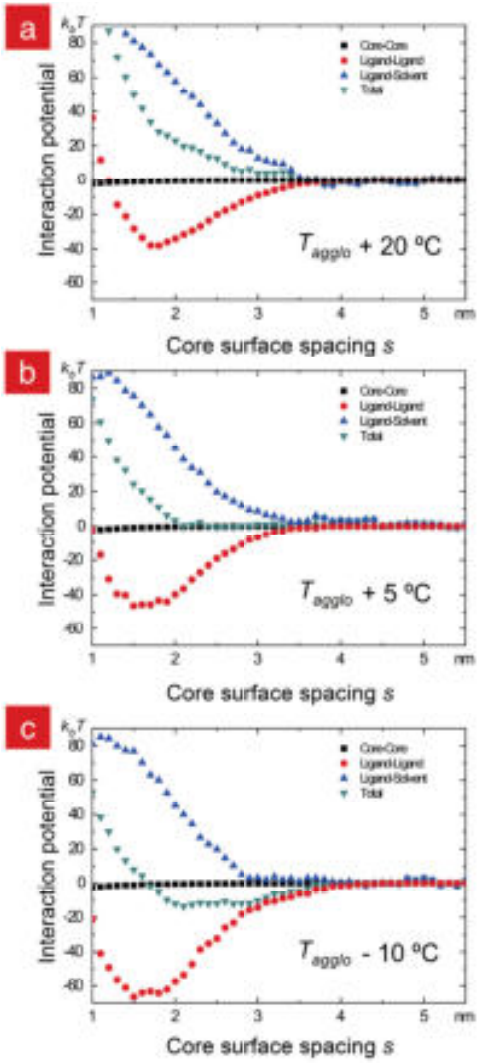

Figure 5: Components of the Potential of Mean Force (PMF) obtained from constrained molecular dynamics simulations for pairs of 4 nm Au−SC_{16} particles in hexane at temperatures around the experimental T_{agglo}. The total potential is green, the ligand-ligand contribution is red, the ligand-solvent contribution is blue, and the core-core contribution is black.

Figure 6 shows the total number of pair interactions between ligand CH_x groups as a function of the separation between them, the solvent and the temperature. The temperature at which the ligands order (T_{order}) differs between solvents, but the average structure of the ligand shell is virtually the same in all solvents when the temperature is expressed relative to T_{order}. Radial density distributions for the ligand and solvent molecules surrounding the

particles are shown in Figure 7.

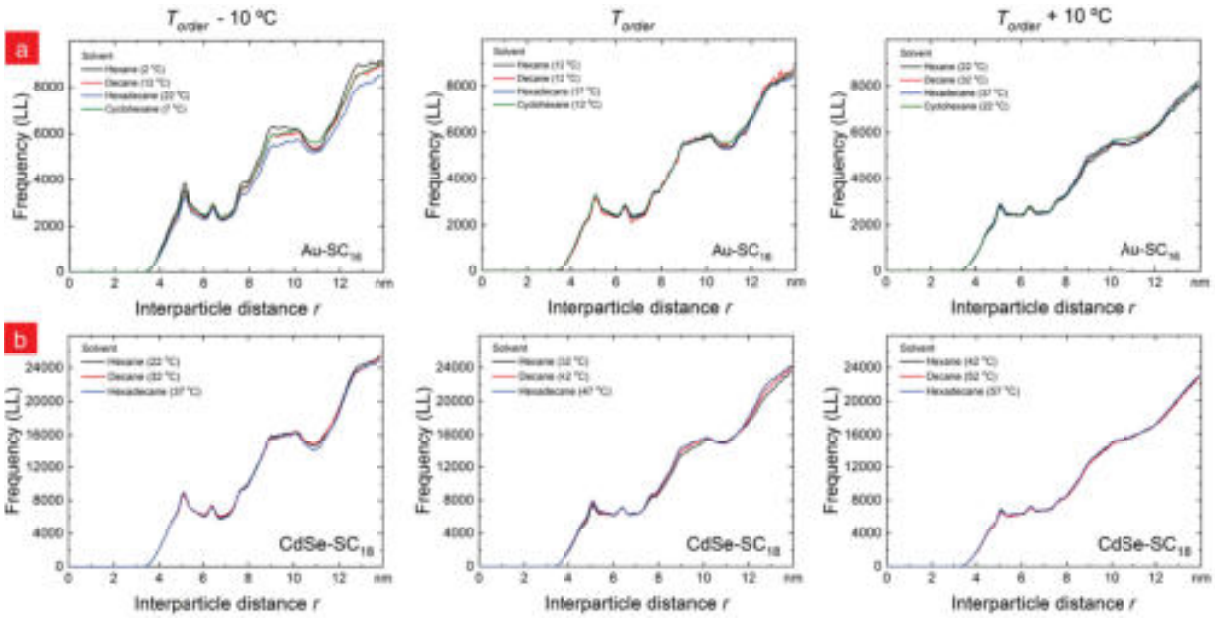

Figure 6: The number of ligand-ligand CH_x-CH_x interactions as a function of the distance between them for (a) 4 nm $Au-SC_{16}$ and (b) 5.8 nm $CdSe-SC_{18}$ particles shows that the ligands order similarly in all solvents for the same temperature relative to the ordering transition.

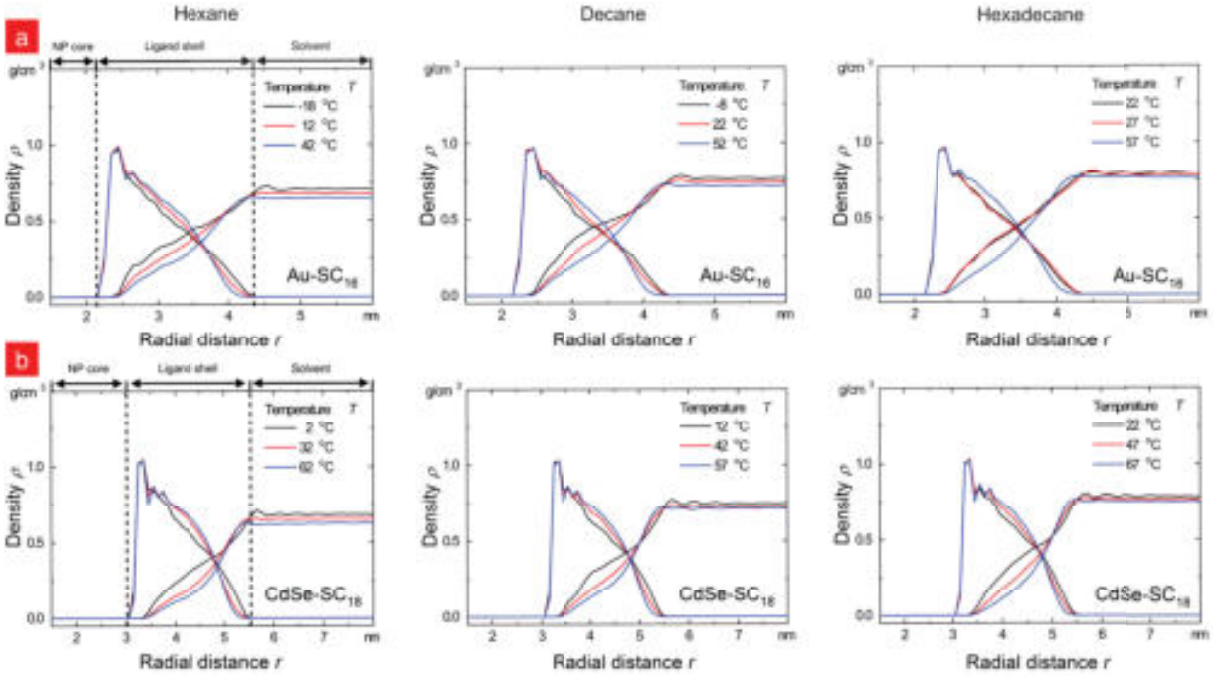

Figure 7: Radial density distributions for the ligand and solvent molecules for Au and CdSe NP in different alkane solvents and temperatures, plotted as a function of the distance r from the center of the nanoparticle core. The red lines indicate the density profile at the ligand ordering temperature T_{order}. In all cases, the radially averaged solvent density within the ligand shell increases upon cooling.

Figure 8 shows the contribution to the ligand-solvent interaction energy as a function of the distance between CH_x groups. Energies are normalized by the number of ligands on the nanoparticle: 280 ligands for AuNP, and 580 ligands for CdSeNP.

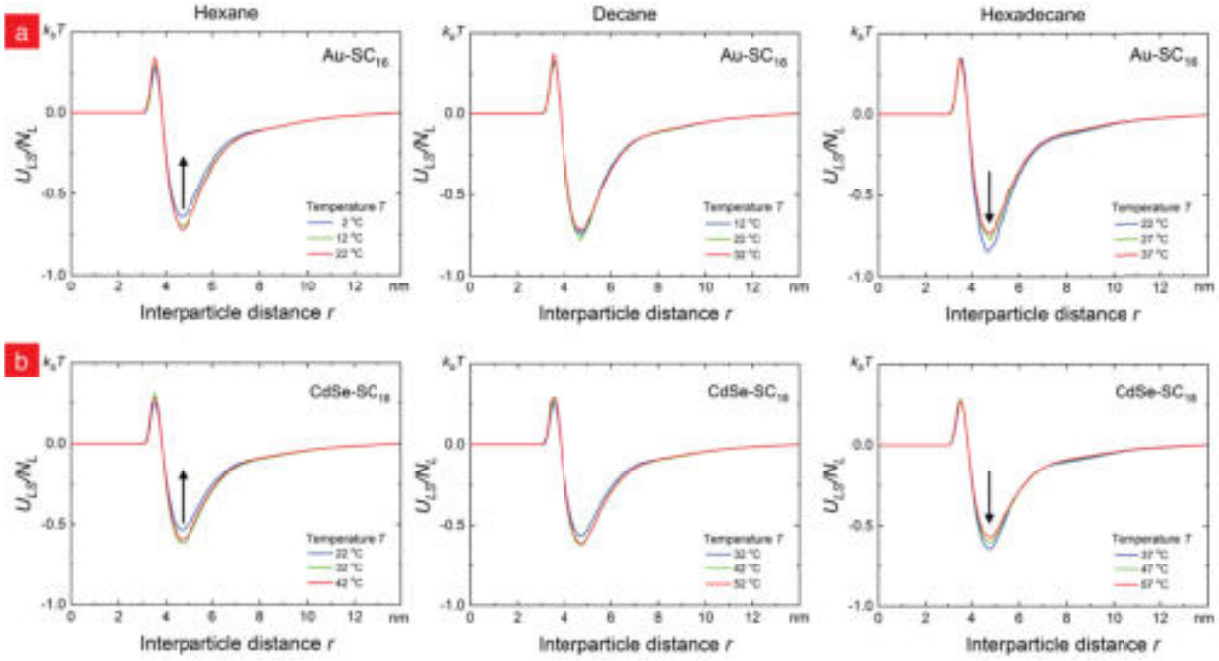

Figure 8: Contribution to the ligand-solvent interaction energy as a function of distance between pairs of interacting CH_x groups for (a) 4 nm Au−SC_{16} and (b) 5.8 nm CdSe−SC_{18} particles in different solvents. For longer alkanes, there is an increase in the number of ligand and solvent atoms that are close to one another upon cooling. All energies are normalized by the number of ligand molecules on the nanoparticle N_L.

The average dihedral angle of the solvent molecules (Figure 9 for CdSeNPs) was calculated separately for two regions of the simulation cell: (i) within the spherical ligand shell, *i.e.* the region where the radially averaged ligand density is nonzero; and (ii) a region sufficiently far from the nanoparticle that the solvent molecules behave as bulk solvent.

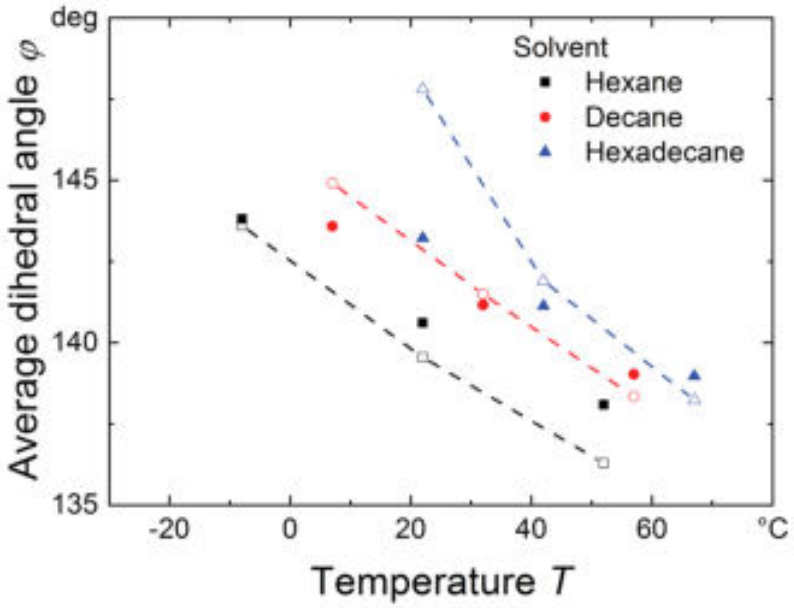

Figure 9: Average dihedral angle of solvent molecules that are in the bulk region (closed symbols) and within the 1-octadecanethiol ligand shell (open symbols) covering 5.8 nm CdSeNP.

Table 2: Parameters used for analytical calculations of the entropies of mixing using equations 1 and 2.

parameter	value
ligand surface coverage	5.5 ligands nm^{-2}
ligand length L for hexadecanethiol	2.28 nm
ligand length L for octadecanethiol	2.54 nm
volume ligand molecule ν_L for hexadecanethiol	0.550 nm^3
volume ligand molecule ν_L for octadecanethiol	0.616 nm^3
volume solvent molecule ν_S for hexane	0.215 nm^3
volume solvent molecule ν_S for decane	0.324 nm^3
volume solvent molecule ν_S for hexadecane	0.487 nm^3

References

1. Brandrup, J.; Immergut, E. H.; Grulke, E. A. *Polymer Handbook*; Wiley-Interscience: New York, 1999; p 2250.

3.4 Publication 4

Doblas, D., Kister, T., Cano-Bonilla, M., González-García, L., & Kraus, T. (2019). Colloidal solubility and agglomeration of apolar nanoparticles in different solvents. Nano Letters, 19(8), 5246-5252.

DOI: 10.1021/acs.nanolett.9b01688

NANO LETTERS
Cite This: Nano Lett. 2019, 19, 5246−5252
Letter
pubs.acs.org/NanoLett

Colloidal Solubility and Agglomeration of Apolar Nanoparticles in Different Solvents

David Doblas,[†] Thomas Kister,[†] Marina Cano-Bonilla,[†] Lola González-García,[†] and Tobias Kraus*[,†,‡]

[†]INM − Leibniz-Institute for New Materials, Campus D2 2, 66123 Saarbrücken, Germany
[‡]Colloid and Interface Chemistry, Saarland University, 66123 Saarbrücken, Germany

Supporting Information

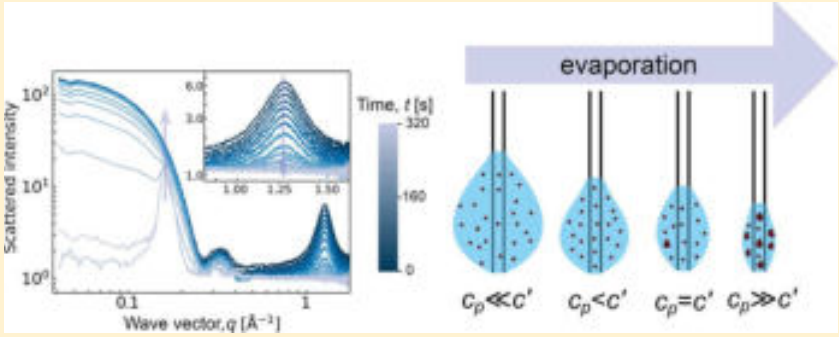

ABSTRACT: We studied the concentration-dependent agglomeration of apolar nanoparticles in different solvents. Octanethiol-stabilized gold nanoparticles (AuNPs) in evaporating liquid droplets were observed *in situ* using small-angle X-ray scattering. Concurrent analysis of liquid volume and particle agglomeration provided time-dependent absolute concentrations of free and agglomerated particles. All dispersions underwent an initial stage where the particle concentration increased but no agglomerates formed. Subsequently, agglomeration started at concentrations that varied by several orders of magnitude for different solvents. While agglomerates grew, the concentration of the dispersed particles remained at a constant "colloidal solubility" in most solvents. We consistently found that the colloidal stability of AuNPs decreased as cyclohexane > heptane > nonane > decane > toluene and suggest that details of the molecular interactions between solvent and ligand shell set this order.

KEYWORDS: *Nanoparticle stability, apolar, nanoparticles, self-assembly, colloidal stability, agglomeration, gold*

Inorganic nanoparticles with apolar organic ligands are common in technology and research, but remarkably little is known on their concentration-dependent colloidal stability. Whereas the molecular solubilities of all important industrial chemicals are known, the maximal concentrations of apolar nanoparticles that can be reached without agglomeration are not. One reason for this gap is that the particles are synthesized at low concentrations to better control average size and size distribution.[1] Another reason is the technical difficulty of working with nanoparticles at high concentrations: Concentrated dispersions tend to coat the inner surfaces of vessels. As a consequence, not only is it unknown how solvent structure affects nanoparticle dispersion stability, it is also unclear whether colloidal stability is so different from the properties of molecular solutions that the term "solubility" is misleading.

This is a technically relevant question. Many production processes that involve apolar nanoparticles are affected by the onset of agglomeration. When printing conductive structures via inkjet, imprint, or dip-pen techniques, agglomeration affects the maximal resolution and the conductivity of the resulting structures.[2] Optical nanocomposites rely on uniform particle distributions that provide optical homogeneity; agglomerates cause scattering and reduce transparency.[3] Quantum dot-enhanced displays and sensors require uniform particle distributions in polymer films; premature particle agglomeration compromises their quality.[4] Future production processes that use self-assembly to define functional structures in materials will have to ensure that assembly occurs at a suitable stage.[5] It is necessary, therefore, to predict when agglomeration sets in.

The concentration-dependent stability of charge-stabilized, polar nanoparticles is well-established, with DLVO theory providing a reliable theoretical framework for its prediction.[6] Electrostatic repulsion is comparatively long-ranged, so that the distances between the particles' surfaces are large at the relevant maximal concentrations, and the exact molecular

Received: April 24, 2019
Revised: June 19, 2019
Published: June 28, 2019

DOI: 10.1021/acs.nanolett.9b01688
Nano Lett. 2019, 19, 5246−5252

configurations are less important. The interactions of apolar nanoparticles are weaker (see ref 7 for a comprehensive review), and recent research suggests that molecular details such as the mobilities of ligand shells strongly affect their stability.[8−11]

It is not yet possible to predict the stability of such nanoparticles using molecular dynamics simulations because the required systems scale by $O(n^2)$, where n is the number of atoms, if all pairwise electrostatic and van der Waals interactions must be accounted for explicitly.[12]

A common procedure to measure the saturation concentration of apolar molecules is to prepare a mixture that contains a sediment, remove some of the supernatant, and measure its concentration. Analogous procedures have been used to estimate the concentration-dependent stability of nanoparticles.[11] It is difficult to ensure that there are no agglomerates contained in the supernatant, however, and the method does not allow the operator to follow agglomeration above the concentration in the supernatant. Using this method implies that the nanoparticle stability is close to an ideal solubility, which is not known *a priori*.

We propose a different route that is based on the quantification of the agglomeration of apolar dispersions during slow evaporation and concurrent concentration measurements. Similar concepts have been applied to study nanoparticle self-assembly: Agthe et al. followed the arrangement of iron oxide nanocubes during solvent evaporation by time-resolved small-angle X-ray scattering (SAXS) and analyzed the assembled structure using *ex situ* electron microscopy (EM).[13] Their objective was to follow the formation of mesocrystals as a route to new materials.[14] Sen and co-workers used scanning SAXS with a focused X-ray beam to measure the distribution of assembling SM 30 LUDOX nanoparticles in water during evaporation.[15] None of them provided time-dependent, absolute particle concentrations.

In order to precisely measure particle concentration and agglomerate fraction, we illuminated a hanging dispersion droplet with a relatively wide X-ray beam (4.8 mm^2) to capture the entire volume, avoid the risk of radiation damage that is posed by the micron-sized beams of synchrotrons,[16] and obtain a sufficient signal-to-noise ratio by integrating over the entire droplet. We used a sample-to-detector (SDD) distance that simultaneously gave access to scattering from the apolar solvent,[17] the particles, and their superstructures. Careful analysis of the scattering signals provided reproducible values for solvent content, the concentration of dispersed particles, and the agglomerate fraction. We used the values to compare particle stability to classical solubility models and found that the dispersion can be likened to a molecular solution only for certain solvents.

Figure 1 illustrates the setup that was used to create hanging droplets with a reproducible volume of 2.5 μL in the beam path of a SAXS laboratory machine. We used different solvents that contained nanoparticles composed of 3.4 nm diameter gold cores covered with a octanethiol ligand shell at a density of 5.9 nm^{-2} ("AuNPs"). A 50 μm diameter fused silica capillary with a blunt end was connected to a syringe pump, and a droplet with a diameter of 1.7 mm was formed. The droplet enclosed the capillary (Figure 1a) and remained attached to it during the entire experiment. A scan was used to center the droplet in the 4.8 mm^2 cross-section of the X-ray beam. Two-dimensional scattering patterns from the droplet were recorded

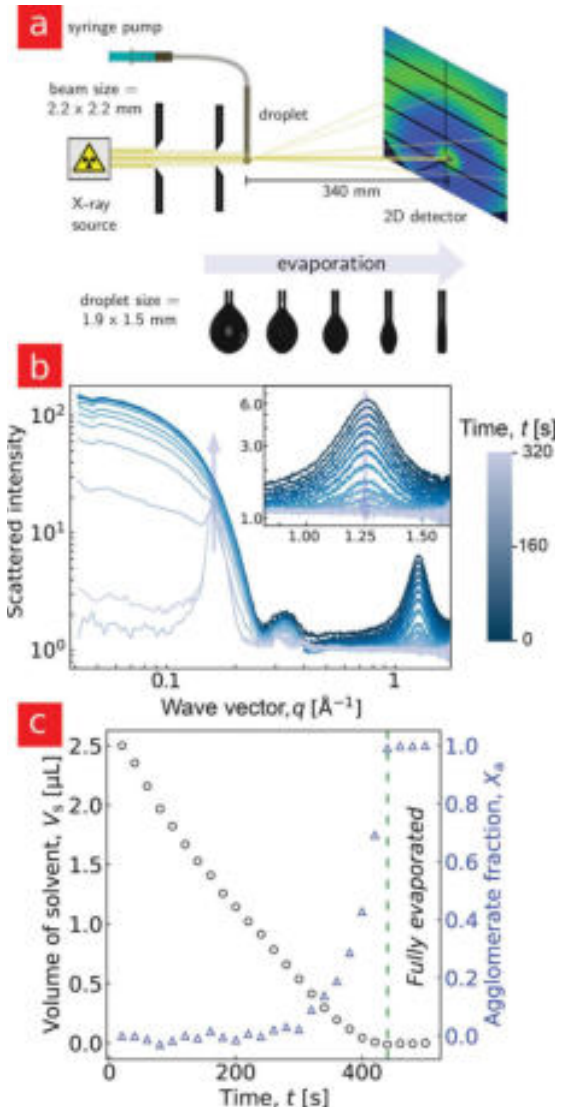

Figure 1. (a) Setup for scattering experiments on an evaporating droplet of suspension with photographs of a droplet of cyclohexane containing AuNPs. (b) *In situ* SAXS from the evaporating dispersion with peaks originating from the solvent, the dispersed particles, and their agglomerates. Inset: Evolution of the solvent peak. (c) Volume of solvent in the evaporating droplet calculated from the solvent peak area (left vertical axis, open circles) and fraction of agglomerated particles calculated from its structure peak (right vertical axis, open triangles).

at a SDD of 340 mm with a two-dimensional (2D) solid-state detector.

Droplets containing AuNPs in different organic solvents were left to evaporate until all scattering from the solvent had vanished after 5−15 min, depending on the solvent (Figure 1b). The surrounding air was kept at a temperature of 20 °C and a humidity of 30%. Scattering patterns were recorded continuously, with 15−60 s integration time for individual measurements depending on the solvent.

We simultaneously obtained particle concentrations and agglomeration states directly from different parts of the scattering signal using the following procedure. All scattering

DOI: 10.1021/acs.nanolett.9b01688
Nano Lett. 2019, 19, 5246−5252

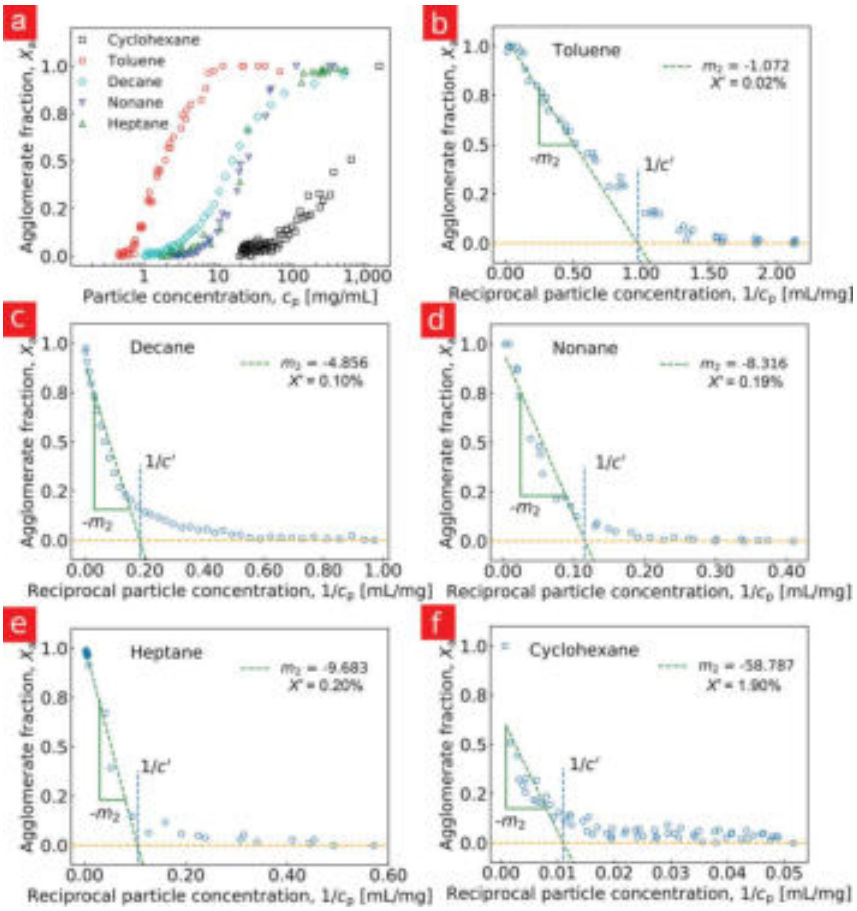

Figure 2. (a) Agglomerate fraction (X_a) of AuNPs dispersions in different solvents as a function of overall particle concentration c_p. The concentrations c' at which agglomeration occurred differed by orders of magnitude from the worst solvent (toluene) to the best (cyclohexane). (b–e) Agglomerate fractions X_a as a function of the reciprocal particle concentration $1/c_p$ for (b) toluene, (c) decane, (d) nonane, (e) heptane, and (f) cyclohexane. The concentration c_s of dispersed particle that coexisted with agglomerates ("colloidal solubility") was calculated from the slope m_2 of the agglomerate fraction in stage 2 (see text).

images were radially integrated and represented as a time series, as shown in Figure 1b for AuNPs in cyclohexane. The initial scattering at low wave vectors q (0.04–0.25 Å^{-1} in this example) was dominated by the form factor $F(q)$ of spheres, as expected for fully dispersed particles. At high q, the solvent scattering peak (1.25 Å^{-1} for cyclohexane)[17] appeared with an area proportional to the amount of solvent in the droplet. The scattering peak of the solvent and the structure factor peak of the agglomerated particles (see eq 1 below) were fitted with Lorentz functions to quantify the overall solvent volume and dispersed particle content.[18]

The decrease of solvent volume was almost linear in time during the entire evaporation procedure (Figure 1c), and the number of particles in the beam remained constant throughout the experiment. Given the known initial particle concentration, our procedure provides precise measurements of the particle concentration in the dispersion for each time step.

Evaporation led to a slow increase of particle concentration. The onset of agglomeration was clearly indicated by the emergence of structure peaks with a primary peak at 0.16 Å^{-1} (cf. Figure 1b).[19,20] We used a sphere model to fit the scattering pattern of the fully dispersed particles and obtained an average form factor $F'(q)$.[21] The effective structure factor, $S_{eff}(q)$, of the agglomerates, as defined in eq 1, was then calculated for each time step by dividing the total scattering patterns $I_{tot}(q)$ by the average form factor:[22]

$$S_{eff}(q) = \frac{I_{tot}(q)}{F'(q)} \quad (1)$$

We quantified the concentration of particles in the droplet $c(t)$ for every time step by comparing the areas of the solvent peak and the structure peak. The overall number of particles n in the droplet remains constant, while the solvent volume $V(t)$ shrinks:

$$c(t) = \frac{n}{V(t)} \quad (2)$$

The solvent peak provides $V(t)$, and the time-dependent concentration follows for each time step from the known initial particle concentration.

The fraction of agglomerates X_a was obtained from the structure peak that emerged upon agglomeration. We define the agglomerate fraction as a function of the time-dependent number of particles in agglomerates $n_a(t)$:

$$X_a(t) = n_a(t)/n \quad (3)$$

DOI: 10.1021/acs.nanolett.9b01688
Nano Lett. 2019, 19, 5246–5252

with a range between $X_a = 0$ for a perfect dispersion and $X_a = 1$ for a fully agglomerated sample. The structure peak areas are then directly proportional to X_a, as shown in Figure 1c.[23] All of our experiments started with $X_a = 0$ and proceeded until all solvent evaporated, where the structure peak area reached a plateau, and $X_a = 1$. All intermediate X_a were obtained from the area of the structure peak area by linear interpolation (refer to the SI for the detailed procedure).

Note that this approach does not assume a scattering model for the particles and can only provide relative values. This is an acceptable limitation because we always cover the full range from dispersion to agglomeration in our experiments; a scattering model would be required to provide absolute particle (and agglomerate) densities from a single scattering experiment.

We used our technique to quantify the effect of different solvents on the agglomeration of 3.4 nm core diameter octanethiol-stabilized gold nanoparticles (AuNPs). Dispersions with particle concentrations close to saturation were prepared by repeated centrifugation (3−4 cycles), redispersion, and the removal of remaining agglomerates with a 450 nm porosity filter. Droplets of the resulting dispersions were tested for concentration-dependent stability by slowly evaporating the solvent. X-ray scattering indicated that the originally dispersed particles started agglomerating upon evaporation of the solvent after 5−15 min, depending on the solvent. The agglomerate fraction then increased as evaporation proceeded (Figure 2a).

The ability of nanoparticles to remain dispersed rather than to agglomerate in different solvents has sometimes been called their "solubility".[24,25] This term should not be misunderstood to imply a molecular solution. It is used in the sense of a solution defined by IUPAC as a "liquid or solid phase containing more than one substance, when for convenience one (or more) substance, which is called the solvent, is treated differently from the other substances, which are called solutes".[26] In the following, we define the "colloidal solubility" as the maximal concentration c_s of dispersed particles that coexist with agglomerates in equilibrium. This definition is similar to that used in molecular solubility equilibria, where dissolution and precipitation occur at similar rates and set an equilibrium concentration. We use the term "agglomeration concentration" to denote the maximal concentration c' reached before agglomeration sets in.

In order to extract exact concentration values from the scattering data, we used a model of the evaporating droplet. Assume that dispersed particles with a constant concentration c_s coexist with agglomerates in the droplet, as illustrated in Figure 3a. The overall number of particles is the sum of dispersed particles n_d and particles that are contained in agglomerates n_a:

$$n = n_a + n_d \tag{4}$$

or, in terms of the agglomerate fraction X_a:

$$n = X_a n + c_s V(t) \tag{5}$$

We obtain a relation between agglomerate fraction and time-dependent droplet volume:

$$X_a(t) = 1 - c_s/c_p \tag{6}$$

with the overall concentration of particles (dispersed and agglomerated) in the droplet, c_p.

Eq 6 suggests plotting the agglomerate fraction X_a as a function of reciprocal particle concentration $1/c_p$ as in Figure 2b−f. First, consider panels b−e that show results for different solvents in increasing order of particle stability. Follow the data points from right to left to retrace the experiments. During the first few minutes of solvent evaporation, there was no sign of agglomeration while the concentration of the dispersed particles steadily increased (stage 1). At a concentration c', agglomeration set in, indicated by the emergence of structure peaks in the SAXS pattern (stage 2). The onset of agglomeration was sudden and well-defined for nonane and heptane and less abrupt for toluene and decane. Note that the shape of the curves (including their nonlinearity) was remarkably repeatable; all plots contain data points from three independent agglomeration experiments that led to similar results. The growth of the agglomerate fraction in stage 2 was inversely proportional to the reciprocal particle concentration with a slope c_s as expected from eq 6. We conclude that the model of the evaporating droplet above, which assumes ideal solubility, fits the situation at least moderately well for toluene, decane, nonane, and heptane.

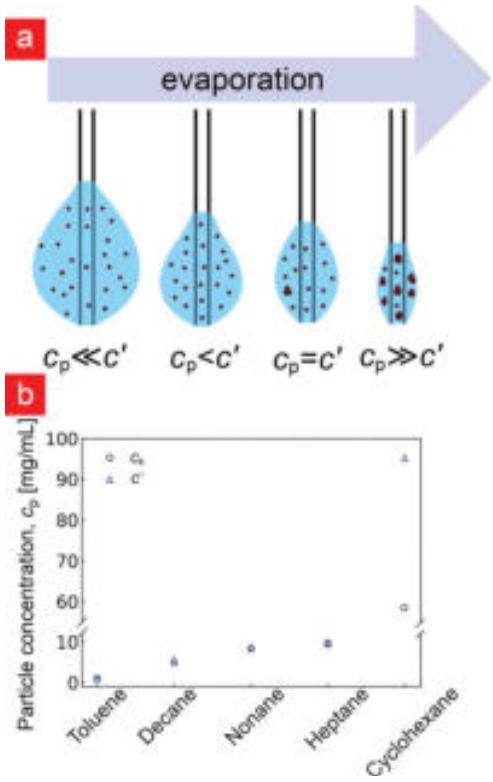

Figure 3. (a) Coexistence of dispersed particles and agglomerates while the droplets evaporates. We assume that the nanoparticles have a solubility similar to that of molecular solutes. (b) Agglomeration concentration c' and colloidal solubility c_s for AuNPs in different solvents derived from the data shown in Figure 2.

In cyclohexane (Figure 2f), agglomeration set in at a concentration that was 2 orders of magnitude greater than for any other solvent. Agglomerate growth was nonlinear, and much of it occurred rapidly at the end of the evaporation process at high concentrations. Agglomeration of particles in cyclohexane clearly deviated from ideal solubility.

The magnitudes of c' and c_s strongly depended on the solvent. In order to provide their numerical values, we used a least-squares linear fit to the last 15 points, that is, those with

DOI: 10.1021/acs.nanolett.9b01688
Nano Lett. 2019, 19, 5246−5252

the highest c_p (5 from each droplet) of agglomerate fraction as a function of reciprocal particle concentration in stage 2 (eq 6). The absolute slope of the fitted function m_2 was taken as c_s; its x-axis intersection was taken as c' as shown in Figure 3b (refer to Table S2 in the SI for the numerical values of all fits and the deviation of the agglomeration fraction in stage 1 from zero). We found $c' \approx c_s$ for all solvents but cyclohexane. Toluene was clearly the worst solvent, while the alkanes that are similar in structure to the ligand alkanethiols led to stabilities that increased with decreasing solvent chain length. Cyclohexane was a remarkably good solvent and the only case where $c' > c_s$.

The classical model of ideal solubility assumes local, dynamic equilibrium. Solutes that constantly join and leave the precipitate set the saturation concentration. Many nanoparticle types cannot act as solutes of this type. For example, the aggregation of polar, charge-stabilized metal nanoparticles that reach the primary minimum of their interaction potentials will not lead to solution equilibria. The agglomeration of the nanoparticles studied here, by contrast, appears to be sufficiently reversible in some solvents to approximate ideal solubility.

The worst solvent that we used (toluene) led to almost ideal solubility, while the best solvent (cyclohexane) led to strong deviations. Classical colloid theory predicts the greatest stability for particles with the most repulsive interparticle potential. As we see here, this does not imply reversibility of agglomeration; in other words, the absolute strength of attractive interaction does not predict solubility. Discrepancies between (predicted and measured) interaction potentials and agglomeration concentrations have already been reported for AuNPs with size distributions above 10% by Hajiw et al.,[27] who studied the structure factor of their dispersions. The group of Kotov argued that certain interactions between nanoparticles are not additive.[28] Some of us have shown that the temperature-dependent stability of apolar AuNPs depends on strongly nonlinear structural transitions in the ligand shell that can only be explained with molecular models.[8,9] There is no 1:1 mapping between a simple particle interaction parameter and the particles' colloidal solubility.

We believe that nanoparticle solubility must be understood as a multibody phenomenon that involves both particles and solvent molecules. Molecular detail is essential, for example, the bulk properties of cyclohexane are similar to that of the used alkanes and cannot explain the large differences in solubility reported above. Similar interactions have been previously reported for the synthesis of AuNPs,[24] for the self-assembly of ultrathin gold nanowires,[29] and for the agglomeration of particles in solvent mixtures.[30] Recent molecular dynamics simulations show that the ligand shells of the particles used here are mobile[8,9] and that the quality of the solvent depends on the exact configuration of the solvation shell. We propose that the agglomerates can be likened to supramolecular complexes, with at least partially defined arrangement of solvent molecules between the particles, rather than fully disordered fluids.

Closely related are kinetic effects. The particle volume fractions at c' that we found were far below dense packing even for the best solvents (1.9% at the onset of agglomeration for cyclohexane), but particles inside the agglomerates and on their surfaces are densely packed, which drastically reduces their mobility. Part of the nonlinearity observed for good solvents may be due to the slow process of finding a suitable particle arrangement in and on the agglomerate. The large relative c' for cyclohexane could be an extreme case of this kinetic effect, where it is difficult for the incipient agglomerate "nucleus" to form because only specific configurations are low in free energy. Critical nucleation theory predicts larger supersaturation for particles nuclei with low interfacial energy, too, which may be a second contributing factor.[31]

The differences in solubility for the different solvents are large, and we are convinced that our results are robust enough to support the above conclusions. The exact values of c_s and c' need to be considered with care, however, given the inherent challenges of the experiments. Our analysis assumes a homogeneous particle concentration in the entire droplet. We therefore needed to exclude accumulation of particles at gas−liquid or solid−liquid interfaces that was reported previously.[32] Additional experiments were used to estimate errors in the calculated particle concentrations and agglomerate fractions. First, we tested whether particles segregated to the gas−liquid interface by measuring the surface tension of a 3 μL hanging droplet in air using an optical contact angle measuring system. Nanoparticles that segregate to the air−liquid interface could reduce its surface energy and cause a change in surface tension, but the observed change was below 13% for decane and below 8% in all other solvents (Table S1 in the SI). We conclude that there was no appreciable segregation to the interface.

Other potential sources of error are the adsorption of particles to the liquid−solid interface between the droplet and the capillary and insufficient mixing inside the droplet by convection and diffusion during evaporation that could lead to concentration gradients inside the hanging droplet. We performed experiments with two different droplet sizes and compared them to exclude such effects. Droplets with volumes of 12 μL were dispensed from a polyimide tube with an inner diameter of 1.52 mm and remained attached only to the end of the capillary. These droplets did not wet the surface of the tubing (see the first photograph at the bottom of Figure 1a), thus minimizing the solid−liquid interfacial area. Figure S4 in the SI shows that particle agglomeration proceeded in a very similar manner for both droplet sizes, suggesting that such effects are absent or too weak to affect the measurement. The variation of values extracted from subsequent, independent evaporation experiments using the same dispersions led to values that varied by <2%.

In conclusion, we introduced a method to precisely measure the concentration-dependent agglomeration of apolar nanoparticles that provides unprecedented precision even at high particle concentrations. We used it to demonstrate that AuNPs in bad solvents (toluene) at increasing particle concentration exhibit almost ideal solubility, while the same particles in very good solvent (cyclohexane) deviated from it. We suggest a picture of solubility that considers supramolecular interactions between ligands and solvent molecules. Studies of other nanoparticle cores, shells, and solvents are currently underway.

Our results contribute to the long-standing debate on the concentration dependence of apolar particle stability in general. In a seminal monograph, Napper called the stability of sterically stabilized dispersions a "critical flocculation point (CFPT)" and stated that "whether or not the experimentally observed CFTP depends significantly upon the particle number concentration is a rather complex issue".[33] Our measurements prove that particle stability is strongly affected by concentration for nanoparticles.

DOI: 10.1021/acs.nanolett.9b01688
Nano Lett. 2019, 19, 5246−5252

Materials and Methods. *Synthesis of Nanoparticles.* Gold nanoparticles (AuNPs) with core diameters d = 3.4 nm and a size dispersion (standard deviation over the mean) of 8% were synthesized using a modified version of the route from Wu et al.[24] that has been published previously.[34] Briefly, amine-capped AuNPs were produced in a one-pot synthesis where a mixture of $HAuCl_4 \cdot H_2O$, oleylamine (OAm, Sigma-Aldrich, technical grade, 70%), and pentane (Sigma-Aldrich, 98%) was reduced by *tert*-butylamine-borane complex (Sigma-Aldrich, 97%). The nanoparticles were purified by precipitation with ethanol and redispersed in toluene. Finally, they were characterized by transmission electron microscopy and SAXS (cf. SI).

Ligand Exchange Reaction. An excess of octanethiol (Sigma-Aldrich, 98.5%) was added to the dispersion of the as-synthesized OAm-capped AuNP, and the mixture was kept stirring at 70 °C for 20 min. The resulting colloidal dispersion was washed and purified by precipitation with ethanol, centrifugation at 4000 rpm for 5 min, and resuspension in cyclohexane.

Small-Angle X-ray Scattering. Small-angle X-ray scattering (SAXS) experiments were performed using a Xeuss 2.0 (Xenocs SA, France) setup equipped with a copper K_α X-ray source with a wavelength of λ = 0.154 nm and a PILATUS 1 M (DECTRIS, Switzerland) hybrid photon counting detector. The sample-to-detector distance (SDD) was 340 mm covering from 0.04 $Å^{-1}$ to 2.5 $Å^{-1}$ with the scattering vector $q = \frac{4\pi \sin\theta}{\lambda}$.

The 2D diffraction patterns were recorded and radially integrated using the FOXTROT v.3.3.4 (Synchrotron SOLEIL) software suite. Data analysis was done following the procedure described previously.[8]

Syringe Pump. A computer-controlled pulsation-free syringe pump ("NEMESYS", cetoni GmbH) was used to produce a droplet of the desired volume by pushing the gold dispersion through a glass syringe (500 μL model 1750 TLLX SYR, Hamilton, USA) that were connected with standard HPLC tubing (0.8 mm diameter, fluorinated ethylene propylene for extensive solvent compatibility) to a fused silica tubing (BGB, 30 μm-ID).

■ ASSOCIATED CONTENT

Supporting Information

The Supporting Information is available free of charge on the ACS Publications website at DOI: 10.1021/acs.nanolett.9b01688.

Details on nanoparticle characterization, the calculation of the agglomerate fractions, experimental data on the effect of droplet size, agglomeration data expressed as volume fractions (PDF)

■ AUTHOR INFORMATION

Corresponding Author

*E-mail: tobias.kraus@leibniz-inm.de.

ORCID

Thomas Kister: 0000-0002-9827-1380
Lola González-García: 0000-0002-8474-6517
Tobias Kraus: 0000-0003-2951-1704

Notes

The authors declare no competing financial interest.

■ ACKNOWLEDGMENTS

The authors thank Dr. Asaph Widmer-Cooper for useful discussions, Dr. Björn Kuttich for his analysis of the scattering caused by agglomerates, and Prof. E. Arzt for his continuing support of the project.

■ REFERENCES

(1) Zheng, N.; Fan, J.; Stucky, G. D. *J. Am. Chem. Soc.* **2006**, *128*, 6550−6551.
(2) Kister, T.; Maurer, J. H.; González-García, L.; Kraus, T. *ACS Appl. Mater. Interfaces* **2018**, *10*, 6079−6083.
(3) Tao, P.; Li, Y.; Rungta, A.; Viswanath, A.; Gao, J.; Benicewicz, B. C.; Siegel, R. W.; Schadler, L. S. *J. Mater. Chem.* **2011**, *21*, 18623−18629.
(4) Ankah, G.; Büchele, P.; Poulsen, K.; Rauch, T.; Tedde, S.; Gimmler, C.; Schmidt, O.; Kraus, T. *Org. Electron.* **2016**, *33*, 201−206.
(5) Ikkala, O.; ten Brinke, G. *Science* **2002**, *295*, 2407−2409.
(6) Evans, D. F.; Wennerström, H. *The colloidal domain: where physics, chemistry, biology, and technology meet*; Wiley-VCH: New York, 1999.
(7) Lyklema, J. *Curr. Opin. Colloid Interface Sci.* **2013**, *18*, 116−128.
(8) Kister, T.; Monego, D.; Mulvaney, P.; Widmer-Cooper, A.; Kraus, T. *ACS Nano* **2018**, *12*, 5969−5977.
(9) Monego, D.; Kister, T.; Kirkwood, N.; Mulvaney, P.; Widmer-Cooper, A.; Kraus, T. *Langmuir* **2018**, *34*, 12982−12989.
(10) Yang, Y.; Qin, H.; Jiang, M.; Lin, L.; Fu, T.; Dai, X.; Zhang, Z.; Niu, Y.; Cao, H.; Jin, Y.; Zhao, F.; Peng, X. *Nano Lett.* **2016**, *16*, 2133−2138.
(11) Yang, Y.; Qin, H.; Peng, X. *Nano Lett.* **2016**, *16*, 2127−2132.
(12) Coveney, P.; Giordanetto, F.; Stringfellow, N. Obtaining Scalable Performance from Molecular Dynamics Codes on HPC Machines. Proceedings from the *CUG Summit 2002*, Manchester, UK, May 20−24, 2002; University of Manchester: Manchester, UK, 2002.
(13) Agthe, M.; Plivelic, T. S.; Labrador, A.; Bergström, L.; Salazar-Alvarez, G. *Nano Lett.* **2016**, *16*, 6838−6843.
(14) Dreyer, A.; Feld, A.; Kornowski, A.; Yilmaz, E. D.; Noei, H.; Meyer, A.; Krekeler, T.; Jiao, C.; Stierle, A.; Abetz, V.; Weller, H.; Schneider, G. A. *Nat. Mater.* **2016**, *15*, 522.
(15) Sen, D.; Bahadur, J.; Mazumder, S.; Santoro, G.; Yu, S.; Roth, S. V. *Soft Matter* **2014**, *10*, 1621−1627.
(16) Sanishvili, R.; Yoder, D. W.; Pothineni, S. B.; Rosenbaum, G.; Xu, S.; Vogt, S.; Stepanov, S.; Makarov, O. A.; Corcoran, S.; Benn, R.; Nagarajan, V.; Smith, J. L.; Fischetti, R. F. *Proc. Natl. Acad. Sci. U. S. A.* **2011**, *108*, 6127−6132.
(17) Stewart, G. *Phys. Rev.* **1929**, *33*, 889.
(18) Pauw, B. R. *J. Phys.: Condens. Matter* **2013**, *25*, 383201.
(19) Sztucki, M.; Narayanan, T.; Belina, G.; Moussaid, A.; Pignon, F.; Hoekstra, H. *Phys. Rev. E* **2006**, *74*, 051504.
(20) Pontoni, D.; Narayanan, T.; Petit, J.-M.; Grübel, G.; Beysens, D. *Phys. Rev. Lett.* **2003**, *90*, 188301.
(21) Kotlarchyk, M.; Chen, S.-H. *J. Chem. Phys.* **1983**, *79*, 2461−2469.
(22) Brunner-Popela, J.; Glatter, O. *J. Appl. Crystallogr.* **1997**, *30*, 431−442.
(23) Johnson, J. E. *J. Appl. Polym. Sci.* **1959**, *2*, 205−209.
(24) Wu, B.-H.; Yang, H.-Y.; Huang, H.-Q.; Chen, G.-X.; Zheng, N.-F. *Chin. Chem. Lett.* **2013**, *24*, 457−462.
(25) Powell, J.; Schwieters, R.; Bayliff, K.; Herman, E.; Hotvedt, N.; Changstrom, J.; Chakrabarti, A.; Sorensen, C. *RSC Adv.* **2016**, *6*, 70638−70643.
(26) Ewing, M.; Lilley, T.; Olofsson, G.; Ratzsch, M.; Somsen, G. *Pure Appl. Chem.* **1994**, *66*, 533−552.
(27) Hajiw, S.; Schmitt, J.; Impéror-Clerc, M.; Pansu, B. *Soft Matter* **2015**, *11*, 3920−3926.
(28) Silvera Batista, C. A.; Larson, R. G.; Kotov, N. A. *Science* **2015**, *350*, 1242477.

DOI: 10.1021/acs.nanolett.9b01688
Nano Lett. 2019, 19, 5246−5252

(29) Reiser, B.; Gerstner, D.; Gonzalez-Garcia, L.; Maurer, J.; Kanelidis, I.; Kraus, T. *Phys. Chem. Chem. Phys.* **2016**, *18*, 27165−27169.
(30) Rabani, E.; Egorov, S. *Nano Lett.* **2002**, *2*, 69−72.
(31) Volmer, M.; Weber, A. *Z. Phys. Chem.* **1926**, *119*, 277−301.
(32) Born, P.; Schon, V.; Blum, S.; Gerstner, D.; Huber, P.; Kraus, T. *Langmuir* **2014**, *30*, 13176−13181.
(33) Napper, D. H. *Polymeric stabilization of colloidal dispersions*; Academic Press: Cambridge, MA, 1983; Vol. 3.
(34) Kister, T.; Mravlak, M.; Schilling, T.; Kraus, T. *Nanoscale* **2016**, *8*, 13377−13384.

DOI: 10.1021/acs.nanolett.9b01688
Nano Lett. 2019, 19, 5246−5252

Supporting Information for: Colloidal solubility and agglomeration of apolar nanoparticles in different solvents

David Doblas,[†] Thomas Kister,[†] Marina Cano-Bonilla,[†] Lola González-García,[†] and Tobias Kraus*[,†,‡]

[†]*INM - Leibniz Institute for New Materials, Campus D2 2, 66123 Saarbrücken, Germany*

[‡]*Colloid and Interface Chemistry, Saarland University, Saarbrücken, Germany*

E-mail: tobias.kraus@leibniz-inm.de

Characterization of the nanoparticles and dispersions

Figure S 1 show SAXS and TEM data of the octanethiol-capped AuNPs. The SASfit v.0.94.6 software of the Paul Scherrer Institute was used to fit the data using the built-in scattering model (Schulz-Zimm) for spheres.

Table S 1 shows the mean values of surface tensions measurements (5 experiments) for droplets of pure solvents and for the dispersions in the same solvents using the method explained in the main text.

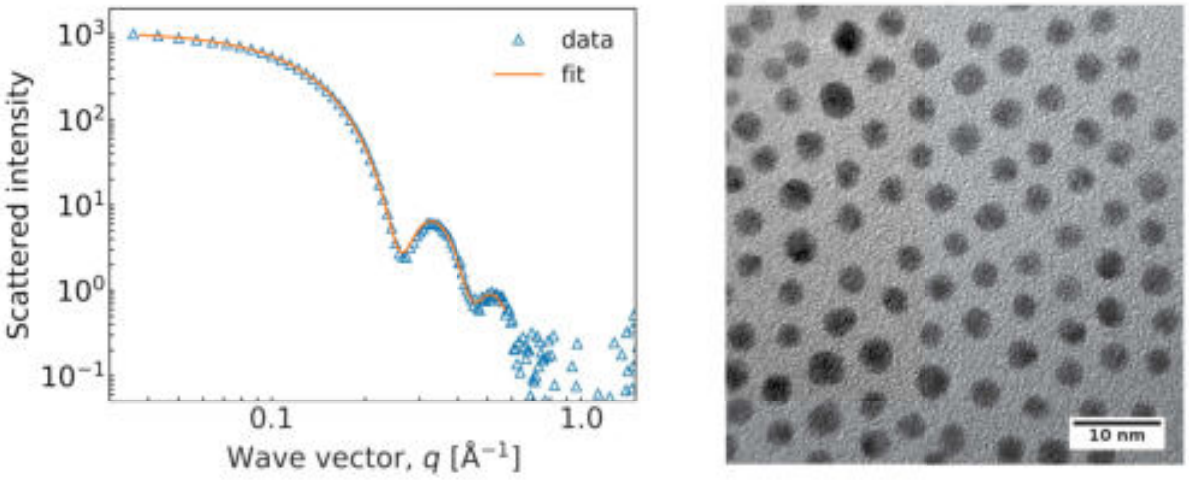

Figure S 1: Small angle X-ray scattering data of the AuNPs used in this study. The data was fitted using a sphere scattering model to extract the radius and width of size distribution.

Table S 1: Surface tension results using AuNPs of 3.4 nm in diameter capped with octanethiol.

Sample	*Surface tension, mN/m*
Cyclohexane	27.9 ± 0.4
Cyclohexane + AuNPs	27.7 ± 0.1
Toluene	31.5 ± 0.2
Toluene + AuNPs	31.1 ± 0.2
Decane	24.2 ± 0.1
Decane + AuNPs	27.9 ± 0.3
Nonane	24.5 ± 0.2
Nonane + AuNPs	26.6 ± 0.2
Heptane	22.7 ± 0.5
Heptane + AuNPs	24.7 ± 0.7

Determination of the ligand coverage by thermogravimetric analysis

A volume of 1 mL of dispersion containing AuNPs capped with octanethiol was deposited in a TGA ceramic crucible by drop-wise evaporation. The crucible was then placed in a vacuum oven at 35 °C for 2 days to remove any residual solvent.

Thermogravimetric analysis was performed in a NETZSCH STA 449F3 by heating from 20 °C to 800 °C under an Ar atmosphere at a heating rate of 5 °C min^{-1} resulting in a mass loss of 13.5% between 200 °C to 300 °C that corresponds to the decomposition of the organic shell.

Calculation of the agglomerate fraction X_a and the solvent volume

Figure S 2 shows the time-dependent scattering curves for different solvents. Both particle concentration and the fraction of agglomerates were obtained from these curves by integration of different q-ranges using the methods explained below.

The solvent volume was estimated by integration the full scattering from 0.8 Å^{-1} to 1.7 Å^{-1} in Figure S 2. Linear interpolation using all areas was then performed assuming that

- at $t = 0$, $A_{solvent} = A_0 \Rightarrow V_{solvent} = 2.5\,\mu$L, and
- at $t =$end, $A_{solvent} = 0 \Rightarrow V_{solvent} = 0$.

This provided droplet volumes for each time step.

In order to calculate the time-dependent fraction of agglomerates

$$X_\mathrm{a}(t) = n_\mathrm{a}(t)/n, \tag{1}$$

we exploit the fact that scattering at $t = 0$, when all AuNPs are dispersed, is purely dominated by the particles' form factor. At any $t \neq 0$, the integrated scattering was divided the scattering at $t = 0$ in order to obtain the contribution of the structure factor as shown in Figure S 3. This provided clear structure factor peaks for each time step after agglomeration as shown in Figure S 3. The positions of the peaks remained constant indicating an unchanged agglomerate

structure, while their areas increased as more particles agglomerated.

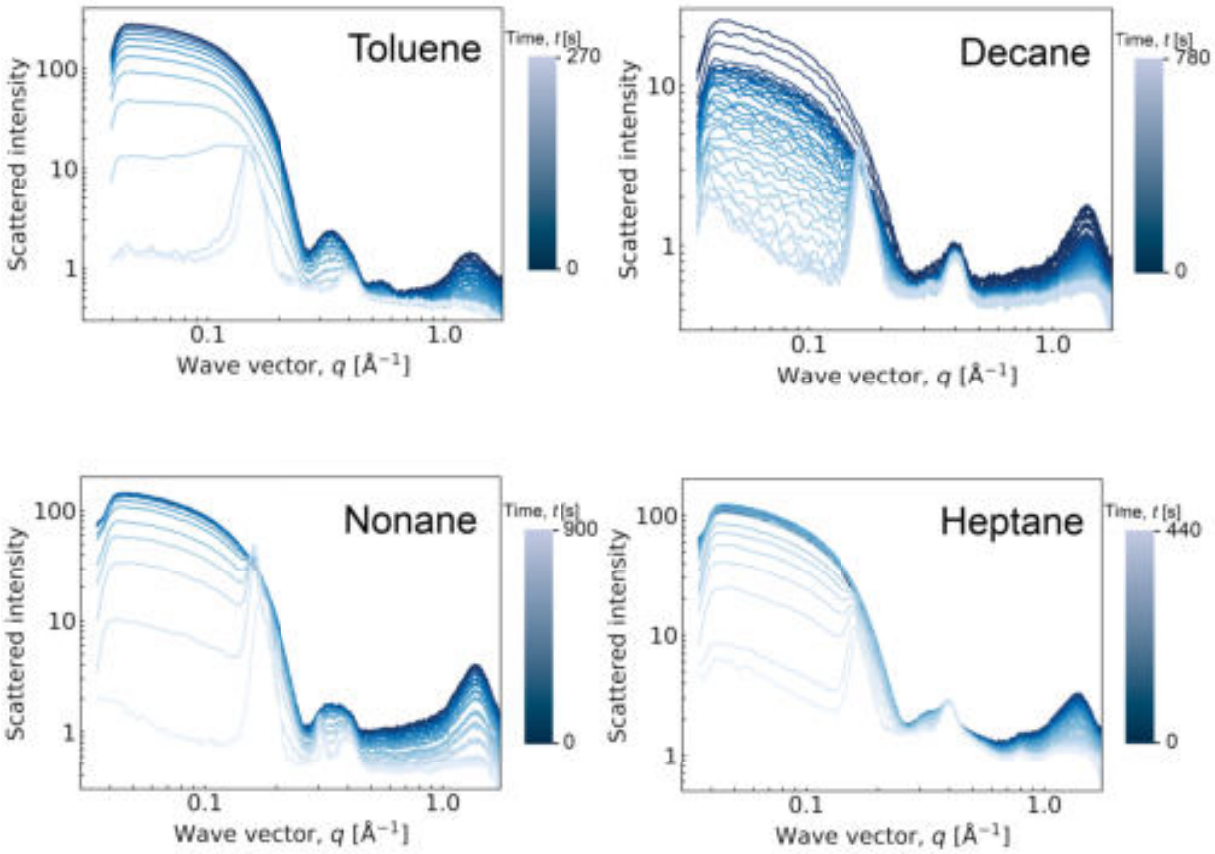

Figure S 2: Time-dependent small-angle scattering of evaporating dispersion droplets with different solvents.

Structure factors at different stages of agglomeration

The area of the agglomerates' structure factor peak was obtained by integration from 0.14 $Å^{-1}$ to 0.20 $Å^{-1}$ as indicated by the dashed lines in Figure S 3. Linear interpolation using all areas was then performed assuming that

- at $t = 0$, $A_{peak} = 0 \Rightarrow X_a = 0$, and
- at t =end, $A_{peak} = A' \Rightarrow X_a = 1$.

This provided agglomerate fractions for each time step.

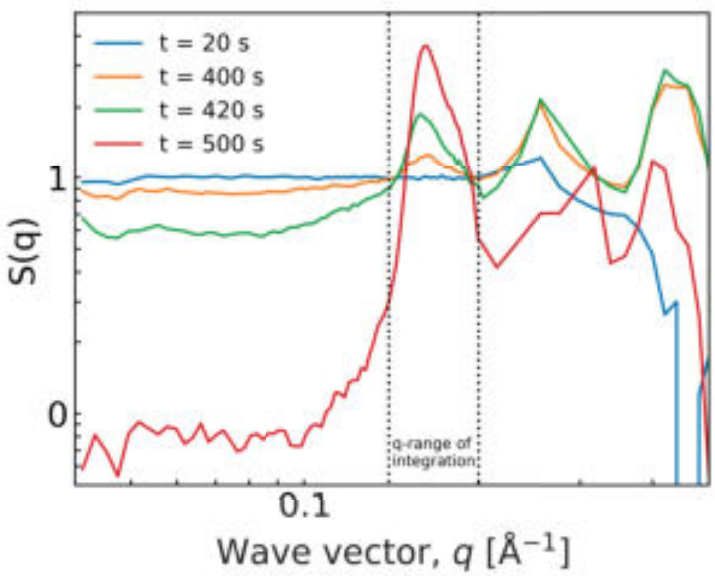

Figure S 3: Structure factors at different stages of the experiments described in the manuscript. Dashed lines from 0.14 $Å^{-1}$ to 0.20 $Å^{-1}$ show the q-range in which integration was performed.

Effect of the droplet size

Figure S 4 shows the agglomerate fractions in "small" (2.5 µL) and "large" (12 µL) droplets during evaporation in cyclohexane. The differences between the different volumes are small, indicating that the data is not affected by concentration gradients inside the droplets or adsorption of particles to interfaces.

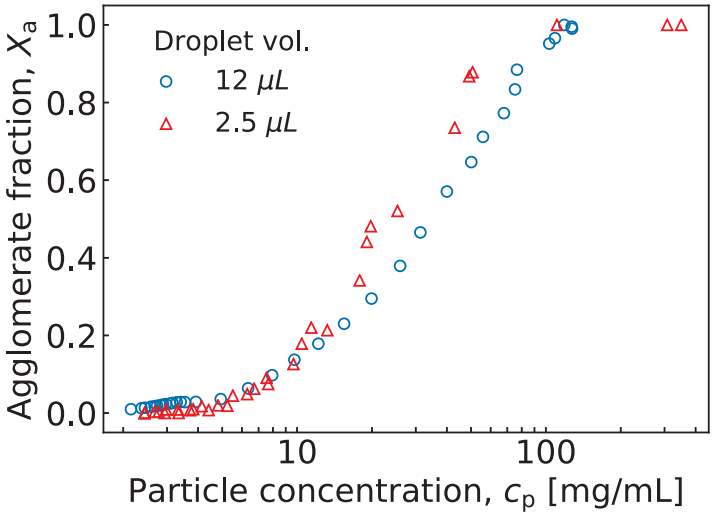

Figure S 4: Time-dependant agglomerate fractions in "small" (2.5 µL) and "large" (12 µL) droplets during evaporation in cyclohexane.

Agglomerate fractions X_a as a function of the reciprocal particle volume fraction $1/X_p$ for different solvents

Figure S 5 shows the agglomerate fraction of 3.4 nm in diameter gold nanoparticles (the same data presented in the main article's Figure 2) as a function of the reciprocal particle volume fraction for different solvents.

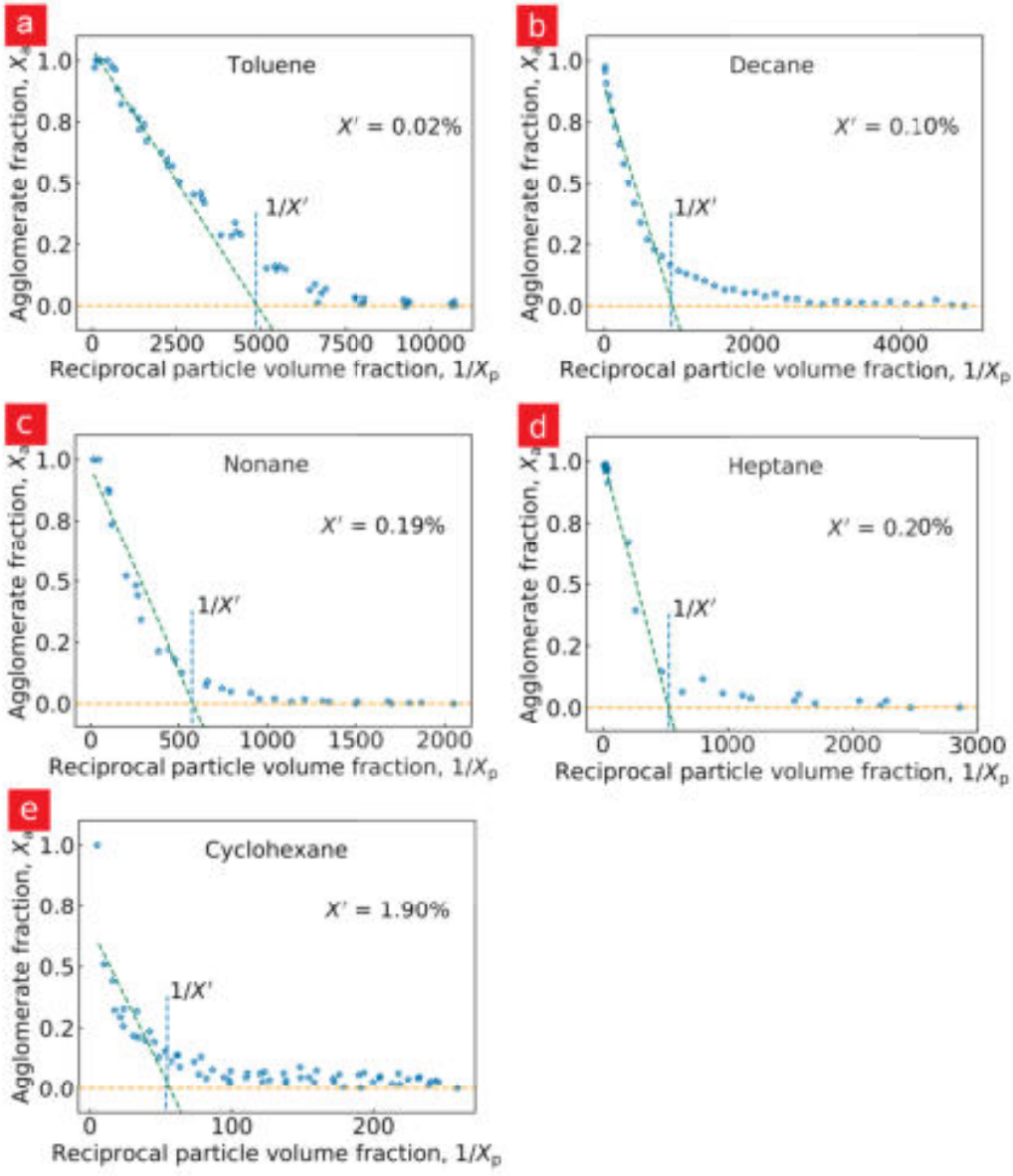

Figure S 5: Agglomerate fractions X_a as a function of the reciprocal particle volume fraction $1/X_p$ for (a) toluene, (b) decane, (c) nonane, (d) heptane, and (e) cyclohexane.

Table S 2 summarizes the slopes of the fittings of the initial points in Figure 2 of the main text.

Table S 2: Slopes of linear least-square fits of the of the 15 initial (low concentration values) particle concentrations for the experiments presented in Figure 2 of the main text.

Solvent	*Initial slope*
Toluene	0.006
Decane	0.020
Nonane	0.017
Heptane	0.051
Cyclohexane	0.532

Table S 3 summarizes the values found for colloidal solubility c_s, agglomeration concentration c', and particle volume fractions X' at c' for the different solvents investigated.

Table S 3: Colloidal solubilities c_s, agglomeration concentrations c', and volume fractions X' at c' for the different solvents.

Solvent	c_s, *mg/mL*	*c', mg/mL*	*X', %*
Toluene	1.07	1.03	0.02
Decane	4.86	5.56	0.10
Nonane	8.31	8.69	0.19
Heptane	9.68	9.52	0.20
Cyclohexane	58.79	95.24	1.90

3.5 Publication 5

Kister, T., Maurer, J. H., González-García, L., & Kraus, T. (2018). Ligand-Dependent Nanoparticle Assembly and Its Impact on the Printing of Transparent Electrodes. ACS applied materials & interfaces, 10(7), 6079-6083.

DOI: 10.1021/acsami.7b18579

ACS APPLIED MATERIALS & INTERFACES

Letter

Cite This: ACS Appl. Mater. Interfaces 2018, 10, 6079−6083

www.acsami.org

Ligand-Dependent Nanoparticle Assembly and Its Impact on the Printing of Transparent Electrodes

Thomas Kister,[‡,†] Johannes H. M. Maurer,[‡,†] Lola González-García,[‡] and Tobias Kraus*[,‡,§]

[‡]INM - Leibniz Institute for New Materials, Campus D2 2, 66123 Saarbrücken, Germany

[§]Colloid and Interface Chemistry, Saarland University, Saarbrücken, Germany

Supporting Information

ABSTRACT: Metal grids with submicron line diameters are optically transparent, mechanically flexible, and suitable materials for transparent and flexible electronics. Printing such narrow lines with dilute metal nanoparticle inks is challenging because it requires percolation throughout the particle packing. Here, we print fully connected submicron lines of 3.2 nm diameter gold nanoparticles and vary the organic ligand shell to study the relation between colloidal interactions, ligand binding to the metal core, and conductivity of the printed lines. We find that particles with repulsive potentials aid the formation of continuous lines, but the required long ligand molecules impede conductivity and need to be removed after printing. Weakly bound alkylamines provided sufficient interparticle repulsion and were easy to remove with a soft plasma treatment after printing, so that grids with a transparencies above 90% and a conductivity of 150 Ω sq^{-1} could be printed.

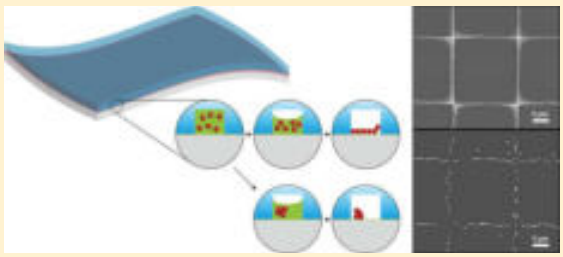

KEYWORDS: *nanoparticles, ligand design, nanoimprinting, self-assembly, transparent electrodes*

Transparent electrodes are critical components of displays, solar cells, and touch screens. Particularly suitable for such materials are grids of very thin metal wires: regular arrays of metal lines with widths below 1 μm on polymer substrates equal or outperform transparent conductive oxides such as indium tin oxide in conductivity and transparency, can be made from abundant metals, and are mechanically flexible and suitable for new device architectures.[1] The common trade-off between conductivity and transparency is readily controlled through the density of the mesh.

It is highly appealing to print such grids using nanoparticle-based inks. Functional nanoparticles are proven building blocks for micro- and macroscopic electronic circuits.[2] Metal inks composed of nanoparticles dispersed in a solvent or a solvent mixture are already commonly applied.[3] Such inks can be printed under ambient conditions, fewer processing steps are required than in top-down technology, and less material is wasted because material is only deposited where needed.[4] High-throughput and low-cost processing in large sheet or roll-to-roll production becomes possible.

Despite of the advantages of printing, it has proven challenging to print transparent conductive lines of common nanoparticles. Spherical nanoparticles tend to agglomerate already at low concentrations.[5] This leads to disconnected agglomerates that interrupt the printed lines and prevent macroscopic conductivity. As a result, literature only reports the printing of small areas using either highly concentrated (up to 15% by weight,[6] where we use inks with 0.64% here), viscous inks or by using comparatively slow nanodrip printing. Existing reports employ annealing at high temperatures, which limits substrate compatibility.[7] One alternative are ultrathin gold nanowires with core diameters below 2 nm that have the tendency to form continuous bundles due to their ligands' interactions[8] and readily form percolating meshes during printing.[9,10] The wires make it much easier to print percolating structures and have been successfully employed to create conductive transparent electrodes, but nanowire synthesis is still in its infancy. Wire dispersions prepared using the existing protocols are unstable, and only very few materials can be prepared as ultrathin nanowires.

Here, we show that it is possible to print very narrow, continuous lines of spherical nanoparticles depending on their colloidal interactions. This opens the possibility to print a variety of materials as fine meshes: many elegant synthetic routes are available to produce spherical nanoparticles with a variety of core materials, and ligands have been successfully used to control the particles' interactions and prevent premature self-assembly.[11−13]

We systematically varied the ligands of gold nanoparticles (AuNPs) to tune the imprinting performance and studied the influence on the particles' self-assembly, electronic behavior, and sintering characteristics. Grids with submicron line width were printed and analyzed regarding their electrical and optical properties and their changes after plasma sintering. The results show which colloidal interactions are necessary to print

Received: December 6, 2017
Accepted: February 5, 2018
Published: February 5, 2018

DOI: 10.1021/acsami.7b18579
ACS Appl. Mater. Interfaces 2018, 10, 6079−6083

percolating meshes, and which binding chemistries are amendable to soft sintering.

Spherical AuNPs with a mean diameter of d = 3.2 nm ±8.7% were synthesized by a route adapted from Wu et al. that caps the gold core with oleylamine[14] (see Figure S1). A detailed protocol is described in the Methods section. We replaced the oleylamine with alkanethiols that are commonly employed in metal nanoparticle inks for printed electronics.[15−17] The length of the carbon chain was systematically varied from butanethiol (AuNP@C4-thiol) to octanethiol (AuNP@C8-thiol) and dodecanethiol (AuNP@C12-thiol). The particles were redispersed in cyclohexane (particle concentration 5 mg/mL) that permeated the elastomer stamp at a rate appropriate for the imprinting process. Small-angle X-ray scattering (SAXS) analysis of the particles after ligand exchange revealed well-dispersed nanoparticles (see Figure S2).

Figure 1 shows a schematic diagram of the imprinting process that we used to study the assembly behavior and thus,

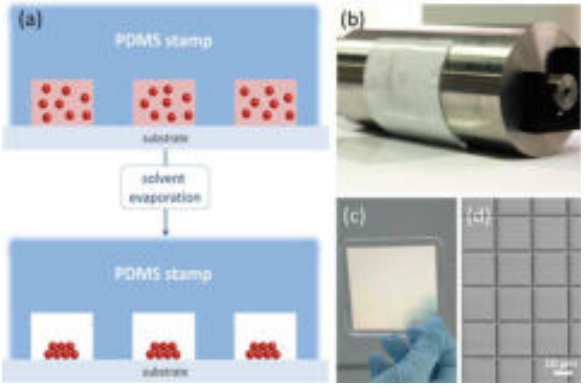

Figure 1. (a) Schematic diagram of the imprinting process. (b) Photograph of the imprinting setup. (c) Photograph of a PDMS stamp. (d) SEM image of a PDMS stamp carrying pillar arrays with square geometry.

the printability of different AuNPs. A prepatterned elastomer stamp is pressed into the liquid particle ink, displaces the liquid, and confines the dispersed particles in its cavities. The solvent permeates through the stamp material; the particles self-assemble and deposit onto the substrate, replicating the stamp pattern. Imprinting was performed in a roll-to-plate configuration reported in previous work.[10] Briefly, the prepatterned stamp was attached on a steel roller moved by a commercial film applicator (Figure 1b). The weight of the roller provides the pressure required for the imprinting (see Methods section for further details). We used stamps made of polydimethylsiloxane (PDMS) carrying an array of square-shaped pillars with a pitch of 19.5 μm, a pillar spacing of 1.8 μm, and a pillar height of 4 μm (Figure 1c, d).

Figure 2a−c shows scanning electron microscopy (SEM) images of the printed grids on glass (see also Figure S3). The stamp pattern was replicated by the particles that formed lines in the center of the stamp's grooves. The morphology of the lines depended on the ligand shell: with increasing ligand length, it changed from large, unconnected agglomerates (AuNP@C4-thiol, Figure 2a) to smaller, more evenly spread, but still unconnected agglomerates (AuNP@C8-thiol, Figure 2b), and finally to continuous, percolating lines (AuNP@C12-thiol, Figure 2c). SAXS analysis of printed metal grids (Figure 2d−f) on polyimide (Kapton tape) supported the SEM results: with decreasing ligand length, the peaks of the structure factor became narrower and more intense, indicating an increase in agglomerate size. The surface-to-surface distance between the particles increased from 1.16 to 1.96 nm as the ligand length increased from C4 to C12 (see Figure S4). The insets show transmission electron microscopy (TEM) images of the structures that the inks formed upon drying on carbon-coated TEM grids (see also Figure S3). Their morphology resembles that of the printed lines. AuNP@C4-thiol formed large agglomerates with diameters up to 500 nm, while AuNP@C12-thiol formed a monolayer of particles.

All inks initially contained the same particle concentrations, and there were no differences in the rheology or interface properties. Contact angle measurements on glass showed no significant influence of the ligand length on the wetting of the dispersion (see Figure S5). The differences in the printed morphologies must therefore be connected with colloidal properties of the particles that are affected by the ligand length. Lohman and Sorensen indicated that the concentration at which particle assembly sets in depends on ligand length.[5] We suggest that it is this concentration that dominates the morphologies.

Nanoparticles with shorter ligands assemble at a stage where the liquid film is relatively thick, and the particles can still move freely, whereas nanoparticles with longer ligand assemble at a very late stage, when the liquid film is already extremely thin and confinement is severe. Unconfined assembly leads to disconnected compact agglomerates that are deposited as discontinuous traces; confinement causes assembly in compact, continuous lines. The situation reminds of the formation of regular supraparticles in evaporating emulsion droplets, where the assembly kinetics dominate the level of ordering of the final structure.[18]

The unconnected clusters of the grids printed from AuNP@C4-thiol and AuNP@C8-thiol were discontinuous and therefore not conductive. AuNP@C12-thiol formed continuous, percolating lines, but they were not conductive after printing because the organic ligands shell impeded electron transport. A common way to remove the barriers and form direct metal−metal contacts is thermal sintering; the required temperature increases with the length of the carbon chain for alkanethiol-coated gold nanoparticles. A temperature of 120 °C was reported to turn AuNP@C4-thiol layers conductive, while AuNP@C12-thiol layers required temperatures between 170 and 200 °C.[15,16,19]

Sintering at such temperatures damaged our printed grids: the thin lines (line width <1 μm) rapidly dewetted and lost connectivity after 5 min at 200 °C (see Figure S6). Plasma treatment, a gentle alternative,[20] was recently used to sinter oleylamine coated ultrathin gold nanowires at room temperature.[21,22] We applied a plasma to the grids printed from AuNP@C12-thiol and found that an H_2/Ar-plasma did not improve conductivity, whereas an O_2-plasma led to a high resistance in the kΩ sq^{-1} range, probably due to oxidation of the thin lines that induces stress and interrupts conductive pathways.[23]

The results shown in Figure 2 suggest that the printing quality depended on the alkyl chain length, but not on the specific chemical linkage to the gold core. We therefore exchanged the thiol-gold bond with a weaker amine-gold bond that is known to be easier to remove.[24] AuNP@amines showed similar printing behavior to AuNP@thiols, albeit providing

DOI: 10.1021/acsami.7b18579
ACS Appl. Mater. Interfaces 2018, 10, 6079−6083

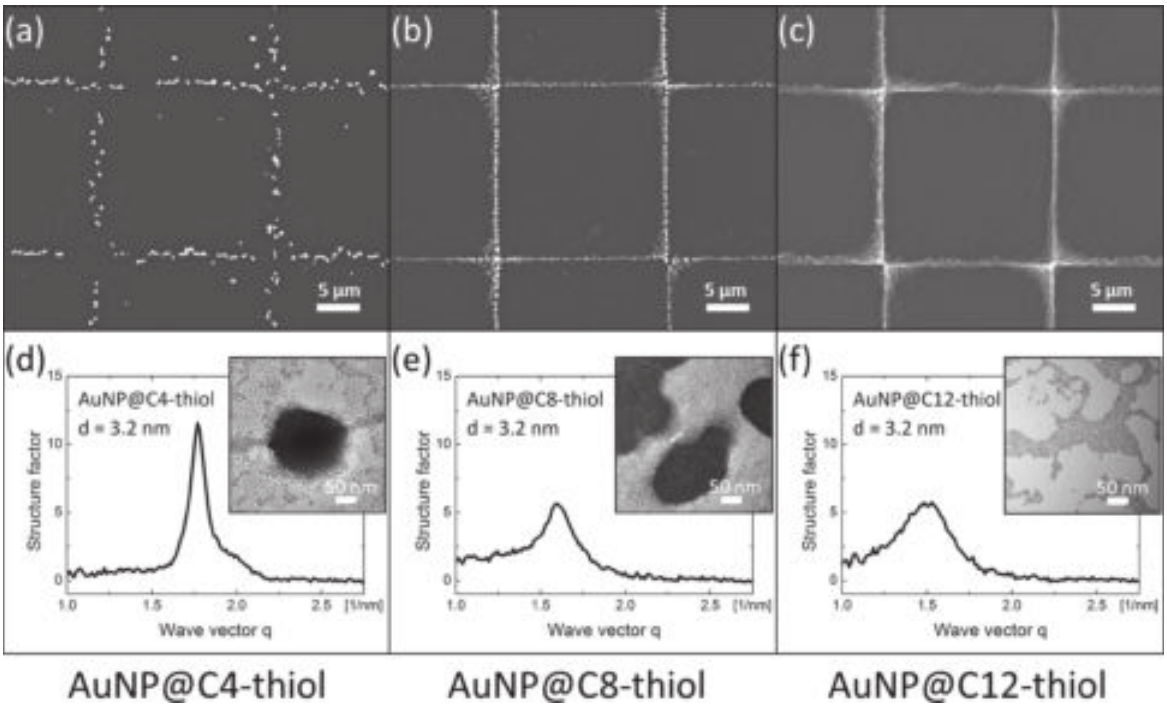

Figure 2. SEM images of ligand-dependent microstructure of printed lines for (a) AuNP@C4-thiol, (b) AuNP@C8-thiol, and (c) AuNP@C12-thiol. (d–f) Corresponding SAXS pattern of metal grids printed on polyimide. The insets shows TEM images of gold nanoparticles capped with the respective ligands.

slightly inferior colloidal stability; AuNP@C4-amine could not be redispersed at the same particle concentration (see Figure S7). The binding energy of amines to gold is smaller than that of thiols, and the ligand shell density may be locally reduced, which decreases colloidal stability.

Printing AuNP@C12-amine resulted in continuous, percolating lines similar to AuNP@C12-thiol (see Figure 3a). SAXS analysis revealed a similar particle–particle distance (see Figure S8). The obtained grids had line widths below 1 μm (inset Figure 3a) and exhibited high optical ballistic transmittance of ≈91% at 500 nm (Figure 3b). Plasma sintering in an H_2/Ar atmosphere was successfully applied for grids printed from AuNP@C12-amine; after 15 min plasma treatment, the sheet resistance dropped to 150 Ω sq^{-1}, a value that is sufficient for several applications such as touch sensors.[25] The amine-gold bond is considerably weaker than the thiol-gold bond, and removal of the amine should be easier than removal of the thiol.[24,26] Furthermore, sulfur atoms might remain bonded to gold even if (part of) the alkyl chain has been removed by the plasma, thus creating defects and insulating barriers.

In summary, we showed that the printing submicron lines of spherical gold nanoparticles is strongly affected by the ligand shell structure. Continuous lines formed only when agglomeration was suppressed until the very end of solvent evaporation. This required thick (C12) ligand shells that constitute high tunnel barriers in the final lines. Choosing a suitable amine ligand chemistry made it possible to remove the ligands without destroying the submicron lines and create fully metallic meshes. The result were transparent conductive electrodes with competitive properties.

The particles used here were ligand-dominated in their behavior, and other metal or semiconductor particles have very similar colloidal properties. The principle of high stability with labile anchoring should apply to any inorganic core and can be used to print heterostructures of different nanoparticles, for example.

METHODS

Unless noted otherwise, all chemicals were obtained from Sigma-Aldrich and used without further purification.

Nanoparticle Synthesis. Gold nanoparticles (AuNPs) with a diameter of d = 3.2 nm were synthesized using an adapted protocol from Wu and Zheng:[14] A mixture of 16 mL of pentane (reagent grade, 98%), 16 mL of oleylamine (technical grade, 70%), and 200 mg of $HAuCl_4xH_2O$ was stirred at room temperature and 500 rad min^{-1} for 45 min. Afterward, 80 mg of *tert*-butylamine borane (97%, ABCR) in a mixture of 4 mL of pentane and 4 mL of oleylamine was added. The color of the solution immediately turned to brown. After stirring for 60 min at room temperature, the nanoparticles were purified by precipitating with a mixture of 30 mL of ethanol and 30 mL of methanol and centrifuged at 3000 rpm for 5 min. The supernatant was discarded and the precipitated NPs were redispersed in 20 mL toluene. The NPs were characterized by transmission electron microscopy and small-angle X-ray scattering (micrographs and plotted data in the Supporting Information).

Ligand Exchange. Ligand exchange was performed to coat the AuNPs with 1-butanethiol (99%), 1-octanethiol (≥98.5%), or 1-dodecanethiol (≥98%). The oleylamine-stabilized AuNPs described above were heated between 70 and 80 °C under argon, and ligand (10 times the molar amount of gold) was added. The solution was kept hot for 10 min, cooled to room tempreature, and purified twice by precipitating with a mixture of methanol and ethanol and centrifugation at 3000 rad min^{-1} for 5 min. The resulting NPs were redispersed in cyclohexane to the desired concentration. The same protocol was used to perform ligand exchange from oleylamine to butylamine (99.5%), octylamine (99%, Alfa Aesar), and dodecylamine (≥98%, Fluka); it was repeated three times for all amines.

Fabrication of Polydimethylsiloxane (PDMS) Stamps. The PDMS stamps were prepared in a two-step molding process. A

DOI: 10.1021/acsami.7b18579
ACS Appl. Mater. Interfaces 2018, 10, 6079–6083

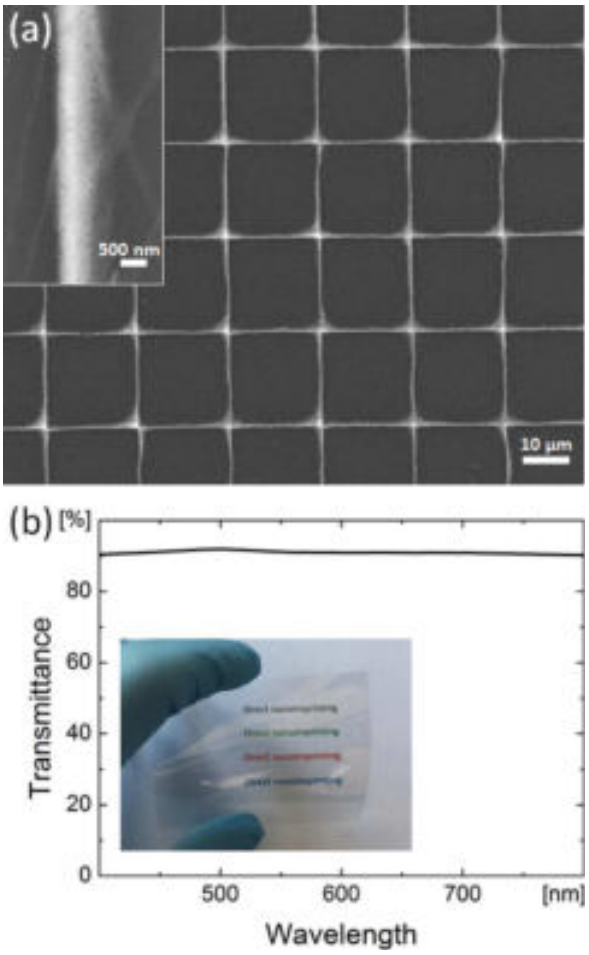

Figure 3. (a) SEM image of a printed grid on glass from AuNP@C12-amine. (b) Corresponding optical ballistic transmittance spectra. Inset shows a photograph of a printed grid on PET foil.

lithographically fabricated silicon master (AMO GmbH, Germany) that carried the desired pattern of the final stamp (patterned area: 7 × 7 cm^2) served as mold for a first PDMS replica, which itself acted as a mold in the final stamp fabrication. The molding procedure was identical for both steps: the prepolymer and the cross-linker of a PDMS kit (10:1 weight ratio; Sylgard 184, Dow Corning) were mixed and degassed in a Speedmixer 5000 HP (Hauschild & Co KG, Germany) at a speed of 2350 rad min^{-1} and a pressure of 1 mbar for 3 min. The mixture was then poured on the structured mold (silicon or PDMS), which had been silanized with trichloro(octadecyl)silane before. A PTFE ring was used as spacer with a glass plate as top sealing and ensured a homogeneous thickness of the PDMS layer. The PDMS was then fully cured at 70 °C, and the PDMS replica was peeled off. We used stamps that carried an array of square-shaped pillars with a pitch of 19.5 μm, a spacing of 1.8 μm, and a height of 4 μm.

Nanoimprinting. The PDMS stamp (3.5 × 7 cm^2) was attached to a steel roller with double-sided tape, and the roller was mounted on a commercial film applicator (TQC GmbH, Germany). The linear movement of the carrier was translated into a rolling motion of the steel roller with the attached stamp. The roller had a diameter of 8 cm and a weight of 3 kg (pressure ≈ 1.4 bar). A volume of 40 μL AuNP dispersion in cyclohexane was dispensed onto the respective substrate. The imprint procedure was immediately started at a speed of 5 mm s^{-1}.

Annealing. thermal treatments were performed on a heating plate (Harry Gestigkeit, Germany) in air. Plasma treatments (5 min) were performed in a RF PICO plasma system (Diener electronic, Ebhausen, Germany) operating at 0.3 mbar gas pressure and 100 W (13.56 MHz) power using either a mixture of 5% hydrogen in argon or pure oxygen.

Characterization. SEM images were recorded using a Quanta 400 ESEM (FEI, Germany). TEM images were acquired with a JEOL JEM 2010 at 200 kV. UV−vis spectroscopy in transmission mode was performed in a Cary 5000 (Varian). The glass substrate was taken as references. SAXS measurements were conducted on a Xeuss 2.0 system (Xenocs SA, France) equipped with a Cu Kα X-ray source (λ = 0.154 nm) operating at 50 kV and 0.6 mA and a Hybrid Photon Counting detector (PILATUS 1M, DECTRIS, Baden, Switzerland). The sample−detector distance was 585 mm. For SAXS measurements of the grids, grids were printed on polyimide (Kapton tape) under the same conditions as on glass. Measurements of the particles in dispersion were performed using capillaries with an inner diameter of 2 mm. Electrical resistance was measured in a 2-point configuration on an area of 1 × 1 cm^2 with an ohmmeter (Voltcraft, Germany). Contacts were made with silver paste. Static contact angle measurements with the needle-in method were performed on glass substrate with an OCA 35 setup (DataPhysics, Neuhausen, Germany).

■ ASSOCIATED CONTENT

Supporting Information

The Supporting Information is available free of charge on the ACS Publications website at DOI: 10.1021/acsami.7b18579.

SAXS of NP dispersion; metal grids printed on glass from AuNP@thiols; SAXS patterns (structure factor) of metal grids; contact angle measurements on glass substrate (PDF)

■ AUTHOR INFORMATION

Corresponding Author

*E-mail: tobias.kraus@leibniz-inm.de.

ORCID

Thomas Kister: 0000-0002-9827-1380

Lola González-García: 0000-0002-8474-6517

Author Contributions

†T.K. and J.H.M.M. contributed equally to this work

Notes

The authors declare no competing financial interest.

■ ACKNOWLEDGMENTS

Funding from the German Federal Ministry of Education and Research in the NanoMatFutur program is gratefully acknowledged. The authors thank Eduard Arzt for his continuing support of the project.

■ REFERENCES

(1) Catrysse, P. B.; Fan, S. Nanopatterned metallic films for use as transparent conductive electrodes in optoelectronic devices. *Nano Lett.* **2010**, *10*, 2944−2949.

(2) Choi, J.-H.; Wang, H.; Oh, S. J.; Paik, T.; Sung, P.; Sung, J.; Ye, X.; Zhao, T.; Diroll, B. T.; Murray, C. B.; Kagan, C. R. Exploiting the colloidal nanocrystal library to construct electronic devices. *Science* **2016**, *352*, 205−208.

(3) Kamyshny, A.; Magdassi, S. Conductive nanomaterials for printed electronics. *Small* **2014**, *10*, 3515−3535.

(4) Morag, A.; Jelinek, R. "Bottom-up" transparent electrodes. *J. Colloid Interface Sci.* **2016**, *482*, 267−289.

(5) Lohman, B. C.; Powell, J. A.; Cingarapu, S.; Aakeroy, C. B.; Chakrabarti, A.; Klabunde, K. J.; Law, B. M.; Sorensen, C. M. Solubility of gold nanoparticles as a function of ligand shell and alkane solvent. *Phys. Chem. Chem. Phys.* **2012**, *14*, 6509−6513.

(6) Hu, P.; Li, K.; Chen, W.; Peng, L.; Chu, D.; O'Neill, W. Fabrication of an organic field effect transistor using nano imprinting

DOI: 10.1021/acsami.7b18579
ACS Appl. Mater. Interfaces 2018, 10, 6079−6083

of Ag inks and semiconducting polymers. *J. Micromech. Microeng.* **2010**, *20*, 075032.
(7) Schneider, J.; Rohner, P.; Thureja, D.; Schmid, M.; Galliker, P.; Poulikakos, D. Electrohydrodynamic nanodrip printing of high aspect ratio metal grid transparent electrodes. *Adv. Funct. Mater.* **2016**, *26*, 833−840.
(8) Reiser, B.; Gerstner, D.; Gonzalez-Garcia, L.; Maurer, J. H. M.; Kanelidis, I.; Kraus, T. Multivalent bonds in self-assembled bundles of ultrathin gold nanowires. *Phys. Chem. Chem. Phys.* **2016**, *18*, 27165−27169.
(9) Maurer, J. H. M.; González-García, L.; Reiser, B.; Kanelidis, I.; Kraus, T. Templated self-assembly of ultrathin gold nanowires by nanoimprinting for transparent flexible electronics. *Nano Lett.* **2016**, *16*, 2921−2925.
(10) Maurer, J. H. M.; González-García, L.; Backes, I. K.; Reiser, B.; Schlossberg, S. M.; Kraus, T. Direct Nanoimprinting of a Colloidal Self-Organizing Nanowire Ink for Flexible, Transparent Electrodes. *Adv. Mater. Technol.* **2017**, *2*, 1700034.
(11) Boles, M. A.; Engel, M.; Talapin, D. V. Self-assembly of colloidal nanocrystals: From intricate structures to functional materials. *Chem. Rev.* **2016**, *116*, 11220−11289.
(12) Talapin, D. V.; Lee, J.-S.; Kovalenko, M. V.; Shevchenko, E. V. Prospects of colloidal nanocrystals for electronic and optoelectronic applications. *Chem. Rev.* **2010**, *110*, 389−458.
(13) Wünscher, S.; Abbel, R.; Perelaer, J.; Schubert, U. S. Progress of alternative sintering approaches of inkjet-printed metal inks and their application for manufacturing of flexible electronic devices. *J. Mater. Chem. C* **2014**, *2*, 10232−10261.
(14) Wu, B.-H.; Yang, H.-Y.; Huang, H.-Q.; Chen, G.-X.; Zheng, N.-F. Solvent effect on the synthesis of monodisperse amine-capped Au nanoparticles. *Chin. Chem. Lett.* **2013**, *24*, 457−462.
(15) Huang, D.; Liao, F.; Molesa, S.; Redinger, D.; Subramanian, V. Plastic-compatible low resistance printable gold nanoparticle conductors for flexible electronics. *J. Electrochem. Soc.* **2003**, *150*, G412−G417.
(16) Wu, Y.; Li, Y.; Ong, B. S.; Liu, P.; Gardner, S.; Chiang, B. High-performance organic thin-film transistors with solution-printed gold contacts. *Adv. Mater.* **2005**, *17*, 184−187.
(17) Wu, Y.; Li, Y.; Liu, P.; Gardner, S.; Ong, B. S. Studies of gold nanoparticles as precursors to printed conductive features for thin-film transistors. *Chem. Mater.* **2006**, *18*, 4627−4632.
(18) Lacava, J.; Born, P.; Kraus, T. Nanoparticle clusters with Lennard-Jones geometries. *Nano Lett.* **2012**, *12*, 3279−3282.
(19) Martin, J. E.; Odinek, J.; Wilcoxon, J. P.; Anderson, R. A.; Provencio, P. Sintering of alkanethiol-capped gold and platinum nanoclusters. *J. Phys. Chem. B* **2003**, *107*, 430−434.
(20) Cademartiri, L.; Ghadimi, A.; Ozin, G. A. Nanocrystal plasma polymerization: from colloidal nanocrystals to inorganic architectures. *Acc. Chem. Res.* **2008**, *41*, 1820−1830.
(21) Maurer, J. H. M.; González-García, L.; Reiser, B.; Kanelidis, I.; Kraus, T. Sintering of ultrathin gold nanowires for transparent electronics. *ACS Appl. Mater. Interfaces* **2015**, *7*, 7838−7842.
(22) Maurer, J. H. M.; Gonzalez-Garcia, L.; Reiser, B.; Kanelidis, I.; Kraus, T. Ultrathin gold nanowires for transparent electronics: Soft sintering and temperature stability. *Phys. Status Solidi A* **2016**, *213*, 2336−2340.
(23) Koslowski, B.; Boyen, H.-G.; Wilderotter, C.; Kästle, G.; Ziemann, P.; Wahrenberg, R.; Oelhafen, P. Oxidation of preferentially (111)-oriented Au films in an oxygen plasma investigated by scanning tunneling microscopy and photoelectron spectroscopy. *Surf. Sci.* **2001**, *475*, 1−10.
(24) Hoft, R. C.; Ford, M. J.; McDonagh, A. M.; Cortie, M. B. Adsorption of amine compounds on the Au (111) surface: a density functional study. *J. Phys. Chem. C* **2007**, *111*, 13886−13891.
(25) Hecht, D. S.; Kaner, R. B. Solution-processed transparent electrodes. *MRS Bull.* **2011**, *36*, 749−755.
(26) Pensa, E.; Cortés, E.; Corthey, G.; Carro, P.; Vericat, C.; Fonticelli, M. H.; Benítez, G.; Rubert, A. A.; Salvarezza, R. C. The chemistry of the sulfur−gold interface: in search of a unified model. *Acc. Chem. Res.* **2012**, *45*, 1183−1192.

DOI: 10.1021/acsami.7b18579
ACS Appl. Mater. Interfaces 2018, 10, 6079−6083

Supporting Information

Ligand-dependent nanoparticle assembly and its impact on the printing of transparent electrodes

Thomas Kister, Johannes H. M. Maurer, Lola Gonzalez-Garcia, and Tobias Kraus*

INM – Leibniz Institute for New Materials, Campus D2 2, 66123 Saarbrücken, Germany.

E-mail: tobias.kraus@leibniz-inm.de

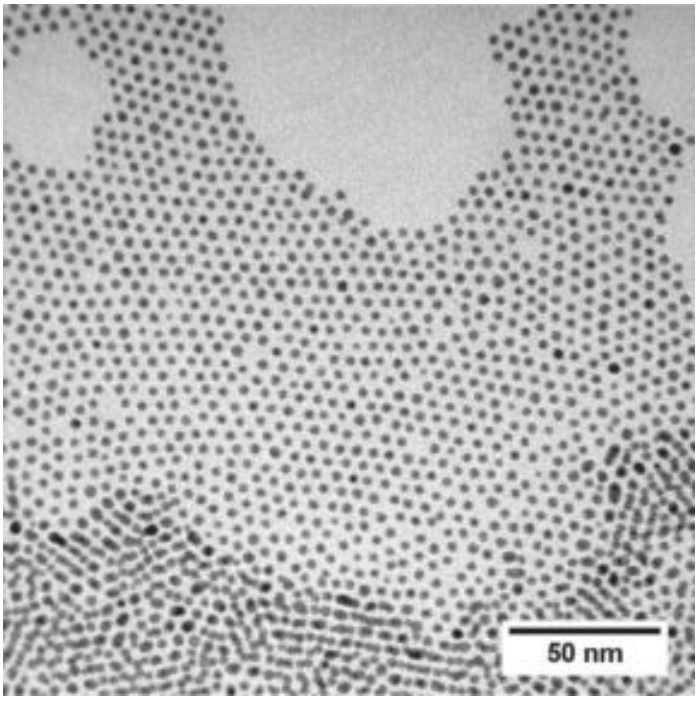

Figure S1. Transmission electron micrograph of AuNP@oleylamine.

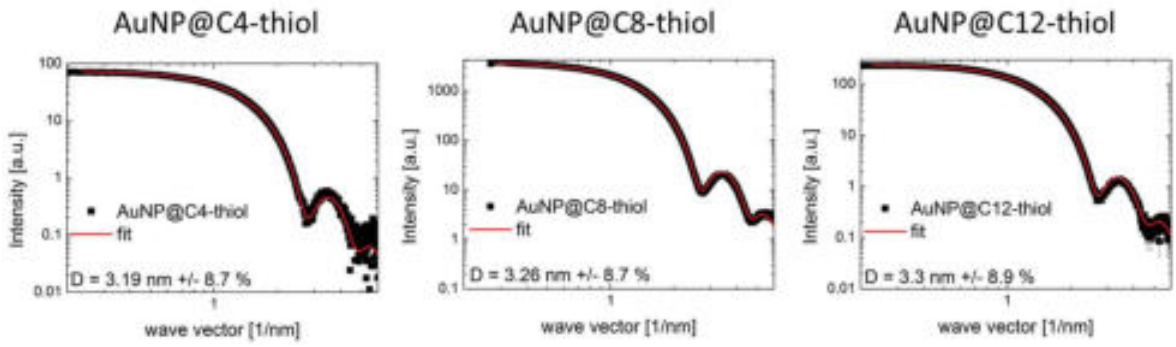

Figure S2. SAXS patterns of AuNP@thiols in cyclohexane after ligand exchange.

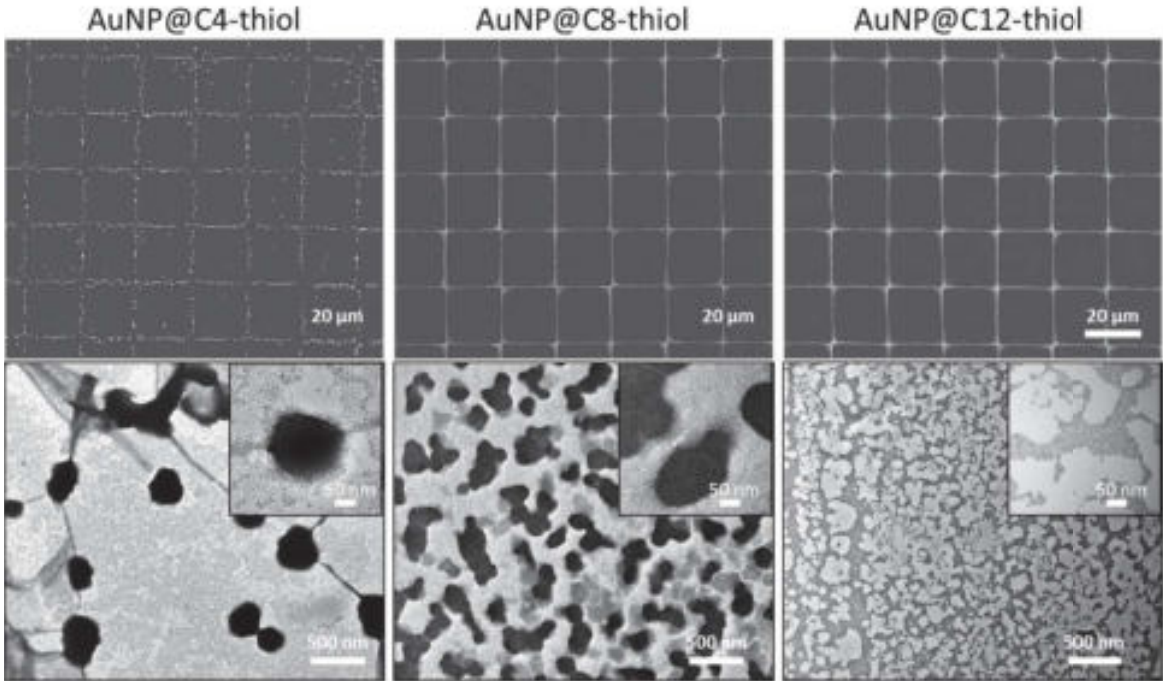

Figure S3. Scanning and transmission electron microscopy micrographs of metal grids printed on glass from AuNP@thiols.

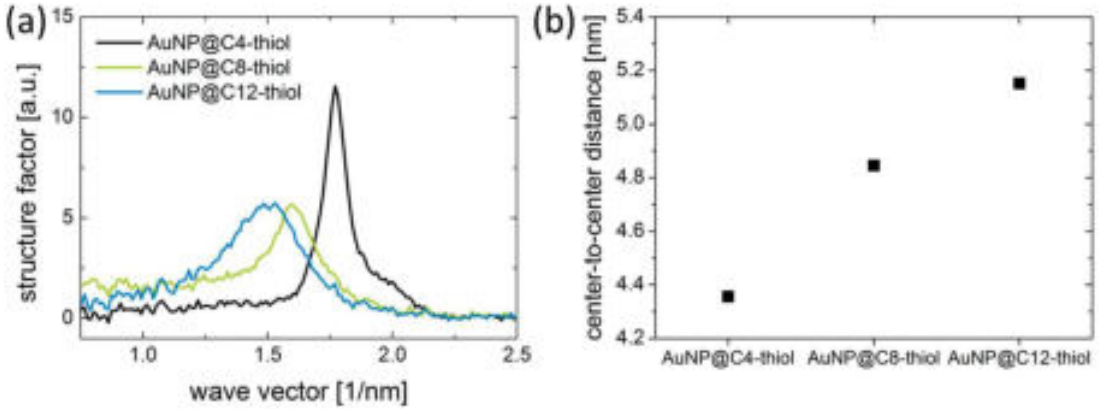

Figure S4. (a) SAXS patterns (structure factor) of metal grids printed on polyimide (Kapton^{TM}). (b) Center-to-center distance between particles in the printed lines calculated from the peak positions in (a).

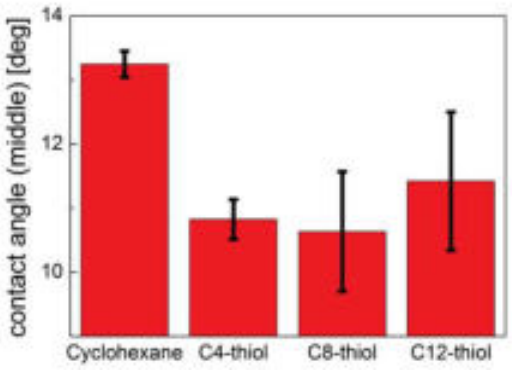

Figure S5. Contact angle measurements on glass substrate for cyclohexane and dispersions of AuNP@thiols in cyclohexane.

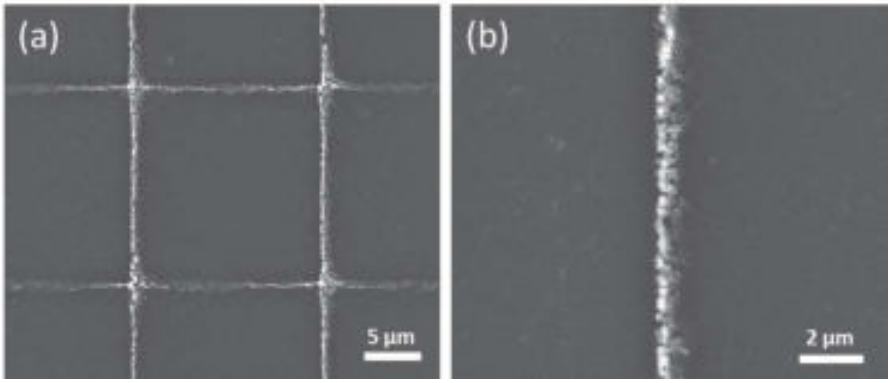

Figure S6. Scanning electron micrographs of printed metal grids from AuNP@C12-thiol after 5 min sintering at 200°C. (a) shows a low magnification and (b) a high magnification micrograph of the same area.

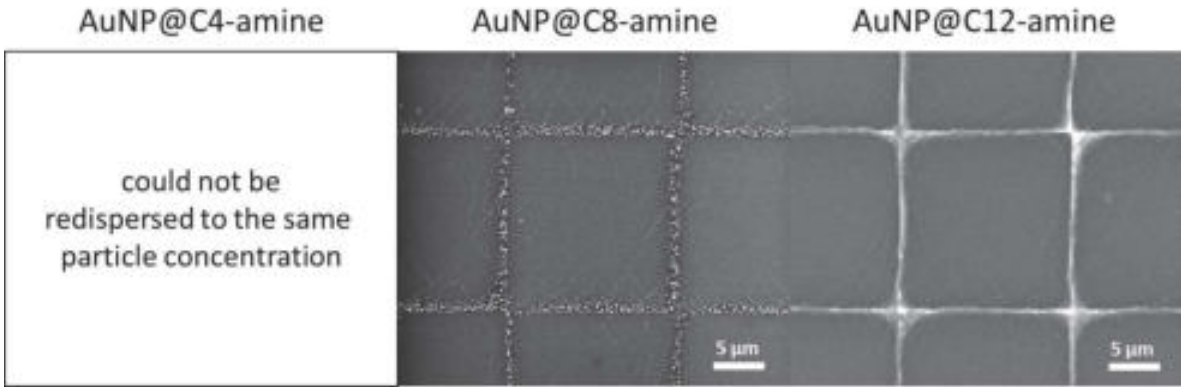

Figure S7. Scanning electron micrographs of printed metal grids from AuNP@amines.

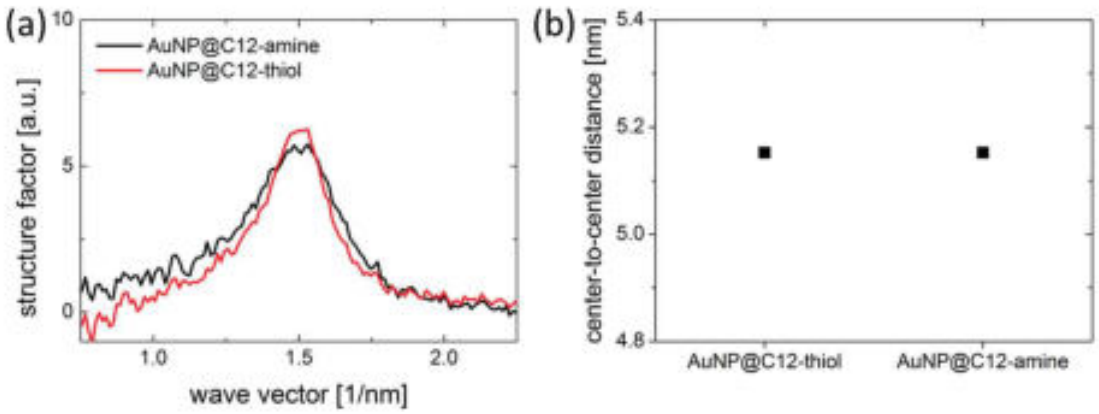

Figure S8. (a) SAXS patterns (structure factor) of metal grids from AuNP@C12-thiol and AuNP@C12-amine printed on polyimide (Kapton™). (b) Center-to-center distance between particles in the printed lines calculated from the peak positions in (a).

3.6 Publication 6

Reproduced from

Kister, T., Mravlak, M., Schilling, T., & Kraus, T. (2016). Pressure-controlled formation of crystalline, Janus, and core–shell supraparticles. Nanoscale, 8(27), 13377-13384.

DOI: 10.1039/C6NR01940D (Paper) Nanoscale, 2016, 8, 13377-13384

with permission from the Royal Society of Chemistry.

Nanoscale

PAPER

View Article Online
View Journal | View Issue

Cite this: *Nanoscale*, 2016, **8**, 13377

Pressure-controlled formation of crystalline, Janus, and core–shell supraparticles†

Thomas Kister,[a] Marko Mravlak,[b] Tanja Schilling[b] and Tobias Kraus*[a]

Received 7th March 2016,
Accepted 18th June 2016

DOI: 10.1039/c6nr01940d

www.rsc.org/nanoscale

Binary mixtures of nanoparticles self-assemble in the confinement of evaporating oil droplets and form regular supraparticles. We demonstrate that moderate pressure differences on the order of 100 kPa change the particles' self-assembly behavior. Crystalline superlattices, Janus particles, and core–shell particle arrangements form in the same dispersions when changing the working pressure or the surfactant that sets the Laplace pressure inside the droplets. Molecular dynamics simulations confirm that pressure-dependent interparticle potentials affect the self-assembly route of the confined particles. Optical spectrometry, small-angle X-ray scattering and electron microscopy are used to compare experiments and simulations and confirm that the onset of self-assembly depends on particle size and pressure. The overall formation mechanism reminds of the demixing of binary alloys with different phase diagrams.

1 Introduction

Confined nanoparticles can spontaneously arrange into regular superlattices.[1–3] Binary mixtures of uniform particles thus arrange at liquid–air interfaces,[1] liquid–liquid interfaces,[3] and inside droplets.[4] Self-assembly can be explained by a combination of entropic space-filling arguments and minimization of the interparticle potentials, with relative contributions that depend on the particle core, ligand shell, solvent, and process parameters. The large parameter space leads to a remarkable structural diversity of the superstructures.[1,2] Particle films are probably the best-studied system, and they may find applications as semiconductor layers in devices.[5,6]

Less is known on particle self-assembly mechanisms inside droplets. Mixtures of particles have not yet been assembled inside emulsions, although uniform nanoparticle dispersions confined to the dispersed phase of an emulsion form well-defined clusters known as supraparticles.[4,7,8] Similar structures have been created by drying droplets on superamphiphobic surfaces.[8]

In this contribution, we study the structure of binary supraparticles that form inside emulsions. We obtained supraparticles with different structures when evaporating the droplets of an oil-in-water emulsion (Fig. 1). Supraparticles with AB_{13} superlattice structure,[1] Janus-type demixed supraparticles,[9] or core–shell particles[10] formed (Fig. 1) from the same particle mixtures depending on surfactant or external pressure. Structured particles are of interest for a range of applications: Patchy particles self-assemble into soft materials,[11] Janus particles form extremely stable Pickering emulsions,[12] and metal–oxide particles improve homogeneous (photo)catalysis,[13] for example.

Particle assembly in emulsions lends itself naturally to *in situ* observation. In contrast to superlattices that form in a highly dynamic evaporating liquid film, evaporating emulsions are easily observed *via* spectrometry. We used a combination of scattering and transmission methods to assess the formation routes of the different supraparticle geometries. A comparison with detailed molecular dynamics simulations strongly suggests that even moderate pressure differences inside the droplets change the interparticle potentials, affect the nucleation behavior, and trigger different assembly routes.

2 Experimental section

All chemicals were obtained from Sigma Aldrich (unless noted otherwise) and used without further purification.

2.1 Nanoparticle synthesis

Gold nanoparticles (AuNP) with diameters of 4 nm or 8 nm were synthesized using a modified protocol based on the original method by Wu and Zheng.[14] 8 nm nanoparticles were produced as follows. A mixture of 8 mL benzene (puriss. ≥99.7%), 8 mL oleylamine (technical grade, 70%) and 100 mg of $HAuCl_4{\cdot}xH_2O$ was stirred at 20 °C and 500 rad min^{-1} for

[a]*INM – Leibniz Institute for New Materials, Campus D2 2, 66123 Saarbrücken, Germany. E-mail: tobias.kraus@leibniz-inm.de; Fax: +49681 9300 279; Tel: +49681 9300 389*

[b]*Theory of Soft Condensed Matter, Physics and Materials Science Research Unit, Université du Luxembourg, L-1511 Luxembourg, Luxembourg*

†Electronic supplementary information (ESI) available. See DOI: 10.1039/C6NR01940D

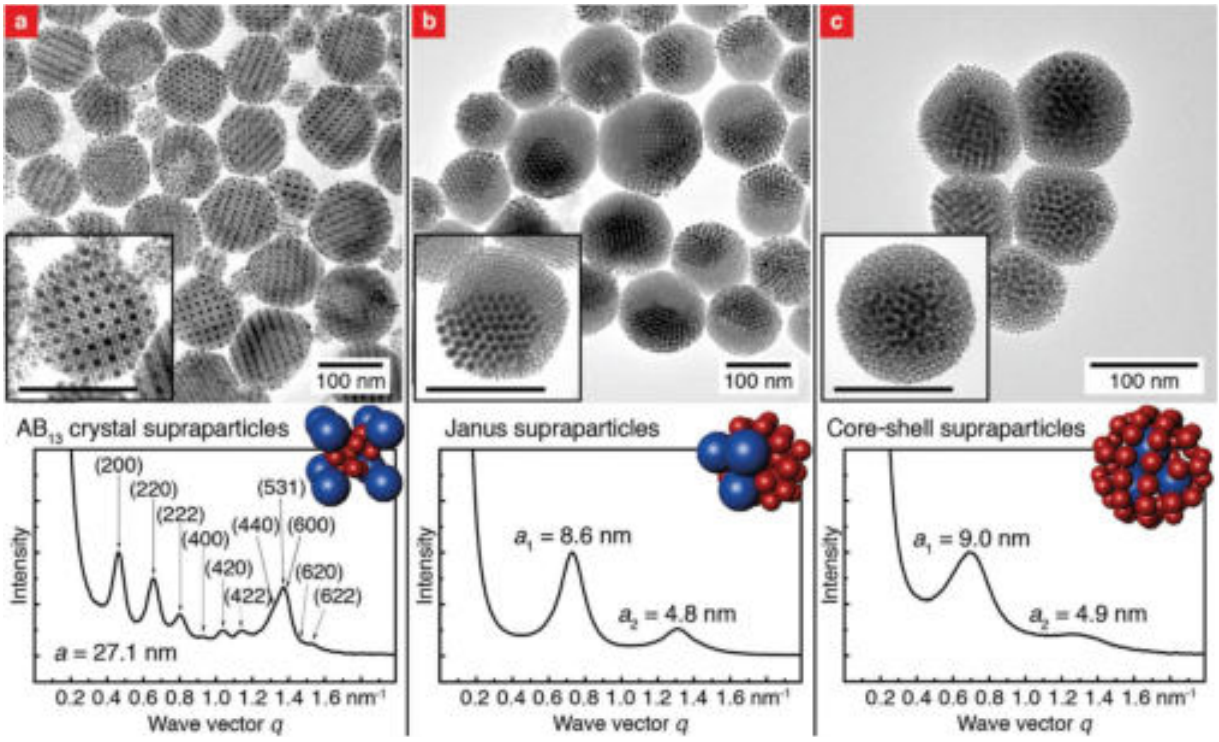

Fig. 1 Supraparticles containing hexadecanethiol-coated gold nanoparticles with diameters of 4 nm and 8 nm in a concentration ratio of 13 : 1 observed with transmission electron microscopy (TEM) and small-angle X-ray scattering (SAXS). All supraparticles were formed in hexane-in-water emulsions stabilized with different surfactants. (a) Superlattice particles formed with Triton X-100. The peaks correspond to the AB_{13} structure.[17] (b) Janus supraparticles formed with Triton X-102 or X-165. Each was composed of two pure, single nanoparticle crystals that cause distinct peaks in SAXS. (c) Core–shell supraparticles formed with Triton X-705. A crystalline core of 8 nm particles was surrounded by a random dense packing of 4 nm particles that cause a broad, shifted peak in SAXS. The supraparticle radii and dispersities for (a), (b) and (c) were 47.0 nm ± 31%, 46.2 nm ± 22% and 47.8 nm ± 26%, respectively.

1 min. Afterwards 40 mg *tert*-butylamine borane (ABCR, 97%) which was dissolved in 2 mL benzene and 2 mL oleylamine was added to the solution. The color of the solution immediately became dark purple. After stirring for 60 min at 20 °C, the nanoparticles were purified once by precipitating with 30 mL ethanol and centrifugation at 4000 rad min^{-1} for 5 min. The precipitated nanoparticles were redispersed in 20 mL heptane (puriss. ≥99%). AuNP with a diameter of 4 nm were obtained using pentane (reagent grade, 98%) instead of benzene and stirring for 30 min before adding *tert*-butylamine borane.

2.2 Nanoparticle characterization

The core size of the NPs was measured by analyzing transmission electron microscopy (TEM) micrographs taken with a JEOL JEM 2010 at 200 kV (Fig. S1 and S2 in the ESI†). A minimum of 2000 particles was counted with the ImageJ 1.45s software for each size.

2.3 Ligand exchange

The ligands of the AuNP were exchanged to make them suitable for supraparticle formation.

Oleylamine-stabilized AuNP from above were heated to 80 °C under argon. A solution of triphenylphosphine (≥98.5% GC, 5 times the amount of gold) in heptane was also heated to 80 °C and added to the AuNP. After stirring for 60 s, the color of the solution turned from dark purple to dark blue and finally to black, indicating agglomeration. Upon addition of 1-hexadecanethiol (≥95.0% GC, 10 times the amount of gold), the solution immediately returned to purple, indicating deagglomeration. The mixture was stirred at 80 °C for 10 min. The resulting particles were purified once by precipitation with ethanol and centrifugation and resuspended in hexane (CHROMASOLV ≥ 95%).

2.4 Supraparticle synthesis

All supraparticles contained AuNP with core diameters of 4 nm and 8 nm.

To prepare supraparticles, 16 mL of ultrapure water containing a surfactant[15] (Triton X-100 (laboratory grade), X-102 (Dow Chemical, 100%), X-165 (Dow Chemical, 70%), X-305 (Dow Chemical, 70%), X-405 (Dow Chemical, 70%), X-705 (Dow Chemical, 70%), or sodium dodecyl sulfate (≥98.0% GC), concentrations listed in Table 1) and 320 μL of hexane with AuNP

Table 1 Concentration of the surfactants in the water phase and the corresponding critical micelle concentrations

Surfactant	Concentration [g L^{-1}]	CMC [g L^{-1}]
X-100	9.45	0.189
X-102	13.4	0.267
X-165	28.5	0.570
X-305	19.2	1.92
X-405	24.4	2.44
X-705	35.9	3.59

carrying 1-hexadecanethiol ligand shells were stirred with an Ultra-Turrax (Janke Kunkel, T25 S5) shear emulsifier at 20 000 rad min^{-1} for 30 min. The resulting hexane-in-water emulsion was heated to 50 °C for 12 h in an open vessel. Upon evaporation of the hexane the nanoparticles arranged into supraparticles.[4]

2.5 Supraparticle characterization

The structure of the supraparticles was analyzed by TEM (JEOL JEM 2010 at 200 kV) and small angle X-ray scattering (SAXS) in a Xeuss 2.0 (Xenocs SA, Grenoble, France) setup equipped with a copper Kα (λ = 0.154 nm) X-ray source and a Hybrid Photon Counting detector (PILATUS 1M, DECTRIS, Baden, Switzerland). Sample to detector distance was capped between 1240 mm and 2500 mm.

The size of the supraparticles was measured from the dynamic light scattering (DLS) at 90 degree using a Wyatt Technology DynaPro Titan with a laser wavelength of 831.2 nm. The dispersity (indicated after the respective mean radius) is defined as the ratio of standard deviation and mean radius. The evaluated regularization expansion of the autocorrelation was fitted with the Dynals algorithm (supplied by Alango).

The supraparticles were washed twice for TEM analysis (centrifugation at 500 rcf for 20 min, removing supernatant and redispersing with clear water) to remove the excess surfactant. Small angle X-ray scattering showed no effect of the washing steps on the supraparticles' structure.

2.6 Pendant drop tensiometry

Interfacial tensions were measured using the pendant drop method in an OCA 35 (Dataphysics, Neuhausen, Germany) setup. An aqueous solution of the surfactant in question with the concentration used in the emulsion was held in a glass cuvette. Pure hexane was injected from a J-shaped cannula until a drop formed. The volume of the drop was adjusted to almost detach from the cannula. The shape of the pendant drop was recorded by a digital camera until the drop reached equilibrium. The final shape was fitted with the Young–Laplace equation to calculate interfacial tension. The arithmetic mean and the standard deviation were calculated from a minimum of 200 calculated tension values obtained in the equilibrium state.[16] The measurements were performed at 25 °C and 50 °C.

2.7 Pressure dependent experiments

A pressure chamber (type: Drifton 25-DY, Drifton, 2650 Hvidovre, Denmark) was used to produce supraparticles under external hydrostatic pressure. Freshly prepared emulsion was placed into an open vessel inside the chamber. Excess pressure was applied by filling the headspace with compressed nitrogen. A mechanical manometer indicated the pressure inside the chamber.

Pressure-dependent *in situ* SAXS measurements were performed in a capillary with two open ends. A valve was mounted at the output of the capillary to close the channel after the sample had been introduced. A syringe pump (Nemesys) held a gas-tight glass syringe that we connected to the open end of the capillary to apply pressure. An electronic pressure sensor was mounted between the syringe pump and the flow capillary to monitor the applied pressure.

3 Results and discussion

Hexane-in-water emulsions were prepared with nanoparticles in the oil phase and non-ionic surfactants (octylphenol ethoxylates, trade name 'Triton') with hydrophilic tails of varying molecular weights in the aqueous phase. We mainly used hexane for its conveniently low boiling point, but heptane or toluene led to similar results (not shown here).

The nanoparticles had gold cores with diameters of 4 nm and 8 nm and narrow size distributions with relative standard deviations of the diameter between 5 and 7%. They were coated with hexadecanethiol self-assembled monolayers that made them dispersible in hexane but incompatible with water. The particle concentrations were 3.9×10^{15} mL^{-1} and 3×10^{14} mL^{-1} for 4 nm and 8 nm, respectively.

Supraparticles were formed by gently evaporating the oil phase at 50 °C. Hexane slowly evaporated from the emulsion until the droplets had shrunk from their initial diameter of 2 μm to an average of 150 nm. Typical standard deviations were around 15% to 20% as measured by dynamic light scattering.

During evaporation, the nanoparticle mixtures in the droplets arranged into regular structures. Fig. 1a shows supraparticles that remind of $NaZn_{13}$, a phase that has been reported for nanoparticle superlattices in thin films.[1] The AB_{13} lattice appears to be almost undisturbed even in small supraparticles. This is in contrast to supraparticles consisting of only one particle size, which deviate from close packing and exhibit lower-symmetry geometries known from atomic clusters.[4]

AB_{13} supraparticles only formed with Triton X-100 (Fig. 1a). Surfactants with longer hydrophilic tails such as Triton X-102 and X-165 led to the formation of Janus-type supraparticles composed of two 'pure' supercrystals of nanoparticles each (Fig. 1b). The surfactants with the longest hydrophilic chains, Triton X-305, X-405, and X-705, gave rise to core–shell supraparticles in which a crystalline core of large nanoparticles was surrounded by a randomly packed shell of smaller nanoparticles (Fig. 1c).

Different formation mechanisms could be evoked to explain the surfactant-dependent structure of the supraparticles. Marangoni flows can separate nanoparticles with different sizes in sessile drops.[18,19] Such flows are characterized by the Marangoni number Ma ≡ $|d\sigma/dT|\Delta TR/(\eta\alpha)$, where $d\sigma/dT$ is the change of the interfacial tension with temperature, ΔT is a temperature difference, R the radius of the droplet, a the dynamic viscosity and α the thermal diffusivity. An upper bound for Ma for hexane as used in our experiments is 5, far below the critical number of 80 reported for the onset of Marangoni flows,[19] which excludes Marangoni flows as an explanation for the formation of different supraparticles.

Pickering-Ramsden emulsions with nanoparticles trapped at the liquid–liquid interfaces[20,21] can also be excluded as structure-directing mechanism. Alkanethiol-coated gold nanoparticles with 6 nm diameter do not segregate to hexane–water interfaces with Triton X-100.[16] Likewise, interfacial tension measurements that we performed indicated no segregation for any of the surfactants that we used here.

We believe that the formation of supraparticles is dominated by nucleation: different supraparticles form when self-assembly starts at different particle concentrations. Dispersibility sets an upper critical concentration for agglomeration (in the following, we call all processes that lead to dense particle packings 'agglomeration', regardless of whether the particles self-assemble into regular lattices or form amorphous structures). If dispersibility is high (for repulsive interparticle potentials), agglomeration occurs late in the evaporation process, when high particle concentrations are reached. If it is low (for attractive interparticle potentials), agglomeration occurs earlier, at lower particle concentrations.

Fig. 2a shows the formation of AB_{13} supraparticles in emulsions stabilized by Triton X-100 (with an average of 9 to 10 ethoxylate units as hydrophilic chain). First changes became visible after 150 min; an AB_{13} structure formed after 180 min. Further evaporation did not change the structure, but the lattice spacing decreased as indicated by peak shifts.

Now consider the evaporation of emulsions stabilized by Triton X-165 (with an average of 16 ethoxylate units as hydrophilic chain) shown in Fig. 2b: after 240 min of evaporation, the larger nanoparticles started to agglomerate, as indicated by a peak in SAXS. After 420 min, a second peak indicated the agglomeration of the smaller particles that have a larger critical concentration. Large particles agglomerate first because they attract each other more strongly than smaller particles.[22] The smaller particles agglomerate in a separate crystal later, and both are joined into a Janus supraparticle by the shrinking droplet.

The onset of self-assembly was shifted to even larger concentrations when using Triton X-705 (with an average of 55 ethoxylate units) as shown in Fig. 2c. Agglomeration of the larger particles set in after 270 min, and the smaller nanoparticles did not agglomerate until an abrupt transition after 660 min. At this point, there was little free volume left; the small particles arranged into a shell around the existing crystal of large particles and formed a core–shell supraparticle.

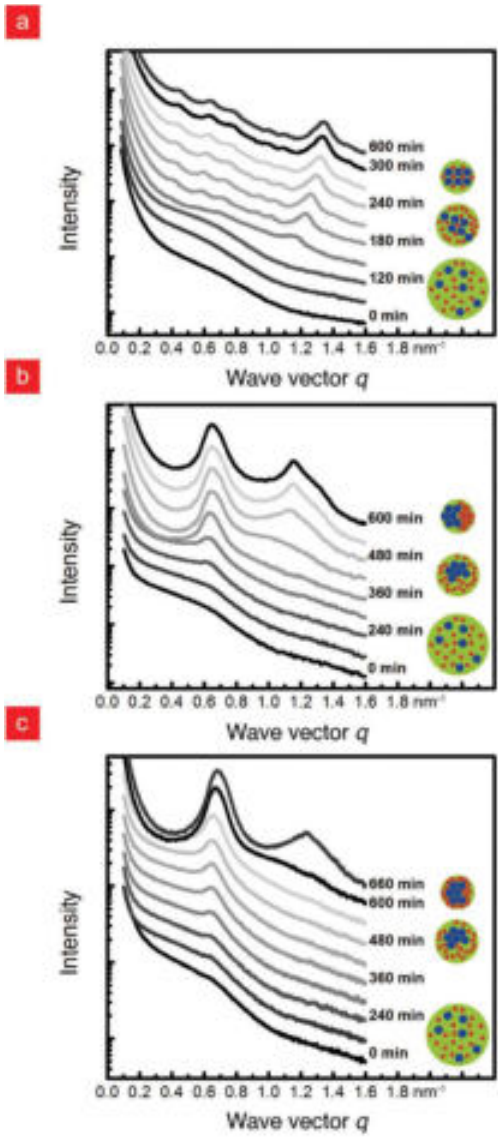

Fig. 2 (a) Evaporation of a Triton X-100 stabilized emulsion. Minor changes became visible after 150 min of evaporation. A clear AB_{13} superlattice formed after 180 min. (b) Evaporation of a Triton X-165 stabilized emulsion. After 240 min of evaporation, the larger particles began to agglomerate and caused a broad SAXS peak. Upon prolonged evaporation, the larger nanoparticles agglomerated further, followed by agglomeration of the smaller particles after an additional 200 min. Further increase of confinement compressed the agglomerates and shifted the peaks. (c) SAXS observation of the evaporation of a particle-containing emulsion stabilized with Triton X-705 at larger Laplace pressure. After 270 min of evaporation, the larger particles began to agglomerate. The smaller particles remained dispersed much longer than for Triton X-165 and abruptly agglomerated in the end.

In contrast, particles in emulsion droplets stabilized with Triton X-100 (with an average of 9.5 ethoxylate units) agglomerated at a critical concentration that was reached long before all

hexane had evaporated, much earlier than for X-165 and X-705. This is readily explained if we assume a stronger attraction between nanoparticles in droplets with Triton X-100 than between nanoparticles in droplets with Triton X-165.

We performed molecular dynamics simulations[23] to test which interaction potentials between nanoparticles lead to the observed structures. Disordered binary mixtures of 7000–14 000 nanoparticles were confined in a hard spherical container and then left to equilibrate. The self-assembly of particles with a purely repulsive Weeks–Chandler–Andersen (WCA) pair potential[24] was compared to particles with a more attractive Lennard-Jones potential. Intermediate cases were modeled by linearly superimposing the potentials.

Fig. 3a–c shows the final configurations for different interaction potentials. Purely repulsive particles that were confined at high concentrations to a container with fixed volume readily arranged into AB_{13} crystals. This is in agreement with previous studies.[17,25] Adding identical attraction to all particles (regardless of their size) in the same container led to AB_{13} crystals, too.

Simulations in shrinking containers emulate the effect of droplet evaporation. When we added attractive interactions only to the large particles in a mixture that we confined to a shrinking container, core–shell supraparticles formed. This models cases where the van der Waals attraction between larger particles dominates agglomeration.[22] When we added attractive interactions to both particle types, Janus supraparticles formed. Fig. 3d shows the formation stages of a Janus supraparticle: separate agglomerates of the larger particles nucleated and merged, while the smaller particles remained disordered. Crystallization of the smaller particles occurred at a later stage. This is consistent with our assembly model and the SAXS data presented above: larger particles exhibit stronger attractive interactions than smaller particles with the same ligand molecules.

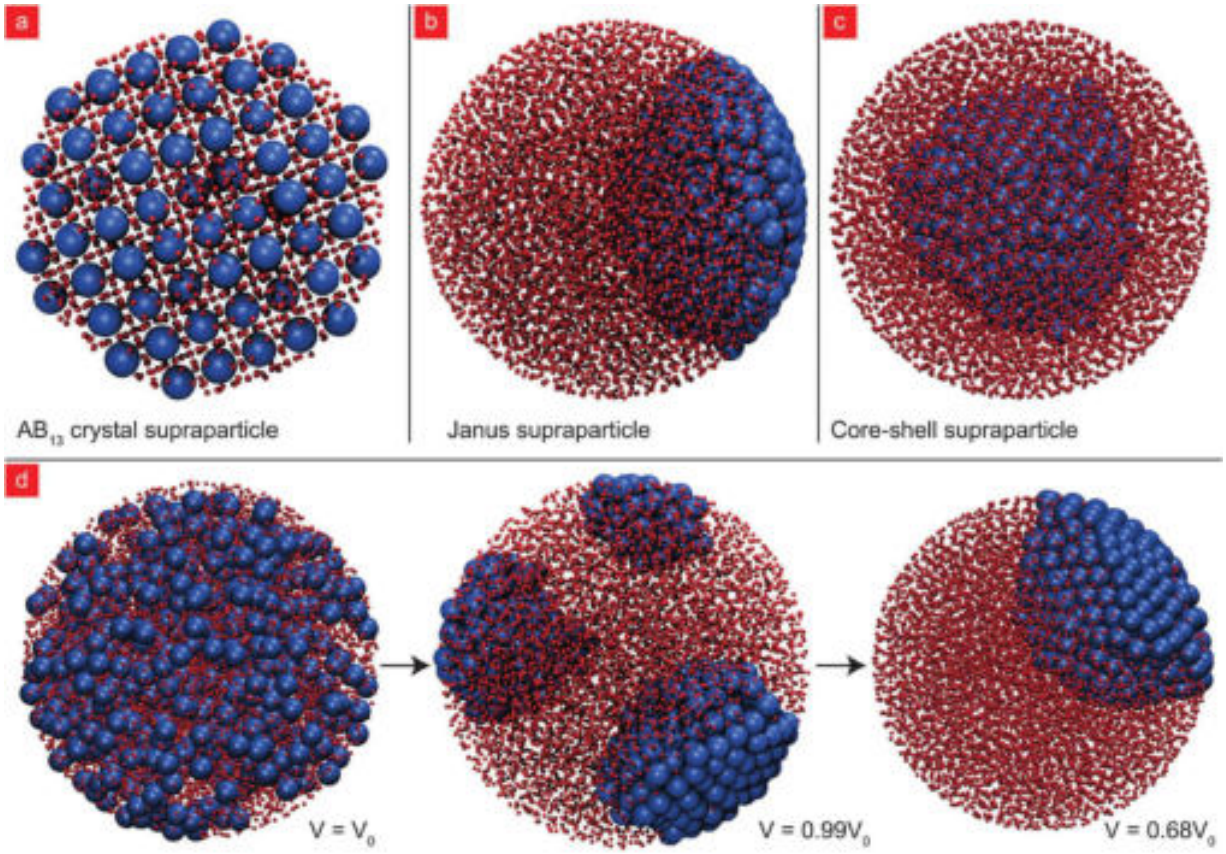

Fig. 3 Molecular dynamic simulations of nanoparticles confined in a spherical container that shrank during the simulation (with the exception of panel (a)). (a) AB_{13}-structured supraparticles with entropically dominated structures formed with purely repulsive particle interactions that approximate the high pressure regime. The same AB_{13} lattice also formed when all particles attracted each other, as in the low pressure experiments. (b) Weak interactions between the larger nanoparticles led to a core–shell structure. (c) Attractions that scale with particle size led to Janus particles. (d) Snapshots of the formation of a Janus supraparticle in a shrinking container. The left image shows the fully dispersed state just before agglomeration occurred. The larger particles agglomerated slowly in different parts of the volume, moving in between the disordered smaller particles. The agglomerates then joined to form a crystal at one side of the volume. Finally, the smaller particles crystallized in the remaining volume. The volume change between the first agglomeration events and the fully arranged state is approximately 30%.

But how do the emulsion surfactants change the potentials between nanoparticles inside the droplets? The members of the Triton class of surfactants differ solely in the length of their polyethylene glycol chains. It is highly unlikely that chemical interactions with the liquid–liquid interface can change the interactions between particles inside the oil droplets. The experiments that we discuss below strongly suggest that *pressure* links surfactant and particle interactions. Detailed molecular-scale studies will be required to reveal the precise mechanism that may be connected to the solubility of water in the oil and the arrangement of the ligand shell.

The pressure inside an emulsion droplet of radius r depends on the interfacial tension γ of the liquid–liquid interface through the Laplace pressure, $\Delta p_L = 2\gamma/r$.[26] The interfacial tension, in turn, depends on the surfactant. We measured γ of the hexane–water interface for different surfactants by tensiometry on macroscopic drops at concentrations above the critical micelle concentration (CMC) (Fig. 4a). The results imply that droplets with a diameter of 150 nm (the average final size of the evaporating droplets) have Laplace pressures between 10 kPa for Triton X-100 and 300 kPa for Triton X-705.

The supraparticle structure depended on interfacial tension but not on the exact chemical nature of the surfactant. For example, the anionic surfactant sodium dodecyl sulfate (SDS) produced Janus-type supraparticles just as Triton X-165. This suggests that it is the Laplace pressure that affects interparticle potential and thus, supraparticle formation.

Pressure affects the dispersibility of nanoparticles in supercritical fluids. Korgel demonstrated that the critical concentration for the agglomeration of alkylthiol-stabilized gold nanoparticles in supercritical ethane increases with pressure.[27] When we applied *external* isostatic pressure to particle-laden emulsions, SAXS indicated pressure-dependent dispersibility (Fig. 4b), too: agglomerates of the larger particles dissolved when we increased the pressure and formed when we lowered it. The transition was reversible and fast; agglomerates decomposed in seconds. Small particles were consistently more soluble than big particles, probably due to the size dependence of van der Waals attraction.[22] We conclude that pressure reduces the attractive interactions between particles.

To test our hypothesis, we emulated the effect of Laplace pressure by applying external isostatic pressure on evaporating emulsions stabilized with Triton X-100 (Fig. 5a–d). AB_{13} superlattices formed at environmental pressure. Janus supraparticles formed at an external pressure of 100 kPa, and core–shell supraparticles at 300 kPa, respectively. The pressures necessary to 'switch' between different supraparticle structures were comparable to the differences in Laplace pressure caused by different surfactants.

The core–shell structures formed at 300 kPa of external pressure had cores with a higher degree of crystalline perfection than supraparticles formed with Triton X-705. The reason is probably the dependence of Laplace pressure on droplet size. When an emulsion stabilized with Triton X-705 evaporates, droplets shrink and the Laplace pressure strongly changes with time. Interactions between particles change continuously and perturb assembly. In contrast, external pressure is independent of droplet size, and crystallization is less perturbed.

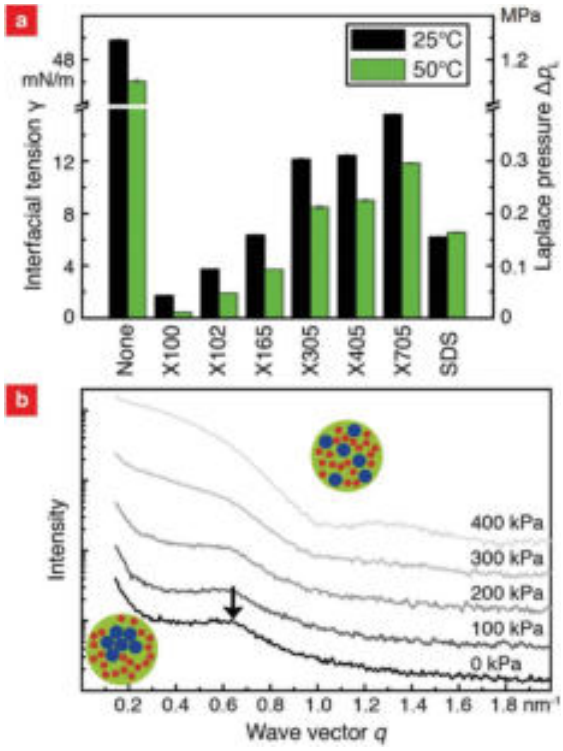

Fig. 4 (a) The pressure inside emulsion droplets depends on the surfactant. Hanging droplet tensiometry indicates the interfacial tensions between *n*-hexane and water with different surfactants at 25 and 50 °C. The right axis indicates the calculated Laplace pressure that acted on the particles in a droplet with a radius of 80 nm for the respective surfactant. (b) Pressure-dependent SAXS of particle-containing emulsions stabilized with Triton X-165 proves the pressure-dependent dispersibility of nanoparticles. The emulsion was partially evaporated for 240 min at 50 °C and ambient pressure. After this time the larger nanoparticles began to agglomerate (SAXS peak is indicated by an arrow). Upon applying external isostatic pressure on the partially evaporated emulsion, the agglomerates rapidly dissolved, and the peak was replaced by the characteristic Porod rise towards large q that indicates dispersion.

Surprisingly, the low-density AB_{13} structure (28% volume fraction of cores) gradually returned in the supraparticles when increasing external pressure up to 1000 kPa (Fig. 5c and d). The external pressure required to return to AB_{13} was larger for Triton X-100 than for Triton X-165 or X-705. Janus and core–shell supraparticles had a packing fraction above 40% (see ESI†). This excludes simple space-filling arguments as an explanation for the pressure-dependent supraparticle structure. The effects of external pressure on supraparticle structure can only be explained by pressure-dependent particle–particle interactions that change the sequence of nanoparticle agglomeration during solvent evaporation.

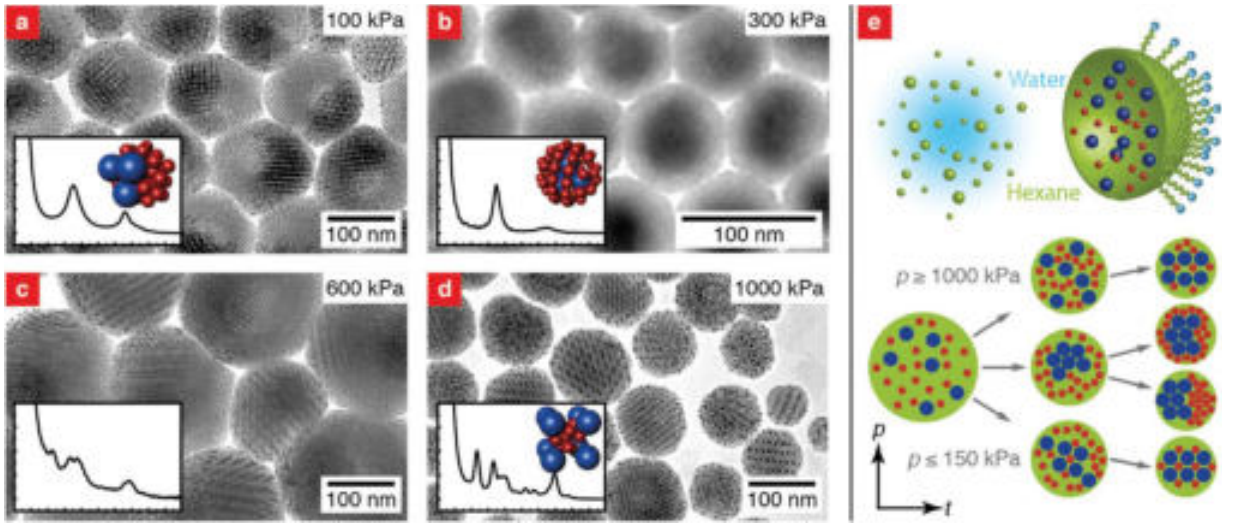

Fig. 5 Supraparticles formed in emulsions stabilized by Triton X-100, with external pressure applied. (a) 100 kPa isostatic external pressure yielded Janus supraparticles, (b) 300 kPa yielded core–shell supraparticles. (c) At 600 kPa, supraparticles with partial AB_{13} and Janus formed, and at (d) 1000 kPa, the entire supraparticles had AB_{13} structures. Inserts show the respective SAXS data. (e) Proposed formation mechanisms of the supraparticles. If the pressure inside an emulsion droplet is low, agglomeration happens early and supraparticles form *via* nucleation-and-growth. If it is high, particles remain dispersed and confinement causes late supraparticle formation. Intermediate pressures lead to intermediate situations due to the different dispersibility of large and small nanoparticles. The supraparticle radii and dispersities for (a), (b), (c) and (d) were 53.4 nm ± 26%, 119.5 nm ± 30%, 87.4 nm ± 18% and 44.8 nm ± 22%, respectively.

A formation mechanism based on a combination of agglomeration and confinement sketched in Fig. 5e explains the observations. Some of the processes described below are akin to the formation of Janus particles in flame spray pyrolysis, where a mixed phase decomposes into a solid and a liquid that solidifies later.[28]

At low pressures, agglomeration occurs long before all hexane has evaporated, and AB_{13} forms. At high pressures, dispersibility is increased, and the particles remain dispersed until almost all hexane has evaporated. The AB_{13} lattice then forms due to confinement. At intermediate pressures, the larger particles agglomerate at high particle concentrations, when little hexane remains. Low solvent content reduces the spacing between particles and inhibits relative particle motion. The particles' mobility is insufficient to reach the complex AB_{13} arrangement. Instead, the smaller particles agglomerate into single crystals, and Janus supraparticles form. A narrow range of pressures exists where agglomeration of the large particles is possible, but the smaller particles remain dispersed until almost all hexane has evaporated. This situation leads to core–shell supraparticles: confinement holds a disordered shell of small particles around the previously formed core of larger particles.

The particle–particle interactions depended on the type of ligand used. Particles with dodecanethiol required higher pressures to form Janus or core–shell structures than particles with hexadecanethiol. Shorter ligands probably cause increased attraction between the particles[29] that has to be reduced by pressure to arrive at the levels required for self-assembly.

4 Conclusions

We showed that nanoparticles can arrange into binary crystalline structure inside evaporating emulsion droplets. Furthermore, we demonstrated that pressure can be used to manipulate the interactions of nanoparticles and thus, the overall structure of the supraparticles.

The binary supraparticles that we introduce here are an interesting new class of structured particles. In contrast to diblock copolymer particles,[30] they contain inorganic cores. Such cores are available with magnetic, plasmonic, fluorescent, catalytic and many other properties. Supraparticles combine them in a well-defined configuration.

Pressure is a simple and convenient stimulus to define supraparticle structure. Moderate pressure changes have surprisingly large effects on dispersibility and structure. It remains to be seen whether nanoparticle self-assembly in liquid films (often used to create superlattices) is also affected by pressure.

Molecular-scale studies of the ligand shell will give insight on the mechanism that causes the pressure-dependent interaction potentials. The pressure-dependent stability of alkanethiol-coated nanoparticle probably stems from the solvation of the ligand shell by the solvent.[27] We expect that other nanoparticle types that can be also coated with alkane ligands (if necessary, using linker chemistries other than thiols) can also be arranged in supraparticles using our route. This will allow to combine plasmonic metal particles, catalytic oxide particles, and fluorescent semiconductor quantum dots into structured

particles with new functionalities that are due to energy exchange between the constituent particles. Sintering such supraparticles will lead to new alloy particles that are impossible to create by direct synthesis.

Recent results suggest that particle agglomerates retain some mobility depending on the ligand shells.[31] Pressure-induced structural changes may also be possible in the fully formed supraparticles. Such active supraparticles could provide pressure-sensitive properties for externally controlled self-assembly.

Acknowledgements

We thank A. Kleemann for technical support during synthesis and L. González-García for 3D illustrations. This work was financial supported by the DFG – Deutsche Forschungsgemeinschaft – and the Luxembourgish Fonds National de la Recherche (FNR). We thank E. Arzt for his continuing support of this project.

References

1 E. V. Shevchenko, D. V. Talapin, N. A. Kotov, S. O'Brien and C. B. Murray, *Nature*, 2006, **439**, 55–59.
2 W. H. Evers, B. D. Nijs, L. Filion, S. Castillo, M. Dijkstra and D. Vanmaekelbergh, *Nano Lett.*, 2010, **10**, 4235–4241.
3 O. Velev, K. Furusawa and K. Nagayama, *Langmuir*, 1996, **12**, 2385–2391.
4 J. Lacava, P. Born and T. Kraus, *Nano Lett.*, 2012, **12**, 3279–3282.
5 Z. Nie, A. Petukhova and E. Kumacheva, *Nat. Nanotechnol.*, 2010, **5**, 15–25.
6 K. Whitham, J. Yang, B. H. Savitzky, L. F. Kourkoutis, F. Wise and T. Hanrath, *Nat. Mater.*, 2016, **15**(5), 557–563.
7 B. de Nijs, S. Dussi, F. Smallenburg, J. D. Meeldijk, D. J. Groenendijk, L. Filion, A. Imhof, A. van Blaaderen and M. Dijkstra, *Nat. Mater.*, 2015, **14**, 56–60.
8 S. Wooh, H. Huesmann, M. N. Tahir, M. Paven, K. Wichmann, D. Vollmer, W. Tremel, P. Papadopoulos and H.-J. Butt, *Adv. Mater.*, 2015, **27**, 7338–7343.
9 S.-H. Hu and X. Gao, *J. Am. Chem. Soc.*, 2010, **132**, 7234–7237.
10 O. Chen, L. Riedemann, F. Etoc, H. Herrmann, M. Coppey, M. Barch, C. T. Farrar, J. Zhao, O. T. Bruns, H. Wei, P. Guo, J. Cui, R. Jensen, Y. Chen, D. K. Harris, J. M. Cordero, Z. Wang, A. Jasanoff, D. Fukumura, R. Reimer, M. Dahan, R. K. Jain and M. G. Bawendi, *Nat. Commun.*, 2014, **5**, 5093.
11 S. C. Glotzer and M. J. Solomon, *Nat. Mater.*, 2007, **6**, 557–562.
12 M. Lattuada and T. A. Hatton, *Nano Today*, 2011, **6**, 286–308.
13 M. R. Hoffmann, S. T. Martin, W. Choi and D. W. Bahnemann, *Chem. Rev.*, 1995, **95**, 69–96.
14 B.-H. Wu, H.-Y. Yang, H.-Q. Huang, G.-X. Chen and N.-F. Zheng, *Chin. Chem. Lett.*, 2013, **24**, 457–462.
15 T. D. C. Company, *Technical Data Sheet*, Triton, http://www.dow.com, 2015.
16 J. Lacava, A.-A. Ouali, B. Raillard and T. Kraus, *Soft Matter*, 2014, **10**, 1696–1704.
17 A. Schofield, P. Pusey and P. Radcliffe, *Phys. Rev. E: Stat. Phys., Plasmas, Fluids, Relat. Interdiscip. Top.*, 2005, **72**, 031407.
18 E. Hendarto and Y. B. Gianchandani, *J. Micromech. Microeng.*, 2013, **23**, 075016.
19 J. J. Hegseth, N. Rashidnia and A. Chai, *Phys. Rev. E: Stat. Phys., Plasmas, Fluids, Relat. Interdiscip. Top.*, 1996, **54**, 1640–1644.
20 V. N. Manoharan, M. T. Elsesser and D. J. Pine, *Science*, 2003, **301**, 483–487.
21 W. Ramsden, *Proc. R. Soc. A*, 1903, 156–164.
22 V. A. Parsegian, *van der Waals forces: a handbook for biologists, chemists, engineers, and physicists*, Cambridge University Press, New York, 2005.
23 S. Plimpton, *J. Comput. Phys.*, 1995, **117**, 1–19.
24 J. D. Weeks, D. Chandler and H. C. Andersen, *J. Chem. Phys.*, 1971, **54**, 5237–5247.
25 M. Eldridge, P. Madden and D. Frenkel, *Nature*, 1993, **365**, 35–37.
26 F. Menger, *J. Phys. Chem.*, 1979, **83**, 893–893.
27 P. S. Shah, J. D. Holmes, K. P. Johnston and B. A. Korgel, *J. Phys. Chem. B*, 2002, **106**, 2545–2551.
28 G. A. Sotiriou, A. M. Hirt, P.-Y. Lozach, A. Teleki, F. Krumeich and S. E. Pratsinis, *Chem. Mater.*, 2011, **23**, 1985–1992.
29 S. J. Khan, F. Pierce, C. Sorensen and A. Chakrabarti, *Langmuir*, 2009, **25**, 13861–13868.
30 M. A. C. Stuart, W. T. Huck, J. Genzer, M. Müller, C. Ober, M. Stamm, G. B. Sukhorukov, I. Szleifer, V. V. Tsukruk, M. Urban, F. Winnik, S. Zauscher, I. Luzinov and S. Minko, *Nat. Mater.*, 2010, **9**, 101–113.
31 T. Geyer, P. Born and T. Kraus, *Phys. Rev. Lett.*, 2012, **109**, 128302.

Electronic Supplementary Material (ESI) for Nanoscale.

Supporting Information

Pressure-controlled formation of crystalline, Janus, and core-shell supraparticles

Thomas Kister,[†] Marko Mravlak,[‡] Tanja Schilling,[‡] and Tobias Kraus[*,†]

[†]*INM — Leibniz Institute for New Materials, Campus D2 2, 66123 Saarbrücken, Germany*

[‡]*Theory of Soft Condensed Matter, Physics and Materials Science Research Unit, Université du Luxembourg, L-1511 Luxembourg, Luxembourg*

E-mail: tobias.kraus@leibniz-inm.de

Calculation of packing fraction

The volume fraction θ_{AB13} of AuNP cores in the AB_{13} supraparticles was estimated as

$$\theta_{\mathrm{AB13}} = \frac{V_{\mathrm{NP}}}{V_{\mathrm{UC}}} = \frac{\frac{4}{3}\pi(104R_1^3 + 8R_2^3)}{a_{\mathrm{AB13}}^3} \tag{1}$$

with the total volume V_{NP} of AuNP cores (without the ligand) in the unit cell and the volume V_{UC} of the AB_{13} unit cell. R_1 and R_2 are the core radii of the different AuNP and a_{AB13} is the edge length of the AB_{13} unit cell.

We measured the NP core radii R_1 and R_2 in TEM micrographs by counting more than 2500 nanoparticles of each type with ImageJ 1.45s. The calculated radii and standard deviations were 2.00(16) nm and 4.00(18) nm for R_1 and R_2, respectively.

The unit cell edge length a_{AB13} of the AB_{13} unit cell was calculated from SAXS data as

$$a_{\mathrm{AB13}} = \frac{2\pi\sqrt{h^2 + k^2 + l^2}}{q_{(hkl)}} \tag{2}$$

were h, k, and l are Miller's indices and q is the scattering vector. The resulting value of $a_{\mathrm{AB13}} = 27.1\,\mathrm{nm}$ leads to an overall packing fraction of $\theta_{\mathrm{AB13}} = 0.283$.

The core volume fraction of the Janus-type and the core-shell supraparticles was calculated by assuming crystalline face-centered cubic (fcc) packings of both nanoparticle types. The theoretical fcc packing fraction for hard spheres is $\theta_{\mathrm{fcc}} = 0.74$. To estimate the packing fraction of the cores, the ratio between the core volume and the volume of the cores with the soft ligand shell was multiplied by the theoretical packing fraction of fcc:

$$\theta = 0.74\frac{V_{core}}{V_{core+shell}} = 0.74\frac{\frac{4}{3}\pi(13R_1^3 + R_2^3)}{\frac{4}{3}\pi[13(R_1 + L_1)^3 + (R_2 + L_2)^3]} \tag{3}$$

with the thicknesses of the ligand shells in the packing L_1 and L_2. Note that the ligand shells are considerably compressed during assembly. We estimated the compressed ligand shell thickness from SAXS data and found $L_1 \approx 0.4\,\mathrm{nm}$ and $L_2 \approx 0.3\,\mathrm{nm}$ for Janus particles, which

corresponds to a core volume fraction of $\theta_{\text{Janus}} = 0.48$. Core-Shell-particles had $L_1 = 0.45\,\text{nm}$ and $L_2 = 0.5\,\text{nm}$, which corresponds to a core volume fraction of $\theta_{\text{Core-shell}} = 0.44$.

Molecular dynamics simulations

We performed molecular dynamics simulations[1] of a binary mixture of nanoparticles confined to a spherical container. To mimic varying solubility, we blended between an attractive Lennard-Jones potential and a purely repulsive but finite WCA (Weeks-Chandler-Andersen) potential[2]

$$V_{ij}(r, \lambda_{ij}) = (1 - \lambda_{ij}) WCA_{ij}(r) + \lambda_{ij} LJ_{ij}(r) \tag{4}$$

The properties of the mixture were specified by choosing the mixing parameters λ_{AA}, λ_{BB} and λ_{AB}. The Lennard-Jones parameter σ, which corresponds to the particle "diameter", is additive for the inter-species interaction, $\sigma_{\text{AB}} = (\sigma_{\text{AA}} + \sigma_{\text{BB}})/2$. We set the diameter ratio to $\sigma_{\text{BB}}/\sigma_{\text{AA}} = 0.55 - 0.58$. For this ratio the icosahedral AB_{13} lattice has been shown to form entropically.[3,4] The length and energy scales were set by $\sigma_{\text{AA}} = 1$ and $\epsilon_{\text{AA}} = \epsilon_{\text{BB}} = \epsilon_{\text{AB}} = 1 k_B T$, where k_B is the Boltzmann constant, T is the temperature and ϵ is the interaction strength. We used identical parameters in the WCA and the Lennard-Jones potential. The interactions of the nanoparticles with the walls of the spherical container were modeled using the WCA potential with parameters $\epsilon_{\text{WA}} = \epsilon_{\text{WB}} = \sigma_{\text{AW}} = 1$ and $\sigma_{\text{WB}} = 0.775 - 0.79$. The number ratio between big and small particles was 1/13.

Initial particle configurations were prepared as disordered fluid mixtures. Most simulations were performed under shrinking confinement to emulate the evaporating emulsion droplets. The exception were simulations in which all particles interacted with strongly attractive potentials (modeling low pressure) and those in which all interactions were purely repulsive (modeling high pressure). We kept the volume of the container, and thus the particle density, constant for these extreme cases in which nucleation of the crystalline phase is a rare event.

All simulations were run in parallel on the 12 cores of two Intel Xeon L5640 2,26 GHz CPUs. A simulation leading to an AB_{13} crystals of 1750 particles at a fixed container volume required approximately 3 days to finish. The AB_{13} crystal formed at a temperature $T_{LJ} = 0.6\,k_B/\epsilon_{AA}$ and a packing fraction $\rho = 0.8$, which we estimated using the effective radius of the particles, $r_{eff} = 2^{1/6}\sigma/2$. All simulations were carried out at the same temperature and the same final packing fraction as those leading to AB_{13} crystals.

We used a time step of $0.004(\epsilon_{AA}/m/\sigma_{AA}^2)^{1/2}$, where m is the mass of particle. For constant volume simulations we allowed up to 10^9 steps to equilibrate the system, for the shrinking container 10^7. Most simulations converged to a crystalline structure in that time. The crystallization event was accompanied by a drop in the potential energy and a decrease in the slope of the average mean square displacement of particles as shown in figure S4 for a system with periodic boundary conditions and a fixed volume.

As a consequence of the curved boundary conditions imposed by the walls of the spherical container the central core with the AB_{13} crystal structure is surrounded by a disordered shell made of both types of particles as shown in figure S5.

Table S1: Minimum free energy structures obtained by simulation for different combinations of λij.

λ_{AA}	λ_{BB}	λ_{AB}	structure
0	0	0	AB_{13}[1]
1	0	0.1	core-shell
1	0.01	0.1	core-shell
≥ 0.8	0	0	Janus
1	≥ 0.1	0.1	Janus
1	1	1	AB_{13}

Table S1 summarizes the structures of supraparticles that form for different interactions. The structures are affected by entropy, the interactions between the different particle types, and the interactions with the wall. Crystalline AB_{13}, core-shell and Janus supraparticles were the only ordered final states that we found for our set of interactions and the mixing ration of 1/13. Most parameter combinations led to disordered structures with a fluid-like

mixture of the different particles.

References

(1) Plimpton, S. *J. Comput. Phys.* **1995**, *117*, 1–19.

(2) Weeks, J. D.; Chandler, D.; Andersen, H. C. *J. Chem. Phys* **1971**, *54*, 5237–5247.

(3) Eldridge, M.; Madden, P.; Frenkel, D. *Nature* **1993**, *365*, 35–37.

(4) Schofield, A.; Pusey, P.; Radcliffe, P. *Phys Rev E* **2005**, *72*, 031407.

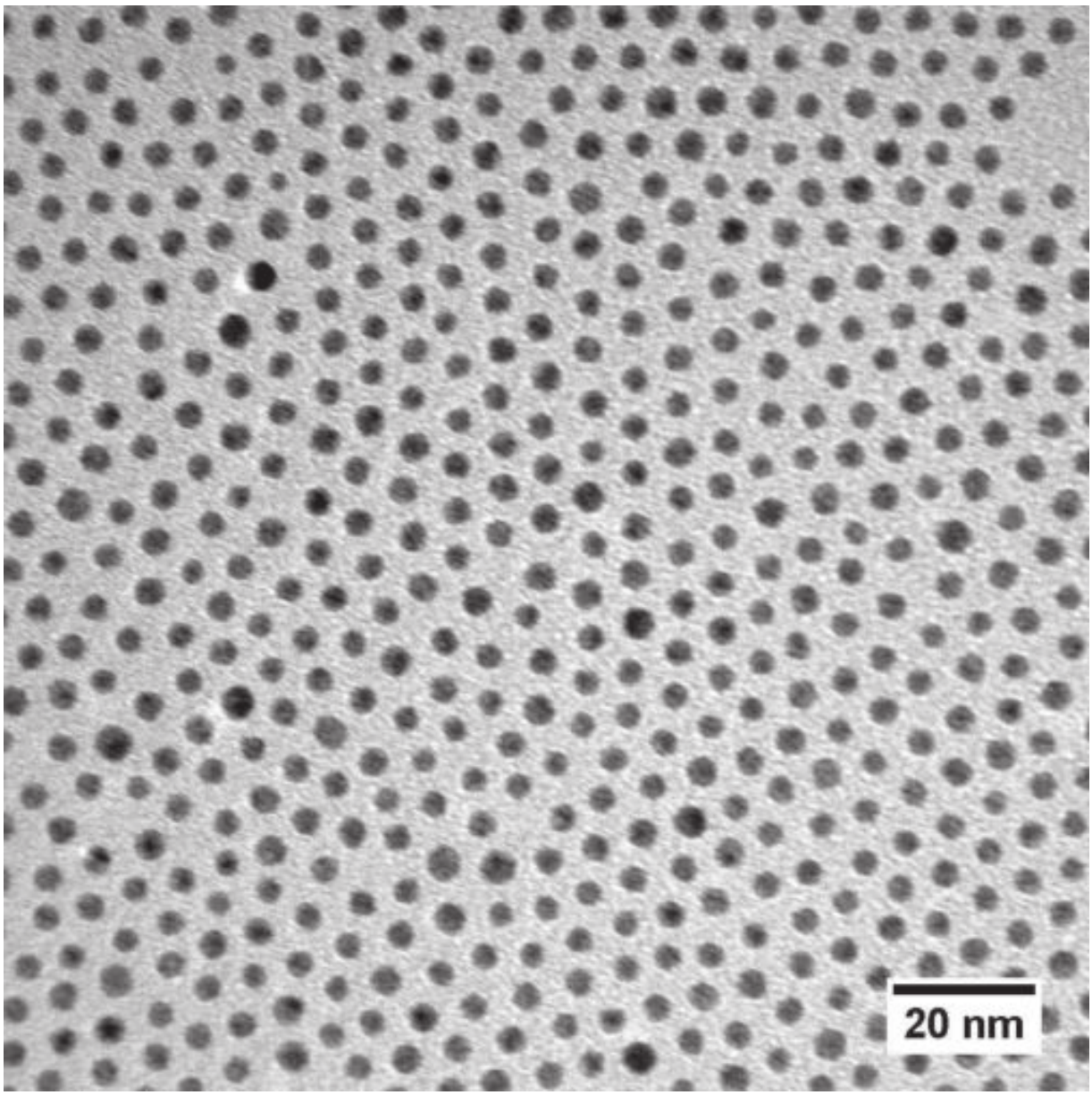

Figure S1: TEM micrograph of 4 nm Au nanoparticles

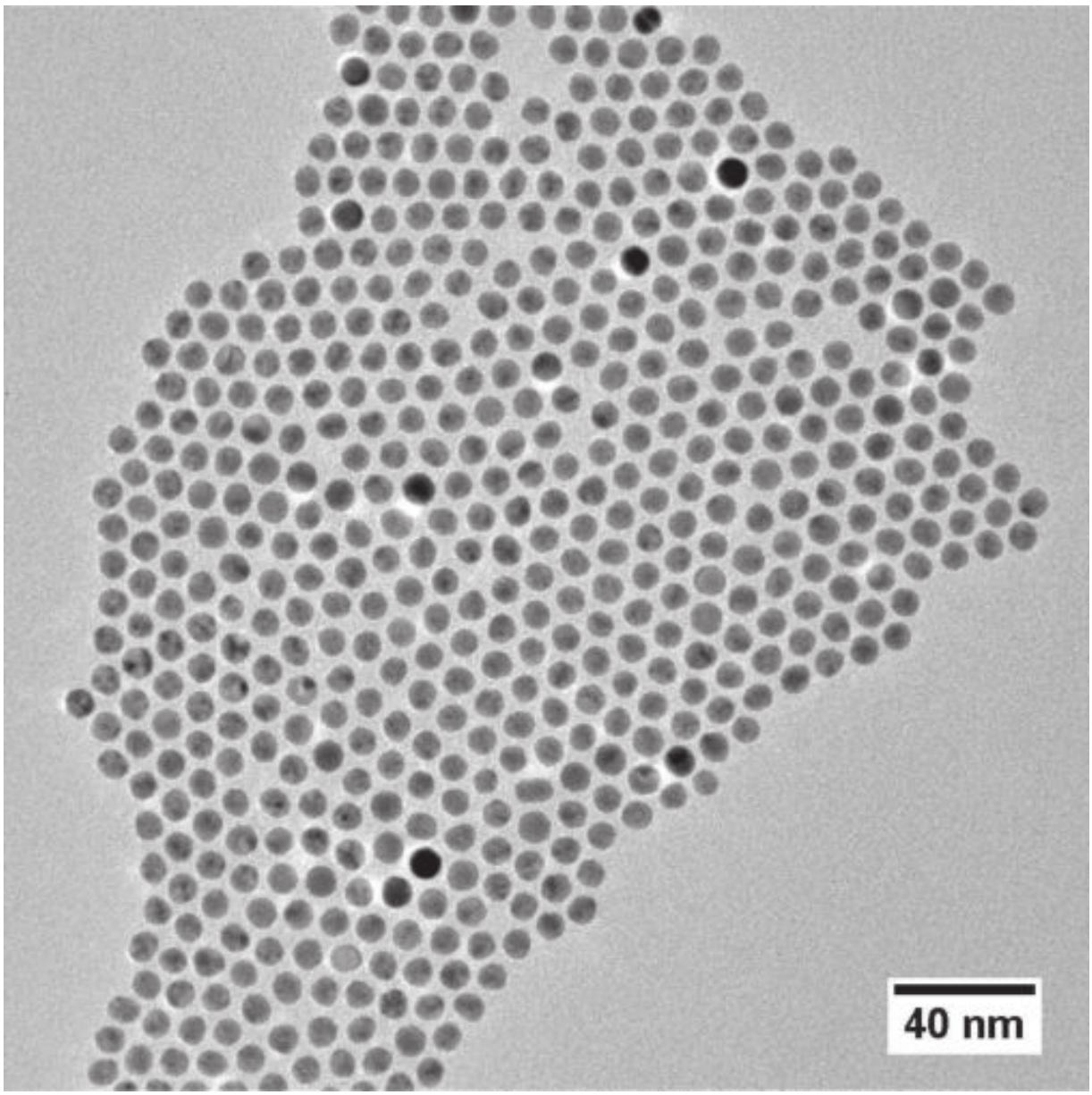

Figure S2: TEM micrograph of 8 nm Au nanoparticles

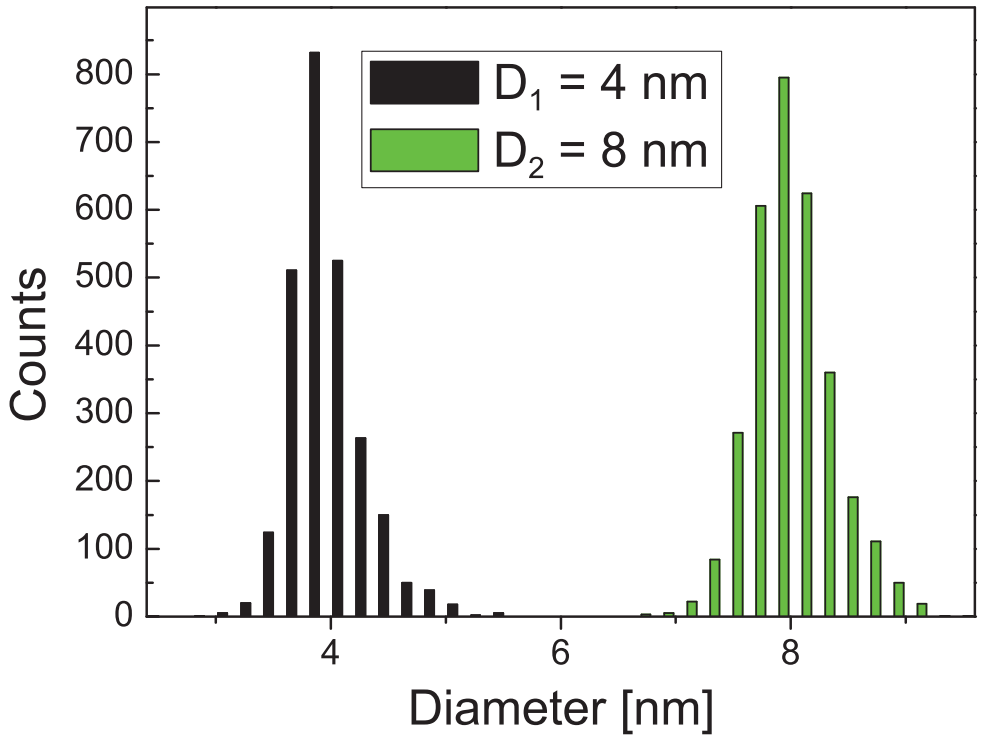

Figure S3: Histogram of the size distribution of 4 nm and 8 nm nanoparticles.

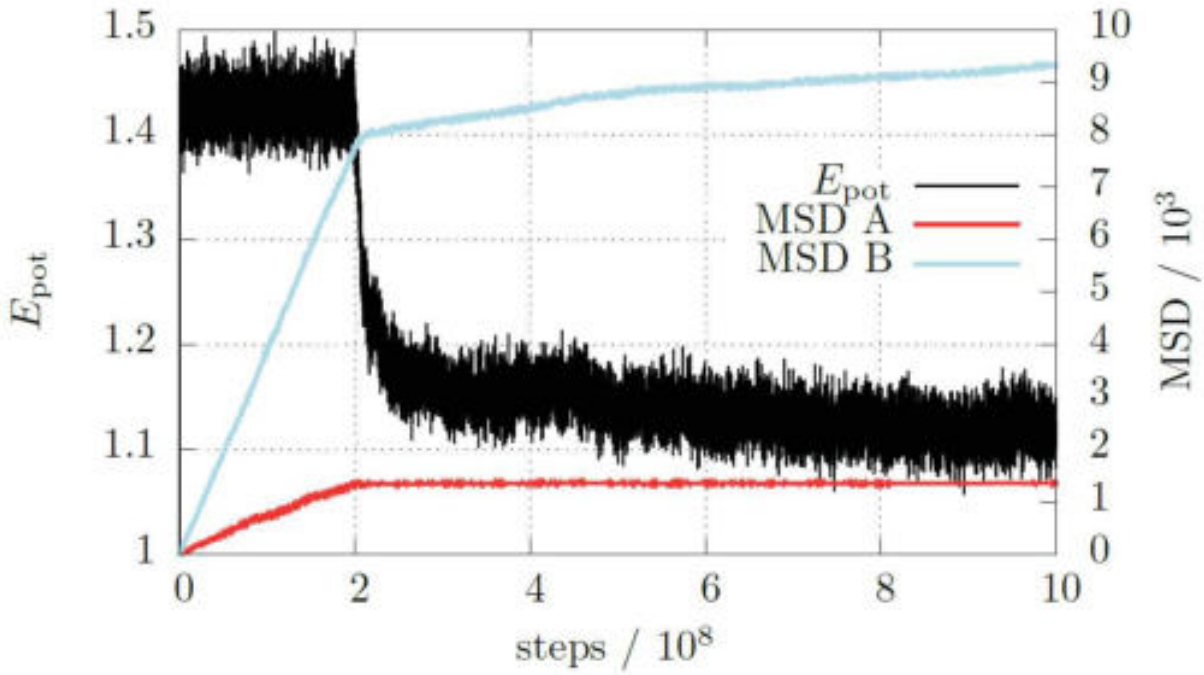

Figure S4: Crystallization of AB_{13} binary lattice for 1750 particles in bulk.

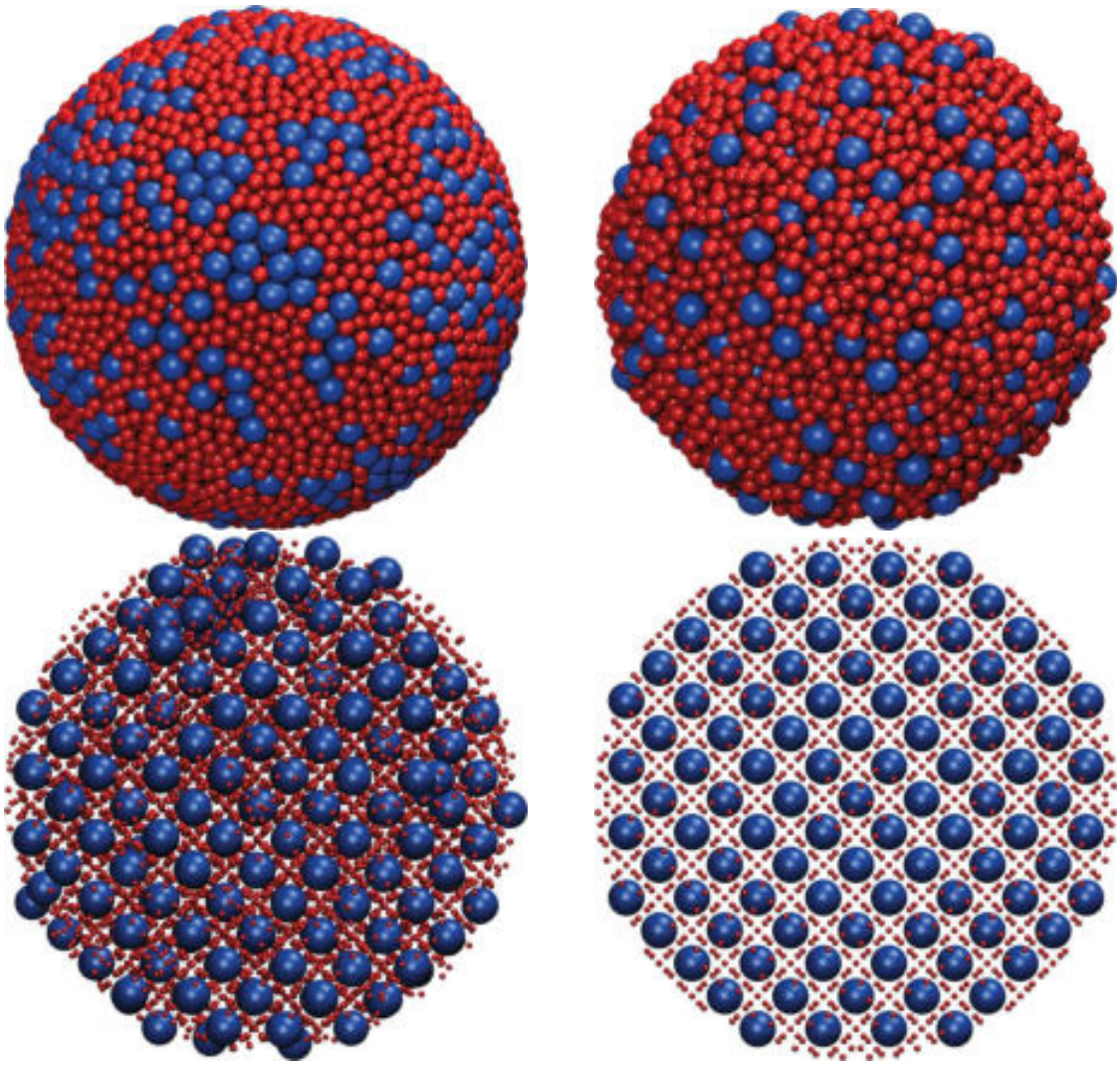

Figure S5: Supraparticle with the AB_{13} crystal structure which resulted from the simulation of a binary mixture of 14000 nanoparticles with a size ratio of 0.55 in a fixed spherical container at $T = 0.6$ and $\rho = 0.8$. (a) Complete supraparticle including the disordered shell. (b) The crystalline core of supraparticle without the disordered shell. (c) The size of small particles is decreased for clarity. (d) Model of a supraparticle with AB_{13} crystal structure without defects.

4. Discussion

4.1 Stability of non-polar nanoparticles

The results published in publications 1 and 2 indicate that vdW interactions can dominate the agglomeration and thus, the stability of alkanethiol coated AuNPs. The agglomeration temperature of hexadecanethiol coated AuNPs increased by 15°C when increasing their core diameter from 4.1 nm to 7.5 nm, corresponding to a slope of 4.4°C/nm. The agglomeration was shell-dominated in this core size range. Core diameters of 8.3 nm to 9.7 nm increased the temperature by approximately 30°C/nm, which is explained by a core-dominated mechanism. The nonlinear transition from shell-dominated to core-dominated stability depends on the combination of the core and the ligand. If the ligand shells of two NP are in contact and the attractive potential caused by vdW interactions is above $G_{vdW} > 0.35\ k_B T$, the NPs agglomerated. Brownian motion then becomes insufficient to keep the NPs separated. Studies on AuNPs with core diameters of 8.3 nm coated with dodecane-, hexadecane-, and octadecanethiol confirmed the non-linear transition to a core-dominated regime. While the agglomeration temperature of octadecanethiol coated AuNPs was around the melting point of the

pure ligand, it increased for dodecanethiol and hexadecanethiol coated AuNPs to 100°C and 40°C, respectively. Note the strong attractive contribution of large cores: the agglomeration temperatures were approximately 110°C above that of cores with 6 nm diameter coated with dodecanethiol and 25°C above the same cores coated with hexadecanethiol [83].

Publications 3 and 4 indicate that the stability of alkanethiol coated AuNPs in different solvents does not follow predictions obtained using simple models with the Flory parameter. The Flory parameter suggest that hexadecanethiol coated NPs should have a higher stability in hexadecane than in shorter alkanes such as hexane or decane. Fig. 1 in publication 3 illustrates that hexadecanethiol coated AuNPs have a higher agglomeration temperature in hexadecane than in decane or hexane. Merely changing the solvent from hexane to decane increased the agglomeration temperature by approximately 12°C. As it is shown in Fig. 4.1, hexadecanethiol coated AuNPs with a diameter of 7.5 nm remained well-dispersed at room temperature in hexane, but not in decane or hexadecane.

The solvent also affected the maximal concentration of NPs that could be dispersed without agglomeration as shown in Fig. 3 of publication 4. The limiting concentration increased with decreasing chain length of alkane solvents. This may be related to the interdigitation of the solvent molecules into the ligand shell. Since the arrangement of alkanethiols on the surface of the particles is rather dense — around 5.5 ligands per nm^2 as measured by thermogravimetric analysis, see the SI of publication 1 — the spacing between the ligand molecules is too small for longer alkane solvent molecules to fully align with them.

I exploited the increased understanding of ligand- and solvent-dependent particle stability for the optimization of a NP imprint process. Publication 5 revealed that the morphology of imprinted lines of alkanethiol coated AuNPs with a core diameter of 3.2 nm changes with the length of the ligand. Butanethiol

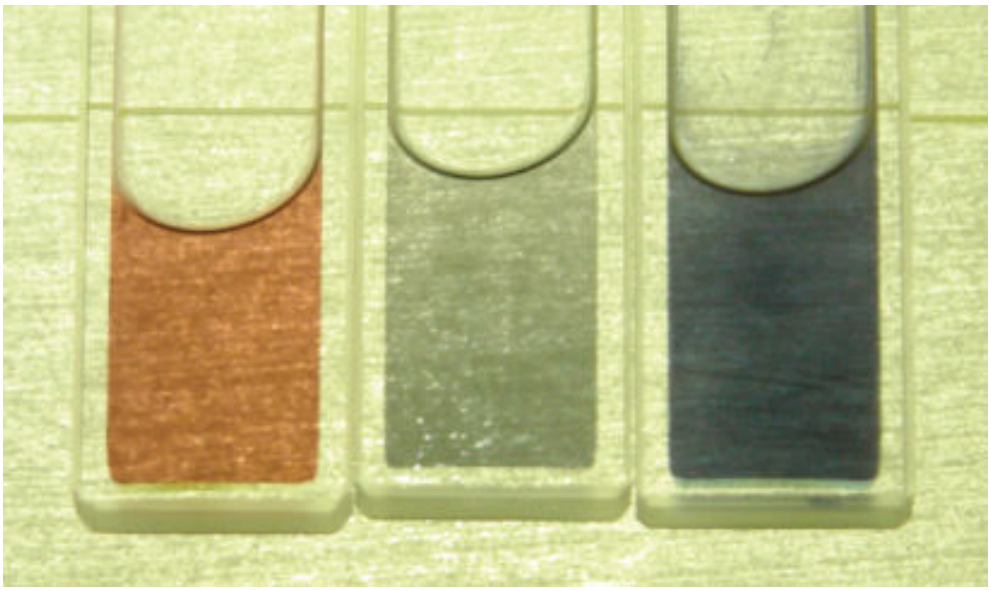

FIGURE 4.1: Hexadecanethiol coated AuNPs with a diameter of 7.5 nm. The particles were dispersed in hexane (left), decane (middle) and hexadecane (right). The AuNPs were deagglomerated in hexane and agglomerated in decane and hexadecane. The picture was taken at room temperature.

coated NPs formed large, isolated clusters, octanethiol coated NPs assembled into small, partially connected clusters, while dodecanethiol coated NPs formed percolating lines. This can be explained by the stability of the AuNPs. Butanethiol coated NPs agglomerate at an early stage of evaporation and have enough time to form large clusters. Octanethiol coated NPs assemble later and form smaller clusters that move until they dry. Dodecanethiol coated NPs remain dispersed until the solvent almost completely evaporated. The NP concentration becomes so large that they form percolating lines. Since the initial particle concentration was kept constant, the differences must be due to different stabilities that depended on ligand length. I used the effect in order to imprint conductive and transparent electrodes. Suitable particle diameters and ligands yielded electrodes with a sheet resistance of around 150 Ω/sq at a transparency above 90 %.

4.2 Binary Supraparticles from non-polar nanoparticles

Publication 4 showed that the onset concentration of agglomeration depends on particle size, ligand, and solvent. The structure of the SPs formed through "emulsion assisted particle assembly" is affected by size, ligand, and solvent, too, but also depended on the surfactant that stabilized the emulsion. I studied the effect of different surfactants on the assembly of particles in emulsion droplets in publication 6 and found that Triton X-100, X-165, and X-705 led to different concentrations at which NP assembled. This enabled the production of binary SPs with crystalline structure, Janus structure, and core-shell structure, as shown in Fig. 1 of publication 6. Comparable results were achieved by varying the ambient pressure during evaporation using Triton X-100 as the surfactant. Increasing the total pressure to 200 kPa and 400 kPa during evaporation led to the formation of Janus-type and core-shell supraparticles.

In-situ small angle X-ray scattering measurements indicated that the onset concentration of agglomeration increased in the order Triton X-100, X-165, and X-705. The interfacial tension increased in the same order; we hypothesized that the Laplace pressure was responsible for the different onset concentration of agglomeration and thus, for the different structures of binary SPs.

Molecular dynamic simulations confirmed that the different SP structures observed can form in spherical confinement when changing the interaction potentials. Crystalline SPs can form for particles with purely repulsive interactions or with identical interactions between small and big NPs. Janus SPs can form if both particles had different attractive interaction potentials, and core-shell SPs can form if only one of the particles types had attractive interaction potentials.

5. Conclusion and Outlook

The effect of core size, ligand length, and solvent type on the stability of sterically stabilized non-polar NPs was systematically investigated at different temperatures using small angle X-ray scattering. A well-known particle system was chosen in order to keep experiments and simulations as simple as possible and enable comparison with theoretical models. Spherical gold cores with narrow size distributions and a uniform and homogeneous ligand shell of alkanethiols were distributed in alkanes and a few other solvents.

A non-linear transition from a ligand-dominated to a core-dominated agglomeration regime was found. In the ligand-dominated regime, agglomeration was induced by a phase transition of the ligand shell from disordered to ordered that changed particle solubility. In the core-dominated regimes, vdW interactions were strong enough to induce agglomeration even though the ligand shell was disordered. The existence of this transition has consequences for the effect of the ligand on the stability of the NPs. In the shell-dominated regime, the stability decreased with the ligand length; in the core-dominated regime, the stability increased with the ligand length.

While the vdW interactions in the core-dominated regime are described very well by the current theoretical models, the models fail in the ligand-dominated

regime. The models do not consider changes in ligand structure from disordered and isotropic to ordered and anisotropic. Ordering of the shell causes a demixing of the ligand and the solvent. The balance between entropy, enthalpy, and vdW interactions between the tails of the ligand molecules shifts such that the ordering of the ligand molecules increases with the length of the solvent molecules. The agglomeration temperature thus increases for longer solvents. Further experiments are needed to get a better understanding of the ligand ordering effect on the stability of NPs, for example to understand how double bonds in the ligand shell or binary ligand mixtures behave on the NPs could provide further insights. Combined studies with simulations could lead to extensions of the interaction potentials.

A new method for the measurement of NP agglomeration states in hanging droplets by small angle X-ray scattering made it possible to study the minimal agglomeration concentration as a function of the solvent and the ligand. The minimal agglomeration concentration of alkanethiol coated AuNPs increased for shorter alkanes and was maximal in cyclohexane. For the measured solvents, the concentration increased with ligand length: longer ligands — up to dodecanethiol — increased the minimum agglomeration concentration. The results showed that the stability of sterically coated NPs does not only depend on size, ligand, and solvent, but also on the concentration. Further experiments and simulations are needed to explain why the minimal agglomeration concentration was so high in cyclohexane and how supramolecular interactions between solvent and ligand are affecting the minimal agglomeration concentration.

Emulsions were used as templates for the assembly of NPs into supraparticles. Variation of surfactant and thus Laplace pressure or external pressure

changes during the evaporation of the dispersed emulsion phase affected the assembly of binary NP mixtures and led to the formation of binary SPs with different structures. In-situ observations by small angle X-ray scattering during SP formation indicated rapid assembly at well-defined concentrations. The concentrations depended on the size of the NPs and on the pressure, where higher pressures increased the concentrations. The effect was exploited in order to produce different SPs from the same binary NP mixture as shown in Fig. 5.1. Increasing the pressure from ambient to 1000 kPa changed the structures gradually from crystalline, to Janus, to core-shell, to a mixture of crystalline and Janus and finally to crystalline.

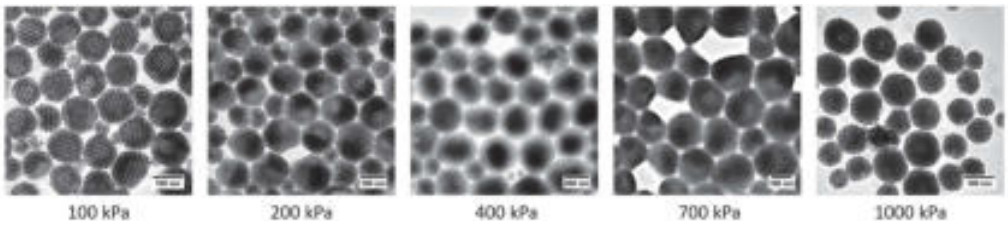

FIGURE 5.1: Assembly of 1-hexadecanethiol coated AuNPs with core diameters of 4 nm and 8 nm at different pressures (effective pressures inside the droplets are indicated). The SPs were produced by the emulsion assisted particle assembly using Triton X-100.

It remains unclear why such small pressure changes influence the concentrations at which NPs start to assemble. One possibility might be an increase of the solubility of the ligand in the solvent due to pressure-dependent solubility parameters. Further studies of the ligand-solvent interactions during evaporation and the degree to which pressure changes them and simulations of the resulting interactions are required to understand this phenomenon.

Bibliography

[1] David J Barber and Ian C Freestone. “An investigation of the origin of the colour of the Lycurgus Cup by analytical transmission electron microscopy”. In: *Archaeometry* 32.1 (1990), pp. 33–45.

[2] Michael Faraday. “X. The Bakerian Lecture.—Experimental relations of gold (and other metals) to light”. In: *Philosophical Transactions of the Royal Society of London* 147 (1857), pp. 145–181.

[3] John Turkevich, Peter Cooper Stevenson, and James Hillier. “A study of the nucleation and growth processes in the synthesis of colloidal gold”. In: *Discussions of the Faraday Society* 11 (1951), pp. 55–75.

[4] Gert Frens. “Controlled nucleation for the regulation of the particle size in monodisperse gold suspensions”. In: *Nature physical science* 241.105 (1973), pp. 20–22.

[5] Mathias Brust et al. “Synthesis of thiol-derivatised gold nanoparticles in a two-phase liquid–liquid system”. In: *Journal of the Chemical Society, Chemical Communications* 7 (1994), pp. 801–802.

[6] M Brust et al. “Synthesis and reactions of functionalised gold nanoparticles”. In: *Journal of the Chemical Society, Chemical Communications* 16 (1995), pp. 1655–1656.

[7] Shouheng Sun and Hao Zeng. “Size-controlled synthesis of magnetite nanoparticles”. In: *Journal of the American Chemical Society* 124.28 (2002), pp. 8204–8205.

[8] Yugang Sun and Younan Xia. “Shape-controlled synthesis of gold and silver nanoparticles”. In: *Science* 298.5601 (2002), pp. 2176–2179.

[9] Temer S Ahmadi et al. “Shape-controlled synthesis of colloidal platinum nanoparticles”. In: *Science* 272.5270 (1996), pp. 1924–1925.

[10] Nanfeng Zheng, Jie Fan, and Galen D Stucky. “One-step one-phase synthesis of monodisperse noble-metallic nanoparticles and their colloidal crystals”. In: *Journal of the American Chemical Society* 128.20 (2006), pp. 6550–6551.

[11] Jongnam Park et al. “Ultra-large-scale syntheses of monodisperse nanocrystals”. In: *Nature materials* 3.12 (2004), pp. 891–895.

[12] Karen J Nordell, Elizabeth M Boatman, and George C Lisensky. “A safer, easier, faster synthesis for CdSe quantum dot nanocrystals”. In: *Journal of chemical education* 82.11 (2005), p. 1697.

[13] Marie-Christine Daniel and Didier Astruc. “Gold nanoparticles: assembly, supramolecular chemistry, quantum-size-related properties, and applications toward biology, catalysis, and nanotechnology”. In: *Chemical reviews* 104.1 (2004), pp. 293–346.

[14] BO Dabbousi et al. “(CdSe) ZnS core-shell quantum dots: synthesis and characterization of a size series of highly luminescent nanocrystallites”. In: *The Journal of Physical Chemistry B* 101.46 (1997), pp. 9463–9475.

[15] CP Bean and JD Livingston. "Superparamagnetism". In: *Journal of Applied Physics* 30.4 (1959), S120–S129.

[16] Tobias Kraus et al. "Nanoparticle printing with single-particle resolution". In: *Nature nanotechnology* 2.9 (2007), pp. 570–576.

[17] Suraj Naskar et al. "Porous aerogels from shape-controlled metal nanoparticles directly from nonpolar colloidal solution". In: *Chemistry of Materials* 29.21 (2017), pp. 9208–9217.

[18] S Link, Zz L Wang, and MA El-Sayed. "Alloy formation of gold- silver nanoparticles and the dependence of the plasmon absorption on their composition". In: *The Journal of Physical Chemistry B* 103.18 (1999), pp. 3529–3533.

[19] Madhuchanda Banerjee et al. "Enhanced antibacterial activity of bimetallic gold-silver core–shell nanoparticles at low silver concentration". In: *Nanoscale* 3.12 (2011), pp. 5120–5125.

[20] Jian Yang et al. "Mesoporous zinc-blende ZnS nanoparticles: synthesis, characterization and superior photocatalytic properties". In: *Nanotechnology* 19.25 (2008), p. 255603.

[21] Chi-Hui Liang et al. "Iron oxide/gold core/shell nanoparticles for ultrasensitive detection of carbohydrate- protein interactions". In: *Analytical chemistry* 81.18 (2009), pp. 7750–7756.

[22] Young-Sang Cho et al. "Self-organization of colloidal nanospheres inside emulsion droplets: Higher-order clusters, supraparticles, and supraballs". In: *Colloids and Surfaces A: Physicochemical and Engineering Aspects* 345.1-3 (2009), pp. 237–245.

[23] Susanne Wintzheimer et al. "Supraparticles: Functionality from uniform structural motifs". In: *ACS nano* 12.6 (2018), pp. 5093–5120.

[24] AL Costa et al. “Synthesis of nanostructured magnetic photocatalyst by colloidal approach and spray–drying technique”. In: *Journal of colloid and interface science* 388.1 (2012), pp. 31–39.

[25] Philip Born, Eoin Murray, and Tobias Kraus. “Temperature-induced particle self-assembly”. In: *Journal of Physics and Chemistry of Solids* 71.2 (2010), pp. 95–99.

[26] Johann Lacava, Philip Born, and Tobias Kraus. “Nanoparticle clusters with Lennard-Jones geometries”. In: *Nano Lett.* 12.6 (2012), pp. 3279–3282.

[27] Younjin Min et al. “The role of interparticle and external forces in nanoparticle assembly”. In: *Nanoscience and Technology: A Collection of Reviews from Nature Journals*. World Scientific, 2010, pp. 38–49.

[28] Siddique J Khan et al. “Self-Assembly of Ligated Gold Nanoparticles: Phenomenological Modeling and Computer Simulations†”. In: *Langmuir* 25.24 (2009), pp. 13861–13868.

[29] Johannes HM Maurer et al. “Templated self-assembly of ultrathin gold nanowires by nanoimprinting for transparent flexible electronics”. In: *Nano letters* 16.5 (2016), pp. 2921–2925.

[30] David Nguyen et al. “An easy way to control the morphology of colloidal polymer-oxide supraparticles through seeded dispersion polymerization”. In: *Langmuir* 26.9 (2010), pp. 6086–6090.

[31] Cristina Lourenco et al. “Steric stabilization of nanoparticles: size and surface properties”. In: *International journal of pharmaceutics* 138.1 (1996), pp. 1–12.

[32] J Kimling et al. “Turkevich method for gold nanoparticle synthesis revisited”. In: *The Journal of Physical Chemistry B* 110.32 (2006), pp. 15700–15707.

[33] Zhen Liu et al. "Ultrathin Homogenous AuNP Monolayers as Tunable Functional Substrates for Surface-Assisted Laser Desorption/Ionization of Small Biomolecules". In: *Journal of the American Society for Mass Spectrometry* 31.1 (2019), pp. 47–57.

[34] Timo Laaksonen et al. "Stability and Electrostatics of Mercaptoundecanoic Acid-Capped Gold Nanoparticles with Varying Counterion Size". In: *ChemPhysChem* 7.10 (2006), pp. 2143–2149.

[35] Jin Xie et al. "One-pot synthesis of monodisperse iron oxide nanoparticles for potential biomedical applications". In: *Pure and Applied Chemistry* 78.5 (2006), pp. 1003–1014.

[36] Stefanos Mourdikoudis and Luis M Liz-Marzán. "Oleylamine in nanoparticle synthesis". In: *Chemistry of Materials* 25.9 (2013), pp. 1465–1476.

[37] Ramesh Sharma et al. "NMR characterization of ligand binding and exchange dynamics in triphenylphosphine-capped gold nanoparticles". In: *The Journal of Physical Chemistry C* 113.37 (2009), pp. 16387–16393.

[38] Thomas Bürgi. "Properties of the gold–sulphur interface: from self-assembled monolayers to clusters". In: *Nanoscale* 7.38 (2015), pp. 15553–15567.

[39] Abraham Ulman. "Formation and structure of self-assembled monolayers". In: *Chemical reviews* 96.4 (1996), pp. 1533–1554.

[40] Martin Kluenker et al. "Monitoring Thiol–Ligand Exchange on Au Nanoparticle Surfaces". In: *Langmuir* 34.4 (2018), pp. 1700–1710.

[41] Amelie Heuer-Jungemann et al. "The role of ligands in the chemical synthesis and applications of inorganic nanoparticles". In: *Chemical reviews* 119.8 (2019), pp. 4819–4880.

[42] Johann Lacava, Anika Weber, and Tobias Kraus. "Ageing of Alkylthiol-Stabilized Gold Nanoparticles". In: *Particle & Particle Systems Characterization* 32.4 (2015), pp. 458–466.

[43] Yuliang Wang and Younan Xia. "Bottom-up and top-down approaches to the synthesis of monodispersed spherical colloids of low melting-point metals". In: *Nano letters* 4.10 (2004), pp. 2047–2050.

[44] A Paul Alivisatos. "Semiconductor clusters, nanocrystals, and quantum dots". In: *Science* 271.5251 (1996), p. 933.

[45] Anna Mignot et al. "A Top-Down synthesis route to ultrasmall multifunctional Gd-Based silica nanoparticles for theranostic applications". In: *Chemistry–A European Journal* 19.19 (2013), pp. 6122–6136.

[46] Vincenzo Amendola et al. "Top-down synthesis of multifunctional iron oxide nanoparticles for macrophage labelling and manipulation". In: *Journal of Materials Chemistry* 21.11 (2011), pp. 3803–3813.

[47] Antonio M Brito-Silva et al. "Laser ablated silver nanoparticles with nearly the same size in different carrier media". In: *Journal of Nanomaterials* 2010 (2010).

[48] P Braunstein et al. "Chloro-1κCl-Bis (Triethylphosphine-1κP) Bis (Triphenyl-Phosphine)-2κP, 3κP-Triangulo-Digold-Platinum (1+) Trifluoromethanesulfonate". In: *Inorg. Synth* 27 (1990), pp. 218–221.

[49] Victor K LaMer and Robert H Dinegar. "Theory, production and mechanism of formation of monodispersed hydrosols". In: *Journal of the American Chemical Society* 72.11 (1950), pp. 4847–4854.

[50] Hiroki Hiramatsu and Frank E Osterloh. "A simple large-scale synthesis of nearly monodisperse gold and silver nanoparticles with adjustable sizes and with exchangeable surfactants". In: *Chemistry of Materials* 16.13 (2004), pp. 2509–2511.

[51] Bing-Hui Wu et al. "Solvent effect on the synthesis of monodisperse amine-capped Au nanoparticles". In: *Chinese Chemical Letters* 24.6 (2013), pp. 457–462.

[52] Sheng Peng et al. "A facile synthesis of monodisperse Au nanoparticles and their catalysis of CO oxidation". In: *Nano research* 1.3 (2008), pp. 229–234.

[53] Sheng Peng et al. "Reversing the size-dependence of surface plasmon resonances". In: *Proceedings of the National Academy of Sciences* 107.33 (2010), pp. 14530–14534.

[54] Vincenzo Amendola et al. "Surface plasmon resonance in gold nanoparticles: a review". In: *Journal of Physics: Condensed Matter* 29.20 (2017), p. 203002.

[55] D Keith Roper, Wonmi Ahn, and M Hoepfner. "Microscale heat transfer transduced by surface plasmon resonant gold nanoparticles". In: *The Journal of Physical Chemistry C* 111.9 (2007), pp. 3636–3641.

[56] Uwe Kreibig and Vollmer Michael. *Optical Properties of Metal Clusters*. Springer, Berlin, 1995.

[57] Stephan Link and Mostafa A El-Sayed. "Size and temperature dependence of the plasmon absorption of colloidal gold nanoparticles". In: *The Journal of Physical Chemistry B* 103.21 (1999), pp. 4212–4217.

[58] Sujit Kumar Ghosh et al. “Solvent and ligand effects on the localized surface plasmon resonance (LSPR) of gold colloids”. In: *The Journal of Physical Chemistry B* 108.37 (2004), pp. 13963–13971.

[59] Sujit Kumar Ghosh and Tarasankar Pal. “Interparticle coupling effect on the surface plasmon resonance of gold nanoparticles: from theory to applications”. In: *Chemical reviews* 107.11 (2007), pp. 4797–4862.

[60] Justin M Zook et al. “Measuring agglomerate size distribution and dependence of localized surface plasmon resonance absorbance on gold nanoparticle agglomerate size using analytical ultracentrifugation”. In: *ACS nano* 5.10 (2011), pp. 8070–8079.

[61] Brian S Chapman et al. “Heteroaggregation approach for depositing magnetite nanoparticles onto silica-overcoated gold nanorods”. In: *Chemistry of Materials* 29.24 (2017), pp. 10362–10368.

[62] A Taleb, C Petit, and MP Pileni. “Optical properties of self-assembled 2D and 3D superlattices of silver nanoparticles”. In: *The Journal of Physical Chemistry B* 102.12 (1998), pp. 2214–2220.

[63] Alan Vanderkooy et al. “Silica shell/gold core nanoparticles: correlating shell thickness with the plasmonic red shift upon aggregation”. In: *ACS applied materials & interfaces* 3.10 (2011), pp. 3942–3947.

[64] Andrew M Smith, Xiaohu Gao, and Shuming Nie. “Quantum dot nanocrystals for in vivo molecular and cellular imaging”. In: *Photochemistry and photobiology* 80.3 (2004), pp. 377–385.

[65] Sadra Sadeghi et al. “Efficient white LEDs using liquid-state magic-sized CdSe quantum dots”. In: *Scientific reports* 9.1 (2019), pp. 1–9.

[66] Alexander O Govorov et al. “Exciton- plasmon interaction and hybrid excitons in semiconductor- metal nanoparticle assemblies”. In: *Nano letters* 6.5 (2006), pp. 984–994.

[67] M Hirasawa et al. “Magnetoabsorption of the lowest exciton in perovskite-type compound (CH3NH3) PbI3”. In: *Physica B: Condensed Matter* 201 (1994), pp. 427–430.

[68] Matthew C Beard, Gordon M Turner, and Charles A Schmuttenmaer. “Size-dependent photoconductivity in CdSe nanoparticles as measured by time-resolved terahertz spectroscopy”. In: *Nano letters* 2.9 (2002), pp. 983–987.

[69] Nurhayati Ariffin et al. “Thiolate-Capped CdSe/ZnS core-shell quantum dots for the sensitive detection of glucose”. In: *Sensors* 17.7 (2017), p. 1537.

[70] Minho Noh et al. “Fluorescence quenching caused by aggregation of water-soluble CdSe quantum dots”. In: *Colloids and Surfaces A: Physicochemical and Engineering Aspects* 359.1-3 (2010), pp. 39–44.

[71] Klaus Boldt et al. “Characterization of the organic ligand shell of semiconductor quantum dots by fluorescence quenching experiments”. In: *ACS nano* 5.10 (2011), pp. 8115–8123.

[72] Boris Derjaguin and Lev Landau. “Theory of the stability of strongly charged lyophobic sols and of the adhesion of strongly charged particles in solutions of electrolytes”. In: *Progress in Surface Science* 43.1-4 (1993), pp. 30–59.

[73] Taehoon Kim et al. “Kinetics of gold nanoparticle aggregation: experiments and modeling”. In: *Journal of colloid and interface science* 318.2 (2008), pp. 238–243.

[74] MJ Grimson and M Silbert. "A self-consistent theory of the effective interactions in charge-stabilized colloidal dispersions". In: *Molecular Physics* 74.2 (1991), pp. 397–404.

[75] Tihamér Geyer, Philip Born, and Tobias Kraus. "Switching between crystallization and amorphous agglomeration of alkyl thiol-coated gold nanoparticles". In: *Physical review letters* 109.12 (2012), p. 128302.

[76] Dominik Gerstner and Tobias Kraus. "Rapid nanoparticle self-assembly at elevated temperatures". In: *Nanoscale* 10.17 (2018), pp. 8009–8013.

[77] Nicolas Goubet et al. "Which forces control supracrystal nucleation in organic media?" In: *Advanced Functional Materials* 21.14 (2011), pp. 2693–2704.

[78] Michael B Sigman, Aaron E Saunders, and Brian A Korgel. "Metal nanocrystal superlattice nucleation and growth". In: *Langmuir* 20.3 (2004), pp. 978–983.

[79] Bertrand Faure, German Salazar-Alvarez, and Lennart Bergström. "Hamaker constants of iron oxide nanoparticles". In: *Langmuir* 27.14 (2011), pp. 8659–8664.

[80] Glenn H Fredrickson, Andrea J Liu, and Frank S Bates. "Entropic corrections to the Flory-Huggins theory of polymer blends: Architectural and conformational effects". In: *Macromolecules* 27.9 (1994), pp. 2503–2511.

[81] Thomas Lindvig, Michael L Michelsen, and Georgios M Kontogeorgis. "A Flory–Huggins model based on the Hansen solubility parameters". In: *Fluid Phase Equilibria* 203.1-2 (2002), pp. 247–260.

[82] Robert Franklin Blanks and JM Prausnitz. "Thermodynamics of polymer solubility in polar and nonpolar systems". In: *Industrial & Engineering Chemistry Fundamentals* 3.1 (1964), pp. 1–8.

[83] Philip Born and Tobias Kraus. "Ligand-dominated temperature dependence of agglomeration kinetics and morphology in alkyl-thiol-coated gold nanoparticles". In: *Physical Review E* 87.6 (2013), p. 062313.

[84] Leyla Ramin and Ahmad Jabbarzadeh. "Odd–even effects on the structure, stability, and phase transition of alkanethiol self-assembled monolayers". In: *Langmuir* 27.16 (2011), pp. 9748–9759.

[85] Leyla Ramin and Ahmad Jabbarzadeh. "Effect of load on structural and frictional properties of alkanethiol self-assembled monolayers on gold: some odd–even effects". In: *Langmuir* 28.9 (2012), pp. 4102–4112.

[86] Yixuan Yu et al. "Nanocrystal superlattices that exhibit improved order on heating: an example of inverse melting?" In: *Faraday discussions* 181 (2015), pp. 181–192.

[87] Richard G Jones et al. "Terminology for aggregation and self-assembly in polymer science (IUPAC Recommendations 2013)". In: *Pure and Applied Chemistry* 85.2 (2012), pp. 463–492.

[88] Andrew K Boal et al. "Self-assembly of nanoparticles into structured spherical and network aggregates". In: *Nature* 404.6779 (2000), p. 746.

[89] David Doblas et al. "Colloidal solubility and agglomeration of apolar nanoparticles in different solvents". In: *Nano Letters* 19.8 (2019), pp. 5246–5252.

[90] Frank Schreiber. "Structure and growth of self-assembling monolayers". In: *Progress in surface science* 65.5-8 (2000), pp. 151–257.

[91] Albert M Hung, Nathan A Konopliv, and Jennifer N Cha. "Solvent-based assembly of CdSe nanorods in solution". In: *Langmuir* 27.20 (2011), pp. 12322–12328.

[92] Laurent Malaquin et al. “Controlled particle placement through convective and capillary assembly”. In: *Langmuir* 23.23 (2007), pp. 11513–11521.

[93] Shantang Liu et al. “Evaporation-induced self-assembly of gold nanoparticles into a highly organized two-dimensional array”. In: *Physical Chemistry Chemical Physics* 4.24 (2002), pp. 6059–6062.

[94] Rupa Mukhopadhyay et al. “Ordering of binary polymeric nanoparticles on hydrophobic surfaces assembled from low volume fraction dispersions”. In: *Journal of the American Chemical Society* 129.44 (2007), pp. 13390–13391.

[95] Cindy Y Lau et al. “Enhanced ordering in gold nanoparticles self-assembly through excess free ligands”. In: *Langmuir* 27.7 (2011), pp. 3355–3360.

[96] Ruiqiang Tao et al. “Critical impact of solvent evaporation on the resolution of inkjet printed nanoparticles film”. In: *ACS applied materials & interfaces* 10.27 (2018), pp. 22883–22888.

[97] Elena V Shevchenko et al. “Structural diversity in binary nanoparticle superlattices”. In: *Nature* 439.7072 (2006), pp. 55–59.

[98] Natalie A Frey and Shouheng Sun. “Magnetic nanoparticle for information storage applications”. In: *Inorganic Nanoparticles: Synthesis, Application, and Perspective* (2010), pp. 33–68.

[99] Orlin Dimitrov Velev, K Furusawa, and K Nagayama. “Assembly of latex particles by using emulsion droplets as templates. 1. Microstructured hollow spheres”. In: *Langmuir* 12.10 (1996), pp. 2374–2384.

[100] Vinayak Rastogi et al. “Synthesis of light-diffracting assemblies from microspheres and nanoparticles in droplets on a superhydrophobic surface”. In: *Advanced Materials* 20.22 (2008), pp. 4263–4268.

[101] Sanghyuk Wooh et al. “Synthesis of Mesoporous Supraparticles on Superamphiphobic Surfaces”. In: *Adv. Mater.* 27.45 (2015), pp. 7338–7343.

[102] Johann Lacava et al. “On the behaviour of nanoparticles in oil-in-water emulsions with different surfactants”. In: *Soft matter* 10.11 (2014), pp. 1696–1704.

[103] Bart de Nijs et al. “Entropy-driven formation of large icosahedral colloidal clusters by spherical confinement”. In: *Nat. Mater.* 14.1 (2015), pp. 56–60.

[104] D Zanchet, BD Hall, and D Ugarte. “Structure population in thiol-passivated gold nanoparticles”. In: *The Journal of Physical Chemistry B* 104.47 (2000), pp. 11013–11018.